Gutzwiller-RVB Theory of High Temperature Superconductivity:

Results from Renormalized Mean Field Theory and Variational Monte Carlo Calculations

Dissertation
zur Erlangung des Doktorgrades
der Naturwissenschaften

vorgelegt beim Fachbereich Physik
der Johann Wolfgang Goethe-Universität
in Frankfurt am Main

von
Bernhard Edegger
aus Deutschlandsberg

Frankfurt 2007

vom Fachbereich Physik
der Johann Wolfgang Goethe-Universität
als Dissertation angenommen.

Dekan:	Prof. Dr. W. Aßmus
Gutachter:	Prof. Dr. C. Gros Prof. Dr. P. W. Anderson

Datum der Disputation: 13.03.2007

Abstract of the thesis

We consider the theory of high temperature superconductivity from the viewpoint of a strongly correlated electron system. In particular, we discuss Gutzwiller projected wave functions, which incorporate strong correlations by prohibiting double occupancy in orbitals with strong on-site repulsion. After a general overview on high temperature superconductivity, we discuss Anderson's resonating valence bond (RVB) picture and its implementation by renormalized mean field theory (RMFT) and variational Monte Carlo (VMC) techniques. In the following, we present a detailed review on RMFT and VMC results with emphasis on our recent contributions. Especially, we are interested in spectral features of Gutzwiller-Bogoliubov quasiparticles obtained by extending VMC and RMFT techniques to excited states. We explicitly illustrate this method to determine the quasiparticle weight and provide a comparison with angle resolved photoemission spectroscopy (ARPES) and scanning tunneling microscopy (STM). We conclude by summarizing recent successes and by discussing open questions, which must be solved for a thorough understanding of high temperature superconductivity by Gutzwiller projected wave functions.

Contents

1 Introduction 5
- 1.1 Motivation 5
- 1.2 Experiments 7
  - 1.2.1 Angle resolved photoemission spectroscopy 9
  - 1.2.2 Scanning tunneling microscopy 16
- 1.3 Theories 17
  - 1.3.1 Electronic models 17
  - 1.3.2 Resonating valence bond picture 18
  - 1.3.3 Spin fluctuation models 18
  - 1.3.4 Inhomogeneity-induced pairing 19
  - 1.3.5 $SO(5)$ - theory 19
  - 1.3.6 Cluster methods 20
  - 1.3.7 Competing orders 20
  - 1.3.8 BCS-BEC crossover 21

2 Resonating valence bond concept 22
- 2.1 The RVB state - basic ideas 22
  - 2.1.1 RVB states in half-filled Mott-Hubbard insulators . . . 23
  - 2.1.2 RVB spin liquid at finite doping 25
- 2.2 Realizations and instabilities of the RVB state 25
- 2.3 Predictions of the RVB hypothesis for HTSC 28
- 2.4 Transformation from the Hubbard to the t-J model 30
- 2.5 Implementations of the RVB concept 32
  - 2.5.1 Gutzwiller projected wave functions 33
  - 2.5.2 Slave boson mean field theory (SBMFT) 34
- 2.6 Variational approaches to correlated electron systems 36
  - 2.6.1 Order parameters 36
  - 2.6.2 Jastrow correlators 37

3 Gutzwiller approximation 40
- 3.1 Basic principles of the Gutzwiller approximation 40

- 3.1.1 Counting arguments 41
- 3.1.2 Infinite dimensions 47
- 3.2 Canonical and grand canonical scheme 48
  - 3.2.1 Incorporation of a fugacity factor 49
  - 3.2.2 Singular particle number renormalization 51
  - 3.2.3 Gutzwiller renormalization factors 55
- 3.3 Partially projected states 58
  - 3.3.1 Occupancy of the reservoir site 59
  - 3.3.2 Renormalization of mixed hopping terms 61
  - 3.3.3 Comparison with VMC calculations 63

4 Renormalized mean field theory 65
- 4.1 Overview on the RMFT method 65
- 4.2 Derivation of the RMFT gap equations 67
  - 4.2.1 Derivation of the renormalized t-J Hamiltonian 67
  - 4.2.2 Mean field decoupling of the renormalized Hamiltonian 68
  - 4.2.3 Solutions of the RMFT gap equations 69
  - 4.2.4 Local $SU(2)$ symmetry in the half-filled limit 71
- 4.3 RMFT for the Hubbard model and application to HTSC . . . 73
  - 4.3.1 Generalized gap equations for the strong coupling limit 73
  - 4.3.2 Results from the generalized gap equations 75
- 4.4 Possible extensions and further applications 78
  - 4.4.1 Incorporation of antiferromagnetism 78
  - 4.4.2 Applications to inhomogeneous systems 80
  - 4.4.3 Gossamer superconductivity 81
  - 4.4.4 Time-dependent Gutzwiller approximation 82

5 Variational Monte Carlo calculations 83
- 5.1 Details on the VMC method 83
  - 5.1.1 Real space representation of the trial wave function . . 84
  - 5.1.2 Implementation of the Monte Carlo simulation 86
- 5.2 Improvements of the trial wave function 88
  - 5.2.1 Antiferromagnetism and flux states 89
  - 5.2.2 Increasing the number of variational parameters 90
- 5.3 Ground state properties - VMC results 92
  - 5.3.1 Superconducting gap and order parameter 92
  - 5.3.2 Derivation of spectral features 93
- 5.4 Investigation of the Pomeranchuk instability 98
  - 5.4.1 Isotropic lattice 99
  - 5.4.2 Anisotropic lattice 105

6 Quasiparticle states within RMFT 106
6.1 Coherent and incoherent spectral weight 106
    6.1.1 Sum rules for the spectral weight 107
    6.1.2 Definition of coherent quasiparticle excitations 108
    6.1.3 Incoherent background of the spectral weight 110
    6.1.4 Divergent **k**-dependent self-energy 110
6.2 Calculation of the quasiparticle weight within RMFT 111
    6.2.1 Norms of the quasiparticle excitations 111
    6.2.2 Gutzwiller approximation for the quasiparticle weight . 113
6.3 Quasiparticle weight for the Hubbard model 115
    6.3.1 Non monotonic behavior of the QP weight at $(\pi, 0)$ . . 117
6.4 Quasiparticle current renormalization 118
6.5 Fermi surface features in HTSC 122
    6.5.1 Fermi vs. Luttinger surface 123
    6.5.2 Fermi surface determination 124
    6.5.3 Renormalization of the Fermi surface 128

7 Quasiparticle states in the VMC scheme 131
7.1 Direct calculation of the quasiparticle weight 131
    7.1.1 Momentum dependence of the quasiparticle weight . . 133
    7.1.2 Doping dependence of the mean quasiparticle weight . 135
7.2 VMC calculations for the quasiparticle energy 137

8 Summary and outlook 140

A Deutsche Zusammenfassung 143

Bibliography 148

Curriculum Vitae 163

Veröffentlichungen 165

Danksagung 167

Chapter 1

Introduction

In this introduction we motivate this thesis on the Gutzwiller-RVB theory of high temperature superconductivity. We also give an overview on experimental observations in the high temperature superconductors (HTSC), where we concentrate on angle resolved photoemission spectroscopy (ARPES) and scanning tunneling microscopy (STM) due to their relevance for our theoretical considerations. At the end of the chapter, we briefly discuss a selection of alternative theories to illustrate the complexity and variety of the present field.

1.1 Motivation

Twenty years ago Bednorz and Müller [1] discovered high temperature superconductivity in Sr-doped La_2CuO_4. Subsequently high temperature superconductivity was reported in many other Cuprates, which all share a layered structure made up by one or more copper-oxygen planes (see figure 1.1). It was soon realized that the HTSC possess an insulating antiferromagnetic parent compound and become superconducting only if doped with holes or electrons. Such a behavior is fundamental different from any previously reported superconductor and clearly indicates the presence of a novel mechanism.

These unusual observations in the HTSC stimulated an enormous amount of experimental as well a theoretical works, which brought about numerous new insights into these fascinating compounds. The *d*-wave nature of the superconducting pairs [3] as well as the generic temperature-doping phase diagram

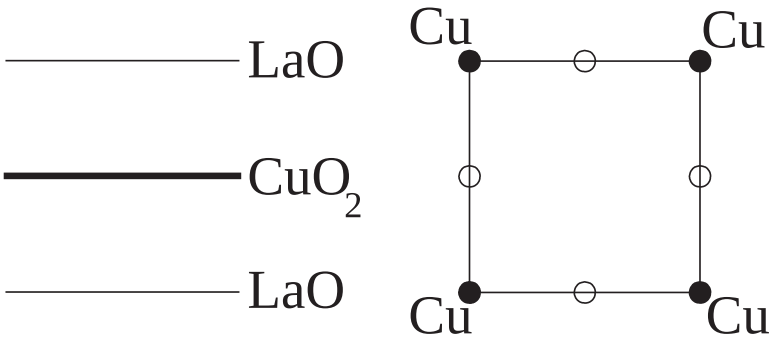

Figure 1.1: Crystal structure of La_2CuO_4. Left panel shows the layer structure along the c-axis, the right panel the structure of the CuO_2 plane. From [2].

(figure 1.2) are nowadays experimentally well established. On the theoretical side several approaches successfully describe at least some features of the HTSC. In addition, new sophisticated numerical techniques provide us with a better understanding of strong correlation effects present in the HTSC. This experimental and theoretical progresses in the field of high temperature superconductivity have also influenced substantially many other fields in condensed matter physics. Thus, the research on HTSC has a very fruitful history, which considerably broadened our knowledge on strongly correlated electron systems.

Despite above undeniable successes, there is still no generally agreement about the mechanism responsible for superconductivity in the Cuprates. However, as stated recently by D.J. Scalapino [4], the problem is not a lack of proposals, but rather that we do not have a consensus on which proposed mechanism contains the appropriate description. It is therefore of key importance to carefully examine the weaknesses and strengths of theoretical approaches and to check if calculable quantities match experimental observations. Only such thorough considerations can sort useful from inadequate ideas and lead to an improved understanding of the origin of the superconducting pairing in the Cuprates.

To contribute to this ambitious task, we carefully consider the resonating valence bond (RVB) concept from the perspective of Gutzwiller projected wave functions. We discuss the vast number of theoretical calculations based on this Gutzwiller-RVB picture in the context of our recent contributions [5, 6, 7, 8, 9, 10]. These studies are in general agreement with experimental observations, giving significant support for this approach. In this context, we pay particular attention to quasiparticle features determined from renor-

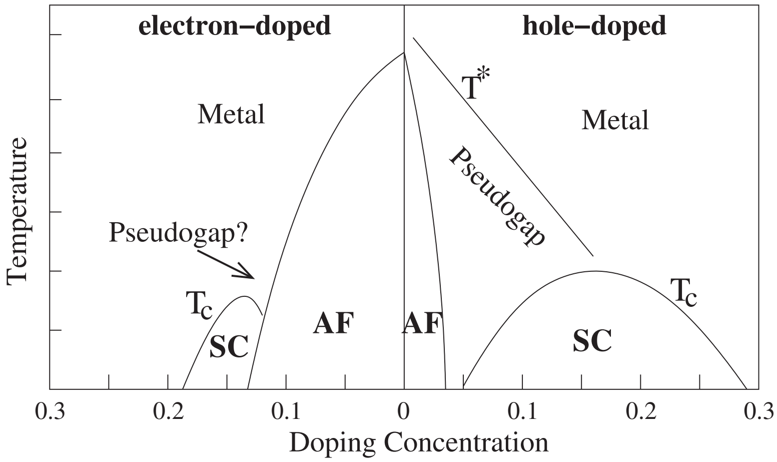

Figure 1.2: Generic phase diagram for the high temperature superconductors (antiferromagnetic region AF, superconducting phase SC). The temperature below which superconductivity (a pseudogap) is observed is denoted by T_c (T^*).

malized mean field theory (RMFT) and variational Monte Carlo (VMC) calculations, which qualitatively match with photoemission as well as tunneling experiments.

We are aware that the calculations presented within this thesis cannot cover all aspects of the HTSC problem. Thus we are not able to rule out other theories on the basis of current knowledge. To obtain a more complete picture today's Gutzwiller-RVB calculations should be extended and combined with useful concept of other theories, especially with regard to finite-temperature extensions of the $T = 0$ Gutzwiller-RVB results. In this spirit, the present work should provide a starting point for further studies clarifying if the Gutzwiller-RVB picture is indeed an appropriately description for the HTSC.

1.2 Experiments

The discovery of high temperature superconductivity presented a great challenge for condensed matter physicists and stimulated the development of numerous new experimental techniques. However, apart from some details on ARPES and STM experiments, we will only briefly mention major achievements. For a more detailed overview we refer to review articles with more general introductions [2, 3, 11, 12, 13, 14].

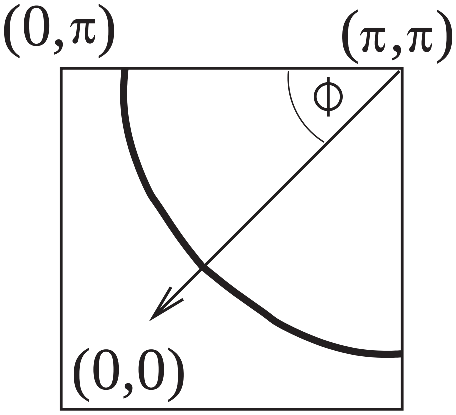

Figure 1.3: A schematic picture of the 2D Fermi surface (thick black line) of HTSC in the first quadrant of the first Brillouin zone. The lattice constant a is set to unity. The ϕ defines the Fermi surface angle.

One major experimental result was the unveiling of the generic temperature-doping phase diagram (see figure 1.2). It shows the antiferromagnetic phase in the undoped (half-filled[1]) compound with a Neel temperature of about $T_N \approx 300K$. Upon doping antiferromagnetism is suppressed and superconductivity with a characteristic dome like transition temperature (T_c) emerges. Electron- and hole-doped HTSC share many common features, however, they also exhibit some significant differences, *e.g.*, the antiferromagnetic region persists to much higher doping levels for electron-doped Cuprates.

For hole-doped compounds, on which we will concentrate since they are characterized experimentally better, a so-called pseudogap phase with a partially gapped excitation spectrum is clearly present above the superconducting dome. The onset temperature of the pseudogap linearly decreases with doping and disappears in the overdoped[2] regime. The origin of this pseudogap is one of the most controversial topics in the high-T_c debate, and it is not clear how it connects with other important features such as the presence of a Nernst phase [16, 17], charge inhomogeneities [18], the famous neutron scattering resonance [19], marginal Fermi liquid behavior [20], or disorder [21]. For a detailed and sound discussion of the pseudogap problem we refer to a recent article by Norman, Pines, and Kallin [12].

---

[1] The copper ion is in a d^9 configuration, so that there is a single hole in the d-shell per unit cell. According to Zhang and Rice [15] this situation corresponds to a half-filled band in an effective single-band model.

[2] The superconducting phase is often divided into an optimal doped (doping level with highest T_c), an overdoped (doping level higher than optimal doped), and an underdoped (doping level lower than optimal doped) regime.

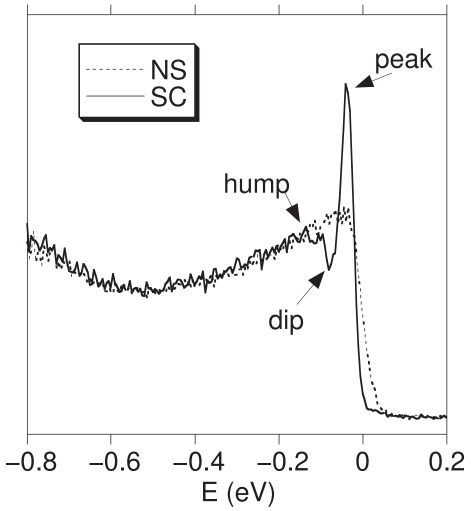

Figure 1.4: Energy distribution curve (EDC) at fixed momentum $\mathbf{k} = (\pi, 0)$ for an overdoped (87K) $Bi_2Sr_2CaCu_2O_{8+\delta}$ (Bi2212) sample in the normal state (NS) and superconducting state (SC). From [2].

Above cited articles summarize well the vast number of findings in the HTSC. In the following, we therefore explicitly discuss only results from angle resolved photoemission spectroscopy (ARPES) and scanning tunneling microscopy (STM), due to their particular importance for the theoretical considerations presented in the later chapters. These two methods have been significantly improved within recent years and provide new insights in the nature of quasiparticles within the superconducting state. As we will show in the following chapters, many features reported by these experiments can be well understood within the framework of the Gutzwiller-RVB theory.

1.2.1 Angle resolved photoemission spectroscopy

By measuring energy and momentum of photon-emitted electrons ARPES provides information about the single particle spectral function, $A(\mathbf{k}, \omega)$, which is related to the electron Green's function by $A(\mathbf{k}, \omega) = -\frac{1}{\pi}\text{Im}\, G(\mathbf{k}, \omega)$ (momentum $\mathbf{k}$, energy ω). Here, we present some key results for $A(\mathbf{k}, \omega)$ but omit discussions about technical details. Such information can be found in the extensive ARPES reviews by Damascelli, *et al.* [13] and Campuzano, *et al.* [14].

In figure 1.3 we illustrate a schematic picture of the two-dimensional (2D) Fermi surface (FS) of HTSC in the first quadrant of the first Brillouin zone.

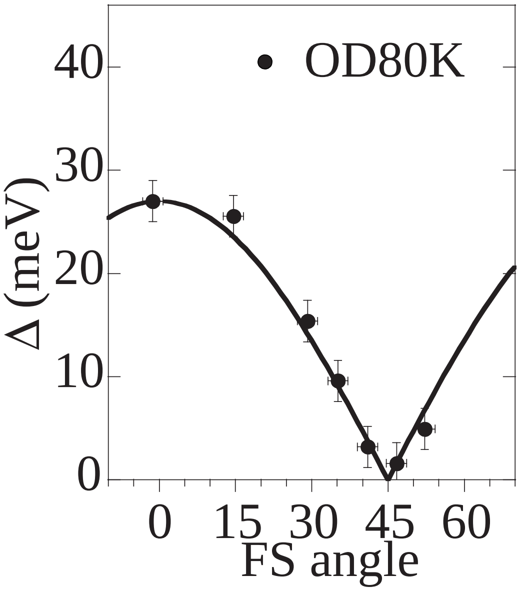

Figure 1.5: Momentum dependence of the spectral gap Δ at the FS in the superconducting state of an overdoped Bi2212 sample from ARPES. The black line is a fit to the data. For a definition of the FS angle ϕ see figure 1.3. From [22].

It can be obtained by ARPES scans along different angles ϕ. The FS for each ϕ is then determined in general (but not in the underdoped region [9]) by looking at the minimum energy of the coherent peak along this direction in momentum space. A typical energy distribution curve (EDC), *i.e.*, photoemission intensity as function of energy at fixed momentum, from an ARPES experiment is given by figure 1.4. In the figure the measurement is done at the $(\pi, 0)$-point in the superconducting state ($T \ll T_c$) as well as in the normal state ($T_c > T$). In the superconducting state one sees the characteristic peak-dip-hump structure; the peak can be associated with a coherent quasiparticle. Above T_c coherence is lost and the sharp peak disappears.

In the first years after the discovery of high temperature superconductivity it was rather unclear if the pairing symmetry is isotropic (s-wave like), as in conventional phonon-mediated superconductors, or anisotropic. Nowadays several experiments consistently confirm the anisotropic, *i.e.*, the d-wave, nature of the superconducting pairing [3]. The angular dependence of the gap function is nicely seen in ARPES measurements on HTSC (figure 1.5), which accurately determine the superconducting gap $|\Delta_{\mathbf{k}}|$ at the FS. As illustrated in figure 1.5 for a $Bi_2Sr_2CaCu_2O_{8+\delta}$ (Bi2212) sample, the gap vanishes for $\phi = 45°$. This direction is often referred as the "nodal direction", the point

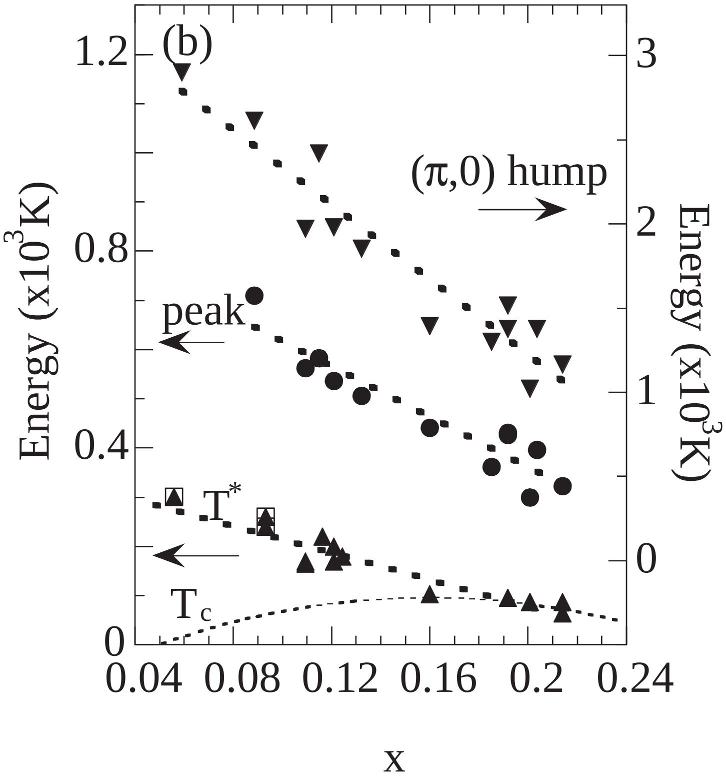

Figure 1.6: Doping dependence of T^* (the onset of the pseudogap, compare with figure 1.2), and of the peak and hump binding energies in the superconducting state (see figure 1.4). The empirical relation between T_c and doping x is given by $T_c/T_c^{\max} = 1 - 82.6(x - 0.16)^2$ with $T_c^{\max} = 95$ K. Data for Bi2212, from [23].

at the FS is then called the "nodal point" or "Fermi point". In contrary, the gap becomes maximal for $\phi = 0°$, $90°$, *i.e.*, at the "anti-nodal point".

Another feature well established by ARPES is the doping dependence of the superconducting gap and the opening of the pseudogap at T^*. Unlike conventional superconductors, HTSC exhibit a strong deviation from the BCS-ratio[3] of $2\Delta/(k_B T_c) \approx 4.3$ for superconductors with a d-wave gap function. In HTSC this ratio is strongly doping dependent and becomes quite large for underdoped samples, where the transition temperature T_c goes down, while the superconducting gap still grows. As illustrated in figure 1.6 for a Bi2212 sample, the binding energy of the peak at $(\pi, 0)$, *i.e.*, the superconducting gap[4], linearly increases when approaching half-filling. Interestingly, the open-

---

[3] Note that the conventional (s-wave) BCS-ratio is $2\Delta/(k_B T_c) \approx 3.5$.

[4] If we speak about (the magnitude of) the superconducting gap Δ in a d-wave state

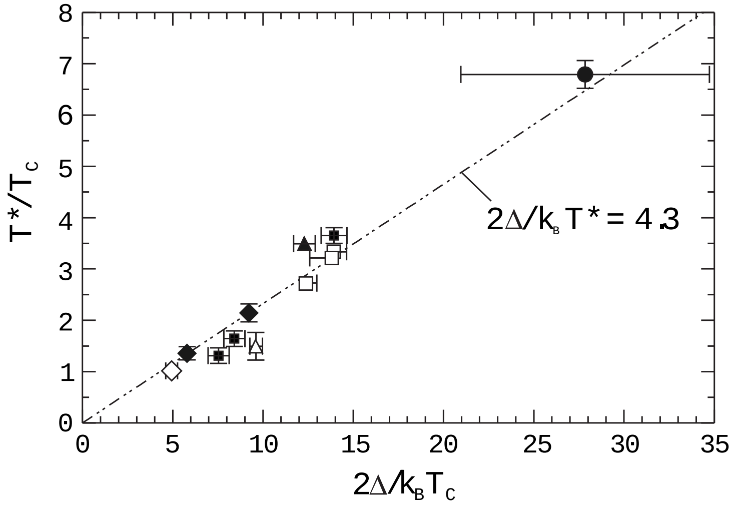

Figure 1.7: T^*/T_c versus $2\Delta/(k_B T_c)$ for various Cuprates compared to the mean field relation, $2\Delta/(k_B T^*) = 4.3$, valid for d-wave superconductivity [24], where T^* replaces T_c. From [25].

ing of the pseudogap at temperature T^* is tightly related to the magnitude of the gap. The modified ratio $2\Delta/(k_B T^*)$ is quite constant for HTSC at all doping levels and about 4.3 (see figure 1.7). This value agrees well with the BCS-ratio for a d-wave superconductor, although here T_c is substituted by T^*. This experimental result comes as a remarkable confirmation of early predictions from Gutzwiller-RVB theory, as we will discuss in further detail in latter chapters. Figure 1.6 also reveals that the hump feature (see EDC in figure 1.4) scales with the binding energy of the peak at $(\pi, 0)$.

An additional doping dependent feature extracted from ARPES data is the spectral weight of the coherent quasiparticle (QP) peak. Feng, *et al.* [26] defined a superconducting peak ration (SPR) by comparing the area under the coherent peak with those of the total spectral weight. Figure 1.8 depicts EDCs at several doping levels together with the computed SPR as a function of doping. The QP spectral weight strongly decreases with decreasing doping and finally vanishes. Such a behavior is well understood by invoking the projected nature of the superconducting state as we will discuss in following chapters.

ARPES is both a momentum and energy resolved probe and thus allows for the measurement of the dispersion of the coherent peak. Here, we concentrate on the nodal point, where the excitations become gapless even in the

---

without specifying the moment $\mathbf{k}$, we mean the size of the gap $|\Delta_{\mathbf{k}}|$ at $\mathbf{k} = (\pi, 0)$.

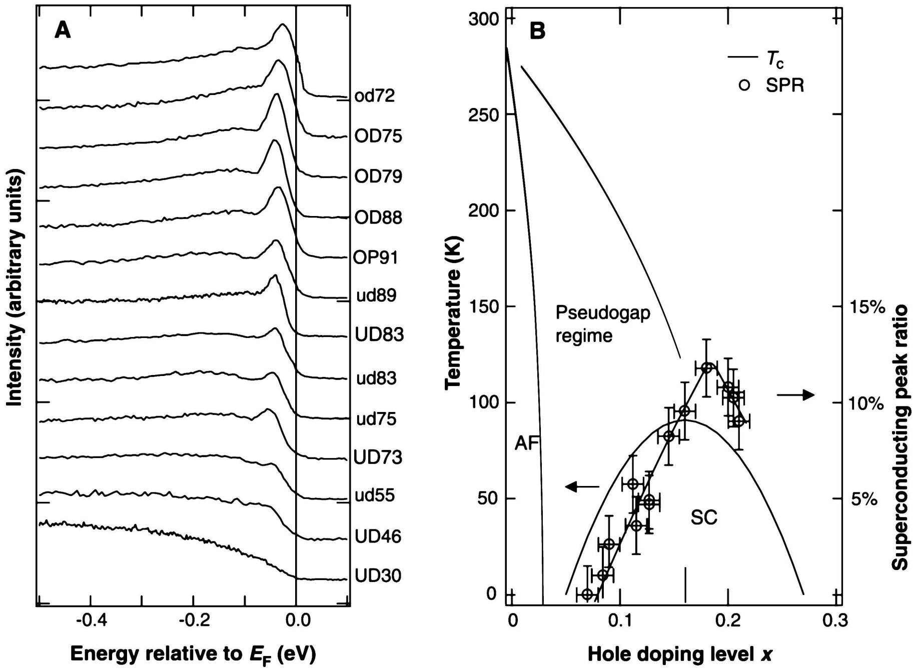

Figure 1.8: a) Doping dependence of the superconducting state spectra in Bi2212 at $(\pi, 0)$ taken at $T \ll T_c$. The doping level is decreasing form the top curve downwards. Samples are denoted by OD (overdoped), OP (optimal doped), and UD (underdoped), respectively, together with their T_c in Kelvin, *e.g.*, OD75 denotes an overdoped sample with $T_c = 75K$. b) The doping dependence of superconducting peak ratio (spectral weight of coherent peak with respect to the total spectral weight) is plotted over a typical Bi2212 phase diagram for the spectra in a). AF, antiferromagnetic regime; SC, superconducting regime. From [26].

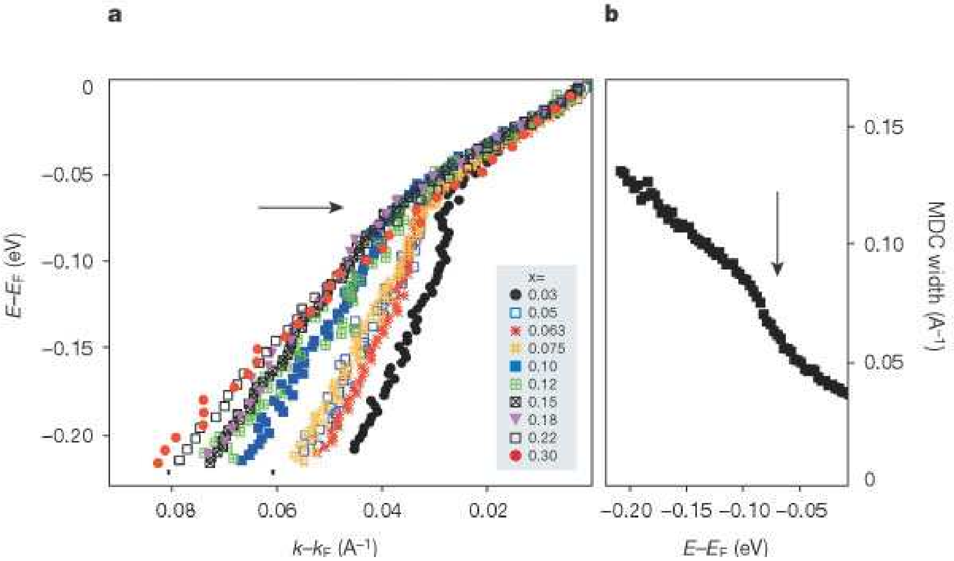

Figure 1.9: Electron dynamics in the $La_{2-x}Sr_xCuO_4$ (LSCO) system. a) Dispersion energy, E, as a function of momentum, $\mathbf{k}$, of LSCO samples with various dopings measured along the nodal direction. The arrow indicates the position of the kink that separates the dispersion into high-energy and low-energy parts with different slopes. E_F and $\mathbf{k}_F$, are Fermi energy and Fermi momentum, respectively. b) Scattering rate as measured by MDC width of the LSCO (x=0.063). From [27].

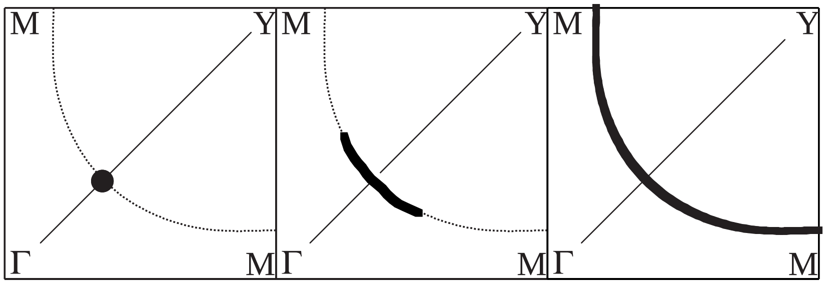

Figure 1.10: Schematic illustration of the temperature evolution of the Fermi surface in underdoped Cuprates as observed by ARPES. The *d*-wave node below T_c (left panel) becomes a gapless arc above T_c (middle panel) which expands with increasing T to form the full Fermi surface at T^* (right panel). From [31].

superconducting state due to the *d*-wave symmetry of the gap. The dispersion around the nodal point is well approximated by Dirac cones, whose shape is characterized by two velocity, v_F and v_Δ. The Fermi velocity v_F is determined by the slope of the dispersion along the nodal direction at the nodal point, whereas the gap velocity v_Δ is defined by the slope of the "dispersion" perpendicular to the nodal direction at the nodal point. Since all other **k**-points are gapped, the shape of the Dirac-like dispersion around the nodal point is of particular importance for the description of any effect depending on low-lying excitations.

Figure 1.9(a) illustrates the slope of the dispersion along the nodal direction for $La_{2-x}Sr_xCuO_4$ (LSCO) samples at various dopings. The ARPES data reveals a significant splitting in high-energy and low-energy parts, whereas the low-energy part corresponds to the Fermi velocity v_F. Within ARPES data [see figure 1.9(a)] the Fermi velocity v_F is only weakly doping-dependent. ARPES can also determine the gap velocity v_Δ by looking at the spectral gap along the Fermi surface as done in figure 1.5. Together with the v_F, the v_Δ determines the shape of the Dirac cones, which, according to ARPES, is quite anisotropic ($v_F/v_\Delta \approx 20$ around optimal doping) [22]. This result is confirmed by thermal conductivity measurements [28], which give similar asymmetries than the ARPES data. Another generic feature of HTSC is a kink seen in the ARPES nodal dispersion as shown in figure 1.9(a). This kink also effects the scattering rate of the coherent quasiparticles as measured by the momentum distribution curves (MDC) width, see figure 1.9(b) and [13, 14].

An interesting feature seen in ARPES is the shrinking of the Fermi surface

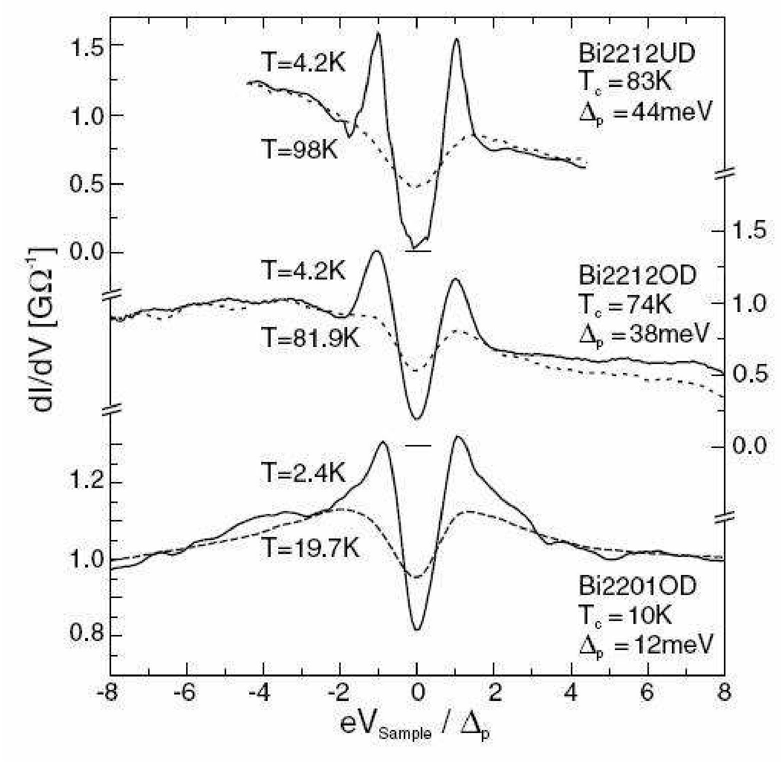

Figure 1.11: STM data for underdoped (UD) and overdoped (OD) Bi2212, and overdoped Bi2201; comparison between the pseudogap (dashed line, $T > T_c$) and the gap in the superconducting state (solid line, $T < T_c$). The underdoped data exhibit a significant asymmetry between positive and negative voltage. From [25].

when the pseudogap opens at T^*. With decreasing temperature more and more states around the antinodal region become gapped and thus the Fermi surface becomes continuously smaller. Instead of a full Fermi surface the pseudogap only exhibit Fermi arcs [29, 30, 31, 32], which finally collapse to single nodal Fermi points at $T = T_c$ (see figure 1.10). For more detailed discussions about this and further ARPES observations we refer to the above mentioned ARPES reviews [13, 14].

1.2.2 Scanning tunneling microscopy

In contrast to ARPES, STM is a momentum integrated probe. However, its ability to measure the local density of occupied as well as unoccupied states with a high energy resolution gives very valuable insights into HTSC. An example for a STM study of Bismuth-based HTSC is given in figure 1.11. The data for the superconducting state reveals a density of states, which is characteristic for a *d*-wave gap, *i.e.*, there is no full gap in contrast to *s*-wave superconductivity. In the pseudogap state (above T_c) the density of states is still suppressed around $\omega = 0$ (zero voltage), however, the characteristic peaks disappear. Another interesting feature seen in figure 1.11 is the striking asymmetry between positive and negative voltage, which becomes more pronounced for the underdoped sample. An explanation for this generic property of HTSC will be discussed in detail within the following chapters.

A key advantage of STM is the possibility to obtain spatial information. For example, STM experiments are able to investigate the electronic structure around impurities [33, 34, 35] as well as around vortex cores [36, 37, 38] in the superconducting state. Two other interesting features recently reported by STM are a checkerboard like charge density wave [39, 40] and the existence of spatial variations in the superconducting gaps [41]. The origin of these observations is presently under intensive discussion.

1.3 Theories

To give a brief overview on theories of high temperature superconductivity is quite a tough task. Due to the enormous complexity of the experimentally observed features it is difficult to agree on the key ingredients necessary for setting up a comprehensive theory. Further, the decision to trust or not to trust new experimental results is often hard, since the sample quality, the experimental resolution, and the way the data is extracted are often not completely clear. These circumstances have been a fertile ground for the development of numerous theoretical approaches, motivated respectively by distinct aspects of the HTSC.

1.3.1 Electronic models

To find an appropriate microscopic reference model is the first step in formulating any theory. Such a model should be simple enough on the one hand to be treated adequately, but on the other hand it must be complex enough to explain the relevant properties. In the case of the HTSC, it is widely accepted that strong correlations in the two-dimensional (2D) layers play an essential role. The copper-oxygen layers are appropriately described by a three-band Hubbard model, which includes the Cu $d_{x^2-y^2}$-orbital and the two O p-orbitals [42, 43]. Its simplified version is an one-band Hubbard model, where each site corresponds to a copper orbital with repulsive on-site interaction between electrons [15]. The derivation of this model Hamiltonian is well illustrated in the reviews of Lee, *et al.* [11] and Dagotto [44]. Although some theories deny that a one-band Hubbard model incorporates the key properties to understand high T_c superconductivity [42, 43], the majority of investigators consider it as an appropriate microscopic starting point for theoretical considerations. However, extracting physical properties from the two-dimensional Hubbard model[5] remains difficult and requires severe approximations, since it is still a highly complex many body problem.

1.3.2 Resonating valence bond picture

Soon after the discovery of high T_c superconductivity Anderson suggested the concept of a resonating valence bond (RVB) state [45] to be relevant for the HTSC. In this picture the half-filled Hubbard model is considered as a Mott insulator with one electron per site. The charged states, doublons and holons, form bound charge-neutral excitations in the Mott insulating state and electrical conductivity vanishes consequently. Equivalently one can talk of virtual hopping causing a superexchange interaction J between the electrons at the copper sites. Therefore, the half-filled systems can be viewed as Heisenberg antiferromagnet with a coupling constant J. Anderson proposed that upon doping quantum fluctuations melt the antiferromagnetic Neel lattice and yield a spin liquid ground state (denoted the RVB state) in which the magnetic singlet pairs of the insulator become the charged superconducting pairs. We will show in the following chapters that the RVB picture provides an explanation for several key features of the HTSC such as the shape of the superconducting dome, the existence of a pseudogap phase, the strong deviations from the BCS-ratio, and the singular **k**-dependence of the one-particle self-energy when approaching half-filling.

1.3.3 Spin fluctuation models

While the RVB idea approaches the problem from the strong coupling site, *i.e.*, large on-site electron repulsion U, spin fluctuation models[6] start from the weak coupling (small U) limit. The technique extends the Hartree Fock (HF) random phase approximation and leads to a pairing state with d-wave symmetry. Within this picture superconductivity is mediated by the exchange of antiferromagnetic spin fluctuations.

---

[5] In the following we always mean the one-band Hubbard model if we solely say Hubbard model.

[6] For more details we refer to the review articles by Moriya and Ueda [46], Yanase, *et al.* [47], and Chubukov, *et al.* [48].

Weak-coupling approaches as spin fluctuation models essentially remain within the context of Landau theory of Fermi liquids for which the quasiparticle renormalization is $Z = m/m^*$, whenever the self-energy is not strongly $\mathbf{k}$-dependent, where $m^* \sim v_F^{-1}$ and m the bare band mass, respectively. The Fermi liquid relation $Z \sim v_F$, is however difficult to reconcile with experimental results for the HTSC, as $Z \rightarrow 0$ and $v_F \rightarrow$ const for doping $x \rightarrow 0$, as we will discuss in more detail in section 6.1.4.

1.3.4 Inhomogeneity-induced pairing

This class of theories assumes that the superconducting pairing is closely connected to a spontaneous tendency to phase-separate into hole rich and hole poor regions at low doping. Then, the repulsive interaction could lead to a form of local superconductivity on certain mesoscale structures such as stripes. Calculations show that the strength of the pairing tendency decreases as the size of the structures becomes too large. The viewpoint of the theory is now as following: Below a critical temperature the fluctuating mesoscale structures condensate into a global phase-ordered superconducting state. Such a condensation will happen easier if the system is more homogeneous, however, that will cause larger mesoscale structures and thus less pairing. Therefore, the optimal T_c is obtained at an optimal inhomogeneity, where mesoscale structures are large enough to facilitate phase coherence, but also small enough to induce enough pairing. Within the phase-separation scenario spontaneous inhomogeneities tend to increase even in clean systems when approaching half-filling. In this framework the pseudogap in the underdoped regime can be understand as a phase, which is too granular to obtain phase coherence, but has strong local pairing surviving above T_c. These ideas are detailed reviewed by several papers of Kivelson and collaborators [18, 49, 50].

1.3.5 $SO(5)$ - theory

Motivated by the vicinity of antiferromagnetism and superconductivity in the phase diagram of the HTSC, the $SO(5)$-theory [51] attempts to unify these collective states of matter by a symmetry principle. In the $SO(5)$ picture the 5 stands for the five order parameters used to set up the theory; three degrees of freedom for antiferromagnetic state (N_x, N_y, N_z) and two degrees of freedom for the superconducting state (real and imaginary parts of the superconducting order parameter). On this foundations the rich phenomenology of HTSC is described through a single low-energy effective model. To incorporate strong correlation effects a so called projected $SO(5)$-theory was proposed. Several studies support tentatively the phenomenological $SO(5)$-approach on a microscopic basic (see review by Demler, *et al.* [51]).

1.3.6 Cluster methods

Exact numerical methods [44] like Lanczos or quantum Monte Carlo can only treat small clusters. Therefore, all statements about the thermodynamic limit become imprecise due to significant finite size effects. That yielded to the development of quantum cluster theories [52], which treat correlations within the cluster explicitly, and correlations at longer length scales either perturbatively or within a mean field approximation. Within recent years several different quantum cluster studies were used to extract ground state properties from the Hubbard model. Many studies were able to reproduce several features of the Cuprate phase diagram and report d-wave pairing in the Hubbard model. However, even these sophisticated numerical methods are not accurate enough to settle once forever if the Hubbard model has indeed a superconducting ground state.

1.3.7 Competing orders

In most of above mentioned theories the pseudogap is represented by preformed pairs. Hence, there are two relevant temperature for the underdoped regime. At T^* pairs form, but they are not phase coherent; only at T_c the pairs condensate and form a superconducting state. The intermediate region then gives a natural explanation for the pseudogap. However, there are another class of theories that assume that the pseudogap and superconductivity are two phases, which compete with each other. In these scenarios the pseudogap is characterized by an own order parameter, *e.g.*, given by an orbital current state [53] or a d-density wave [54], which is in reality a π-flux state. The pseudogap suppresses superconductivity in the underdoped regime, but also partially survives within the superconducting state. These approaches predict that the pseudogap line ends in a quantum critical point

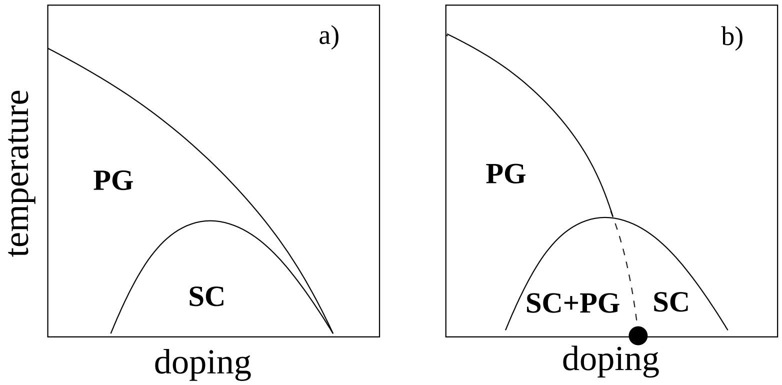

Figure 1.12: Two proposed theoretical phase diagrams for the Cuprates. a) RVB picture; b) Competing order scenario: the pseudogap (PG) ends in a quantum critical point (black dot); pseudogap and superconducting state (SC) can coexist (SC+PG).

which is screened by the superconducting dome. The obtained phase diagram is compared with a preformed pairs picture in figure 1.12.

1.3.8 BCS-BEC crossover

Within this scenario the pseudogap is explained by a crossover from BCS to Bose Einstein condensation (BEC) [55]. While in the BCS limit the fermionic electrons condensate to a superconducting pair state, the BEC limit describes the condensation of already existing pairs. In the crossover regime one expects a behavior very similar than observed in the pseudogap of HTSC; a formation of pairs with a corresponding excitation gap at a temperature T^*, but a condensation to a superconducting state only at significant lower temperature $T_c < T^*$. It is interesting to note that the physics behind this idea can be nicely described by a generalization of the BCS ground state wave function, $|\Psi_0\rangle$ [55]. It is however unclear how to incorporate the antiferromagnetic Mott-Hubbard insulating state close to half-filling within a BCS-BEC crossover scenario.

Chapter 2

Resonating valence bond concept

The resonating valence bond (RVB) state describes a liquid of spin singlets, which gives quite good variational energy for the 2D Heisenberg model. Upon doping the magnetic singlets of the RVB liquid become mobile and form charged superconducting pairs. This mechanism provides a promising approach for the HTSC as we will show in this chapter. We will discuss possible realizations of RVB superconductors together with predictions resulting from this picture. We also give a outlook on implementations of the RVB picture by Gutzwiller projected wave functions and slave boson mean field theory.

2.1 The RVB state - basic ideas

Within the resonating valence bond (RVB) picture strong electron correlations are essential for superconductivity in the Cuprates. The Hubbard model is viewed as an appropriate microscopic basis and the corresponding many-body Hamiltonian is given by,

$$H = -\sum_{\langle ij\rangle,\sigma} t_{(ij)} \left(c_{i\sigma}^{\dagger} c_{j\sigma} + c_{j\sigma}^{\dagger} c_{i\sigma} \right) + U \sum_{i} n_{i\uparrow} n_{i\downarrow} \ , \tag{2.1}$$

where $c_i^{\dagger}$ creates and c_i annihilates an electron on site i. The hopping integrals, $t_{(ij)}$, connect sites i and j. We will restrict our attention to nearest neighbor hopping t for the moment, later we will also discuss the influence of additional hopping terms. The operator $n_{i\sigma} \equiv c_{i\sigma}^{\dagger} c_{i\sigma}$ denotes the local

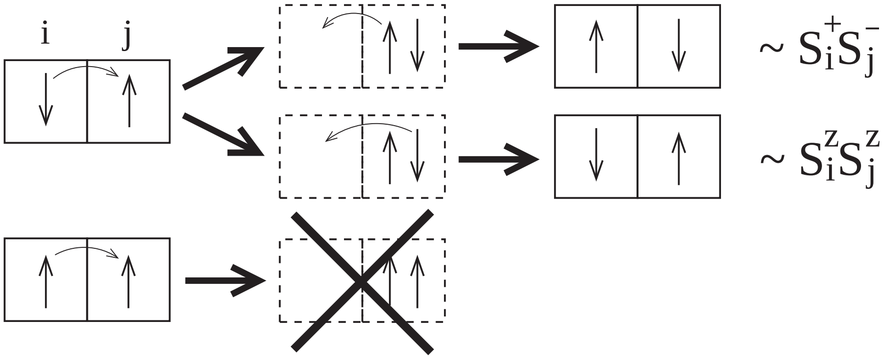

Figure 2.1: Hopping processes with a virtual doubly occupied site corresponding to the $S_i^z S_j^z$ and $S_i^+ S_j^-$ term of the Heisenberg Hamiltonian, respectively; in the case of parallel spins virtual hopping is not possible.

density of spin $\sigma = \downarrow, \uparrow$ on site i. We consider an on-site repulsion $U \gg t$, *i.e.*, we work in the strong coupling limit, which is a reasonable assumption for the HTSC.

2.1.1 RVB states in half-filled Mott-Hubbard insulators

We concentrate initially on the half-filled case. Since U is much larger than t the mean site occupancy is close to charge neutrality, namely one. If an electron wants to hop to a neighboring site it costs energy of the order U. This potential energy is much higher than the energy the electron can regain by the kinetic process. Thus, the motion of electrons is frozen and the half-filled lattice becomes a Mott-Hubbard insulator. However, there are virtual hopping processes, where an electron hops to its neighboring site, builds a virtual doubly occupied site, and hops back to the empty site. Such virtual hoppings lower the energy by an amount of the order $J = 4t^2/U$. Pauli exclusion principle allows double occupancy only for electrons with opposite spin (see figure 2.1). Thus, virtual hopping favors anti-parallel spins of neighboring electrons and we obtain an effective antiferromagnetic Heisenberg Hamiltonian,

$$H = J \sum_{\langle ij \rangle} \mathbf{S_i} \cdot \mathbf{S_j} \ , \qquad J > 0 \ , \tag{2.2}$$

with an antiferromagnetic exchange constant $J = 4t^2/U$, the spin-operator $\mathbf{S_i}$ on site i, and $\langle ij \rangle$ denoting a sum over nearest neighbor sites. On the mean field level, *i.e.*, treating the spins classical, the 2D Heisenberg model on a

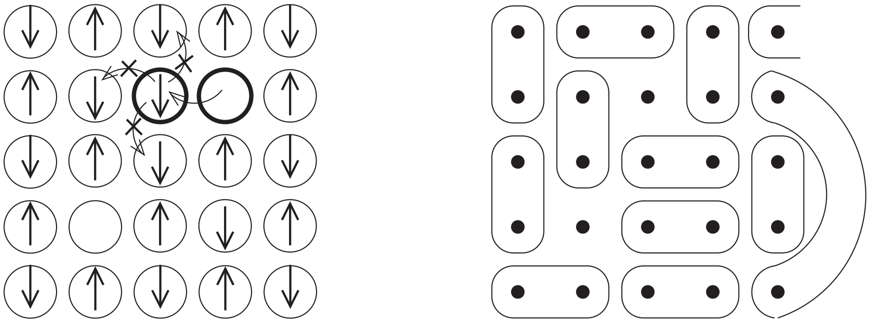

Figure 2.2: Left: Antiferromagnetic Neel lattice with some holes. The motion of a hole (consider bold circles) frustrates the antiferromagnetic order of the lattice. Right: Snapshot of the RVB state. A configuration of singlet pairs with some holes is shown. The RVB liquid is a linear superposition of such configurations.

square lattice has an antiferromagnetic Neel ground state with long range order and broken symmetry (left panel of figure 2.2). This molecular-field prediction is experimentally (by neutron scattering studies [56]) as well as theoretically (by a quantum nonlinear σ model [57]) well established.

Anderson [45] suggested that a resonating valence bond (RVB) liquid[1] is very close in energy to the Neel state for undoped Cuprates. Instead of long range antiferromagnetic order a fluid of singlet pairs is assumed, *i.e*, the state is built by a sum over all kind of spin singlet configurations (see right panel of figure 2.2). For spin $S = 1/2$, such singlets can be favored rather than classically antiparallel orientated spins due to quantum fluctuations. To explain this behavior, we consider an one-dimensional (1D) chain (see figure 2.3). In this case, a Neel state with $S_z = \pm 1/2$ gives an energy of $-J/4$ per site. On the other hand the ground state of two antiferromagnetic coupled spins $S = 1/2$ is a spin singlet with $-S\,(S+1)\,J = -3/4\,J$. It follows that a chain of singlets (see figure 2.3) has an energy of $-3/8\,J$ per site, much better than the Neel-ordered state. This simple variational argument shows that a singlet state is superior in 1D. Similar considerations for the 2D Heisenberg model give the energies $-1/2\,J$ per site for the Neel lattice, the singlet state remains at $-3/8\,J$ per site. Following this reasoning we find that singlets become much worse than the Neel state in higher dimensions.

Liang, Doucot, and Anderson [60] showed that the singlet "valence bonds" re-

---

[1] Long before the discovery of HTSC Anderson and Fazekas [58, 59] proposed the RVB liquid as a possible ground state for 2D triangular.

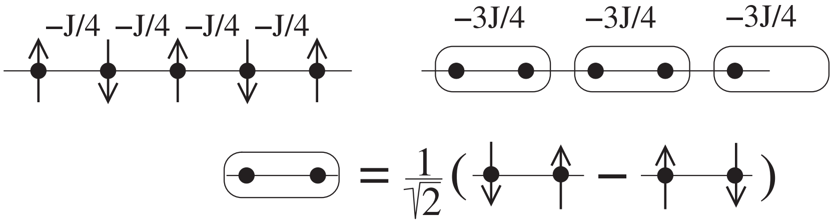

Figure 2.3: Neel state (left) and singlet state (right) for 1D antiferromagnetic spin $S = 1/2$ chain.

gain some of the lost antiferromagnetic exchange energy by resonating among many different singlet configurations and become therefore competitive with the Neel state in 2D. Above discussed resonating singlets are very similar to benzene rings with its fluctuating C-C links between a single and a double bond; an analogy that motivated the term “RVB”.

2.1.2 RVB spin liquid at finite doping

The Neel state is realized in the undoped insulator, but it melts with only a few percent of doped holes. To understand this, consider figure 2.2 (left), which shows that moving holes cause frustration in the antiferromagnetic but not the RVB state, figure 2.2 (right). A single hole moving in an antiferromagnetic spin background was intensively studied in literature[2], and analytical calculations showed that the coherent hole motion is strongly renormalized by the interactions with the spin excitations [61, 62]. When more holes are injected into the system, the interaction of the holes with the spin background completely destroys the antiferromagnetic Neel state and an RVB liquid (or spin liquid) state becomes superior in energy. Then the singlet pairs of the RVB liquid are charged and may condense to a superconducting ground state.

2.2 Realizations and instabilities of the RVB state

Wether there exist two dimensional models with an $T = 0$ RVB ground state is an open question todate. We may however regard the RVB state as an unstable fixpoint [63] prone to various instabilities. The situation is then analogous to that of the Fermi liquid, which becomes generically unstable in the low-temperature limit either towards superconductivity or the various magnetic orderings. In figure 2.4 we present an illustration of the concept of the RVB state as an unstable fixpoint. We discuss now this point.

---

[2] The single hole problem together with the corresponding literature is discussed in [11] in more detail.

Besides the simple square lattice with nearest neighbor hopping, the RVB spin liquid was proposed for the Mott insulating state in a square lattice with further neighbor hopping as well as in a triangular lattice. Although the simple Neel ordered state is destroyed due to frustration in these cases, the RVB spin liquid (at $n = 1$) does not become the ($T = 0$) ground state, which is either a valence bond crystal state [64, 65, 66, 67, 68] or a coplanar 120^o antiferromagnetic ordered state [69], respectively. In addition, instabilities against inhomogeneous states like stripes [18, 49, 50] are conceivable, but not explicitly included in figure 2.4.

Nevertheless an RVB state can be realized if a finite number of hole is induced into the system, *viz.*, when the bosonic spin state realized at half-filling turns into a free fermionic state by the introduction of charge carriers. The hopping processes then destroy above instabilities towards magnetic or valence bond crystal ordering and a superconducting RVB state can be stabilized. A schematic picture of this scenario is presented in figure 2.4.

In the case of HTSC, holes are created by changing the doping concentration. A similar mechanism was proposed for superconductivity in the triangular lattice based Cobaltates [70, 71]. Within RMFT calculations such a triangular model would result a $d+id$-wave pairing state [72]. On the other hand, an RVB superconducting state at half-filling just below the Mott transition was recently suggested for organic superconductors [73, 74, 75]. Here, the necessary holes could result from a finite number of conducting doubly occupied sites as illustrated in figure 2.4. In this case one might denote the resulting state as “gossamer superconductor”, as it is slaved to the metal-insulator transition occuring at half-filling for finite t/U in frustrated systems.

In summary, an RVB superconductor could emerge by two different mechanisms starting from a Mott insulating system ($n = 1$ and $U > U_c$); either upon doping ($n \neq 1$), or from the half-filled system close to the border line of the Mott-Hubbard transition ($U \sim U_c$). Within this thesis we investigate the former, *i.e.*, the occurrence of an RVB superconductor in a doped Mott-Hubbard insulator.

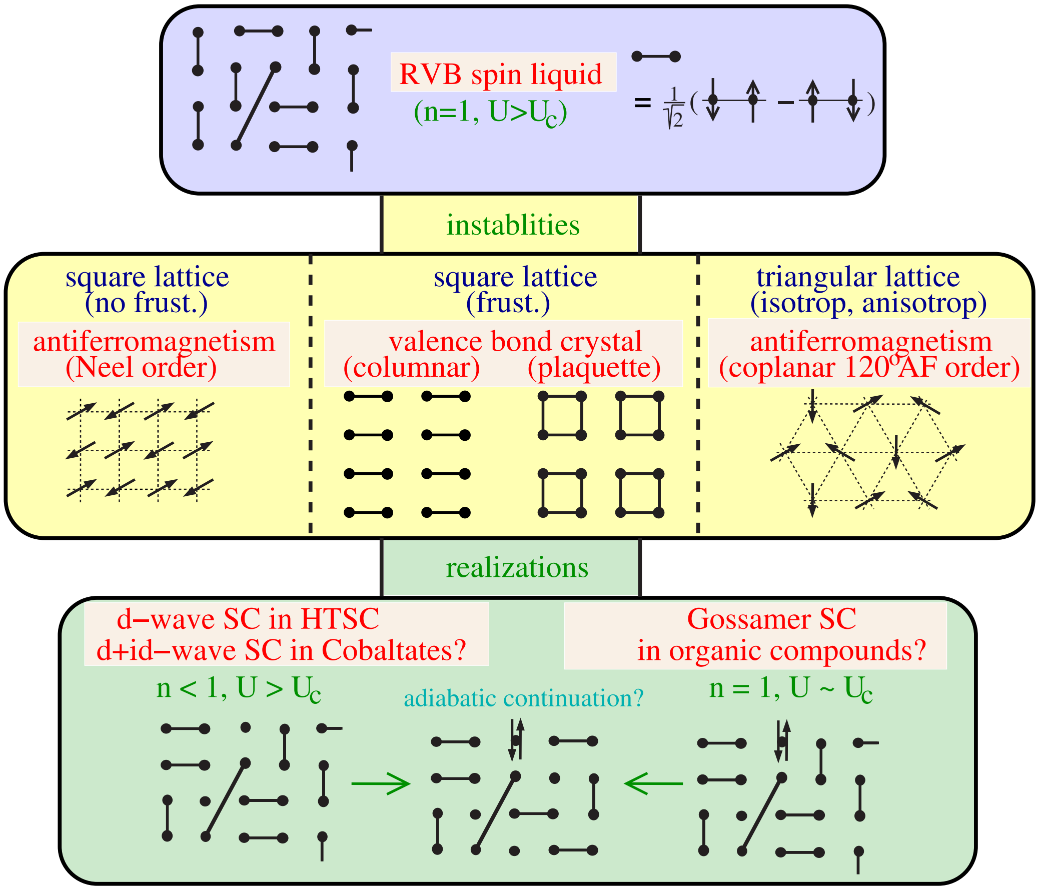
RVB spin liquid
(n=1, U>U$_c$)
$= \frac{1}{\sqrt{2}}(\downarrow\uparrow - \uparrow\downarrow)$
instablities
square lattice
(no frust.)
antiferromagnetism
(Neel order)
square lattice
(frust.)
valence bond crystal
(columnar)
(plaquette)
triangular lattice
(isotrop, anisotrop)
antiferromagnetism
(coplanar 120°AF order)
realizations
d−wave SC in HTSC
d+id−wave SC in Cobaltates?
Gossamer SC
in organic compounds?
n < 1, U > U$_c$
adiabatic continuation?
n = 1, U ~ U$_c$

Figure 2.4: Schematic picture of instabilities and realizations of the RVB spin liquid state, *viz.*, of the RVB state as an unstable fixpoint. The top panel shows an RVB spin liquid at half-filling in the Mott-Hubbard insulating limit ($U > U_c$). In the middle, we illustrate instabilities of the RVB liquid state in a square lattice, a frustrated square lattice, and a triangular lattice in the half-filled limit. The lower panel shows realizations of the RVB liquid, which are realized at finite doping or close to the Mott-Hubbard transition ($U \sim U_c$).

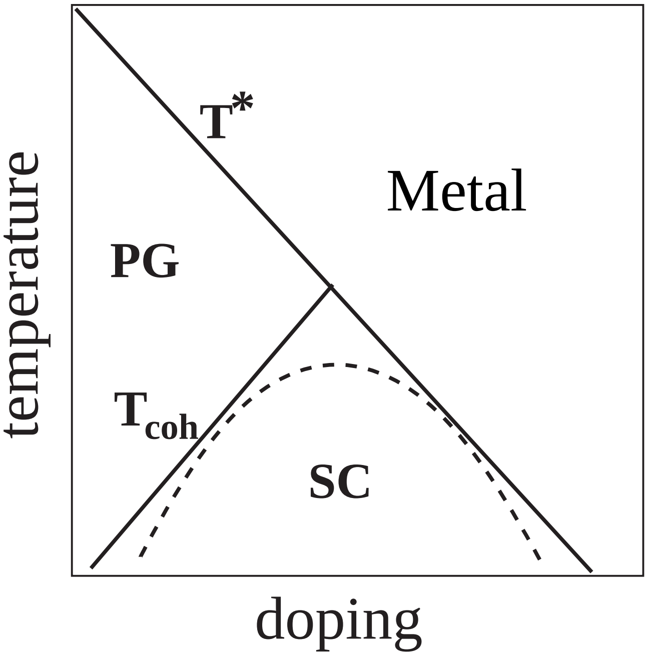

Figure 2.5: RVB phase diagram with singlet pairing temperature T^* and phase coherence temperature T_{coh} (superconducting state SC, pseudogap PG).

2.3 Predictions of the RVB hypothesis for HTSC

Within this section we discuss some predictions from RVB theory, which nicely agree with experimental observations. As we will show in following chapters, below explanations are well confirmed by more detailed microscopic calculations.

Within the RVB picture, a possible explanation for the temperature-doping phase diagram is obtained by considering two temperatures scales (figure 2.5). The singlets of the RVB liquid form at temperature T^*, which decreases when going away from half-filling. This is due to the weakening of singlet pairs by the increasing number of holes in between them. Holes, on the other hand, allow for particle number fluctuations, which are fully suppressed at half-filling, and thus enhence the stability of the superconducting state against thermal fluctuations. This results a second temperature, T_{coh}, which increases with doping and below which the superconducting carriers become phase coherent. The superconducting transition temperature T_c is therefore determined by the minimum of T^* and T_{coh} as shown in figure 2.5.

It is evident from above picture that a pseudogap forms for $T_{\text{coh}} < T < T^*$, *i.e.*, for underdoped samples. In this state, although phase coherence is lost, the RVB singlet pairs still exist. Therefore, we have to break a pair to remove an electron from the copper-oxygen layers within the pseudogap regime. The resulting excitation gap manifests itself, *e.g.*, in the c-axis conductivity or in ARPES measurements.

Above schematic explanations are to some extent confirmed by the $T = 0$ behavior seen in analytical as well as numerical calculations. RMFT and VMC methods show an increase of the superconducting gap, but a vanishing superconducting order parameter, when approaching half-filling. This behavior is agreement with the $T = 0$ observations in experiments. It also explains the strong deviation from the BCS-ratio in the underdoped regime of the HTSC, if we relate the superconducting order parameter to T_c. Furthermore, the doping dependence of the onset temperature of the pseudogap T^* can be related to the magnitude of the gap at $T = 0$ (in agreement with experiments, see figure 1.7).

Remarkably, the d-wave nature of the superconducting state was predicted by RVB based studies already in 1988 [76, 77, 78, 79, 80], long before the pairing symmetry was experimentally established. This early calculations also correctly described the vanishing of superconductivity above about 30% doping.

Implementing the RVB idea by projected wave functions, explains the suppression of the Drude weight and of the superfluid density in the underdoped regime as well as the particle-hole asymmetry in the density of states. As a further success, RVB calculations predict a rather constant nodal Fermi velocity, but a quasiparticle weight deceasing with doping x in agreement with ARPES experiments. These effects can be understood by a decrease of freely moving carriers at low doping, which results in a dispersion mainly determined by virtual hopping processes (proportional to the superexchange J). In the half-filled limit, this behavior results in a divergence of the $\mathbf{k}$-dependence of the electron's self-energy, $\lim_{\omega\to 0} \partial\Sigma(\omega, \mathbf{k} = \mathbf{k}_F)/\partial\omega \sim 1/x \to \infty$, which transcends the nature of orthodox Fermi liquids, as discussed in more detail in chapters 6 and 7.

Beyond above key features of HTSC, RVB theory was successfully applied to several other problems such as charge density patterns [81, 82, 83, 84], the interplay between superconductivity and antiferromagnetism [85, 86, 87, 88, 89, 90], impurity problems [91, 92, 93], and vortex cores [94, 95].

In conclusion, analytical and numerical results give significant support to the RVB concept. However, most RVB studies are restricted to zero temperature[3], making above finite temperature picture somewhat speculative. Within the RVB picture the superconductivity in the underdoped samples is destroyed by the suppression of particle number fluctuations close to half-filling, or otherwise stated, by a loss of phase coherence due to phase fluctuations [97]. It is presently an unsettled question to which extend this picture is equivalent to alternative formulations, such as an increase of inhomogeneities (like in the "inhomogeneity-induced pairing" picture [18, 49, 50]) or a destruction of the superfluid density due to nodal quasiparticle excitations (see section 6.4), which were also proposed in order to describe the transition from the RVB superconducting state to the pseudogap state in the underdoped regime. Further work is necessary to unambiguously clarify this point.

2.4 Transformation from the Hubbard to the t-J model

The RVB scenario rests on the existence of a strong antiferromagnetic superexchange J. The superexchange process via virtual hopping processes results in an effective Heisenberg Hamiltonian as discussed before, see figure 2.1. For a more formal derivation we consider a canonical transformation, e^{-iS}, of the Hubbard Hamiltonian in the strong coupling limit ($U \gg t$) to remove off-diagonal processes, *i.e.*, hopping processes that change the number of double occupancies and thus involve energies of the order U. Such a transformation makes the Hamiltonian block diagonal in subspaces with a fixed number of double occupancies. By restricting ourselves to the energetically lowest subspace, *viz.*, the subspace of no double occupancies, we find an effective low energy Hamiltonian.

We evaluate now the canonical transformation in lowest order in t/U [98, 99]. First we assume that S is of the order $\mathcal{O}(t/U)$ and expand the transformation as,

---

[3] A possible ansatz for finite temperatures was recently proposed by Anderson [96]. He suggests a spin-charge locking mechanism within the Gutzwiller-RVB theory to describe the pseudogap phase in the underdoped Cuprates as a vortex liquid state.

$$\begin{aligned}
H^{(eff)} &= e^{iS} H e^{-iS} = e^{iS}(\hat{T}+\hat{U})e^{-iS} && \text{(2.3a)}\\
&= \hat{T}+\hat{U} + i\,[S,\ \hat{T}+\hat{U}] + \frac{i^2}{2}\,[S,[S,\hat{T}+\hat{U}]] + \ldots && \text{(2.3b)}\\
&= \hat{U} + \underbrace{\hat{T}+i[S,\hat{U}]}_{\mathcal{O}(t)} + \underbrace{i\,[S,\hat{T}] + \frac{i^2}{2}\,[S,[S,\hat{U}]]}_{\mathcal{O}(t^2/U)} + \underbrace{\ldots}_{\mathcal{O}(t^3/U^2)}\,. && \text{(2.3c)}
\end{aligned}$$

Here, we split the Hubbard Hamiltonian H into the kinetic energy part $\hat{T}$, the first term of (2.1), and the potential energy part $\hat{U}$, the second term of (2.1) (includes the parameter U). In (2.3c) we have ordered the terms with respect to t/U. For a block diagonal Hamiltonian $H^{(eff)}$ in order $\mathcal{O}(t/U)$, the term, $\hat{T}+i\,[S,\hat{U}]$, in (2.3c) may not contain any hopping processes changing the total number of doubly occupied sites. An appropriate choice for S is given by,

$$S = -i \sum_{\langle ij\rangle,\sigma} \frac{t_{(i,j)}}{U} \left(a^\dagger_{i,\sigma} d_{j,\sigma} + a^\dagger_{j,\sigma} d_{i,\sigma} \ - \ \text{h.c.} \right)\ , \tag{2.4}$$

because then,

$$\hat{T} + i\,[S,\hat{U}] = - \sum_{\langle ij\rangle,\sigma} t_{(ij)} \left(a^\dagger_{i\sigma} a_{j\sigma} + d^\dagger_{i\sigma} d_{j\sigma} + \ \text{h.c.} \right)\ , \tag{2.5}$$

does not involve hopping process changing the number of double occupancies. Here, we used the operators $a^\dagger_{i,\sigma} \equiv (1-n_{i,-\sigma})c^\dagger_{i,\sigma}$ and $d^\dagger_{i,\sigma} \equiv n_{i,-\sigma}c^\dagger_{i,\sigma}$. Equation (2.5) is block diagonal and verifies the choice of S in (2.4).

The full form of $H^{(eff)}$ is now obtained by evaluating all $\mathcal{O}(t^2/U)$-terms in (2.3c) with S from (2.4). By restricting ourselves to the subspace of no double occupancies (energetically the lowest subspace), we find the t-J Hamiltonian,

$$H_{t-J} \equiv P_G\, H^{(eff)}\, P_G = P_G\, (\, T + H_J + H_3\,)\, P_G\ , \tag{2.6}$$

where,

$$P_G = \sum_i (1 - n_{i\uparrow}\, n_{i\downarrow})\ , \tag{2.7}$$

is the Gutzwiller projection operator that projects out all doubly occupied sites. The terms of the Hamiltonian are given by,

$$\begin{aligned} T &= -\sum_{\langle i,j\rangle,\sigma} t_{(i,j)} \left(c^\dagger_{i,\sigma} c_{j,\sigma} + c^\dagger_{j,\sigma} c_{i,\sigma} \right) \ , & (2.8) \\ H_J &= \sum_{\langle i,j\rangle} J_{(i,j)} \left(\mathbf{S}_i \, \mathbf{S}_j - \frac{1}{4} n_i n_j \right) \ , & (2.9) \\ H_3 &= -\sum_{i,\tau_1 \neq \tau_2,\sigma} \frac{J_{(i+\tau_1,i,i+\tau_2)}}{4} c^\dagger_{i+\tau_1,\sigma} c^\dagger_{i,-\sigma} c_{i,-\sigma} c_{i+\tau_2,\sigma} \\ & \quad + \sum_{i,\tau_1 \neq \tau_2,\sigma} \frac{J_{(i+\tau_1,i,i+\tau_2)}}{4} c^\dagger_{i+\tau_1,-\sigma} c^\dagger_{i,\sigma} c_{i,-\sigma} c_{i+\tau_2,\sigma} \ , & (2.10) \end{aligned}$$

where $J_{(i,j)} = 4t^2_{(i,j)}/U$ and $J_{(i,j,l)} = 4t_{(i,j)}t_{(j,l)}/U$. $\langle i,j\rangle$ are pairs of neighbor sites and $i + \tau_{(1,2)}$ denotes a neighbor site of i. Equation (2.6), together with (2.8)-(2.10), gives the full form of t-J Hamiltonian. However, the so-called correlated hopping or three-site term H_3 is often dropped in literature, since its expectation value is proportional both to t^2/U and the doping level x. Further, the density-density contribution $n_i n_j$ is sometimes neglected within the superexchange term H_J, as it is a constant at half-filling. Note that (2.8) is equivalent to (2.5) due to the projection operators P_G occuring in the definition (2.6) of the t-J Hamiltonian.

Above calculations explain the effect of the superexchange processes for the Hubbard model in the strong coupling limit. The resulting t-J Hamiltonian (2.6) does not allow for double occupancies and therefore each site becomes single occupied at half-filling. In this limit ($n \to 1$), the hopping of electrons is frozen, the kinetic energy vanishes, and the t-J Hamiltonian reduces to an antiferromagnetic Heisenberg model (2.2).

2.5 Implementations of the RVB concept

For an implementation of the RVB concept, the t-J Hamiltonian (2.6) is more suitable than the Hubbard model, because it directly includes the superexchange term, which is responsible for the formation of singlets. However, for exact numerical methods, the t-J Hamiltonian provides only a minor simplification over the Hubbard Hamiltonian, and we must turn to approximative schemes for any calculations on sufficiently large clusters. In the following, we view the t-J Hamiltonian as an appropriate microscopic basis for the HTSC, and present two prevalent methods, which allow for systematic calculations within the RVB picture.

2.5.1 Gutzwiller projected wave functions

Anderson [45] proposed projected BCS wave functions as possible RVB trial states for the t-J model. These states provide a suggestive way to write an RVB liquid in the compact form[4],

$$|\Psi_{\rm RVB}\rangle = P_N\, P_G\, |{\rm BCS}\rangle \;, \tag{2.11}$$

with the BCS wave function

$$|{\rm BCS}\rangle = \prod_{\mathbf{k}} \left(u_{\mathbf{k}} + v_{\mathbf{k}} c^\dagger_{\mathbf{k}\uparrow} c^\dagger_{-\mathbf{k}\downarrow} \right) |0\rangle \;, \tag{2.12}$$

which constitutes a singlet pairing state. Here, the operator P_G (Gutzwiller projection operator) projects out double occupancies and the P_N fixes the particle number to N; $u_{\mathbf{k}}$ and $v_{\mathbf{k}}$ are the variational parameters with the constraint, $u^2_{\mathbf{k}} + v^2_{\mathbf{k}} \equiv 1$. This notation for $|\Psi_{\rm RVB}\rangle$ allows for a straightforward treatment of doping and immediately suggests a connection to superconductivity.

Projected wave functions were originally proposed by Gutzwiller in 1963 to study the effect of correlations presumed to induce ferromagnetism in transition metal compounds [100]. In the following years these wave functions were applied to study the Mott-Hubbard metal insulator transition [101] and for a description of liquid ^{3}He as an almost localized Fermi liquid [98, 102, 103], to give a few examples. However, these early studies considered only a projected Fermi sea,

$$P_G|\Psi_{\rm FS}\rangle \;=\; P_G \prod_{\mathbf{k}<\mathbf{k}_F} c^\dagger_{\mathbf{k}\uparrow} c^\dagger_{\mathbf{k}\downarrow} |0\rangle \;, \tag{2.13}$$

in the Hubbard model, whereas Anderson [45] suggested a projected BCS paired wave function for the t-J model.

To calculate the variational energy of a projected state $|\Psi\rangle \equiv P_G|\Psi_0\rangle$, expectation values of the form

$$\frac{\langle\Psi_0|\, P_G\, \hat{O}\, P_G\, |\Psi_0\rangle}{\langle\Psi_0|P_G P_G|\Psi_0\rangle} \tag{2.14}$$

must be considered, where $\hat{O}$ is a suitable operator. Here, the $|\Psi_0\rangle$ can be any wave function with no restriction in the number of double occupancies, *viz.*, it lives in the so-called “pre-projected” space. In our case we concentrate on $|\Psi_0\rangle = |\mathrm{BCS}\rangle$. In section 2.6 we will give a short review of other types of trial wave functions used to study correlated electron systems. The exact evaluation of (2.14) is quite sophisticated and requires variational Monte Carlo (VMC) techniques that will be discussed in chapter 5. However, approximate analytical calculations can be done by a renormalization scheme based on the Gutzwiller approximation (GA), which will be outlined in the chapters 3 and 4. Within this approximation, the effects of projection on the state $|\Psi_0\rangle$ are approximated by a classical statistical weight factor multiplying the expectation value with the unprojected wave function [102], *i.e.*,

---

[4] For a real space representation of equation (2.11) we refer to section 5.1.1.

$$\frac{\langle\Psi_0|\, P_G\, \hat{O}\, P_G\, |\Psi_0\rangle}{\langle\Psi_0|P_G P_G|\Psi_0\rangle} \;\approx\; g_O\, \frac{\langle\Psi_0|\hat{O}|\Psi_0\rangle}{\langle\Psi_0|\Psi_0\rangle} \quad . \tag{2.15}$$

The so-called Gutzwiller renormalization factor g_O only depends on the local densities and is derived by Hilbert space counting arguments [76, 102, 104] or by considering the limit of infinite dimensions ($d = \infty$) [105, 106, 107, 108]. The GA shows good agreement with VMC results (see [76]) and is discussed detailed in chapter 3.

Implementing the RVB idea by Gutzwiller projected wave functions provides a successful approach for studying HTSC. As we will show in the following chapters, this Gutzwiller-RVB theory explains several key features of the HTSC.

2.5.2 Slave boson mean field theory (SBMFT)

An alternative representation of the t-J Hamiltonian, equation (2.6), is obtained by removing the projection operators P_G, and replacing the creation and annihilation operators by

$$c^\dagger_{i,\sigma} \;\rightarrow\; \tilde{c}^\dagger_{i,\sigma} = c^\dagger_{i,\sigma}\,(1 - n_{i,-\sigma})\ , \text{ and} \tag{2.16a}$$

$$c_{i,\sigma} \;\rightarrow\; \tilde{c}_{i,\sigma} = c_{i,\sigma}\,(1 - n_{i,-\sigma})\ , \tag{2.16b}$$

with $\sigma = \uparrow, \downarrow$ and $-\sigma$ denoting the opposite spin of σ. In this form the restriction to no double occupation is fulfilled by the projected operators $\tilde{c}^\dagger_{i,\sigma}$ and $\tilde{c}_{i,\sigma}$. Thus, only empty and single occupied sites are possible, which can be expressed by the local inequality

$$\sum_\sigma \langle \tilde{c}^\dagger_{i,\sigma} \tilde{c}_{i,\sigma}\rangle \leq 1. \tag{2.17}$$

However, the new operators do not satisfy the fermion commutation relations, which makes an analytical treatment difficult. The slave-boson method [109, 110, 111] handles this problem by decomposing $\tilde{c}^{\dagger}_{i,\sigma}$ into a fermion operator $f^{\dagger}_{i,\sigma}$ and a boson operator b_i via

$$\tilde{c}^{\dagger}_{i\sigma} = f^{\dagger}_{i,\sigma} b_i \ . \tag{2.18}$$

The physical meaning of $f^{\dagger}_{i,\sigma}$ ($f_{i,\sigma}$) is to create (annihilate) a single occupied site with spin σ, those of b_i ($b^{\dagger}_i$) to annihilate (create) an empty site. Since every site can either by single occupied by an ↑-electron, single occupied by a ↓-electron, or empty the new operators must fulfill the condition

$$\langle f^{\dagger}_{i\uparrow} f_{i\uparrow} + f^{\dagger}_{i\downarrow} f_{i\downarrow} + b^{\dagger}_i b_i \rangle = 1 \ \ . \tag{2.19}$$

When writing the Hamiltonian solely by the fermion and the (slave) boson operator this constraint (2.19) must be included by a Lagrangian multiplier λ_i. In the slave-boson representation, the t-J model is thus written as,

$$\begin{aligned} H_{t-J} = & - \sum_{\langle i,j\rangle,\sigma} t_{(i,j)} \left(f^{\dagger}_{i,\sigma} b_i b^{\dagger}_j f_{j,\sigma} + f^{\dagger}_{j,\sigma} b_j b^{\dagger}_i f_{i,\sigma} \right) \\ & - \sum_{\langle i,j\rangle} J_{(i,j)} \left(f^{\dagger}_{i\uparrow} f^{\dagger}_{j\downarrow} - f^{\dagger}_{i\downarrow} f^{\dagger}_{j\uparrow} \right) \left(f_{i\downarrow} f_{j\uparrow} - f_{i\uparrow} f_{j\downarrow} \right) \\ & - \mu_0 \sum_{i,\sigma} f^{\dagger}_{i,\sigma} f_{i,\sigma} + \sum_i \lambda_i \left(f^{\dagger}_{i\uparrow} f_{i\uparrow} + f^{\dagger}_{i\downarrow} f_{i\downarrow} + b^{\dagger}_i b_i - 1 \right) \ , \end{aligned} \tag{2.20}$$

where the Heisenberg exchange term,

$$\mathbf{S}_i \, \mathbf{S}_j - \frac{1}{4} n_i n_j = - \left(f^{\dagger}_{i\uparrow} f^{\dagger}_{j\downarrow} - f^{\dagger}_{i\downarrow} f^{\dagger}_{j\uparrow} \right) \left(f_{i\downarrow} f_{j\uparrow} - f_{i\uparrow} f_{j\downarrow} \right) \ ,$$

is a function of fermion operators only, since it does not involve charge degrees of freedom [112]. Furthermore, a chemical potential term, $-\mu_0 \sum_{i,\sigma} f^{\dagger}_{i,\sigma} f_{i,\sigma}$, is included within the grand canonical ensemble.

The advantage of this representation is that the operators ($f_{i\sigma}$, b_i) obey standard algebra and can thus be treated using field theoretical methods. The partition function Z of (2.20) can be written as a functional integral over coherent Bose and Fermi fields, allowing to calculate observables in the original Hilbert space. The Fermi fields can be integrated out using standard Grassmann variables. Then carrying out a saddle-point approximation for the Bose fields reproduces the mean field level. The incorporation of Gaussian fluctuations around the saddle point approximation provides a possibility for systematic extensions of the SBMFT. Following this idea led to the development of the $U(1)$-gauge and $SU(2)$-gauge theory, which are reviewed in detail in a recent work by Lee, *et al.* [11]. In general, the results from SBMFT are quite similar to those from RMFT, *e.g.*, the early prediction of d-wave superconductivity in the t-J model rests on very similar gap equations in both schemes. The SBMFT result by Kotliar and Liu [77], and Suzumura, *et al.* [78] and the RMFT result by Zhang, *et al.* [76] nearly simultaneously appeared in 1988. For a more detailed review on SBMFT we refer to [11]. In the following chapter, we will only mention SBMFT calculations when comparing them to the RMFT results.

2.6 Variational approaches to correlated electron systems

In this section, we briefly discuss how projected states,

$$|\Psi\rangle = P_G|\Psi_0\rangle \ , \tag{2.21}$$

can be extended to study strongly correlated systems on a wide variational basis. Apart from the HTSC, these states can then be applied to other important topics such as the description of Mott insulators [113], the superconductivity in organic compounds [75, 114], or Luttinger liquid behavior in the t-J model [115, 116].

2.6.1 Order parameters

A prevalent ansatz to extend the trial state (2.21) is to allow for additional order parameters in the mean field wave function $|\Psi_0\rangle$. In section 2.5.1, we restricted ourselves to a superconducting BCS wave function $|\Psi_0\rangle = |\mathrm{BCS}\rangle$. However, antiferromagnetic [86, 85, 87, 88], π-flux [88, 117], or charge ordered [81, 82, 83, 84] mean field wave functions can also be used for $|\Psi_0\rangle$. In addition, a combination of different kind of orders is possible. As an example we give a trial wave function,

$$|\Psi_0\rangle = \prod_{\mathbf{k}} \left(u_{\mathbf{k}} + v_{\mathbf{k}}\, b^\dagger_{\mathbf{k}\uparrow}\, b^\dagger_{-\mathbf{k}\downarrow} \right) |0\rangle \quad , \tag{2.22}$$

with

$$b_{\mathbf{k}} = \alpha_{\mathbf{k}} c_{\mathbf{k}\sigma} + \sigma \beta_{\mathbf{k}} c_{\mathbf{k}+\mathbf{Q}} \ . \tag{2.23}$$

Equation (2.22) includes finite superconducting as well as antiferromagnetic order [86]. Here, $b_{\mathbf{k}}$ is the Hartree-Fock spin-wave destruction operator with $\mathbf{Q} = (\pi, \pi)$ as required for a commensurate antiferromagnet. The parameters, $\alpha_{\mathbf{k}}$ and $\beta_{\mathbf{k}}$ are related to the antiferromagnetic order parameter Δ_{AF} by usual mean field relations; in analogy the superconducting order parameter determines the values of $v_{\mathbf{k}}$ and $u_{\mathbf{k}}$. In the chapters 4 and 5, we will discuss applications of above wave function for the HTSC.

We note that $|\Psi_0\rangle$ is applicable to all kind of lattice geometries and was also used to study superconductivity in triangular lattice based Cobaltates [69, 70, 71, 72] and organic compounds [73, 74, 75, 114]. Recent calculations show that projected states also provide a competitive energy on more exotic models such as a spin-1/2 Heisenberg model on a Kagome lattice [118].

2.6.2 Jastrow correlators

The incorporation of Jastrow correlator $\mathcal{J}$ [119] provides an additional powerful way for extending trial wave functions. In (2.21), the original Gutzwiller projector P_G can be viewed as the simplest form of a Jastrow correlator,

$$P_G = \mathcal{J}_g = g^{\sum_i n_{i,\uparrow} n_{i,\downarrow}} = \prod_i (1 - (1-g) n_{i,\uparrow} n_{i,\downarrow}) \ . \tag{2.24}$$

So far we have considered P_G in the fully projected limit, which corresponds to $g \to 0$ in J_g. However, when using (2.24) in the Hubbard model, g becomes a variational parameter that controls the number of doubly occupied sites.

The variational freedom of the trial wave function can be increased by including further Jastrow correlators,

$$|\Psi\rangle \ = \ \mathcal{J}_s \, \mathcal{J}_{hd} \, \mathcal{J}_d \, P_G \, |\Psi_0\rangle \ = \ \mathcal{J}_s \, \mathcal{J}_{hd} \, \mathcal{J}_d \, \mathcal{J}_g \, |\Psi_0\rangle \ . \tag{2.25}$$

Popular choices of Jastrow correlators are the density-density correlator $\mathcal{J}_d$,

$$\mathcal{J}_d = \exp\left(- \sum_{(i,j)} v_{ij} (1 - n_i)(1 - n_j) \right) , \tag{2.26}$$

the holon-doublon correlator $\mathcal{J}_{hd}$,

$$\mathcal{J}_{hd} = \exp\left(- \sum_{(i,j)} w_{ij} (h_i d_j + d_i h_j) \right) , \tag{2.27}$$

with $h_i = (1 - n_{i\uparrow})(1 - n_{i\downarrow})$ and $d_i = n_{i\uparrow} n_{i\downarrow}$, and the spin-spin correlator $\mathcal{J}_s$,

$$\mathcal{J}_s = \exp\left(- \sum_{(i,j)} u_{ij} S_i^z S_j^z \right) \ . \tag{2.28}$$

The corresponding variational parameter are given by v_{ij}, w_{ij}, and u_{ij}, respectively.

Since the generalized trial wave function (2.25) includes a very high number of variational parameters, many authors do not take all Jastrow correlators into account. In the case of the t-J model the situation is slightly simplified, because double occupancies are forbidden and thus $g \to 0$ and $w_{ij} = 0$.

We now discuss the properties of the density-density correlator in (2.26) and assume $u_{ij} = w_{ij} = 0$ for a moment. A positive v_{ij} implies density-density repulsion, a negative v_{ij} means attraction and may lead to phase separation. Several studies indicate the importance of long range density-density Jastrow correlators for improving the variational energy. Hellberg and Mele [115] showed that the one-dimensional t-J model can be accurately described when $v_{i,j} \sim \log|i - j|$, *i.e.*, when the Jastrow correlator is scale invariant. The incorporation of long-ranged density-density correlations induces Luttinger liquid like behavior in the t-J model [115, 116]. In the one-dimensional Hubbard model an appropriate choice of the density-density correlator in momentum space allows to distinguish between metallic and insulating behavior [113]. In the two-dimensional t-J model, the $\mathcal{J}_d$ is often used to improves the variational energy of a projected superconducting state [120, 121] as we will discuss in section 5.2.

The holon-doublon Jastrow correlator $\mathcal{J}_{hd}$ is important for studying the repulsive Hubbard model on a variational basis. A negative $w_{i,j} < 0$ implies attraction of empty and doubly occupied sites and may induce a Mott-Hubbard insulating state [75, 114]. In two dimensions, a negative nearest neighbor $w_{i,j} \sim -\delta_{\langle ij \rangle}$, substantially decreases the variational energy [75, 114], since these states occur as intermediate states during the superexchange process (compare figure 2.1). Combining these effect with a superconducting wave function $|\Psi_0\rangle = |\mathrm{BCS}\rangle$ then explains key aspects of superconductivity in organic compounds near the Mott-Hubbard transition [75, 114]. The w_{ij} seems to be less important for one dimension, probably a consequence of the very good spin-spin correlation energy of the Gutzwiller wave function in one dimension [98, 122].

The spin-spin Jastrow correlator $\mathcal{J}_s$ is not as often used as the density-density and the holon-doublon Jastrow correlators ($\mathcal{J}_d$ and $\mathcal{J}_{hd}$). However, recent studies show that the inclusion of $\mathcal{J}_s$ is important when considering charge fluctuations within the two-dimensional t-J model [123]. An appropriate spin-spin Jastrow correlator $\mathcal{J}_s$ can also create antiferromagnetic order in a non-magnetic wave function, an example for the ability of Jastrow correlators to induce a new long-range order in a wave function.

Chapter 3

Gutzwiller approximation

The Gutzwiller approximation (GA) is straightforward method to handle Gutzwiller projected wave functions, which incorporate strong electron correlations by prohibiting doubly occupied sites. Within the GA, effects of projection are absorbed by statistical weight factors (Gutzwiller renormalization factors), which then allow for an analytical treatment of strongly correlated Gutzwiller wave functions.

In this chapter, we present the derivation of the Gutzwiller factors by Hilbert space counting argument as well as by considering the limit of infinite dimensions. We discuss furthermore the relevance of fugacity factors within the GA when comparing results to variational Monte Carlo (VMC) calculations in the canonical and grand canonical scheme, respectively. As we will show in the last section of this chapter, the GA can also be extended to the case of partially projected wave functions, where one reservoir site is excepted from projection.

3.1 Basic principles of the Gutzwiller approximation[1]

The Gutzwiller approximation (or Gutzwiller renormalization scheme) constitutes the basis of the RMFT and is a successful method to treat Hilbert space restrictions due to strong electron correlations. Originally [100, 101] it was applied to calculate the variational energy of the projected Fermi sea, $P_G|FS\rangle$, in Hubbard like models. In this context, the projection operator, $P_G = \sum_i (1 - \alpha\, \hat{n}_{i\uparrow}\hat{n}_{i\downarrow})$, was generalized to partial projection with the parameter α determined by optimizing the energy. Such considerations for partially projected states resulted in a successful modeling of normal liquid ^{3}He [102, 124] and heavy fermion systems [125, 126].

---

[1] To avoid confusions we always mark density operators with a "hat" within this section. We write, *e.g.*, $\hat{n}_{i\sigma} = c^{\dagger}_{i\sigma} c_{i\sigma}$.

We concentrate, here, however, onto the t-J model and the large U limit, and we will mainly discuss the fully projected case, *i.e.*, $\alpha = 1$. We will derive the corresponding renormalization factors (Gutzwiller renormalization factors) in this limit, but do not discuss the generalization to finite double occupancy, which can easily be obtained through the same reasoning. The GA,

$$\frac{\langle\Psi_0|\, P_G\hat{O}\, P_G\,|\Psi_0\rangle}{\langle\Psi_0|P_G P_G|\Psi_0\rangle} \;\approx\; g_O\,\frac{\langle\Psi_0|\hat{O}|\Psi_0\rangle}{\langle\Psi_0|\Psi_0\rangle} \quad , \tag{3.1}$$

approximates the expectation value within the projected state $P_G\,|\Psi_0\rangle$ by a corresponding statistical weight g_O multiplying the matrix element within the unprojected wave function $|\Psi_0\rangle$. To determine the Gutzwiller renormalization factor g_O we can either invoke Hilbert space counting arguments [76, 102, 104], or consider the limit of infinite dimensions ($d = \infty$) [105, 106, 107, 108]. In the following, we review both techniques and compare the respective results.

3.1.1 Gutzwiller renormalization factors by counting arguments

Hilbert space counting arguments enable us to derive the renormalization factor g_O through simple physical reasoning. We may use,

$$g_O \;\approx\; \frac{\langle\hat{O}\rangle_\Psi}{\langle\hat{O}\rangle_{\Psi_0}} \tag{3.2}$$

with $|\Psi\rangle \equiv P_G|\Psi_0\rangle$, as a "definition" for the factor g_O; $\langle ...\rangle_\Psi$ denotes the expectation value with respect to a wave function $|\Psi\rangle$. The spirit of the GA rests on calculating the ratio in (3.2) by neglecting correlations in the wave functions $|\Psi\rangle$ and $|\Psi_0\rangle$. The only quantities to be taken into account are the probabilities for a site i to be empty, to be single occupied with spin σ, and to be doubly occupied, respectively. These probabilities are obtained by considering the Hilbert space restrictions and are summarized for $|\Psi\rangle$ and $|\Psi_0\rangle$ in table 3.1. In this context, we must be aware that the densities before projection (n_i^0, $n_{i\downarrow}^0$ and $n_{i\uparrow}^0$) and after projection (n_i, $n_{i\downarrow}$ and $n_{i\uparrow}$) may differ. This is due to the projection operator, $P_G = \prod_i (1 - \hat{n}_{i\downarrow}\hat{n}_{i\uparrow})$, which can, *e.g.*, remove more terms with an $\uparrow$-electron than a $\downarrow$-electron on site i. Such effects become of importance for Gutzwiller projection in antiferromagnetic, charge ordered, or grand-canonical states. Keeping this caveat in mind, the expectation values in (3.2) can be approximated by considering the probability amplitudes of "bar"- and "ket"-configurations that may contribute. We obtain the Gutzwiller renormalization factor by calculating the ratio between these approximative expectation values. Although, we neglect any off-site correlations in the derivation of the Gutzwiller renormalization factor, the GA itself (3.1) incorporates additional correlations by the expectation value of $\hat{O}$ in $|\Psi_0\rangle$.

To illustrate above scheme, we consider the expectation value of the hopping element, $\langle c_{i\uparrow}^\dagger c_{j\uparrow}\rangle$. For a projected state, $|\Psi\rangle = P_G|\Psi_0\rangle$, we can write

$$\langle c_{i\uparrow}^\dagger c_{j\uparrow}\rangle_\Psi = \langle (1-\hat{n}_{i\downarrow}) c_{i\uparrow}^\dagger (1-\hat{n}_{j\downarrow}) c_{j\uparrow}\rangle_\Psi \ . \tag{3.3}$$

We then perform the GA for the right hand side of (3.3), which is written in terms of projected operators $(1-\hat{n}_{i\downarrow})c_{i\uparrow}^\dagger$ and $(1-\hat{n}_{j\downarrow})c_{j\uparrow}$. It is convenient to rewrite the matrix elements in this manner before determining the GA, since it guarantees agreement with the infinite dimensions approach. Next we consider the probability for $\langle (1-\hat{n}_{i\downarrow}) c_{i\uparrow}^\dagger (1-\hat{n}_{j\downarrow}) c_{j\uparrow}\rangle$ in $|\Psi\rangle$ and $|\Psi_0\rangle$. Configurations can only contribute if the bra-vector has a single $\uparrow$-electron on site i and a vacancy on site j. For the ket-vector the interchanged occupancies are necessary, *i.e.*, a single $\uparrow$-electron on site j, and a vacancy on site i. The corresponding hopping process is illustrated in figure 3.1. With the help of table 3.1 we find the amplitudes of the bra- and ket-contribution, whose product gives the probability in $|\Psi\rangle$,

$$\left[n_{i\uparrow}(1-n_j)\right]^{1/2} \cdot \left[n_{j\uparrow}(1-n_i)\right]^{1/2} \ , \tag{3.4}$$

occupancy on site i	probabilities	
	in $\lvert\Psi\rangle$	in $\lvert\Psi_0\rangle$
$\langle(1-\hat{n}_{i\downarrow})(1-\hat{n}_{i\uparrow})\rangle$	$1-n_i$	$(1-n_{i\downarrow}^0)(1-n_{i\uparrow}^0)$
$\langle\hat{n}_{i\downarrow}(1-\hat{n}_{i\uparrow})\rangle$	$n_{i\downarrow}$	$n_{i\downarrow}^0(1-n_{i\uparrow}^0)$
$\langle\hat{n}_{i\uparrow}(1-\hat{n}_{i\downarrow})\rangle$	$n_{i\uparrow}$	$n_{i\uparrow}^0(1-n_{i\downarrow}^0)$
$\langle\hat{n}_{i\downarrow}\hat{n}_{i\uparrow}\rangle$	0	$n_{i\downarrow}^0 n_{i\uparrow}^0$

Table 3.1: Probability for different occupancies on site i in $|\Psi\rangle$ and $|\Psi_0\rangle$. We distinguish between the densities before projection (n_i^0, $n_{i\downarrow}^0$ and $n_{i\uparrow}^0$) and after projection (n_i, $n_{i\downarrow}$ and $n_{i\uparrow}$).

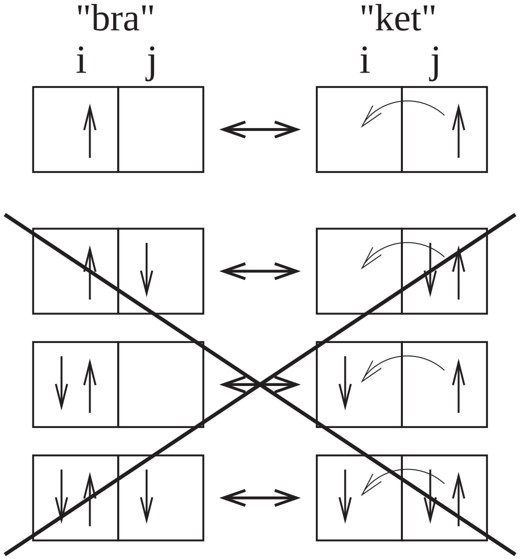

Figure 3.1: Required bar- and ket-configurations, so that $\langle(1-\hat{n}_{i\downarrow})c^\dagger_{i\uparrow}(1-\hat{n}_{j\downarrow})c_{j\uparrow}\rangle$ contributes in $|\Psi\rangle$ and $|\Psi_0\rangle$. Configurations that do not contribute to $\langle(1-\hat{n}_{i\downarrow})c^\dagger_{i\uparrow}(1-\hat{n}_{j\downarrow})c_{j\uparrow}\rangle$ are crossed out.

and in $|\Psi_0\rangle$,

$$\left[n^0_{i\uparrow}(1-n^0_{i\downarrow})(1-n^0_{j\downarrow})(1-n^0_{j\uparrow})\right]^{1/2}\cdot\left[n^0_{j\uparrow}(1-n^0_{j\downarrow})(1-n^0_{i\downarrow})(1-n^0_{i\uparrow})\right]^{1/2}\ . \tag{3.5}$$

The square roots stem from the fact that both bra- and ket-vector only provide amplitudes; the probability is obtained by a product of two amplitudes.

Combining (3.4) and (3.5) yields

$$\frac{\langle(1-\hat{n}_{i\downarrow})c^\dagger_{i\uparrow}(1-\hat{n}_{j\downarrow})c_{j\uparrow}\rangle_{|\Psi\rangle}}{\langle(1-\hat{n}_{i\downarrow})c^\dagger_{i\uparrow}(1-\hat{n}_{j\downarrow})c_{j\uparrow}\rangle_{|\Psi_0\rangle}}$$

$$\approx\tilde{g}_t=\frac{1}{(1-n^0_{i\downarrow})(1-n^0_{j\downarrow})}\cdot\frac{\left[n_{i\uparrow}(1-n_j)n_{j\uparrow}(1-n_i)\right]^{1/2}}{\left[n^0_{i\uparrow}(1-n^0_{j\uparrow})n^0_{j\uparrow}(1-n^0_{i\uparrow})\right]^{1/2}}\ . \tag{3.6}$$

The expectation value in $|\Psi\rangle$ is now obtained by renormalizing the unprojected value by (3.6),

$$\begin{aligned}\langle c^\dagger_{i\uparrow}c_{j\uparrow}\rangle_\Psi &= \langle(1-\hat{n}_{i\downarrow})c^\dagger_{i\uparrow}(1-\hat{n}_{j\downarrow})c_{j\uparrow}\rangle_\Psi && \text{(3.7a)}\\ &\approx \tilde{g}_t\ \langle(1-\hat{n}_{i\downarrow})c^\dagger_{i\uparrow}(1-\hat{n}_{j\downarrow})c_{j\uparrow}\rangle_{\Psi_0} && \text{(3.7b)}\\ &\approx \underbrace{\tilde{g}_t\ (1-n^0_{i\downarrow})(1-n^0_{j\downarrow})}_{=g_t}\ \langle c^\dagger_{i\uparrow}c_{j\uparrow}\rangle_{\Psi_0}\ . && \text{(3.7c)}\end{aligned}$$

In the last row of (3.7) we decoupled the densities in $|\Psi_0\rangle$. The Gutzwiller renormalization factor is then,

$$g_t = \frac{\left[n_{i\uparrow}(1-n_j)n_{j\uparrow}(1-n_i)\right]^{1/2}}{\left[n^0_{i\uparrow}(1-n^0_{j\uparrow})n^0_{j\uparrow}(1-n^0_{i\uparrow})\right]^{1/2}} \ . \tag{3.8}$$

We emphasize that the decoupling in (3.7c) is controlled by the infinite dimensions limit, *viz.*, all neglected decouplings yield off-site correlations of higher order[2] and thus vanish for $d = \infty$. Violating this rule causes deviations from the mathematical thoroughness of the infinite dimension scheme.

For the full determination of the Gutzwiller renormalization factor in (3.8), it is necessary to evaluate the dependence of the densities after projection relative to the densities prior to projection. The situation is particularly simple for a homogeneous wave functions with fixed particle number and spin symmetry, where $n^0_{i\uparrow} = n^0_{i\downarrow} = n^0_i/2 = n/2$ on each site i. Then, $n_{i\uparrow} = n_{i\downarrow} = n/2$, and the Gutzwiller factor simplifies to the well-known result,

$$g_t = \frac{1-n}{1-n/2} \ , \tag{3.9}$$

which incorporates the fact that the kinetic energy in $|\Psi\rangle$ is connected to the motion of holes, vanishing in the undoped case.

However, the relation of the $n_{i\sigma}$ with respect to the $n^0_{i\sigma}$ become more subtle, if we consider, *e.g.*, an antiferromagnet with sublattice magnetization m, where $n^0_{A\sigma} = n/2 \pm m$, and, $n^0_{A\sigma} = n^0_{B-\sigma}$ (sublattices A and B, $\sigma =\uparrow,\downarrow$). In this case, $n_{i\sigma} \neq n^0_{i\sigma}$, and we must invoke counting arguments to determine $n_{i\sigma}$. We consider a canonical ensemble, where the overall particle density is the same before and after projection ($n_i = n_{i\uparrow} + n_{i\downarrow} = n^0_{i\uparrow} + n^0_{i\downarrow} = n^0_i = n$). Furthermore, the density $n_{i\sigma}$ is necessarily related to the probability to find a single σ-electron at site i in $|\Psi_0\rangle$. Thus, $n_{i\sigma} \propto n^0_{i\sigma}(1-n^0_{i-\sigma})$. Due the conserved particle density,

$$n_{i\uparrow} + n_{i\downarrow} = n = n^0 \ , \tag{3.10}$$

this relation is fixed to,

$$n_{i\sigma} = n^0_{i\sigma}(1-n^0_{i-\sigma})\frac{n}{n - 2n^0_{i\uparrow}n^0_{i\downarrow}} \ . \tag{3.11}$$

---

[2] We violate this rule, strictly speaking, by neglecting decouplings which include on-site pairing, $\langle c^\dagger_{i\uparrow}c^\dagger_{i\downarrow}\rangle$. However, we work in the fully projected limit, *i.e.*, $|\Psi\rangle$ does not allow for on-site pairing. It is thus reasonable to prohibit on-site pairing in $|\Psi_0\rangle$ as well and to set $\langle c^\dagger_{i\uparrow}c^\dagger_{i\downarrow}\rangle \equiv 0$.

Inserting this expression in the numerator of (3.8) gives the Gutzwiller renormalization factor,

$$g_t = \frac{1-n}{1-2n_\uparrow^0 n_\downarrow^0/n} \ , \tag{3.12}$$

where $n_\uparrow^0$ and $n_\downarrow^0$ are from the same site. We note that (3.11) is valid for sites i and j on the same as well as on different sublattices as one can show easily and reduces to, $g_t = (1-n)/(1-n/2)$, in the non-magnetic limit, $n_\sigma^0 = n/2$.

The situation becomes yet more complicated if we consider states with an inhomogeneous particle density, where it is difficult to determine n_i, $n_{i\downarrow}$, and $n_{i\uparrow}$. Therefore, most authors assume $n_i = n_i^0$. This assumption is mathematically however not correct, because the operator $P_G = \sum_i (1-\hat{n}_{i\uparrow}\,\hat{n}_{i\downarrow})$ allows for changes in the local particle density. An elegant solution is to redefine the operator P_G, so that $n_i = n_i^0$ or even $n_{i\sigma} = n_{i\sigma}^0$. This conservation of local particle densities can be achieved by incorporating appropriate fugacity factors into a new operator $\tilde{P}_G$ (Gutzwiller correlator), which is then not a projection operator any more. The redefined operator $\tilde{P}_G$ still allows to present any projected wave function as $|\Psi\rangle = \tilde{P}_G|\tilde{\Psi}_0\rangle$, however, the unprojected wave function $|\tilde{\Psi}_0\rangle$ will generally differ from $|\Psi_0\rangle$ defined by $|\Psi\rangle = P_G|\Psi_0\rangle$. The use of $\tilde{P}_G$ instead of P_G is often not explicitly stated in literature, although the assumed conservation of densities is only valid for a generalized Gutzwiller correlator $\tilde{P}_G$. Such a clear differentiation between $\tilde{P}_G$ and P_G becomes of particular importance if results from the GA are compared to VMC calculations, which in general implement the original Gutzwiller projector P_G. The non-conserving of local particle densities by the operator P_G also explain discrepancies between VMC calculations in the canonical and the grand canonical scheme [5], which we will discuss in detail in section 3.2.

Before turning to the $d=\infty$ scheme, we discuss how to determine the Gutzwiller renormalization factor g_S for the superexchange interaction, defined by

$$\langle \mathbf{S}_i\mathbf{S}_j\rangle_\Psi \;=\; g_S\,\langle \mathbf{S}_i\mathbf{S}_j\rangle_{\Psi_0} \ . \tag{3.13}$$

We first consider the GA for the contribution $\langle S_i^+S_j^-\rangle$, *i.e.*,

$$\langle S_i^+S_j^-\rangle_\Psi \;=\; g_S^\pm\,\langle S_i^+S_j^-\rangle_{\Psi_0} \ . \tag{3.14}$$

The procedure resembles the derivation of g_t. We note that the process $S_i^+S_j^-$ requires, an $\uparrow$-spin on site i and a $\downarrow$-spin on site j in the bra-vector, and the reverse in the ket-vector. Therefore, the probability becomes

$$(\,n_{i\uparrow}n_{j\downarrow}n_{i\downarrow}n_{j\uparrow}\,)^{1/2} \tag{3.15}$$

in the state $|\Psi\rangle$, while it is

$$[\,n^0_{i\uparrow}(1-n^0_{i\downarrow})n^0_{j\downarrow}(1-n^0_{j\uparrow})n^0_{i\downarrow}(1-n^0_{i\uparrow})n^0_{j\uparrow}(1-n^0_{j\downarrow})\,]^{1/2} \tag{3.16}$$

in the state $|\Psi_0\rangle$. Using $n_{i,\sigma}$ from (3.11) yields,

$$g_S^{\pm} = \frac{1}{(1-2n^0_\uparrow n^0_\downarrow/n)^2}\ . \tag{3.17}$$

One can show again, that above formula results also for the case of sites belonging to the same sublattice.

Next we evaluate the GA for the diagonal contribution to the superexchange,

$$\langle S^z_i S^z_j\rangle_\Psi \ = \ g_S^z\,\langle S^z_i S^z_j\rangle_{\Psi_0}\ . \tag{3.18}$$

Here, we use, $S^z_i = 1/2(\hat{n}_{i\uparrow}-\hat{n}_{i\downarrow})$, and write,

$$\begin{aligned}4\,\langle S^z_i S^z_j\rangle &= \langle \hat{n}_{i\uparrow}(1-\hat{n}_{i\downarrow})\hat{n}_{j\uparrow}(1-\hat{n}_{j\downarrow})\rangle + \langle \hat{n}_{i\downarrow}(1-\hat{n}_{i\uparrow})\hat{n}_{j\downarrow}(1-\hat{n}_{j\uparrow})\rangle \\ &\quad - \langle \hat{n}_{i\uparrow}(1-\hat{n}_{i\downarrow})\hat{n}_{j\downarrow}(1-\hat{n}_{j\uparrow})\rangle - \langle \hat{n}_{i\downarrow}(1-\hat{n}_{i\uparrow})\hat{n}_{j\uparrow}(1-\hat{n}_{j\downarrow})\rangle\ ,\end{aligned} \tag{3.19}$$

which is valid for any wave function. The Gutzwiller approximations of the terms in (3.19) give a common renormalization factor,

$$g_S^z = \frac{1}{(1-2n^0_\uparrow n^0_\downarrow/n)^2}\ . \tag{3.20}$$

This is seen by considering the term $\langle \hat{n}_{i\uparrow}(1-\hat{n}_{i\downarrow})\hat{n}_{j\uparrow}(1-\hat{n}_{j\downarrow})\rangle$ in (3.19), as an example. By applying the probabilities from table 3.1, we obtain,

$$\frac{\langle \hat{n}_{i\uparrow}(1-\hat{n}_{i\downarrow})\hat{n}_{j\uparrow}(1-\hat{n}_{j\downarrow})\rangle_\Psi}{\langle \hat{n}_{i\uparrow}(1-\hat{n}_{i\downarrow})\hat{n}_{j\uparrow}(1-\hat{n}_{j\downarrow})\rangle_{\Psi_0}} \approx \frac{n_{i\uparrow}n_{j\uparrow}}{n^0_{i\uparrow}(1-n^0_{i\downarrow})n^0_{j\uparrow}(1-n^0_{j\downarrow})} \equiv g_S^z\ , \tag{3.21}$$

where using (3.11) for $n_{i\uparrow}n_{j\uparrow}$ directly confirms (3.20). Since all density terms of (3.19) renormalize in exact the same manner, g_S^z gives the correct renormalization factor for $\langle S^z_i S^z_j\rangle_\Psi$ in (3.18).

From (3.17) and (3.20), we find a common Gutzwiller renormalization factor, $g_S = g_S^{\pm} = g_S^z$, for (3.13), which simplifies to,

$$g_S = \frac{1}{(1-n/2)^2}\ , \tag{3.22}$$

in the non-magnetic limit, $n^0_\sigma = n/2$. At half-filling, $n=1$ and $g_S \to 4$, the magnetic correlations are four times as pronounced in $|\Psi\rangle$ than in $|\Psi_0\rangle$. We note that Gutzwiller approximations for other quantities are easily obtained by following the same reasoning as for g_t and g_S.

3.1.2 Gutzwiller renormalization factors in infinite dimensions

The effects of the Gutzwiller correlator can be evaluated exactly in the limit of infinite dimensions [105, 106]. Gebhard [106] showed that a simple diagrammatic evaluation is possible for $d = \infty$. Using the Gutzwiller renormalization factors from $d = \infty$ for finite dimensions corresponds to a mean field approximation. Thus the $d = \infty$ approach provides a thorough scheme to calculate Gutzwiller factors, which in general agree with results from counting arguments. Here, we briefly present this technique for fully projected states, but refer to recent works of Bünemann, *et al.* [107, 108] for a detailed reasoning.

To simplify calculations, the Gutzwiller projector P_G is reformulated as a Gutzwiller correlator $\tilde{P}_G$ within the $d = \infty$ scheme. This redefinition agrees with the one already discussed before and ensures that local densities are conserved, *viz.*, $n_{i\sigma} = n^0_{i\sigma}$. The Gutzwiller correlator, $\tilde{P}_G = \prod_i \tilde{P}_{G,i}$, is written as a product of local correlators,

$$\tilde{P}_{G,i} = \lambda_i^0 \; (1 - \hat{n}_{i\downarrow})(1 - \hat{n}_{i\uparrow}) \; + \; \lambda_i^\uparrow \; \hat{n}_{i\uparrow}(1 - \hat{n}_{i\downarrow}) \; + \; \lambda_i^\downarrow \; \hat{n}_{i\downarrow}(1 - \hat{n}_{i\uparrow}) \; . \tag{3.23}$$

Physically, the parameters λ_i^0 and λ_i^σ allow to weight locally the probabilities to find empty sites and sites occupied with a spin σ, respectively. The λ_i^0, $\lambda_i^\uparrow$, and $\lambda_i^\downarrow$ are determined by the constraints,

$$\langle \tilde{P}^2_{G,i} \rangle_{\tilde{\Psi}_0} \equiv 1 \; , \tag{3.24}$$

$$\langle c^\dagger_{i\sigma} \tilde{P}^2_{G,i} c_{i\sigma} \rangle_{\tilde{\Psi}_0} \equiv \langle c^\dagger_{i\sigma} c_{i\sigma} \rangle_{\tilde{\Psi}_0} = n^0_{i\sigma} \; . \tag{3.25}$$

Equation (3.24) guarantees the normalization, $\langle \Psi | \Psi \rangle = \langle \Psi_0 | \tilde{P}_G \tilde{P}_G | \Psi_0 \rangle = 1$, of the projected wave function and equation (3.25) provides the conservation of local densities. Evaluating these equations, we find,

$$\lambda_i^0 = \sqrt{\frac{1 - n_i}{(1 - n_{i\downarrow})(1 - n_{i\uparrow})}} \; , \tag{3.26}$$

$$\lambda_i^\sigma = \sqrt{\frac{1}{(1 - n_{i-\sigma})}} \; . \tag{3.27}$$

Using these parameters in the Gutzwiller correlator $\tilde{P}_G$ guarantees via (3.24) a conserved norm and via (3.25) conserved spin densities for any projected wave function, $|\Psi\rangle \equiv \tilde{P}_G |\tilde{\Psi}_0\rangle$. The GA for an operator $\hat{O}_{ij}$ acting on the sites i and j is now obtained by neglecting all correlations except those between sites i and j. This procedure becomes exact in infinite dimensions and is written as,

$$\langle\tilde{\Psi}_0|\tilde{P}_G\hat{O}_{ij}\tilde{P}_G|\tilde{\Psi}_0\rangle = \langle\tilde{\Psi}_0|\tilde{P}_{G,i}\tilde{P}_{G,j}\hat{O}_{ij}\tilde{P}_{G,i}\tilde{P}_{G,j}|\tilde{\Psi}_0\rangle \ . \tag{3.28}$$

Decoupling the right hand site and neglecting all off-site correlations of higher order, provides the exact solution for $d = \infty$, which agrees with results from counting arguments presented in the previous section.

As an example, we consider the hopping process, $\langle c^\dagger_{i\uparrow}c_{j\uparrow}\rangle_{\tilde{P}_G|\Psi_0\rangle}$. Using (3.28), we find,

$$\begin{aligned}
\langle\tilde{\Psi}_0|\tilde{P}_G c^\dagger_{i\uparrow}c_{j\uparrow}\tilde{P}_G|\tilde{\Psi}_0\rangle &= \langle\tilde{\Psi}_0|\tilde{P}_{G,i}c^\dagger_{i\uparrow}\tilde{P}_{G,i}\tilde{P}_{G,j}c_{j\uparrow}\tilde{P}_{G,j}|\tilde{\Psi}_0\rangle && \text{(3.29a)}\\
&= \lambda_i^\uparrow\lambda_i^0\lambda_j^0\lambda_j^\uparrow \ \langle\tilde{\Psi}_0|(1-\hat{n}_{i\downarrow})c^\dagger_{i\uparrow}(1-\hat{n}_{j\downarrow})c_{j\uparrow}|\tilde{\Psi}_0\rangle && \text{(3.29b)}\\
&= \underbrace{\lambda_i^\uparrow\lambda_i^0\lambda_j^0\lambda_j^\uparrow(1-n_{i\downarrow})(1-n_{j\downarrow})}_{=g_t} \ \langle\tilde{\Psi}_0|c^\dagger_{i\uparrow}c_{j\uparrow}|\tilde{\Psi}_0\rangle \, , && \text{(3.29c)}
\end{aligned}$$

where we decoupled the densities in the last row as already done in the discussion using counting arguments. Equation (3.29) is exact in infinite dimensions, and gives the Gutzwiller renormalization factor,

$$g_t = \sqrt{\frac{(1-n_j)(1-n_i)}{(1-n_{j\uparrow})(1-n_{i\uparrow})}} \ , \tag{3.30}$$

which agrees with (3.8) if we assume locally conserved densities. However, we note that this result differs from (3.12), which incorporates the changed spin densities due to the projection operator P_G. Above presented scheme is applicable to any kind of operator, gives the exact result for $d = \infty$, and provides an useful check for results derived from counting arguments. Nevertheless we must keep in mind that results may differ depending on, whether we use P_G and $P_G|\Psi_0\rangle$ together with counting arguments, or $\tilde{P}_G$ and $\tilde{P}_G|\tilde{\Psi}_0\rangle$ in connection with above consideration to derive the Gutzwiller renormalization factor.

3.2 Gutzwiller approximation in the canonical and the grand canonical scheme

In this section we follow Edegger, *et al.* [5] and study the effects of projection on superconducting BCS wave functions,

$$|\Psi_0\rangle = |\mathrm{BCS}\rangle \equiv \prod_{\mathbf{k}}\left(u_{\mathbf{k}} + v_{\mathbf{k}}c^\dagger_{\mathbf{k}\uparrow}c^\dagger_{-\mathbf{k}\downarrow}\right)|0\rangle \quad . \tag{3.31}$$

Since $|\Psi_0\rangle = |\mathrm{BCS}\rangle$ exhibits particle number fluctuations, the projection operator P_G can change the average particle number N of the wave function, *i.e.*, in general,

$$\frac{\langle\Psi_0|\hat{N}|\Psi_0\rangle}{\langle\Psi_0|\Psi_0\rangle} \neq \frac{\langle\Psi_0|P_G\ \hat{N}\ P_G|\Psi_0\rangle}{\langle\Psi_0|P_G^2|\Psi_0\rangle}\ . \tag{3.32}$$

In above equation the equality could be recovered when replacing the Gutzwiller projector P_G by a Gutzwiller correlator $\tilde{P}_G$ which conserves local densities as discussed in the previous section. Here, we follow a different route and try to compensate the effects of projection by using a fugacity factor in the wave function. This ansatz then explains differences observed between VMC calculations in the canonical framework (fixed particle number) and the grand canonical ensemble (fluctuating particle number) using the corresponding GA.

3.2.1 Incorporation of a fugacity factor

The effect of the projection operator P_G can be seen most clearly by examining the particle number distribution in the unprojected and projected Hilbert spaces. Towards this end, let us write the average numbers, $\bar{N}^{(0)}(\bar{N})$ in the unprojected (projected) Hilbert space, as,

$$\bar{N}^{(0)} = \sum_N N\,\rho_N^{(0)}\ , \tag{3.33}$$

$$\bar{N} = \sum_N N\,\rho_N\ . \tag{3.34}$$

Here,

$$\rho_N^{(0)} = \frac{\langle\Psi_0|\,P_N\,|\Psi_0\rangle}{\langle\Psi_0|\Psi_0\rangle}, \tag{3.35}$$

$$\rho_N = \frac{\langle\Psi_0|\,P_G\ P_N\ P_G\,|\Psi_0\rangle}{\langle\Psi_0|P_G\ P_G\,|\Psi_0\rangle}\ , \tag{3.36}$$

are the particle number distributions in the unprojected and projected BCS wave functions respectively. The P_N is an operator which projects onto terms with particle number N. The particle number distributions before and after projection may be related by

$$\underbrace{\frac{\langle\Psi_0|\,P_G\ P_N\ P_G\,|\Psi_0\rangle}{\langle\Psi_0|P_G\ P_G\,|\Psi_0\rangle}}_{\rho_N} = g_N\ \underbrace{\frac{\langle\Psi_0|\,P_N\,|\Psi_0\rangle}{\langle\Psi_0|\Psi_0\rangle}}_{\rho_N^{(0)}}\ , \tag{3.37}$$

where

$$g_N = \underbrace{\frac{\langle\Psi_0|\Psi_0\rangle}{\langle\Psi_0|P_G\ P_G\ |\Psi_0\rangle}}_{=C(=\text{const})} \frac{\langle\Psi_0|\ P_G\ P_N\ P_G\ |\Psi_0\rangle}{\langle\Psi_0|\ P_N\ |\Psi_0\rangle} \ . \tag{3.38}$$

Equation (3.37) constitutes the GA for the projection operator P_N with the corresponding renormalization factor g_N. The parameter C is an irrelevant constant (the ratio of the normalization of the unprojected and projected wave functions), which does not depend on N. Following Gutzwiller, we estimate g_N by combinatorial means, as being equal to the ratio of the relative sizes of the projected and unprojected Hilbert spaces. Then,

$$g_N \approx C\, \frac{\frac{L!}{(L-N_\uparrow-N_\downarrow)!\,N_\uparrow!\,N_\downarrow!}}{\frac{L!}{(L-N_\uparrow)!\,N_\uparrow!}\ \frac{L!}{(L-N_\downarrow)!\,N_\downarrow!}} \,, \tag{3.39}$$

where L is the number of lattice sites and $N_\uparrow$ ($N_\downarrow$) is the number of up-(down)-spins. $N_\uparrow = N_\downarrow = N/2$ with N being the total number of particles in $P_N|\Psi_0\rangle$, and the expression for g_N can consequently be simplified to

$$g_N \approx C\, \frac{((L-N/2)!)^2}{L!\,(L-N)!} \,. \tag{3.40}$$

Hence, if we were to impose the condition that the average particle numbers before and after projection are to be identical, a factor g_N^{-1} needs to be included in (3.34). Then, from (3.34) and (3.37), we obtain the particle number after projection $\bar{N}_{\text{new}}$,

$$\bar{N}_{\text{new}} \equiv \sum_N N\,\frac{1}{g_N}\,\rho_N \ = \ \sum_N N\,\frac{g_N\,\rho_N^{(0)}}{g_N} \ = \ \bar{N}^{(0)} \ , \tag{3.41}$$

which is the desired result.

Now, let us show how this procedure can be implemented for the wave function $|\Psi_0\rangle$. Since the BCS wave function is a linear superposition of states with particle numbers $\ldots, N-2, N, N+2, \ldots$, we consider the effect of projection on two states whose particle numbers differ by two. Then, the ratio is

$$f^2 \ \equiv\ \frac{g_{N+2}}{g_N} \ \approx\ \left(\frac{L-N}{L-N/2}\right)^2 \tag{3.42}$$

in the thermodynamic limit. Equation (3.42) shows that the projection operator acts unequally on the N and $N+2$ particle states; the renormalization of the weight of the $N+2$ particle states g_{N+2}, is f^2 times the weight of the N particle states, g_N. This effect can be rectified as in (3.41) by multiplying every Cooper pair $c^\dagger_{\mathbf{k}\uparrow}c^\dagger_{-\mathbf{k}\downarrow}$ by a amplitude $\frac{1}{f}$ in the BCS wave function. It produces the desired result, *viz.*, the projected and unprojected BCS wave functions have the same average particle number.

Alternatively (following Anderson [127]), we can multiply every empty state by the factor f and write,

$$|\Psi_0^{(f)}\rangle = \prod_k \frac{\left(f\,u_{\mathbf{k}} + v_{\mathbf{k}} c^\dagger_{\mathbf{k}\uparrow}c^\dagger_{-\mathbf{k}\downarrow}\right)}{\sqrt{f^2|u_{\mathbf{k}}|^2 + |v_{\mathbf{k}}|^2}}\,|0\rangle\ . \tag{3.43}$$

Then again by construction, the fugacity factor f in (3.43) ensures that the projected wave function $P_G|\Psi_0^{(f)}\rangle$ and the unprojected wave function $|\Psi_0\rangle$ without fugacity factor have the same particle number. The denominator in (3.43) is the new normalization factor.

The fugacity factor f in (3.42) depends on the variable particle number N. However, since the particle number of the BCS wave function is sharply peaked within the range, $\bar{N}^{(0)} - \sqrt{\bar{N}^{(0)}}$ and $\bar{N}^{(0)} + \sqrt{\bar{N}^{(0)}}$, we will assume that the fugacity factor $f = f(\bar{N}^{(0)})$ in the thermodynamic limit. In this limit, (3.42) reduces to,

$$f^2 \to \left(\frac{1-n}{1-n/2}\right)^2 = g_t^2\ , \tag{3.44}$$

with g_t being the Gutzwiller renormalization factor for the hopping term as discussed before. Then, (3.43) becomes,

$$|\Psi_0^{(f)}\rangle = \prod_{\mathbf{k}} \frac{\left(g_t\,u_{\mathbf{k}} + v_{\mathbf{k}} c^\dagger_{\mathbf{k}\uparrow}c^\dagger_{-\mathbf{k}\downarrow}\right)}{\sqrt{g_t^2|u_{\mathbf{k}}|^2 + |v_{\mathbf{k}}|^2}}\,|0\rangle\ , \tag{3.45}$$

which is the wave function proposed by Anderson [127].

3.2.2 Singular particle number renormalization close to half-filling

We showed that the inclusion of the fugacity factor is necessary for the average particle number in a BCS wave function to remain unchanged when projecting out all doubly occupied sites. Alternatively, one might ask what is the effect of the projection operator on a BCS wave function; *viz.*, if projection changes the mean particle number of a BCS state, how are the particle numbers before and after projection related when no fugacity factors are introduced into the wave function?

In order to ensure this question, we consider two BCS states defined by,

$$|\Psi_0\rangle = \prod_{\mathbf{k}} \left(u_{\mathbf{k}} + v_{\mathbf{k}} c^{\dagger}_{\mathbf{k}\uparrow} c^{\dagger}_{-\mathbf{k}\downarrow} \right) |0\rangle \ , \tag{3.46}$$

$$|\Psi_0^{(r)}\rangle = \prod_{\mathbf{k}} \frac{\left(u_{\mathbf{k}} + g_t\, v_{\mathbf{k}}\, c^{\dagger}_{\mathbf{k}\uparrow} c^{\dagger}_{-\mathbf{k}\downarrow} \right)}{\sqrt{|u_{\mathbf{k}}|^2 + g_t^2 |v_{\mathbf{k}}|^2}} |0\rangle = \prod_{\mathbf{k}} \left(u_{\mathbf{k}}^{(r)} + v_{\mathbf{k}}^{(r)} c^{\dagger}_{\mathbf{k}\uparrow} c^{\dagger}_{-\mathbf{k}\downarrow} \right) |0\rangle \ , \tag{3.47}$$

where,

$$u_{\mathbf{k}}^{(r)} \equiv \frac{u_{\mathbf{k}}}{\sqrt{|u_{\mathbf{k}}|^2 + g_t^2 |v_{\mathbf{k}}|^2}}, \quad v_{\mathbf{k}}^{(r)} \equiv \frac{g_t\, v_{\mathbf{k}}}{\sqrt{|u_{\mathbf{k}}|^2 + g_t^2 |v_{\mathbf{k}}|^2}} \ . \tag{3.48}$$

From (3.42), it is clear that the projection operator reduces the ratio of the weights of $N+2$ and N particle states in a BCS wave function by a factor g_t^2. Then, it follows that,

$$\frac{\langle \Psi_0^{(r)} | \, \hat{N} \, | \Psi_0^{(r)} \rangle}{\langle \Psi_0^{(r)} | \Psi_0^{(r)} \rangle} \approx \frac{\langle \Psi_0 | \, P_G \, \hat{N} \, P_G \, | \Psi_0 \rangle}{\langle \Psi_0 | \, P_G \, | \Psi_0 \rangle} \ , \tag{3.49}$$

with

$$g_t = \frac{L - \langle \hat{N} \rangle_{P_G \Psi_0}}{L - \frac{1}{2} \langle \hat{N} \rangle_{P_G \Psi_0}} \ , \tag{3.50}$$

where we use the particle number $\langle \hat{N} \rangle_{P_G \Psi_0} \approx \langle \hat{N} \rangle_{\Psi_0^{(r)}}$. Furthermore, we have,

$$\langle \hat{N} \rangle_{\Psi_0^{(r)}} \ \equiv \ \frac{\langle \Psi_0^{(r)} | \, \hat{N} \, | \Psi_0^{(r)} \rangle}{\langle \Psi_0^{(r)} | \Psi_0^{(r)} \rangle} \ = \ 2 \sum_k |v_{\mathbf{k}}^{(r)}|^2. \tag{3.51}$$

Since the particle numbers of $|\Psi_0^{(r)}\rangle$ and $P_G|\Psi_0\rangle$ are identical, we can use (3.48) in (3.51) to obtain,

$$\bar{N}_{\text{after}} \equiv \frac{\langle \Psi_0 | \, P_G \, \hat{N} \, P_G \, | \Psi_0 \rangle}{\langle \Psi_0 | \, P_G \, | \Psi_0 \rangle} \approx \frac{\langle \Psi_0^{(r)} | \, \hat{N} \, | \Psi_0^{(r)} \rangle}{\langle \Psi_0^{(r)} | \Psi_0^{(r)} \rangle} = 2 \sum_{\mathbf{k}} \frac{g_t^2 |v_{\mathbf{k}}|^2}{|u_{\mathbf{k}}|^2 + g_t^2 |v_{\mathbf{k}}|^2} \ . \tag{3.52}$$

Note that g_t is specified by the particle in $P_G|\Psi_0\rangle$, *i.e.*, $\bar{N}_{\text{after}}$ ($\approx \langle \hat{N} \rangle_{\Psi_0^{(r)}}$), and (3.52) therefore constitutes a self-consistency relation for $\bar{N}_{\text{after}}$.

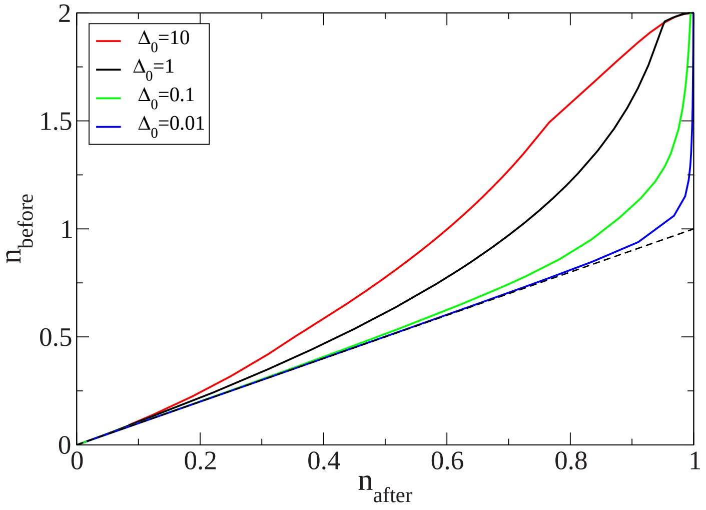

Figure 3.2: Particle density before projection n_{before}, equation (3.53), as a function of the particle density after projection n_{after}, equation (3.52), for different d-wave order parameters Δ. The dashed line indicates the Fermi liquid result $n_{\text{before}} = n_{\text{after}}$. From [5].

Now, since the particle density in the state $|\Psi_0\rangle$ before projection is given by,

$$\bar{n}_{\text{before}} \equiv \frac{\bar{N}_{\text{before}}}{L} = \frac{2}{L}\sum_{\mathbf{k}} |v_{\mathbf{k}}|^2 \ , \tag{3.53}$$

equation (3.52) provides us with a way to calculate the particle number in the state $P_G|\Psi_0\rangle$ *after* projection, whenever the particle number as a function of the identical $u_{\mathbf{k}}$ and $v_{\mathbf{k}}$ is known for $|\Psi_0\rangle$, *viz.*, *before* projection. Equation (3.52) can be solved self-consistently for $\bar{N}_{\text{after}}$. One obtains numerical solutions for (3.52) on a square lattice by using the standard BCS expressions for a d-wave superconductor,

$$v_{\mathbf{k}}^2 = \frac{1}{2}\left(1 - \frac{\xi_{\mathbf{k}}}{E_k}\right) \ , \quad u_{\mathbf{k}}^2 = \frac{1}{2}\left(1 + \frac{\xi_{\mathbf{k}}}{E_k}\right) \ , \tag{3.54}$$

with,

$$E_{\mathbf{k}} = \sqrt{\Delta_{\mathbf{k}}^2 + \xi_{\mathbf{k}}^2}, \tag{3.55a}$$

$$\Delta_{\mathbf{k}} = \Delta\,(\,\cos k_x - \cos k_y\,), \tag{3.55b}$$

$$\xi_{\mathbf{k}} = -2\,(\,\cos k_x + \cos k_y\,) - \mu \ . \tag{3.55c}$$

The only free parameters are the chemical potential μ and the order parameter Δ.

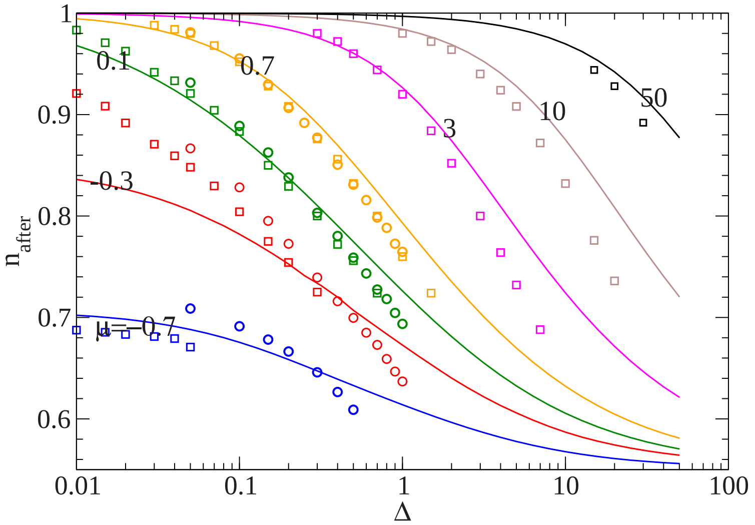

Figure 3.3: The particle density after projection n_{after} as a function of the parameter Δ for a d-wave BCS state at various chemical potentials μ. The figure shows a comparison between results from equation (3.52) (solid lines) and the VMC results of Yokoyama and Shiba [80] [for 6×6 - (circles) and 8×8 -lattices (squares)]. Numbers in the figure denote the chemical potentials of the corresponding curves. From [5].

For fixed values of the order parameter Δ, we have determined the particle numbers (before and after projection) for various chemical potentials. The results for the particle densities are shown in figure 3.2. The results clearly show that the particle density before projection attains its maximal value ($n_{\text{before}} = 2$), when $n_{\text{after}} = 1$ (half-filling). This result holds for any finite value of the order parameter Δ. The case of half-filling, $n_{\text{after}} \to 1$, is therefore singular in the grand canonical scheme and substantial deviations with resect to the canonical framework can be expected (see discussion in the following section).

In the opposite limit, *viz.*, low densities of electrons, n_{before} converges to the value of n_{after} as expected. The size of the intermediate region depends on the magnitude of the order parameter Δ, as illustrated by the results in figure 3.2.

The accuracy of (3.52) can be checked by comparing above results with those of Yokoyama and Shiba (YS) [80], who performed VMC studies of projected BCS wave functions with fluctuating particle number (but without a fugacity factor) . They determined the particle density of the projected d-wave state $P_G \left|\Psi_0\right\rangle$ as a function of the chemical potential μ and the parameter Δ, within a grand canonical scheme. The unprojected wave function $|\Psi_0\rangle$ is specified as usual, through (3.54)-(3.55). Since YS do not include a fugacity factor in their definition of the BCS wave function, projection changes the particle number. So, we use (3.52) to determine n_{after} which we compare with their results for particle number.

As seen in figure 3.3, above results are in good qualitative agreement with YS. Discrepancies are mostly due to finite size corrections. YS used 6×6 and 8×8-lattices, while the analytic calculations are valid in the thermodynamic limit. The results show the singular effect of the projection near the insulating phase (half filling). The chemical potential diverges to infinity in this limit.

3.2.3 Gutzwiller renormalization factors in the canonical and the grand canonical ensemble

Next we discuss the differences between the Gutzwiller approximation in the canonical and grand canonical scheme. After deriving analytical expressions, we check the validity of the statements by a comparison to numerically exact VMC calculations [79, 80].

Let us first consider the canonical case. Here, we are interested in the expectation value of an operator $\hat{O}$ calculated within a projected wave function $P_N P_G|\,\Psi_0\rangle$ with fixed particle number. The corresponding Gutzwiller approximation can be understood as follows:

$$
\begin{aligned}
& \frac{\langle\Psi_0|\,P_G\;P_N\;\hat{O}\;P_N\;P_G\,|\,\Psi_0\rangle}{\langle\Psi_0|\,P_G\;P_N\;P_G\,|\,\Psi_0\rangle} && \text{(3.56a)}\\
\approx\quad & g_O\,\frac{\langle\Psi_0|\,P_N\;\hat{O}\;P_N\,|\,\Psi_0\rangle}{\langle\Psi_0|\,P_N\,|\,\Psi_0\rangle} && \text{(3.56b)}\\
=\quad & g_O\,\frac{\langle\Psi_0|\,\hat{O}\,|\,\Psi_0\rangle}{\langle\Psi_0|\,\Psi_0\rangle}\;, && \text{(3.56c)}
\end{aligned}
$$

where P_N is the projector on the terms with particle number N. The Gutzwiller renormalization factor g_O, corresponds to the operator $\hat{O}$. The term (3.56a) represents a quantity which can be calculated exactly by the VMC scheme with fixed particle number [79, 128]. Since the particle number is fixed, the usual Gutzwiller approximation can be invoked, leading to (3.56b). The equality to the last row is guaranteed only if N is equal to the average particle number of $|\,\Psi_0\rangle$ ($N = \bar{N}$). Then, one can perform a transformation from a canonical to a grand canonical ensemble, which is valid in the pre-projected Hilbert-space in the thermodynamic limit.

In the grand canonical scheme, where we calculate the expectation value of $\hat{O}$ with a particle number non-conserving wave function, this scheme must be modified as follows:

$$\frac{\langle \Psi_0^{(f)} | \, P_G \, \hat{O} \, P_G \, | \, \Psi_0^{(f)} \rangle}{\langle \Psi_0^{(f)} | \, P_G \, P_G \, | \, \Psi_0^{(f)} \rangle} \;\approx\; g_O \, \frac{\langle \Psi_0 | \, \hat{O} \, | \, \Psi_0 \rangle}{\langle \Psi_0 | \, \Psi_0 \rangle} \; , \tag{3.57}$$

where $P_G | \, \Psi_0^{(f)} \rangle$ is the projected d-wave state corrected for fugacity, *i.e.*, a fugacity factor is included simultaneously with the projection. This correction is essential to guarantee the validity of the Gutzwiller approximation; without it, the left hand side (lhs) and the right hand side (rhs) of (3.57) would correspond to states with different mean particle numbers.

Comparing (3.56) and (3.57) we obtain,

$$\frac{\langle \Psi_0 | P_G P_N \hat{O} P_N P_G | \, \Psi_0 \rangle}{\langle \Psi_0 | P_G P_N P_G | \, \Psi_0 \rangle} \;\approx\; \frac{\langle \Psi_0^{(f)} | P_G \hat{O} P_G | \, \Psi_0^{(f)} \rangle}{\langle \Psi_0^{(f)} | P_G^2 | \, \Psi_0^{(f)} \rangle} \; . \tag{3.58}$$

Equation (3.57) and (3.58) constitute a main results of this section. Equation (3.57) shows that when the Gutzwiller approximation is used for a wave function which does not have a fixed particle number, a fugacity factor must be included along with the projection. Equation (3.58) shows that to obtain identical results, one has to use different wave functions in the grand canonical (rhs) and canonical (lhs) scheme. The wave function $| \, \Psi_0^{(f)} \rangle$ is a d-wave state corrected by the fugacity factor, whereas $| \, \Psi_0 \rangle$ is a pure d-wave state. These arguments leading up to (3.57) and (3.58) can be verified by a comparison with VMC studies. We now proceed to do so.

Expectation values in the canonical and grand canonical schemes can be calculated (nearly exactly) by VMC studies. In figure 3.4, we compare VMC results from Gros [79] (fixed particle number VMC, canonical) and from YS [80] (grand canonical VMC). The discrepancy between the two sets of results can be explained readily by (3.58). YS consider a pure d-wave state, *i.e.*, the fugacity factor is not included in their calculations. Equation (3.58) on the other hand shows that this is only to be expected because the particle numbers in the two schemes are not identical without a fugacity factor. In their paper, YS argued that the discrepancies between the two results can be removed by introducing an additional variational parameter α, so that $a_k \equiv v_{\mathbf{k}}/u_{\mathbf{k}}$ is replaced by $a_{\mathbf{k}} \equiv \alpha \, v_{\mathbf{k}}/u_{\mathbf{k}}$ (equation 4.1 in [80]). We opine that the parameter α is directly related to above fugacity factor, *i.e.*, $\alpha = g_t$ in the wave function $| \, \Psi_0^{(f)} \rangle$. This conclusion is supported by the comparison of VMC data to the corresponding Gutzwiller approximation (see below).

The validity of the Gutzwiller approximation in the canonical case (3.56) is well accepted. It is used for instance, in the renormalized mean field theory (RMFT) of Zhang, *et al.*, where all physical quantities are calculated using unprojected wave functions and the corresponding Gutzwiller renormalization factors [76]. A comparison with VMC studies with fixed particle number exhibits a good agreement [76] (also illustrated in figure 3.4).

To compare the grand canonical VMC of YS with the Gutzwiller approximation, we need to modify (3.57). This is necessary because YS did not include the fugacity factor in their considerations, as pointed out earlier. We modify (3.58) by the following procedure:

1. We start with a d-wave BCS state $|\Psi_0\rangle$ for specified values of Δ.
2. We fix the particle density n_{after} of $P_G|\Psi_0\rangle$ and determine the corresponding chemical potential μ by (3.52).
3. We introduce an "inverse" fugacity factor into $|\Psi_0\rangle$ to get $|\Psi_0^{(r)}\rangle$ via (3.47). The fugacity factor is determined for n_{after}. $|\Psi_0^{(r)}\rangle$ and $P_G|\Psi_0\rangle$ correspond to the same particle density n_{after}.
4. In analogy to (3.57), the expectation values within the wave function $P_G|\Psi_0\rangle$ can now be approximated by $|\Psi_0^{(r)}\rangle$ and Gutzwiller renormalization factors, *viz.*,

$$\frac{\langle\Psi_0|\, P_G\, \hat{O}\, P_G\,|\,\Psi_0\rangle}{\langle\Psi_0|\, P_G\, P_G\,|\,\Psi_0\rangle} \;\approx\; g_O\,\frac{\langle\Psi_0^{(r)}|\,\hat{O}\,|\,\Psi_0^{(r)}\rangle}{\langle\Psi_0^{(r)}|\,\Psi_0^{(r)}\rangle}\;. \tag{3.59}$$

In figure 3.4, we compare the GA of the kinetic energy $E^{(1)}$ [T in (2.6)], and the expectation value $E^{(2)}$ of the remaining terms in the t-J model [$H_J + H_3$ in (2.6)] to those obtained by the grand canonical VMC study of YS. A good agreement between the VMC and Gutzwiller results is seen, which confirms the validity of above Gutzwiller approximation for the grand canonical scheme, *i.e.*, equations (3.57) and (3.59).

In figure 3.4, we also show Gutzwiller approximations for the fixed particle number VMC [79]. Clearly, canonical and grand canonical approaches yield different energies (as do the corresponding VMC studies). We emphasize this is because the projection operator P_G changes the particle number in a grand canonical scheme. For these two methods to yield the same results, a fugacity corrected wave function must be used when working in a grand canonical ensemble. Hence, all previous speculations about the coincidence of these two VMC schemes in the thermodynamic limit have to be reformulated carefully.

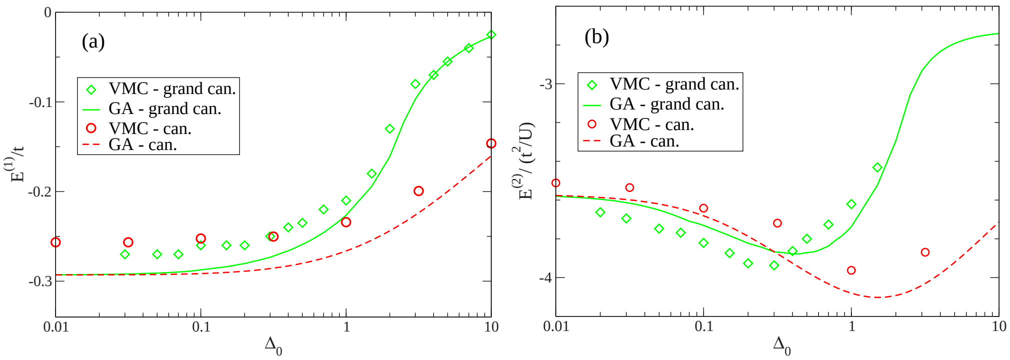

Figure 3.4: (a) The kinetic energy $E^{(1)}$ and (b) the energy of the remaining terms $E^{(2)}$ per site of the t-J model as a function of Δ for the d-wave state at a filling $n = 0.9$. Fixed particle (can., circles) VMC data [79] and grand canonical (grand can., squares) VMC data [80] are compared. The dashed/solid lines represent the corresponding Gutzwiller approximations (GA). From [5].

3.3 Gutzwiller approximation for partially projected states

Till now we concentrated on the Gutzwiller renormalization scheme for fully projected wave functions. It is however necessary to consider sometimes partially projected states of the form

$$|\Psi'_l\rangle \;=\; P'_l\;|\Psi_0\rangle, \qquad P'_l = \prod_{i\neq l}(1-\hat{n}_{i\uparrow}\hat{n}_{i\downarrow})\;. \tag{3.60}$$

The wave function $|\Psi'_l\rangle$ describes a state where double occupancies are projected out on all sites except the site l, which we call the reservoir site. The reason for the appearance of reservoir sites is not far to seek. Consider, for example, the operator $P_G c_{l\uparrow}$. Clearly, it can be rewritten as $c_{l\uparrow}P'_l$. Such commutations become necessary, *e.g.*, for the calculation of the quasiparticle weight (discussed in Chapter 6), where partially projected states arise inevitably.

Before discussing $|\Psi'_l\rangle$ in more detail, we remark that the notation "partially projected" is also used for a projection operator,

$$P_\alpha = \prod_i(1-\alpha\,\hat{n}_{i\uparrow}\hat{n}_{i\downarrow})\;, \tag{3.61}$$

with $\alpha \in [0,1]$. The operator P_α is used for studying Hubbard-like model with "partially projected" wave functions $P_\alpha|\Psi_0\rangle$ (see also section 3.1). Here, the parameter α controls the total number of double occupancies, whereas P_l' in (3.60) yields a fully projected state with only a single unprojected reservoir site i. We emphasize that the respective Gutzwiller approximations for these two projection operators are fundamentally different.

Below we follow the work of Fukushima, *et al.* [6], who developed an analytical method to calculate expectation values for partially projected states [as defined in (3.60)]. The calculations rest on counting arguments, however, similar results can in principle be obtained within the infinite dimensions approach. We first determine the local occupancy of the reservoir site, which is then used to derive the Gutzwiller renormalization factors of specific expectation values. We also provide a comparison to VMC calculations to test the validity of the approximation and to find its limitations.

We are interested in expectation values such as

$$\frac{\langle\Psi_l'|\hat{O}|\Psi_l'\rangle}{\langle\Psi_l'|\Psi_l'\rangle} \;=\; g_O' \,\frac{\langle\Psi_0|\hat{O}|\Psi_0\rangle}{\langle\Psi_0|\Psi_0\rangle}\;, \tag{3.62}$$

that generalize the Gutzwiller approximation to partially projected wave functions. Note that the reservoir site does not have a special role in the unprojected wave function $|\Psi_0\rangle$. This is in contrast to the impurity problem (which we do not consider here), where an impurity site would break the translational invariance of both the unprojected and of the projected wave function.

3.3.1 Occupancy of the reservoir site

In order to evaluate the generalized renormalization parameters g_O' in (3.62), we obviously need the normalization of $\langle\Psi_l'|\Psi_l'\rangle$. We define with

$$X \;=\; \frac{\langle\Psi_0|P_G P_G|\Psi_0\rangle}{\langle\Psi_0|P_l' P_l'|\Psi_0\rangle} \;=\; \frac{\langle\Psi|\Psi\rangle}{\langle\Psi_l'|\Psi_l'\rangle}\;, \tag{3.63}$$

the norm of the fully projected state relative to the state with one reservoir site. Invoking the Gutzwiller approximation, we estimate this ratio by considering the relative sizes of the Hilbert spaces,

$$X \;\sim\; \frac{\frac{L!}{N_\uparrow!N_\downarrow!N_h!}}{\frac{L!}{N_\uparrow!N_\downarrow!N_h!}+\frac{(L-1)!}{(N_\uparrow-1)!(N_\downarrow-1)!(N_h+1)!}}\;, \tag{3.64}$$

where $L = N_\uparrow + N_\downarrow + N_h$, is the number of lattice sites and $N_\uparrow$, $N_\downarrow$ and N_h, the number of up spins, down spins and empty sites, respectively. The first term in the denominator of (3.64) represents the number of states with the reservoir site being empty or singly occupied; the second term represents the state with the reservoir site being doubly occupied.

Equation (3.64) can be simplified in the thermodynamic limit. We obtain,

$$X \;=\; \frac{1-n}{(1-n_\uparrow)(1-n_\downarrow)}\ , \tag{3.65}$$

where $n_\sigma = N_\sigma/L$ ($\sigma = \uparrow, \downarrow$) and $n = n_\uparrow + n_\downarrow$ are the respective particle densities. Note that the X vanishes at half-filling. Above argument can be extended to the case of two unprojected sites. We then get,

$$\frac{\langle\Psi_0|P_G P_G|\Psi_0\rangle}{\langle\Psi_0|P'_{lm}P'_{lm}|\Psi_0\rangle} \;=\; X^2\ , \tag{3.66}$$

where, $P_{lm} = \prod_{i\neq l,m}(1-\hat{n}_{i,\uparrow}\hat{n}_{i,\downarrow})$. We note for later use that

$$\frac{1-X}{X} \;=\; \frac{n_\uparrow n_\downarrow}{(1-n)}\ . \tag{3.67}$$

Assuming translation invariance for the unprojected wave function $|\Psi_0\rangle$, it is possible to derive the following exact expressions,

$$\begin{aligned}
\langle(1-\hat{n}_{l\uparrow})(1-\hat{n}_{l\downarrow})\rangle_{\Psi'_l} \;&=\; X(1-n) = \frac{(1-n)^2}{(1-n_\uparrow)(1-n_\downarrow)}\ , &(3.68)\\
\langle\hat{n}_{l\sigma}(1-\hat{n}_{l-\sigma})\rangle_{\Psi'_l} \;&=\; Xn_\sigma = \frac{(1-n)n_\sigma}{(1-n_\uparrow)(1-n_\downarrow)}\ , &(3.69)\\
\langle d\rangle_{\Psi'_l} \equiv \langle\hat{n}_{l\uparrow}\hat{n}_{l\downarrow}\rangle_{\Psi'_l} \;&=\; 1-X = \frac{n_\uparrow n_\downarrow}{(1-n_\uparrow)(1-n_\downarrow)}\ , &(3.70)
\end{aligned}$$

for the occupancy of the reservoir site, where we used,

$$\langle\ldots\rangle_{\Psi'_l} \equiv \langle\Psi'_l|\ldots|\Psi'_l\rangle/\langle\Psi'_l|\Psi'_l\rangle\ ,$$

and (3.65). The proof is straightforward. Consider for instance, the probability (3.68) of finding the reservoir site empty. Since,

$$\langle\Psi_0|P_G(1-\hat{n}_l)P_G|\Psi_0\rangle \;=\; \langle\Psi_0|P'_l(1-\hat{n}_{l\uparrow})(1-\hat{n}_{l\downarrow})P'_l|\Psi_0\rangle\ , \tag{3.71}$$

we have,

$$\langle(1-\hat{n}_{l\uparrow})(1-\hat{n}_{l\downarrow})\rangle_{\Psi'_l} \;=\; \frac{\langle\Psi|(1-\hat{n}_l)|\Psi\rangle}{\langle\Psi|\Psi\rangle}\frac{\langle\Psi|\Psi\rangle}{\langle\Psi'_l|\Psi'_l\rangle} \;=\; (1-n)X\ . \tag{3.72}$$

Equations (3.69) and (3.70) can be proved analogously. Note that

$$\lim_{n\to 1}\langle d\rangle_{\Psi'_l} \;=\; 1\ , \tag{3.73}$$

i.e., at half-filling the reservoir is exactly doubly occupied.

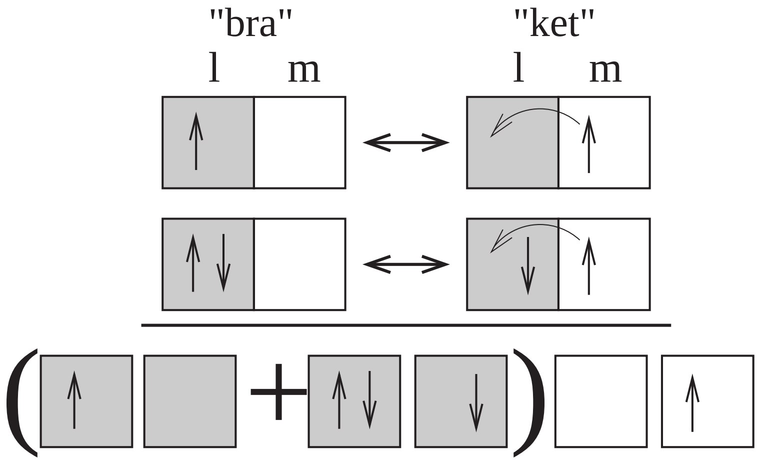

Figure 3.5: Required bar- and ket-configurations, so that $\langle c^\dagger_{l\uparrow}(1-\hat{n}_{m\downarrow})c_{m\uparrow}\rangle$ contribute in $|\Psi'_l\rangle$ when l is a reservoir site (indicated by a shaded background). The last row presents the sum from the two possible contributions as used in (3.76). Boxes with white background indicate the fully projected site m.

3.3.2 Renormalization of mixed hopping terms

The occupancies of the reservoir site, (3.68)-(3.70), directly enter the respective Gutzwiller renormalization factor g'_O. We consider here, as an example, the mixed hopping term,

$$\frac{\langle\Psi_0|P'_l c^\dagger_{l\sigma}c_{m\sigma}P'_l|\Psi_0\rangle}{\langle\Psi_0|P'_l P'_l|\Psi_0\rangle} \approx g'_t\,\frac{\langle\Psi_0|c^\dagger_{l\sigma}c_{m\sigma}|\Psi_0\rangle}{\langle\Psi_0|\Psi_0\rangle}. \tag{3.74}$$

where l denotes the reservoir site and $m \neq l$ is a fully projected site. Following the arguments leading to (3.3), we rewrite,

$$\begin{aligned}
\langle c^\dagger_{l\uparrow}c_{m\uparrow}\rangle_{\Psi'_l} &= \langle c^\dagger_{l\uparrow}(1-\hat{n}_{m\downarrow})c_{m\uparrow}\rangle_{\Psi'_l} && \text{(3.75a)}\\
&\approx \tilde{g}'_t\,\langle c^\dagger_{l\uparrow}(1-\hat{n}_{m\downarrow})c_{m\uparrow}\rangle_{\Psi_0} && \text{(3.75b)}\\
&\approx \underbrace{\tilde{g}'_t(1-n_{m\downarrow})}_{=g'_t}\,\langle c^\dagger_{l\uparrow}c_{m\uparrow}\rangle_{\Psi_0}\quad . && \text{(3.75c)}
\end{aligned}$$

As for (3.3), we perform the GA for the rhs of (3.75a) to guarantee agreement with the infinite dimensions approach. However, the decoupling of $(1-n_{m\downarrow})$ in (3.75c) becomes exact in infinite dimensions and we can recover the GA of (3.74).

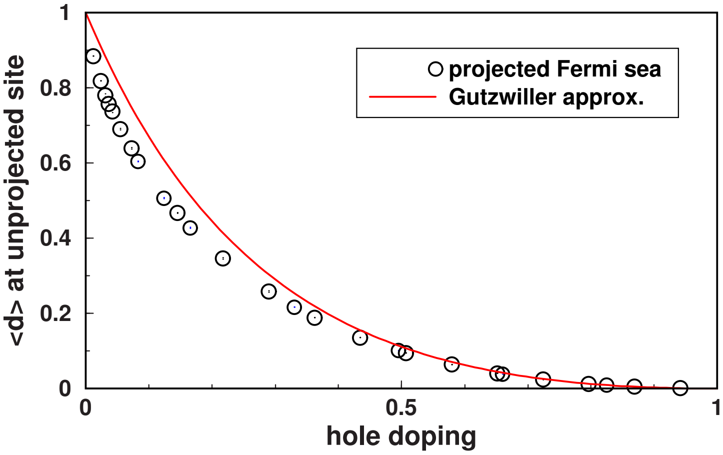

Figure 3.6: Double occupancy of the reservoir site $\langle d \rangle_{\Psi'_l} = \langle \hat{n}_{l\uparrow}\hat{n}_{l\downarrow} \rangle_{\Psi'_l}$ as a function of doping, for the partially projected Fermi sea. Note the good agreement between the Gutzwiller result (solid line), equation (3.70), and the VMC results for the projected Fermi sea (open circles). Statistical errors and finite-size corrections are estimated to be smaller than the symbols. From [6].

In analogy to the calculations in section 3.1, we consider the probability for $\langle c^\dagger_{l\uparrow}(1-\hat{n}_{m\downarrow})c_{m\uparrow} \rangle$ in $|\Psi'_l\rangle$ to determine the corresponding Gutzwiller renormalization factor $\tilde{g}'_t$ entering in (3.75c). We illustrate the two configurations that can contribute, together with the resulting probability from combining the bra- and ket-vectors, in figure 3.5. Using (3.68)-(3.70) for the partially projected site (grey in figure 3.5), we find the probability,

$$\begin{aligned} &\left([X n_{l\uparrow} X(1-n_l)]^{1/2} + [(1-X)X n_{l\downarrow}]^{1/2} \right) \cdot [(1-n_m)n_{m\uparrow}]^{1/2} \\ = \;& X \left([n_{l\uparrow}(1-n_l)]^{1/2} + \left[\frac{1-X}{X} n_{l\downarrow} \right]^{1/2} \right) \cdot [(1-n_m)n_{m\uparrow}]^{1/2} , \end{aligned} \tag{3.76}$$

in $|\Psi'_l\rangle$. With $n_{l\sigma} = n_{m\sigma} = n_\sigma$ and (3.67) above probability simplifies to,

$$X \left[n_\sigma(1-n) + n_\sigma^2 \right] = X\, n_\sigma(1-n_\sigma) \; . \tag{3.77}$$

For the respective probability in $|\Psi_0\rangle$ we use table 3.1 and obtain,

$$\left[n^0_{l\uparrow}(1-n^0_{l\downarrow}) \right]^{1/2} \cdot \left[n^0_{m\uparrow}(1-n^0_{m\downarrow})(1-n^0_{m\downarrow})(1-n^0_{m\uparrow}) \right]^{1/2} \; . \tag{3.78}$$

As pointed out in section 3.1, $n^0_{l\sigma} = n^0_{m\sigma} = n_\sigma$, for non-magnetic wave function. We then get the renormalization factor $\tilde{g}'_t$ by the ratio of (3.77)

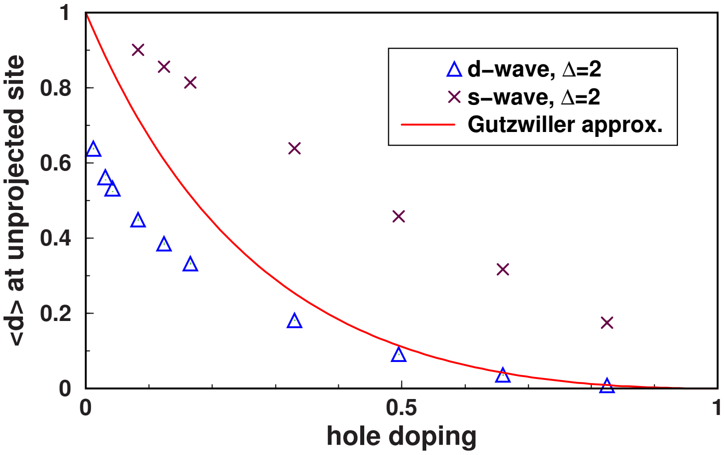

Figure 3.7: Double occupancy of the reservoir site $\langle d\rangle_{\Psi'_l} = \langle \hat{n}_{l\uparrow}\hat{n}_{l\downarrow}\rangle_{\Psi'_l}$ as a function of doping, for the partially projected BCS wave function. The solid line is the GA result from (3.70). The parameterization follows [122]. Statistical errors and finite-size corrections for the VMC results are estimated to be smaller than the symbols. From [6].

and (3.78), *i.e.*,

$$\tilde{g}'_t = \frac{X}{1-n_\sigma} \ . \tag{3.79}$$

Together with (3.75c), we obtain the renormalization factor,

$$g'_t = (1-n_\sigma)\tilde{g}'_t = X = \frac{1-n}{(1-n_\uparrow)(1-n_\downarrow)} \ , \tag{3.80}$$

for the GA in (3.74). Other expectation values in partially projected states can be calculated in analogy to above considerations. We will use above scheme when calculating the quasiparticle weight in chapter 6.

3.3.3 Comparison of the GA for partially projected states with VMC calculations

Before closing this section, we compare (3.70) to VMC results for $\langle d\rangle_{\Psi'_l} = \langle \hat{n}_{l\uparrow}\hat{n}_{l\downarrow}\rangle_{\Psi'_l} = 1 - X$. We find that the results from the generalized Gutzwiller approximation are in excellent qualitative agreement with the VMC results for a partially projected Fermi sea as shown in figure 3.6. We also used VMC to obtain the same quantity using projected s/d-wave BCS states[3] as variational states in the simulation. The results for $\langle d\rangle_{\Psi_l'}$ in BCS states are shown in figure 3.7. In contrast to the projected Fermi sea, a clear deviation from the Gutzwiller approximation is seen. This underscores the importance of pairing correlations in the unprojected wave function that are not completely taken into account by the Gutzwiller approximation scheme. It also explains to a certain extend the discrepancies between the VMC calculations and the GA for the quasiparticle weight as we will discuss in the chapter 7.

---

[3] The BCS states are defined by, $|v_{\mathbf{k}}|^2 = 1/2\,(1-\xi_{\mathbf{k}}/E_{\mathbf{k}})$, and $u_{\mathbf{k}}v_{\mathbf{k}}^* = \Delta_{\mathbf{k}}/(2E_{\mathbf{k}})$, where $\xi_{\mathbf{k}} = -2\,(\cos k_x + \cos k_y) - \mu$ and $E_{\mathbf{k}} = \sqrt{|\Delta_{\mathbf{k}}|^2 + \xi_{\mathbf{k}}^2}$ [s-wave: $\Delta_{\mathbf{k}} = \Delta$, d-wave: $\Delta_{\mathbf{k}} = \Delta\,(\cos k_x - \cos k_y)$].

Chapter 4

Renormalized mean field theory: Basic ideas and recent extensions

On the basis of the GA, Zhang, *et al.* [76] derived a renormalized mean field theory (RMFT) for the t-J model. In this chapter, we present an overview on this approach, which plays a central role within Gutzwiller-RVB theory. We illustrate successes and recent extensions of the RMFT for the HTSC, derive the RMFT gap equation, and review its applications to the Hubbard model in the strong coupling limit. Further extensions to antiferromagnetic and inhomogeneous patterns then provide a quantitative description of the Cuprate phase diagram.

4.1 Overview on the RMFT method

We start with an overview and discuss now how the RMFT allows for a systematic treatment of the Hubbard Hamiltonian in the strong-coupling limit. We present here the basic concepts, which will be then discussed in detail in the corresponding sections. Figure 4.1 summarizes the main steps necessary for the strong-coupling treatment of the Hubbard model within the RMFT. In the following we refer to the individual points illustrated in figure 4.1.

As shown in figure 4.1, the first step is to apply a canonical transformation e^{-iS} to the Hubbard Hamiltonian removing hopping processes that change

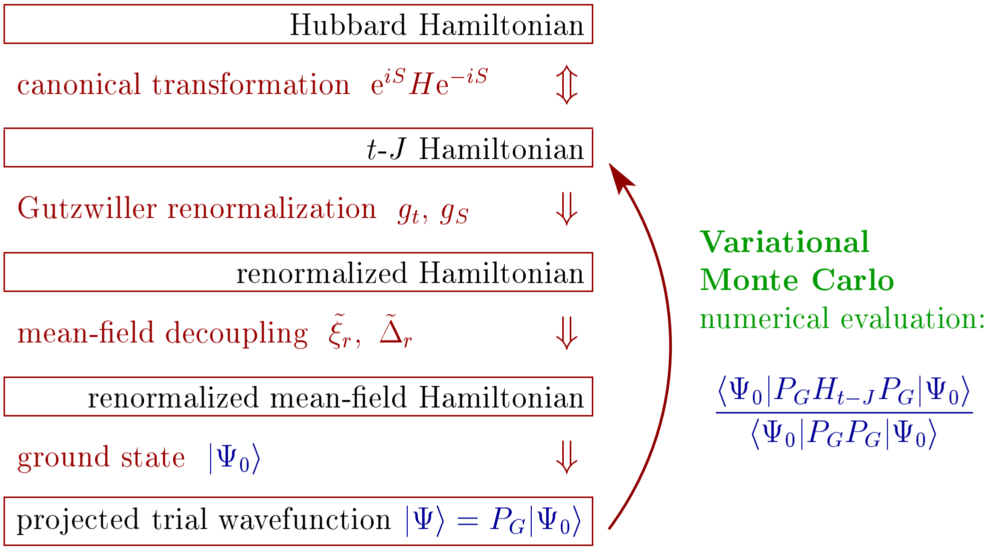
Hubbard Hamiltonian
canonical transformation $e^{iS}He^{-iS}$
t-J Hamiltonian
Gutzwiller renormalization g_t, g_S
renormalized Hamiltonian
mean-field decoupling $\tilde{\xi}_r$, $\tilde{\Delta}_r$
renormalized mean-field Hamiltonian
ground state $|\Psi_0\rangle$
projected trial wavefunction $|\Psi\rangle = P_G|\Psi_0\rangle$
Variational
Monte Carlo
numerical evaluation:
$\frac{\langle\Psi_0|P_G H_{t-J} P_G|\Psi_0\rangle}{\langle\Psi_0|P_G P_G|\Psi_0\rangle}$

Figure 4.1: Schematic illustration of the RMFT method; see text for a detailed description.

the number of doubly occupied sites. Doing so, we obtain the t-J Hamiltonian, which is defined in the subspace excluding double occupancy. The t-J Hamiltonian provides an effective low energy Hamiltonian for the Hubbard model in the strong coupling limit as already discussed in detail in section 2.4.

Next we invoke the Gutzwiller approximation to remove the restriction to projected states within the t-J Hamiltonian. As we will discuss in section 4.2.1, this procedure results in a renormalized Hamiltonian with terms weighted by the corresponding doping-dependent Gutzwiller renormalization factors (see also section 3.1).

We then perform a mean field decoupling for the renormalized Hamiltonian, focusing on hopping amplitudes $\tilde{\xi}_r \equiv \sum_\sigma \langle c^\dagger_{i\sigma} c_{i+r\sigma}\rangle_{\Psi_0}$ and pairing amplitudes $\tilde{\Delta}_r \equiv \langle c^\dagger_{i\uparrow} c^\dagger_{i+r\downarrow} - c^\dagger_{i\downarrow} c^\dagger_{i+r\uparrow}\rangle_{\Psi_0}$. Following this way, we find self-consistent gap equations for the mean field amplitudes (see section 4.2.2).

Solving the gap equations provides us with the mean field ground state $|\Psi_0\rangle$ of the renormalized t-J Hamiltonian in the "pre-projected" Hilbert space. Once $|\Psi_0\rangle$ is known, we can construct the Gutzwiller projected state $|\Psi\rangle = P_G|\Psi_0\rangle$, which then provides an approximative wave function for ground state of the projected t-J Hamiltonian. We can control the RMFT by using $|\Psi\rangle$ as a projected trial wave function within the VMC technique (see chapter 5). Therefore, above scheme provides a consistent ansatz to study Gutzwiller projected wave functions by a combination of RMFT and VMC methods.

The projected wave function $|\Psi\rangle$ allows for the calculation of relevant physical quantities as well as for the definition of excited states within the t-J model. To determine observables within the Hubbard Hamiltonian, we can employ the re-transformed wave function $e^{-iS}|\Psi\rangle$ for the calculation of expectation values. We will discuss this approach in section 4.3.

4.2 Derivation of the RMFT gap equations

In this section we review the work of Zhang, *et al.* [76] and develop a renormalized mean field theory (RMFT) for the t-J model based on the Gutzwiller renormalization scheme ($\hat{=}$ GA, see section 3.1). To illustrate the RMFT, we start with the simplest form of the t-J Hamiltonian,

$$H_{t-J} = P_G \left[-t \sum_{\langle i,j\rangle,\sigma} \left(c^\dagger_{i,\sigma} c_{j,\sigma} + c^\dagger_{j,\sigma} c_{i,\sigma} \right) + J \sum_{\langle i,j\rangle} \mathbf{S}_i \, \mathbf{S}_j \right] P_G \, . \tag{4.1}$$

We restrict ourselves to nearest neighbor hopping t, and a superexchange interaction J. We neglect any further hopping parameters as well as additional contributions in the Hamiltonian like the density-density term and the correlated hopping terms, see equation (2.6). The effects of such extensions are discussed in section 4.3, where we consider an RMFT for the Hubbard model, including next nearest neighbor hopping matrix elements.

4.2.1 Derivation of the renormalized t-J Hamiltonian

Two steps are necessary to obtain explicit analytic expressions for the ground state of the t-J model (4.1) for various doping levels x, where $x = 1-n$. The first is the Gutzwiller approximation, where the effects of the projection P_G are taken into account by appropriate renormalization factors. We search for a Gutzwiller projected state $P_G|\Psi_0\rangle$ that minimizes the energy expectation value,

$$\begin{aligned} E_0 &= \frac{\langle\Psi_0|P_G H_{t-J} P_G|\Psi_0\rangle}{\langle\Psi_0|P_G P_G|\Psi_0\rangle} \\ &= -t\sum_{\langle i,j\rangle,\sigma}\frac{\langle\Psi_0|P_G(c^\dagger_{i,\sigma}c_{j,\sigma}+c^\dagger_{j,\sigma}c_{i,\sigma})P_G|\Psi_0\rangle}{\langle\Psi_0|P_G P_G|\Psi_0\rangle} \\ &\quad + J\sum_{\langle i,j\rangle}\frac{\langle\Psi_0|P_G\mathbf{S}_i\,\mathbf{S}_j P_G|\Psi_0\rangle}{\langle\Psi_0|P_G P_G|\Psi_0\rangle}\ . \end{aligned} \tag{4.2}$$

By invoking a GA for (4.2), we get rid of the projection operator P_G and obtain,

$$E_0 \approx -g_t t\sum_{\langle i,j\rangle,\sigma}\frac{\langle\Psi_0|(c^\dagger_{i,\sigma}c_{j,\sigma}+c^\dagger_{j,\sigma}c_{i,\sigma})|\Psi_0\rangle}{\langle\Psi_0|\Psi_0\rangle} + g_S\,J\sum_{\langle i,j\rangle}\frac{\langle\Psi_0|\mathbf{S}_i\,\mathbf{S}_j|\Psi_0\rangle}{\langle\Psi_0|\Psi_0\rangle}\ . \tag{4.3}$$

The GA for the hopping term [first term in (4.3)] has a renormalization factor, $g_t = (1-n)/(1-n/2)$, which was derived in the previous chapter, equation (3.9). For the superexchange term [second term in (4.3)], the renormalization factor is $g_S = 1/(1-n/2)^2$, where we assume a homogeneous state without any sublattice magnetization, see (3.22).

We can now determine the variational ground state by searching for the state $|\Psi_0\rangle$, that minimizes the renormalized t-J Hamiltonian, $\tilde{H}_{t-J}$, defined as,

$$\tilde{H}_{t-J} = -g_t t\sum_{\langle i,j\rangle,\sigma}(c^\dagger_{i,\sigma}c_{j,\sigma}+c^\dagger_{j,\sigma}c_{i,\sigma})\ +\ g_S\,J\sum_{\langle i,j\rangle}\mathbf{S}_i\,\mathbf{S}_j\ . \tag{4.4}$$

Once $|\Psi_0\rangle$ is known, we may consider the projected state, $P_G|\Psi_0\rangle$, as a trial ground-state of H_{t-J}.

4.2.2 Mean field decoupling of the renormalized Hamiltonian

The next step in derivation of the RMFT, see section 4.1, is the realization that $\tilde{H}_{t-J}$ allows for several types of molecular-fields [7, 76]: For simplification we only concentrate on the singlet pairing amplitude,

$$\tilde{\Delta}_r \equiv \langle c^\dagger_{i\uparrow}c^\dagger_{i+r\downarrow} - c^\dagger_{i\downarrow}c^\dagger_{i+r\uparrow}\rangle_{\Psi_0}\ , \tag{4.5}$$

and the hopping amplitude,

$$\tilde{\xi}_r \equiv \sum_\sigma \langle c^\dagger_{i\sigma} c_{i+r\sigma} \rangle_{\Psi_0} \ , \tag{4.6}$$

where $r = \hat{x}, \hat{y} \mathrel{\hat{=}} (1,0), (0,1)$ connects nearest neighbor sites. This decoupling scheme of the renormalized Hamiltonian leads to a BCS ground state,

$$|\Psi_0\rangle = \prod_{\mathbf{k}} (u_{\mathbf{k}} + v_{\mathbf{k}} c^\dagger_{\mathbf{k}\uparrow} c^\dagger_{-\mathbf{k}\downarrow}) \ |0\rangle \ , \tag{4.7}$$

with,

$$v^2_{\mathbf{k}} = \frac{1}{2}\left(1 - \frac{\xi_{\mathbf{k}}}{E_{\mathbf{k}}}\right) \ , \tag{4.8}$$

and $u^2_{\mathbf{k}} = 1 - v^2_{\mathbf{k}}$. The resulting gap equations are

$$\begin{aligned} \tilde{\Delta}_r &= 1/L \sum_{\mathbf{k}} \cos(\mathbf{k}\, r) \Delta_{\mathbf{k}} / E_{\mathbf{k}} \ , && (4.9) \\ \tilde{\xi}_r &= -1/L \sum_{\mathbf{k}} \cos(\mathbf{k}\, r) \xi_{\mathbf{k}} / E_{\mathbf{k}} \ , && (4.10) \end{aligned}$$

together with the condition, $x = 1/L \sum_{\mathbf{k}} \xi_{\mathbf{k}}/E_{\mathbf{k}}$, for the hole-doping concentration. The dispersion of the mean field excitations is given by, $E_{\mathbf{k}} = \sqrt{\xi^2_{\mathbf{k}} + \Delta^2_{\mathbf{k}}}$, where

$$\begin{aligned} \Delta_{\mathbf{k}} &= \frac{3J}{4}\left(\tilde{\Delta}_x \cos k_x + \tilde{\Delta}_y \cos k_y\right) && (4.11) \\ \xi_{\mathbf{k}} &= -\left(2g_t t + \frac{3J}{4}\tilde{\xi}_x\right)\cos k_x - \left(2g_t t + \frac{3J}{4}\tilde{\xi}_y\right)\cos k_y - \mu \ . && (4.12) \end{aligned}$$

Equation (4.9) resembles the usual BCS gap equation, except that we consider independent pairing along the x- and the y-direction. Together with (4.10), we have four coupled gap equations (for $\tilde{\Delta}_x$, $\tilde{\Delta}_y$, $\tilde{\xi}_x$, $\tilde{\xi}_y$), which must be solved self-consistently. The $\Delta_{\mathbf{k}}$ is obviously related to pairing in the state $|\Psi_0\rangle$, however, it is not identical to the superconducting order parameter in $P_G|\Psi_0\rangle$ as will be shown below. The $\xi_{\mathbf{k}}$ becomes the renormalized dispersion in the absence of pairing and includes a chemical potential μ to regulate the particle density.

4.2.3 Solutions of the RMFT gap equations

The gap equation can be solved numerically for $J = t/3$, which is a reasonable assumption for HTSC. However, we emphasize that the results presented

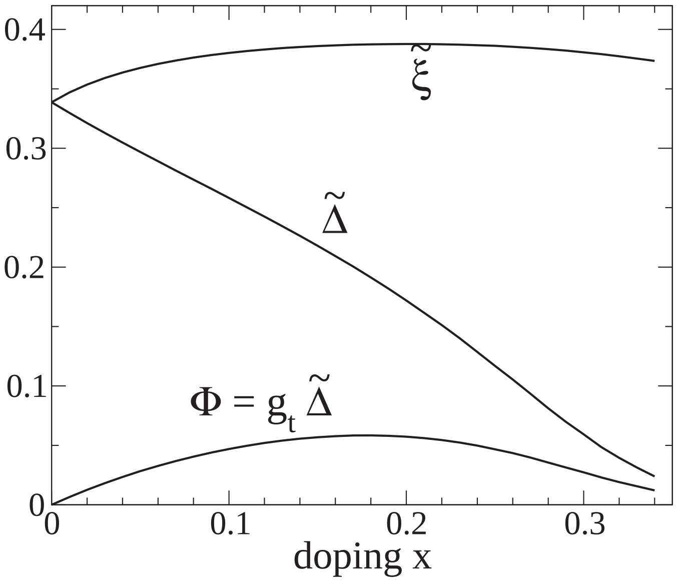

Figure 4.2: Doping dependence of the d-wave pairing amplitude $\tilde{\Delta}$, the hopping amplitude $\tilde{\xi}$, and the superconducting order parameter Φ, see (4.13), in the d-wave ground state for the t-J model (4.1) with $J = t/3$.

below are not sensitive to a particular choice of J. We find that a d-wave pairing state is stable for $x \leq 0.35$. In this case, $\tilde{\Delta} \equiv |\tilde{\Delta}_x| = |\tilde{\Delta}_y|$ with $\tilde{\Delta}_x = -\tilde{\Delta}_y$ and $\tilde{\xi} \equiv \tilde{\xi}_x = \tilde{\xi}_y$. We illustrate the doping dependence of these quantities in figure 4.2. The superconducting order parameter,

$$\Phi \equiv |\langle c^\dagger_{i\uparrow} c^\dagger_{i+\tau\downarrow} - c^\dagger_{i\downarrow} c^\dagger_{i+\tau\uparrow} \rangle_\Psi| \ , \tag{4.13}$$

is an expectation value in the projected ground states, $|\Psi\rangle \equiv P_G|\Psi_0\rangle$, where τ is a neighboring site. Evaluating Φ by the GA (section 3.1) one finds that Φ is renormalized as the hopping amplitude by g_t, namely $\Phi \approx g_t \tilde{\Delta}$. As illustrated in figure 4.2, Φ vanishes linearly near $x = 0$, while $\tilde{\Delta}$ continuously increases towards half-filling. These results are in good agreement with VMC results [99, 122, 128] and the experimentally observed T_c for the d-wave pairing in the HTSC.

For the renormalized Hamiltonian, the $E_{\mathbf{k}}$ corresponds to the dispersion of the Bogoliubov quasiparticles, $|\Psi^\sigma_{\mathbf{k},0}\rangle \equiv \gamma^\dagger_{\mathbf{k}\sigma}|\Psi_0\rangle$, with $\sigma =\uparrow\downarrow$, where the corresponding Bogoliubov operators are defined by, $\gamma^\dagger_{-\mathbf{k}\downarrow} \equiv u_{\mathbf{k}} c^\dagger_{-\mathbf{k}\downarrow} + v_{\mathbf{k}} c_{\mathbf{k}\uparrow}$, and, $\gamma^\dagger_{\mathbf{k}\uparrow} \equiv u_{\mathbf{k}} c^\dagger_{\mathbf{k}\uparrow} - v_{\mathbf{k}} c_{-\mathbf{k}\downarrow}$, respectively. However, $E_{\mathbf{k}}$ also describes the excitation energy of the corresponding projected Gutzwiller-Bogoliubov quasiparticles,

$$|\Psi_{\mathbf{k}\sigma}\rangle \equiv P_G|\Psi^\sigma_{\mathbf{k},0}\rangle \ = \ P_G \gamma^\dagger_{\mathbf{k}\sigma}|\Psi_0\rangle \ . \tag{4.14}$$

To see why, one evaluates the expectation value of the t-J Hamiltonian with respect to $|\Psi_{\mathbf{k}\sigma}\rangle$. Because, $|\Psi_{\mathbf{k}\sigma}\rangle = P_G|\Psi^{\sigma}_{\mathbf{k},0}\rangle$, is renormalized exactly as, $|\Psi\rangle = P_G|\Psi_0\rangle$, we recover the renormalized Hamiltonian $\tilde{H}_{t-J}$, (4.4), by invoking a GA. The state $|\Psi^{\sigma}_{\mathbf{k},0}\rangle$ is now acting onto $\tilde{H}_{t-J}$, yielding in mean field decoupling a Bogoliubov quasiparticle with excitation energy $E_{\mathbf{k}}$. Therefore, the gap $\Delta_{\mathbf{k}}$ in $E_{\mathbf{k}} = \sqrt{\xi^2_{\mathbf{k}} + \Delta^2_{\mathbf{k}}}$ corresponds to the quasiparticle gap in the projected superconducting state and is directly proportional to the mean field amplitude $\tilde{\Delta}$ in figure 4.2. We note that RMFT [76] correctly reported the doping dependence of the d-wave gap, *i.e.*, an increasing gap with decreasing doping, substantially before this behavior was experimentally well established.

Above calculations follow the original work [76] and are restricted to a homogeneous phase without any magnetization. Therefore, the results can not adequately describe the antiferromagnetic region around half-filling as well as the kinds of inhomogeneities observed in HTSC. In order to investigate these effects, we must allow for additional degrees of freedom in the mean field solutions. RMFT studies, which follow this way, are discussed in the following sections and provide a more detailed description of the HTSC.

4.2.4 Local $SU(2)$ symmetry in the half-filled limit

In this subsection, we call attention to the half-filled case. In this limit the kinetic energy renormalizes to zero, since $g_t \to 0$ for $x \to 0$. The t-J model reduces to the antiferromagnetic Heisenberg model, which is conserved under local $SU(2)$ gauge transformations [76, 129],

$$c^{\dagger}_{i\uparrow} \to \alpha_i c^{\dagger}_{i\uparrow} + \beta_i c_{i\downarrow} \ , \quad c_{i\downarrow} \to -\beta^*_i c^{\dagger}_{i\uparrow} + \alpha^*_i c_{i\downarrow} \ , \tag{4.15}$$

where $\alpha_i\alpha^*_i + \beta_i\beta^*_i = 1$. The invariance of the Hamiltonian is due the spin operator $\mathbf{S}_i$, which does not change under $SU(2)$ transformations, as can be proved by applying (4.15) to the operators $S^{\pm}_i$ and S^z_i. For S^+_i we find,

$$\begin{aligned} S^+_i = c^{\dagger}_{i\uparrow}c_{i\downarrow} &\to (\alpha_i c^{\dagger}_{i\uparrow} + \beta_i c_{i\downarrow})(-\beta^*_i c^{\dagger}_{i\uparrow} + \alpha^*_i c_{i\downarrow}) \\ &\to \alpha_i\alpha^*_i \, S^+_i + \beta_i\beta^*_i \, S^+_i = S^+_i \ . \end{aligned} \tag{4.16}$$

The invariance of S^-_i and S^z_i under (4.15) can be shown analogously.

Because of the local $SU(2)$ gauge symmetry the renormalized mean field Hamiltonian has a large degeneracy in the representation of ground states at half-filling, as may be seen by transforming the mean field amplitudes $\tilde{\Delta}_r$ and

$\tilde{\xi}_r$, (4.5) and (4.6), under (4.15). Some of the resulting degenerated states, which are related to each other by appropriate $SU(2)$ transformations, are summarized in table 4.1. Another example among the degenerated states is the staggered π-flux state [129],

$$\xi_{\mathbf{ij}} = |\xi_0|^2 \exp\left(i(-1)^{i_x+i_y}\frac{\pi}{4}\right), \tag{4.17}$$

with a complex hopping amplitude $\xi_{\mathbf{ij}} \equiv \langle c^\dagger_{\mathbf{i}\sigma} c_{\mathbf{i}\sigma}\rangle_0$, but a vanishing pairing amplitude $\Delta_{\mathbf{ij}} \equiv \langle c^\dagger_{\mathbf{i}\uparrow} c_{\mathbf{i}\downarrow}\rangle_0 = 0$.

It is important to note that above degeneracy is not true in terms of the projected wave function, since it only results from using an underdetermined representation. In other words, the states that are degenerated are the unprojected states $|\Psi_0\rangle$, but not the physical states $P_G|\Psi_0\rangle$ [76]. Therefore, the whole set of degenerated grounds states in the renormalized mean field Hamiltonian correspond (except of a phase factor) to a single projected state; for a prove see [76].

All states listed in the table 4.1 and (4.17) have the same superexchange energy, even at finite doping, due the $SU(2)$ invariance. However, the kinetic energy T, (2.8), and the 3-site term H_3, (2.10), which only vanish at half-filling, are not invariant under the $SU(2)$ transformation (4.15). Therefore the degeneracy in $|\Psi_0\rangle$ is lifted at finite doping, where the d-wave pairing state is selected due to its lower kinetic energy.

The $SU(2)$ gauge symmetry of the superexchange term led to the speculation that at finite doping, when the degeneracy is lifted, some among the "degenerated" states may compete with the d-wave state (also one of the degenerated states at half-filling). In particular, it was argued that staggered flux states could serve as a "competing" and/or as a "normal" state

d-wave pairing	$\tilde{\Delta}_x = -\tilde{\Delta}_y = \tilde{\xi}_x = \tilde{\xi}_y = C/\sqrt{2}$
d-wave density matrix*	$\tilde{\Delta}_x = \tilde{\Delta}_y = \tilde{\xi}_x = -\tilde{\xi}_y = C/\sqrt{2}$
chiral state	$\tilde{\Delta}_x = -\,i\,\tilde{\Delta}_y = C\,, \quad \tilde{\xi}_x = \tilde{\xi}_y = 0$
anisotropic state	$\tilde{\Delta}_x = \tilde{\xi}_y = C\,, \quad \tilde{\Delta}_y = \tilde{\xi}_x = 0$

Table 4.1: Examples of degenerated states of the renormalized mean field Hamiltonian at half-filling, see also [76]. The general constant $C = 0.479$ is determined by the RMFT gap equations, (4.9) and (4.10). *We note that the d-wave density matrix is not the d-density wave (DDW) order discussed in [54].

in the underdoped regime of the HTSC [11, 117]. Besides this competing order scenario, a spin-charge locking mechanism [96] resting on the presence of the $SU(2)$ gauge symmetry at half-filling was suggested. Despite above studies the entire consequences of the degeneracy in the unprojected mean field ground states at half-filling are not yet well established.

4.3 RMFT for the Hubbard model and application to HTSC

The RMFT presented so far can be improved by considering all terms contributing to the t-J Hamiltonian (2.6), *i.e.*, including the density-density term (2.9) as well as the correlated hopping terms (2.10). The t-J Hamiltonian H_{t-J} is then connected to the Hubbard model H, equation (2.1), via the canonical transformation $H_{t-J} = P_G e^{iS} H e^{-iS} P_G$ as discussed in section 2.4. Observables for the Hubbard model can be evaluated by considering expectation values in the re-transformed wave function $e^{-iS} P_G |\Psi_0\rangle$. Below we will use this ansatz to study the superconducting order parameter. Before discussing detailed results for above considerations, we note that we will include next nearest neighbor hopping (t') into the Hubbard Hamiltonian in order to allow for qualitative comparisons with experimental results for the HTSC.

4.3.1 Generalized gap equations for the strong coupling limit

We obtain the RMFT gap equations for the Hubbard model in the strong coupling limit by considering the corresponding effective Hamiltonian, *i.e.*, the full t-J Hamiltonian. The gap equations for this t-J Hamiltonian, which includes all terms from equation (2.6), can then be derived in analogy to the previous section.

First we invoke the GA to obtain the renormalized Hamiltonian for (2.6). We note that all (nearest as well as further neighbors) hopping terms are renormalized by $g_t = (1-n)/(1-n/2)$ and all superexchange terms by $g_S = 1/(1-n/2)^2$. Since the density-density term commutes with the projection operator P_G, it does not pick up any Gutzwiller renormalization factor. The new correlated hopping terms, equation (2.10), are of the following form,

$$\begin{aligned}
\langle c^\dagger_{i+\tau_1,\uparrow} c^\dagger_{i,\downarrow} c_{i,\downarrow} c_{i+\tau_2,\uparrow}\rangle_{P_G\Psi_0} &\approx g_3 \,\langle c^\dagger_{i+\tau_1,\uparrow} n_{i,\downarrow}(1-n_{i,\uparrow}) c_{i+\tau_2,\uparrow}\rangle_{\Psi_0} \;, \\
\langle c^\dagger_{i+\tau_1,\downarrow} c^\dagger_{i,\uparrow} c_{i,\downarrow} c_{i+\tau_2,\uparrow}\rangle_{P_G\Psi_0} &\approx g_3 \,\langle c^\dagger_{i+\tau_1,\downarrow} c^\dagger_{i,\uparrow} c_{i,\downarrow} c_{i+\tau_2,\uparrow}\rangle_{\Psi_0} \;, \qquad (4.18)
\end{aligned}$$

involve three sites (i, $i+\tau_1$, and $i+\tau_2$), and are renormalized by a factor $g_3 = (1-n)/(1-n/2)^2$. For a derivation of the GA for the correlated hopping terms we refer to the appendix of [5].

Next we decouple the resulting renormalized Hamiltonian by the same scheme discussed in the previous section, obtaining therefore the same gap equations, (4.9) and (4.10) as before. However, the dispersion relation, $E_{\mathbf{k}} = \sqrt{\xi_{\mathbf{k}}^2 + \Delta_{\mathbf{k}}^2}$, with,

$$\begin{aligned}
\xi_{\mathbf{k}} &= -\left(2g_t t + J\,\frac{\tilde{\xi}}{4}\,x_1 + J_3\,\frac{\tilde{\xi}'}{4}\,x_2\right)(\cos k_x + \cos k_y) \\
&\quad -\left(2g_t t' + J'\,\frac{\tilde{\xi}'}{4}\,x_1 + J_3\,\frac{\tilde{\xi}}{4}\,x_2\right) 2\,\cos k_x \cos k_y \\
&\quad -x_D \sum_{\tau_1\neq\tau_2} \frac{t_{\tau_1} t_{\tau_2}}{4U} \cos\left[\mathbf{k}(\tau_1-\tau_2)\right] - \mu \;, \qquad (4.19) \\
\Delta_{\mathbf{k}} &= J\,\frac{\tilde{\Delta}}{4}\left[3g_s + 1 - (3+x)g_3\right](\cos k_x - \cos k_y) \;, \qquad (4.20)
\end{aligned}$$

incorporates the effects of further neighbor hopping and correlated hopping terms. Above expressions for $\xi_{\mathbf{k}}$ and $\Delta_{\mathbf{k}}$ are valid for $\tilde{\Delta} \equiv |\tilde{\Delta}_x| = |\tilde{\Delta}_y|$, $\tilde{\Delta}_x = -\tilde{\Delta}_y$, $\tilde{\xi} \equiv \tilde{\xi}_x = \tilde{\xi}_y$, *i.e.*, for the d-wave pairing state, which is the most stable solution of the gap equations (4.9) and (4.10). Furthermore we defined new hopping amplitudes for next nearest neighbors, $\tilde{\xi}' \equiv \tilde{\xi}_{x+y} = \tilde{\xi}_{x-y}$. The last sum in (4.19) is a sum over all pairs of non-identical neighboring sites τ_1 and τ_2, where t_{τ_1} and t_{τ_2} are nearest and next nearest neighbor hopping terms. We defined, $J = 4t^2/U$, $J_3 = 4t't/U$, and $J' = 4t'^2/U$ and abbreviated, $x_1 = 3g_s - 1 + 3(3-x)g_3$, $x_2 = 4(3-x)g_3$, and $x_D = (1-x^2)g_3$ in (4.19).

As in section 4.2, the ground state $|\Psi_0\rangle$ of the renormalized t-J Hamiltonian results from above equations. By including a projection operator P_G into the wave function we obtain $P_G|\Psi_0\rangle$, which corresponds to a variational wave function for the ground state of the t-J Hamiltonian in the fully projected Hilbert space. Invoking the canonical transformation e^{-iS} then provides an approximative ground state $e^{-iS}P_G|\Psi_0\rangle$ for the Hubbard model.

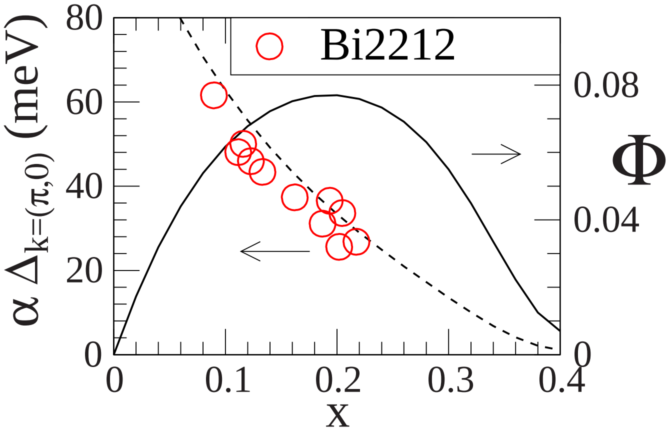

Figure 4.3: Doping dependence of (solid line, right scale) the superconducting order parameter, Φ, and (dashed line, left scale) the superconducting gap, $|\Delta_{\mathbf{k}}|$, at $\mathbf{k} = (\pi, 0)$ for $t = 300$ meV. The RMFT superconducting gap is scaled by a factor $\alpha = 1/2$ for comparison with experimental data (red circles, Bi2122 [14]). From [7].

4.3.2 Results from the generalized gap equations

For comparison with experiments we consider a ratio $t'/t = -1/4$ between next nearest and nearest neighbor hopping amplitudes, which is widely used for the modelling of the band structure of various HTSC [44]. Furthermore, we choose an on-site repulsion $U = 12\,t$, *i.e.*, we work in the strong coupling regime $U \gg t, t'$, where the transformation from the Hubbard to the t-J model is valid approximatively. Above choice of the model parameters reduces the number of free parameters to one energy scale t, which is about $t \approx 300 - 500$ meV for the HTSC.

The doping dependence of the superconducting gap, $|\Delta_{\mathbf{k}}|$ at $\mathbf{k} = (\pi, 0)$, is shown in figure 4.3. It resembles experimental observations quite well. However, the gap is overestimated by a factor of about 2 (see scaling factor $\alpha = 1/2$ in figure 4.3) within mean field theory. We attribute this overall mismatch to the neglecting of dynamical correlations [130] within the RMFT, which is based on the molecular-field approximation and on the incorporation of static on-site correlations.

As mentioned in section 4.2.3, the superconducting gap is not identical to the true superconducting order parameter, $\Phi \equiv |\langle c^\dagger_{i\uparrow} c^\dagger_{i+\tau\downarrow} - c^\dagger_{i\downarrow} c^\dagger_{i+\tau\uparrow} \rangle|$ [76, 128]. Here, we determine the expectation value for Φ within the re-transformed wave function, $e^{-iS} P_G |\Psi_0\rangle$. Following section 2.4, we evaluate the canonical transformation e^{-iS} in order $\mathcal{O}(t/U)$. Doing so, provides systematic t/U-corrections with respect to the result from section 4.2.3, where we used simply $P_G|\Psi_0\rangle$ when calculating the expectation value for the superconducting order parameter.

The required calculations for the expectation value of a general observable $\hat{O}$ within the Hubbard model are summarized by,

$$\begin{aligned} \langle\,\hat{O}\,\rangle_{e^{-iS}P_G\Psi_0} &= \langle\, e^{iS}\hat{O}e^{-iS}\,\rangle_{P_G\Psi_0} & \text{(4.21a)} \\ &\approx \langle\,\hat{O} + i[S,\hat{O}]\,\rangle_{P_G\Psi_0}\ , & \text{(4.21b)} \end{aligned}$$

where the last step corresponds to the evaluation of e^{-iS} in order $\mathcal{O}(t/U)$; compare with section 2.4. Note that (4.21b) corresponds to an expectation value of the operator $O + i[S,\hat{O}]$ in the projected state $P_G|\Psi_0\rangle$. We can therefore use a generalized Gutzwiller approximation by invoking the counting arguments given in section 3.1.

Setting, $\hat{O} = c_{i\uparrow}^\dagger c_{i+\tau\downarrow}^\dagger - c_{i\downarrow}^\dagger c_{i+\tau\uparrow}^\dagger$, we can evaluated the superconducting order parameter Φ for the Hubbard model by above scheme. We find,

$$\Phi \approx g_t\tilde{\Delta} + \frac{t}{U}\, g_3\,(6-x)\,\tilde{\Delta}\,\tilde{\xi}\ . \tag{4.22}$$

In deriving (4.22) we considered $t' \approx 0$ within S, for simplicity, since $|t'| \ll |t|$. As shown in figure 4.3, Φ vanishes as $x \to 0$, and the t/U-corrections do not qualitatively change the result of Zhang, *et al.* [76] near half-filling. We emphasize that above procedure is applicable to all kind of observables and provides a systematic way to study the Hubbard model in the strong coupling limit.

Next we consider the nature of the low lying excitations, *i.e.*, the quasiparticles created at the nodal point, $k_F \equiv k_{F,x} = k_{F,y}$. The nodal dispersion around k_F is characterized by the velocity, v_F, which directly influences a number of experimentally accessible quantities. Within RMFT, v_F is directly obtained by calculating the gradient of $\xi_{\mathbf{k}}$ along the direction, $(0,0) \to (\pi,\pi)$. We use $\xi_{\mathbf{k}}$ from equation (4.19). The result is presented in figure 4.4 (for $t = 0.3, 0.4, 0.5$ eV and $a_0 = 4\mathring{A}$) and is well approximated by the formula,

$$v_F/a_0 \approx \sqrt{2}\sin k_F \left[2g_t(t + 2t'\cos k_F) + x_1\frac{J}{4}\tilde{\xi}\right]\ . \tag{4.23}$$

In the above equation, we have set J' and J'' to zero for simplicity; an approximation that becomes exact in the half-filled limit and only little influences the result. As seen in figure 4.4, v_F increases with x, but remains finite as

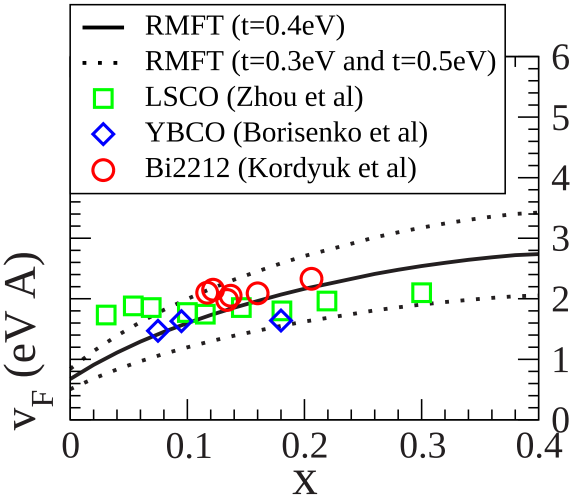

Figure 4.4: Doping dependence of Fermi velocity, v_F. The RMFT results are compared with experimental data from Zhou, *et al.* [27], Borisenko, *et al.* [131], and Kordyuk, *et al.* [132]. From [7].

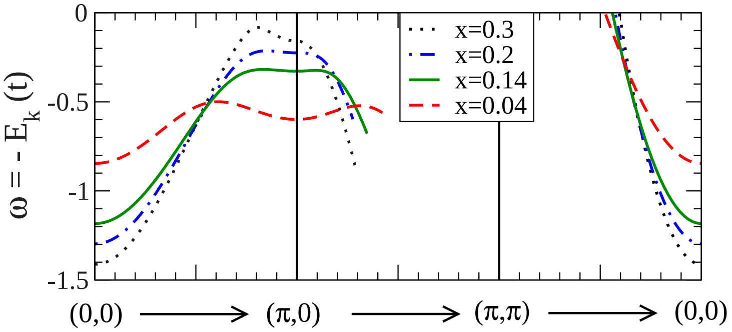

Figure 4.5: Energy dispersion, $\omega = -E_{\mathbf{k}} = \sqrt{\xi_{\mathbf{k}} + \Delta_{\mathbf{k}}}$, of the Gutzwiller-Bogoliubov quasiparticle for different doping x. From [7].

$x \to 0$. As can be inferred from (4.23), the energy scale of the nodal velocity at $x = 0$ is determined by J, *i.e.*, $v_F/(a_0 J) \approx \sqrt{2}\sin(k_F)\frac{11}{4}\tilde{\xi} \approx 1.5$ (for $\tilde{\xi} \approx 0.38$ and $k_F \approx \frac{\pi}{2}$). The observed doping dependence stems from the effects of the Gutzwiller projection P_G. As x increases, holes gain kinetic energy by direct hopping, *viz.*, g_t increases with doping; but g_s decreases, leading to the doping dependence of v_F seen in figure 4.4. Note, that the RMFT results presented in figure 4.4 are absolute in value. No rescaling has been made for comparison with the experiments, contrary to the results for the gap $|\Delta_{\mathbf{k}=(\pi,\pi)}|$ presented in figure 4.3.

Above results agree with the numerical VMC results of Paramekanti, *et al.*, who extracted v_F from the discontinuity of the first moment of the spectral function in the repulsive U Hubbard model [128, 99] and of Yunoki, *et al.*, who obtain v_F from the quasiparticle dispersion in the t-J model [121]. A comparison to ARPES data [27, 131, 132, 133, 134], presented in figure 4.4, shows good agreement. The doping dependence of v_F in the severely underdoped regime remains to be settled experimentally. While some groups report a nearly constant Fermi velocity (see data for LSCO in figure 4.4.), others observe an slight increase with doping (see data for YBCO and Bi2212 in figure 4.4.). The energy scales t and J might be extracted, in principle, from the ARPES data in v_F, whenever data with high accuracy becomes available. By using $\tilde{\xi} \approx 0.38$ and setting k_F and the ratio t'/t to the experimentally observed values, t and J can be fitted by (4.23). Within RMFT, we find that the nodal properties remain essentially unchanged when $\tilde{\Delta}$ is set to 0; *i.e.*, the doping dependence of v_F results from the vicinity of the state to a Mott insulator, rather than the occurrence of superconductivity itself.

In figure 4.5, we present the energy dispersion, $\omega = -E_{\mathbf{k}}$, of the Gutzwiller-Bogoliubov QP along the directions, $(0,0) \to (\pi,0)$, $(\pi,0) \to (\pi,\pi)$, and $(\pi,\pi) \to (0,0)$ for different doping levels x. The dispersion is flattened when approaching half-filling and the gap around $(\pi,0)$ becomes large. We emphasize that these RMFT calculations adequately describe only the low energy sector of the HTSC, and do not seek to explain the “kink” at higher energies [27, 131, 132, 133, 134].

Above calculations present a systematic way to study the Hubbard model in the strong coupling limit. The approach rests on the use of the t-J model as an effective Hamiltonian and on determining expectation values within the re-transformed trial wave function, $e^{-iS}P_G|\Psi_0\rangle$; a scheme that can be straightforward extended to excited states as shown in chapter 6 (see also [7]).

4.4 Possible extensions and further applications

4.4.1 Incorporation of antiferromagnetism

The incorporation of antiferromagnetism is an example of a possible extension of the RMFT. In order to describe an antiferromagnet with finite sublattice magnetization m, we have to allow for an additional degree of freedom in

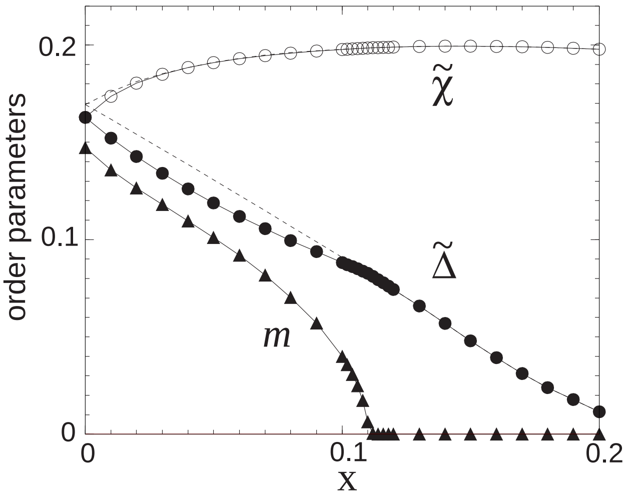

Figure 4.6: RMFT calculations including antiferromagnetism from Ogata and Himeda [90]. The self-consistent parameters $\tilde{\Delta}$ (pairing amplitude), $\tilde{\xi}$ (hopping amplitude), and m (staggered magnetization) are shown as a function of the doping rate $x = 1 - n$ for $J/t = 0.3$ and $t' = J' = 0$. The dashed lines represent the results when the antiferromagnetic order is suppressed, i.e, m is fixed to zero. From [90].

the wave function. When deriving the corresponding gap equation we must keep in mind that the antiferromagnetic correlation effects the GA as discussed in section 3.1. However, Himeda and Ogata [85] showed by VMC calculations that even the formulas from section 3.1 do not adequately describe all aspects in a magnetic ordered state. They determined effective Gutzwiller renormalization factors by comparing the numerically obtained expectation values in the projected state with the respective mean field values before projection. It was found that the z-component of the Gutzwiller renormalization factor g_S^z is enhanced compared with those of the xy-component $g_S^{\pm}$.

Ogata and Himeda [90] argued that the discrepancies stem from spatial correlations neglected by the GA. They derived extended Gutzwiller renormalization factors by considering a cluster around the sites i and j to incorporate further inter-site correlations. Applying these renormalization factors and solving the gap equations including antiferromagnetism yields the results of figure 4.6. We see that for doping, $\delta < 0.1$, long range antiferromagnetic order coexists with superconductivity. For higher doping the magnetization m vanishes and solely the superconducting order remains. This result is obtained neglecting the next nearest neighbor hopping ($t' = 0$) and agrees with previous VMC results [85, 86, 87, 88]. We note that the extended Gutzwiller renormalization factors of Ogata and Himeda are essential for reproducing the VMC calculations. However, figure 4.6 does not quantitatively agree with the experimentally phase diagram of hole-doped Cuprates, where antiferromagnetism already disappears at about $3-5\%$ doping. A better matching may be obtained by considering the effects of t' as already done by VMC [89] and quantum cluster methods [135, 136].

4.4.2 Applications to inhomogeneous systems

The RMFT was also applied to study inhomogeneities, such as stripes and checkerboard charge order [81, 82, 83, 84], vortex cores [94, 95], or magnetic and non-magnetic impurities [91, 92, 93]. These investigations throw light on the interplay between antiferromagnetic correlations, d-wave superconductivity, and charge order and can be compared with STM data.

However, such studies require an unrestricted Hartree-Fock treatment of the renormalized t-J Hamiltonian (4.4), *i.e.*, local expectation values such as, $\tilde{\Delta}_{ij} \equiv \langle c^\dagger_{i\uparrow} c^\dagger_{j\downarrow}\rangle_{\Psi_0}$, and, $\tilde{\xi}_{ij\sigma} \equiv \langle c^\dagger_{i\sigma} c_{j\sigma}\rangle_{\Psi_0}$, must be considered independently for each bond. Furthermore, the local charge densities $n_{i\sigma}$ generally differ from site to site, and thus the Gutzwiller renormalization factors of the renormalized Hamiltonian depend on the site indices i and j (g_t^{ij}, g_S^{ij}). Special attention must be paid when deriving these Gutzwiller renormalization factors, because the local charge densities can differ between the projected and unprojected state (see discussion in section 3.1). For inhomogeneous systems the RMFT gap equations generalize to the so-called Bogoliubov-de Gennes equations, which must then be solved self-consistently.

The investigation of charge modulations within above framework [81, 82, 83, 84] provides an understanding of the recently observed 4×4 checkerboard patterns in the STM data of the HTSC. These studies neglected long range antiferromagnetism and assumed $\tilde{\xi}_{ij} = \tilde{\xi}_{ij\uparrow} = \tilde{\xi}_{ij\downarrow}$ and $n_{i\uparrow} = n_{i\downarrow}$. This is a reasonable assumption since the authors concentrated on doping levels, where antiferromagnetism is not observed experimentally. The renormalized mean field Hamiltonian can then be written as [83],

$$\begin{aligned} H_{\mathrm{MF}} = & - t\sum_{\langle ij\rangle\sigma} g_t^{ij}(c^\dagger_{i,\sigma}c_{j,\sigma} + \mathrm{h.c.}) - \mu\sum_{i\sigma} n_{i,\sigma} \\ & - \frac{3}{4}J\sum_{\langle ij\rangle\sigma} g_S^{ij}(\tilde{\xi}_{ji}c^\dagger_{i,\sigma}c_{j,\sigma} + \mathrm{h.c.} - |\tilde{\xi}_{ij}|^2) \\ & - \frac{3}{4}J\sum_{\langle ij\rangle\sigma} g_S^{ij}(\tilde{\Delta}_{ji}c^\dagger_{i,\sigma}c^\dagger_{j,-\sigma} + \mathrm{h.c.} - |\tilde{\Delta}_{ij}|^2)\ . \end{aligned} \tag{4.24}$$

However, we must abandon above constraints for investigations around vortex cores or impurities, where antiferromagnetic correlations are essential. Doing so and solving the Bogoliubov-de Gennes equations under an uniformly applied magnetic field shows that significant antiferromagnetic correlations develop inside vortex cores [95] in agreement with experimental observations [137, 138, 139, 140, 141, 142]. Tsuchiura, *et al.* [91, 92, 93] also studied the effects of magnetic and non-magnetic impurities onto the local density of states in HTSC within above approach. The obtained results resemble the STM data [33, 34, 35] quite well[1]. The self-consistent determination of order parameters within the renormalized Bogoliubov-de Gennes theory was also applied to study surface effects in 2D superconducting states [144, 145].

To analyze above problems within an unrestricted Hartree-Fock theory most authors consider a large (but finite) unit cell, which exhibits a certain charge ordering pattern or which has a vortex core or an impurity site in the middle. The corresponding renormalized Bogoliubov-de Gennes equations can then be solved by assuming a lattice of unit cells (*e.g.*, $N_c = 20 \times 20$) and making use of Fourier transformations. While most of above studies used the Gutzwiller factors derived in chapter 3 some recent works [95, 93] applied the extensions proposed by Ogata and Himeda [90] (see section 4.4.1). All above studies concentrate on ground state properties ($T = 0$). Although it would be highly interesting to consider finite temperature effects within a renormalized unrestricted Hartree-Fock theory, such studies have not yet been carried out.

4.4.3 Gossamer superconductivity

Another class of renormalized mean field theories concentrates onto a modified version of the Hubbard model, which includes a superexchange interaction J like in the t-J Hamiltonian. This t-J-U model was proposed by Zhang [146] to study the so-called gossamer superconductivity [147]. Here, the form of the GA, which includes finite double occupancy, must be used for the renormalized Hamiltonian [146]. Then RMFT gap equations are obtained in a straightforward manner, whereas the number of double occupancies is determined by optimizing the ground state energy. Within this approach, at half-filling, there is a first order phase transition from a Mott insulating phase at large Coulomb repulsion U to a gossamer superconducting phase at small U. Away from half-filling the Mott insulator evolves into an RVB state, which is adiabatically connected to the gossamer superconductor [148]. Although several works [148, 149, 150, 151, 152] considered this ansatz for the HTSC, it is probably more adequate for describing organic superconductors [73, 74].

---

[1] Nevertheless VMC calculations [143] for a non-magnetic impurity report some minor discrepancies to the corresponding RMFT study [93].

4.4.4 Time-dependent Gutzwiller approximation

The studies discussed so far mainly focused on the superconducting state mediated by the antiferromagnetic superexchange J. Seibold and Lorenzana [153] considered the Hubbard model without superconducting pairing and developed a time-dependent Gutzwiller approximation analogous to the time-dependent Hartree-Fock theory. This new formalism incorporates ground state correlations beyond the GA within the random phase approximation and allows for a computation of the dynamical density-density response function. The scheme successfully describes several interesting features of HTSC, such as the dynamics of stripes [154] or the dispersion of magnetic excitations [155, 156, 157] and was recently applied to investigate checkerboard inhomogeneities [158].

Chapter 5

Variational Monte Carlo calculations for HTSC - an overview

The VMC technique allows for an accurate evaluation of expectation values in Gutzwiller projected wave functions. In this chapter we present technical details on the VMC method and review the variational search for the optimal ground state energy in the Hubbard and t-J model. In this context, we discuss the coexistence of superconductivity with antiferromagnetism and flux states as well as the improvement of the trial wave function by further variational parameters and Jastrow factors. Further we consider doping dependent features of projected wave functions and compare them to experimental findings in HTSC. At the end of the chapter we discuss a recent numerical study dealing with the tendency towards a spontaneous breaking of the Fermi surface symmetry.

5.1 Details on the VMC method

The VMC method was first applied to the study the projected Fermi sea [98, 159], which has a fixed particle number. However, superconducting BCS wave functions $|\Psi_0\rangle$ are generally defined in a grand canonical ensemble, where the wave function shows particle number fluctuations. These particle number fluctuations are also present in the projected BCS wave function, $|\tilde{\Psi}\rangle \equiv P_G\,|\Psi_0\rangle$. Within the VMC scheme we have now two possibilities, we can either directly work with $|\tilde{\Psi}\rangle$ (grand canonical ensemble) [80], or we can project out the particle number fluctuations by a projector P_N that fixes the particle number and work with $|\Psi\rangle \equiv P_N|\tilde{\Psi}\rangle$ (canonical ensemble) [79]. Within this thesis we only present the method of Gros [79, 122], which is used in most recent VMC calculations, since it avoids complications due to the fluctuating particle number. Possible discrepancies between the grand canonical and the canonical VMC scheme are discussed in detail in section 3.2.

5.1.1 Real space representation of the trial wave function

Before performing a VMC calculation we have to rewrite the wave function in an appropriate way. By inserting a complete set of states $\{\,|\alpha\rangle\,\}$ for the subspace that excludes double occupancy and has fixed particle number N, we can remove the projection operator P_N and P_G from the wave function $|\Psi\rangle$,

$$|\Psi\rangle \equiv P_N P_G|\Psi_0\rangle = \sum_\alpha \langle\alpha|\Psi_0\rangle\,|\alpha\rangle\ . \tag{5.1}$$

The most suitable choice of $|\alpha\rangle$ is given by a straightforward real space representation in terms of fermion creation operators,

$$|\alpha\rangle\ =\ c^\dagger_{\mathbf{R}_1,\uparrow}\cdots c^\dagger_{\mathbf{R}_{N_\uparrow},\uparrow}c^\dagger_{\mathbf{R}_1,\downarrow}\cdots c^\dagger_{\mathbf{R}_{N_\downarrow},\downarrow}|0\rangle\ . \tag{5.2}$$

The state (5.2) is specified by two disjoint sets $\{\mathbf{R}_1\ldots\mathbf{R}_{N_\uparrow}\}$ and $\{\mathbf{R}_1\ldots\mathbf{R}_{N_\downarrow}\}$, which determine the positions of the up- and down-spin electrons on a finite lattice.

Next we have to calculate the overlap $\langle\alpha|\Psi_0\rangle$. To determine this quantity by a Monte Carlo calculation, we write the BCS wave function $P_N|\Psi_0\rangle$ as [45],

$$\begin{aligned}
P_N|\Psi_0\rangle\ &\equiv\ P_N\prod_{\mathbf{k}}\left(u_{\mathbf{k}}+v_{\mathbf{k}}\ c^\dagger_{\mathbf{k}\uparrow}c^\dagger_{-\mathbf{k}\downarrow}\right)|0\rangle && \text{(5.3a)}\\
&\propto\ P_N\prod_{\mathbf{k}}\left(1+a_{\mathbf{k}}\ c^\dagger_{\mathbf{k}\uparrow}c^\dagger_{-\mathbf{k}\downarrow}\right)|0\rangle && \text{(5.3b)}\\
&\propto\ \left(\sum_{\mathbf{k}}a_{\mathbf{k}}\ c^\dagger_{\mathbf{k}\uparrow}c^\dagger_{-\mathbf{k}\downarrow}\right)^{N/2}|0\rangle && \text{(5.3c)}\\
&=\ \left(\sum_{\mathbf{R}_{j,\downarrow},\mathbf{R}_{j,\uparrow}}a(\mathbf{R}_{j,\downarrow}-\mathbf{R}_{j,\uparrow})\ c^\dagger_{\mathbf{R}_{j,\uparrow},\uparrow}c^\dagger_{\mathbf{R}_{j,\downarrow},\downarrow}\right)^{N/2}|0\rangle\ . && \text{(5.3d)}
\end{aligned}$$

When going to (5.3b) we defined the quantity $a_{\mathbf{k}} \equiv v_{\mathbf{k}}/u_{\mathbf{k}}$, which becomes

$$a_{\mathbf{k}} = \frac{\Delta_{\mathbf{k}}}{\xi_{\mathbf{k}} + \sqrt{\xi_{\mathbf{k}}^2 + \Delta_{\mathbf{k}}^2}} \tag{5.4}$$

if we use the mean field result from (4.8). Due to the projection operator P_N we can then present the wave function by a product of $N/2$ pairs, where we use $N_\sigma = N_\uparrow = N_\downarrow = N/2$, which is valid for a BCS wave function. In (5.3d) we assumed $a_{\mathbf{k}} = a_{-\mathbf{k}}$, applied a Fourier transformation, and defined

$$a(\mathbf{r}) \equiv \sum_{\mathbf{k}} a_{\mathbf{k}} \cos(\mathbf{k} \cdot \mathbf{r}) \ . \tag{5.5}$$

Finally, we arrive at the real space representation of $P_N|\Psi_0\rangle$ as given in (5.3d).

Since all configurations α in (5.1) have the same to particle number N, $\langle\alpha|\Psi_0\rangle = \langle\alpha|P_N|\Psi_0\rangle$. Making use of (5.3d) one finds that the overlap, $\langle\alpha|\Psi_0\rangle$, is given [79, 122] by the determinant of the matrix A_α which has the form,

$$\begin{pmatrix} a(\mathbf{R}_{1,\downarrow} - \mathbf{R}_{1,\uparrow}) & a(\mathbf{R}_{1,\downarrow} - \mathbf{R}_{2,\uparrow}) & \dots & a(\mathbf{R}_{1,\downarrow} - \mathbf{R}_{N_\sigma,\uparrow}) \\ a(\mathbf{R}_{2,\downarrow} - \mathbf{R}_{1,\uparrow}) & a(\mathbf{R}_{2,\downarrow} - \mathbf{R}_{2,\uparrow}) & & a(\mathbf{R}_{2,\downarrow} - \mathbf{R}_{N_\sigma,\uparrow}) \\ \vdots & & \ddots & \vdots \\ a(\mathbf{R}_{N_\sigma,\downarrow} - \mathbf{R}_{1,\uparrow}) & a(\mathbf{R}_{N_\sigma,\downarrow} - \mathbf{R}_{2,\uparrow}) & \dots & a(\mathbf{R}_{N_\sigma,\downarrow} - \mathbf{R}_{N_\sigma,\uparrow}) \end{pmatrix} .$$

To see this we must expand (5.3d) and gather all terms contributing to the configuration α, which has down-electrons on $\{\mathbf{R}_{1,\downarrow}, \mathbf{R}_{2,\downarrow} \dots \mathbf{R}_{N_\sigma,\downarrow}\}$ and up-electrons on $\{\mathbf{R}_{1,\uparrow}, \mathbf{R}_{2,\uparrow} \dots \mathbf{R}_{N_\sigma,\uparrow}\}$. The number and functional form of these terms are obviously the same as those for $|A_\alpha|$. Next we must order up- and down-electrons in the same way for all terms. By doing so we pick up relative signs, which are exactly reproduced by the determinant of A_α.

We note that above real space representation can be extended [69] to wave functions, which allow for a staggered magnetization and an unequal number of up- and down-electrons, $N_\uparrow \neq N_\downarrow$. Then, the $a(\mathbf{r})$ in (5.3d) and (5.5) becomes spin and site dependent, *i.e.*, $a(\mathbf{r}) \to a(\mathbf{R}_{i,\sigma_i}, \mathbf{R}_{j,\sigma_j}, \sigma_i, \sigma_j)$. The values of $a(\mathbf{R}_{i,\sigma_i}, \mathbf{R}_{j,\sigma_j}, \sigma_i, \sigma_j)$ depend on the particular choice of the mean field wave function and can be evaluated numerically. The overlap $\langle\alpha|\Psi_0\rangle$ is then determined by [69],

$$\langle\alpha|\Psi_0\rangle = P_f(\mathbf{Q}) \ , \tag{5.6}$$

where $P_f(\mathbf{Q})$ is the Pfaffian[1] of the matrix

$$\mathbf{Q} = a(\mathbf{R}_{i,\sigma_i}, \mathbf{R}_{j,\sigma_j}, \sigma_i, \sigma_j) - a(\mathbf{R}_{j,\sigma_j}, \mathbf{R}_{i,\sigma_i}, \sigma_j, \sigma_i) \ . \tag{5.7}$$

---

[1] The Pfaffian is an analog of the determinant that is defined only for antisymmetric matrices. For an antisymmetric matrix A, the square of the Pfaffian is equivalent to its determinant, *viz.*, $P_f(A)^2 = |A|$.

The positions of the electrons, $\mathbf{R}_{i,\sigma_i}$ and $\mathbf{R}_{j,\sigma_j}$ determine the real space configuration α. For a simple BCS wavefunction with $a(\mathbf{R}_{i,\uparrow}, \mathbf{R}_{j,\uparrow}, \uparrow, \uparrow) = a(\mathbf{R}_{i,\downarrow}, \mathbf{R}_{j,\downarrow}, \downarrow, \downarrow) = 0$ and $a(\mathbf{R}_{i,\uparrow} - \mathbf{R}_{j,\downarrow}) = a(\mathbf{R}_{i,\uparrow}, \mathbf{R}_{j,\downarrow}, \uparrow, \downarrow)$, the overlap $\langle \alpha | \Psi_0 \rangle$ in equation (5.6) reduces to the previously discussed determinant $|A_\alpha|$.

5.1.2 Implementation of the Monte Carlo simulation

By using (5.1) we can write the expectation value of an operator $\hat{O}$ in $|\Psi\rangle$ as,

$$\begin{aligned}
\langle \hat{O} \rangle_\Psi &= \frac{\langle \Psi_0 | P_G P_N \hat{O} P_N P_G | \Psi_0 \rangle}{\langle \Psi_0 | P_G P_N P_G | \Psi_0 \rangle} && \text{(5.8a)} \\
&= \sum_{\alpha,\beta} \langle \alpha | \hat{O} | \beta \rangle \frac{\langle \Psi_0 | \alpha \rangle \langle \beta | \Psi_0 \rangle}{\langle \Psi_0 | P_N P_G | \Psi_0 \rangle} && \text{(5.8b)} \\
&= \sum_{\alpha} \left(\sum_{\beta} \frac{\langle \alpha | \hat{O} | \beta \rangle \langle \beta | \Psi_0 \rangle}{\langle \Psi_0 | \alpha \rangle} \right) \frac{|\langle \Psi_0 | \alpha \rangle|^2}{\langle \Psi_0 | P_N P_G | \Psi_0 \rangle} && \text{(5.8c)} \\
&= \sum_{\alpha} f(\alpha)\, p(\alpha) \ , && \text{(5.8d)}
\end{aligned}$$

with

$$\begin{aligned}
f(\alpha) &= \sum_{\beta} \frac{\langle \alpha | \hat{O} | \beta \rangle \langle \beta | \Psi_0 \rangle}{\langle \Psi_0 | \alpha \rangle} \ , && \text{(5.9a)} \\
p(\alpha) &= \frac{|\langle \Psi_0 | \alpha \rangle|^2}{\langle \Psi_0 | P_N P_G | \Psi_0 \rangle} \ . && \text{(5.9b)}
\end{aligned}$$

Here, α and β are some real space configurations as given by (5.2). Since,

$$p(\alpha) \geq 0 \, , \qquad \sum_{\alpha} p(\alpha) = 1 \ , \tag{5.10}$$

are the features of a probability distribution, we can evaluate $\langle \hat{O} \rangle_\Psi$ by a random walk through the configuration space with weight $p(\alpha)$. Therefore, we can analyze (5.8) by a standard Metropolis Monte Carlo calculation. We note that the norm $\langle \Psi_0 | P_N P_G | \Psi_0 \rangle$ in (5.9b) is not of relevance within the Monte Carlo calculation, since only relative probabilities $p(\alpha)$ enter the transition probability.

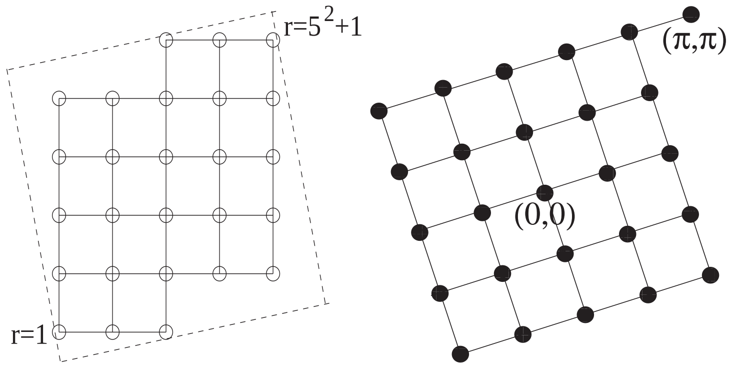

Figure 5.1: (left) Real space picture of the L^2+1 lattice for $L=5$, with periodic boundary conditions, $(5,1)$ and $(-1,5)$, applied along the opposite edges of the tilted square indicated by dashed lines. (right) The **k**-space Brillouin zone of the "tilted lattice" for $L=5$. From [99].

Next, we give some comments on the updating procedure and the calculation of the determinant $|A_\alpha|$. Most VMC calculations generate a new configuration α' by randomly interchanging two electrons with opposite spin or moving an electron to an empty site. The so-constructed random walks are ergodic. In general, to optimize the numerical performance, the rules for generating the random walk through the configuration space should be chosen in order to maximize the acceptance rate, $T(\alpha \to \alpha')$.

The calculation of $|A_\alpha|$ is numerically expensive and is required at each Monte Carlo step for the computation of $p(\alpha)$. Therefore it is advantageous to determine the ratio $|A_{\alpha'}|/|A_\alpha|$ between new and old determinant (new and old configuration α' and α) instead of directly evaluating $|A_{\alpha'}|$ for every configuration. According to Ceperley, *et al.* [160], this ratio can be efficiently computed within $\mathcal{O}(N_\sigma^2)$ computation steps, while a direct evaluation of $|A_{\alpha'}|$ requires $\mathcal{O}(N_\sigma^3)$ steps. The trick is to store not only the matrix A_α, but also its inverse A_α^{-1}. For the commonly used updating procedures mentioned above, α' differs from α only by the interchange of two electrons with opposite spins or the interchange of an electron and an empty site. Thus, the matrices $A_{\alpha'}$ and A_α differ only by one row and one column, and $|A_{\alpha'}|/|A_\alpha| = |A_{\alpha'}A_\alpha^{-1}|$, which enters the transition rate $T(\alpha \to \alpha')$, can easily be computed.

A general advantage of the Monte Carlo method is the possibility to estimate the numerical accuracy systematically with the error being proportional to the inverse square root of the number of Monte Carlo steps N_r. Present computer capacities allow to consider sufficiently large cluster, for which finite size effects play a minor role. However, $a_{\mathbf{k}} = v_{\mathbf{k}}/u_{\mathbf{k}}$, equation (5.4), becomes singular whenever $\Delta_{\mathbf{k}} = 0$ and $\xi_{\mathbf{k}} \leq 0$. In particular, that is problematic for a d-wave gap, where $\Delta_{\mathbf{k}} = 0$ for all k-points along the Brillouin zone diagonals, *i.e.*, $|k_x| = |k_y|$. It is thus convenient to avoid these $\mathbf{k}$-points by an appropriate choice of boundary conditions. There are three different approaches discussed in literature. The first possibility is a tilted lattice with periodic boundary conditions (PBCs). Such a lattice has $L^2 + 1$ sites with odd L, preserves the fourfold rotational symmetry of the lattice, and does not introduce any twist in the boundary conditions. An example for these widely used boundary conditions (see, *e.g.*, [79, 99, 128, 122]) is illustrated in figure 5.1. Another choice are $L \times L$ lattices with even L and periodic and antiperiodic boundary conditions in the x- and the y-direction, respectively. Finally it is possible to use a rectangular $L_x \times L_y$ lattice with PBCs and mutually coprime dimensions L_x and L_y, *i.e.*, the greatest common divisor of L_x and L_y is 1.

5.2 Improvements of the trial wave function

The early VMC calculations for projected BCS states of Gros [79] and Yokoyama and Shiba [80] were carried out to check whether a Gutzwiller projected superconducting wave function constitutes a competitive candidate for the ground state in the t-J model. To limit the number of variational parameters they used a dimensionless dispersion, $\xi_{\mathbf{k}} = -2\,(\cos k_x + \cos k_y) - \mu$, and various superconducting gap functions $\Delta_{\mathbf{k}}$ to calculate $a_{\mathbf{k}} = \Delta_{\mathbf{k}}/(\xi_{\mathbf{k}} + \sqrt{\xi_{\mathbf{k}}^2 + \Delta_{\mathbf{k}}^2})$. In his original work, Gros [79] compared variational energies of s-wave, $\Delta_{\mathbf{k}} = \Delta$, d-wave, $\Delta_{\mathbf{k}} = \Delta\,(\cos k_x - \cos k_y)$, and extended s-wave, $\Delta_{\mathbf{k}} = \Delta(\cos k_x + \cos k_y) - \mu$, functions. By optimizing solely[2] the variational parameter Δ, he found that a d-wave gap can substantially lower the energy compared to projected Fermi sea ($\Delta_{\mathbf{k}} = 0$) at half-filling as well as at finite doping. The result is consistent with other early works such as the VMC calculations of Yokoyama and Shiba [80] or the mean field theories of Zhang, *et al.* [76] and Kotliar and Liu [77].

More detailed studies showed that the optimal superconducting state remains a pure d-wave even if mixed states of s- and d-wave pairing are considered [161]. The optimal variational parameter Δ decreases when going away from half-filling and vanishes at about 30% doping. The exact dimension of the

---

[2] Due to the fixed particle number, the chemical potential μ becomes an additional free parameter. However, this parameter was fixed in [79] by setting the chemical potential μ to those of the unprojected wave function.

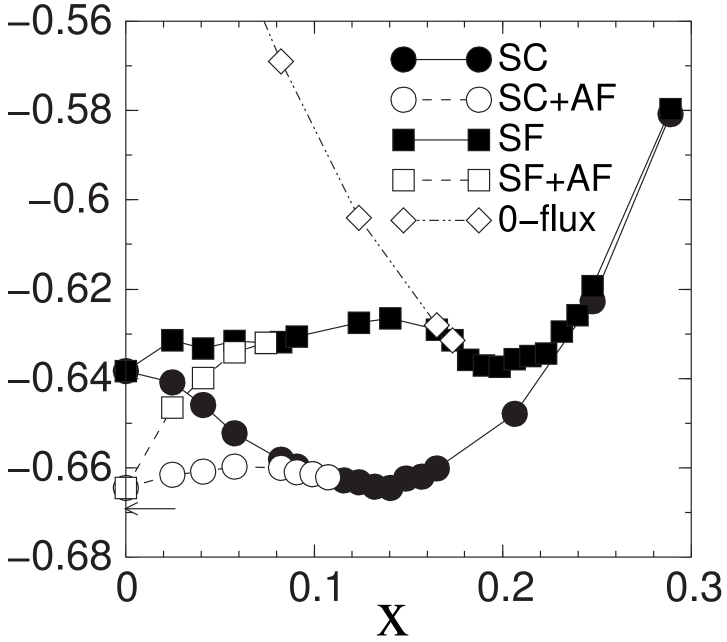

Figure 5.2: Optimal energies per site (in units of J) for five different Gutzwiller projected wave functions with a linear part subtracted ($E - \mu_{\text{sep}}$) as a function of doping x. Wave functions: superconducting without antiferromagnetism (SC, solid circles), superconducting with antiferromagnetism (SC+AF, empty circles), staggered-flux without antiferromagnetism (SF, solid squares), staggered-flux with antiferromagnetism (SF+AF, empty squares), and zero-flux (projected Fermi sea, empty diamonds). The arrow in the panel shows the best variational estimate for the half-filled system ($E = -0.669J$ per site) [162, 163]. Only nearest neighbor hopping is considered and $J/t = 0.3$. From [88].

superconducting region in the phase diagram depends on the choice of J/t as well as on the inclusion of the correlated hopping term [161].

5.2.1 Antiferromagnetism and flux states

Further extensions [85, 86, 87, 88, 89] considered the incorporation of antiferromagnetism for a more accurate description of the t-J model near half-filling. These studies show a coexistence between superconductivity and antiferromagnetic long-range order (AFLRO) for doping $x \leq 0.1$. At half-filling, the optimal so-constructed wave function has a staggered magnetization of 0.75 and a variational energy of $-0.664J$ per site; impressively close to the best numerical estimate of $-0.669J$ per site by Green's function Monte Carlo techniques [162, 163]. A comparison of the variational energies of the different wave functions is given in figure 5.2. The figure also reveals an upward convexity of the ground state energy (SC+AF state) as a function of doping. That indicates a phase separation at $x_{\text{sep}} = 0.13$ (see figure 5.2). However, Ivanov [88] demonstrated that a sufficiently strong nearest neighbor Coulomb repulsion can suppress the formation of separated phases. Further VMC calculations showed that the coexistence of superconductivity and AFLRO is nearly absence if next and next next nearest neighbor hopping are included [89]. For these more realistic model parameters, the AFLRO disappears at about 6% doping in better agreement with experimental observations [89].

Apart from the superconducting states, the projected staggered-flux state was considered as a competitive variational state, however, its energy lies above those of the d-wave for all dopings (figure 5.2). As discussed in chapter 4, the flux state becomes identical to the superconducting state at half-filling explaining the collapse of the energies in figure 5.2 (see also [117]). This behavior is due to $SU(2)$-symmetry, which is also made responsible for the occurrence of staggered-vorticity correlations of current in the d-wave state at small dopings [164].

5.2.2 Increasing the number of variational parameters

In up-to-date VMC calculations, the chemical potential μ as well as the next nearest neighbor hopping t'_{var} are chosen as additional variational parameters, which are optimized numerically. While the chemical potential has minor influence onto the optimal state [161], a variational t'_{var} can significantly effect the shape of the Fermi surface. Himeda and Ogata [165] reported that for a bare dispersion $t' = 0$ and a doping level of $x = 0.15$ the lowest energy is provided by a variational $t'_{\text{var}} = -0.1t$, causing a spontaneous deformation of the Fermi surface. More detailed VMC studies [166] include next nearest (t') and next next nearest (t'') neighbor hopping in the bare dispersion and also use variational parameters t'_{var} and t''_{var}. The obtained momentum distribution $n(\mathbf{k})$ (related to the Fermi surface, see section 6.5) together with the optimal variational Δ and t'_{var} from these calculations are illustrated in figure 5.3. This work of Shih, *et al.* [166] also revealed that the more negative the bare ratio t'/t the higher the superconducting pairing in the optimal variational state of the t-J model. This is in agreement with band-structure calculations [167] that suggest that the ratio t'/t is essential to raise T_c.

By concentrating on inhomogeneous patterns, VMC calculations [168] found

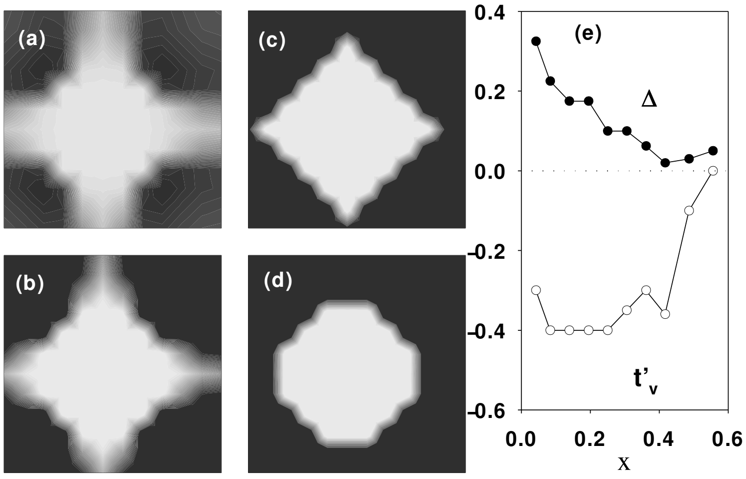

Figure 5.3: Momentum distribution $n(\mathbf{k})$ in the first Brillouin zone for doping $x =$ (a) 0.19, (b) 0.31 (c) 0.42 (d) 0.49 for 12×12 lattice with $J/t = 0.3$, $t' = -0.3t$, and $t'' = 0$. (e) optimal parameters t'_v (squares) and Δ (circles). From [166].

that around $x = 1/8$ stripe states with spatially oscillating d-wave superconductivity can lower the variational ground state energy in the two-dimensional t-J model. More recent studies report that at $x = 1/8$ a bond-order modulated staggered flux state can also overcome the RVB superconductor for sufficiently large short range Coulomb repulsion [169]. However, the energy gains within these studies are often quite small and sensitively depend on model parameters. Nevertheless these VMC calculations show that the slightly doped t-J model exhibits tendencies towards various inhomogeneities, which could be relevant for explaining experimental observations in the underdoped HTSC.

The energy of the projected d-wave state can further be improved by the incorporation of Jastrow factors (see section 2.6). Sorella, *et al.* [120] numerically showed that the so-obtained wave function lowers the variational energy and still exhibits long range superconducting order. Nevertheless there is still a continuing controversy (see [170, 171, 172]) whether the superconductivity within the VMC scheme results only from a biased choice of the wave function or is indeed a ground state property of the t-J model. This debate is however, in our opinion, not an obstacle for an improved understanding of the HTSC, because we are mainly interested in physical properties of projected wave functions rather than in exact ground states, which we will probably never find. We may let us inspire by Anderson, *et al.* [173], who stated: *"The philosophy of this method is analogous to that used by BCS for superconductivity, and by Laughlin for the fractional quantum Hall effect: simply guess a wave function. Is there any better way to solve a non-perturbative many-body problem?"*

5.3 Ground state properties - VMC results

Within this section we discuss ground state properties of the HTSC by considering observables in a Gutzwiller projected superconducting state. We follow, in part, Paramekanti, *et al.* [99, 128], who studied the Hubbard model in the strong coupling limit using the re-transformed trial wave function, $e^{-iS}P_G|\Psi_0\rangle$ (see chapter 4). By evaluating the canonical transformation e^{-iS} to $\mathcal{O}(t/U)$, this ansatz can be treated within the VMC scheme. The t/U-corrections due to e^{-iS} provide a more accurate description of the HTSC, however, the qualitative nature of the results is not changed compared to the t-J model. We note that a coexistence of superconductivity with a flux state, antiferromagnetism, or a charge ordered pattern is neglected in the following considerations.

5.3.1 Superconducting gap and order parameter

In the previous section we have seen that the variational parameter Δ, which is proportional to the superconducting gap $\Delta_{\mathbf{k}}$, increases when going towards half-filling. The doping dependence of Δ is illustrated in figure 5.3 and resembles the RMFT result (figure 4.3) as well as the experimental observed gap at $\mathbf{k} = (\pi, 0)$. However, we cannot deduce the relevant energy scale of the gap from Δ, since it is a dimensionless parameter within the VMC calculations. For detailed statements about the gap we have to consider the energy of excited states as we will do in the chapters 6 and 7.

When considering the variational parameter Δ, we must realize that it does not correspond to the true superconducting order $\Phi \equiv |\langle c_{i\uparrow}^\dagger c_{i+\tau\downarrow}^\dagger - c_{i\downarrow}^\dagger c_{i+\tau\uparrow}^\dagger\rangle|$ as discussed in chapter 4. For this quantity we can analyze the off-diagonal long range order (ODLRO) [79, 122, 128] defined by,

$$F_{\alpha,\beta}(\mathbf{r}-\mathbf{r}') = \langle c_\uparrow^\dagger(\mathbf{r}) c_\downarrow^\dagger(\mathbf{r}+\hat{\alpha}) c_\downarrow(\mathbf{r}) c_\uparrow(\mathbf{r}+\hat{\beta})\rangle \ ,$$

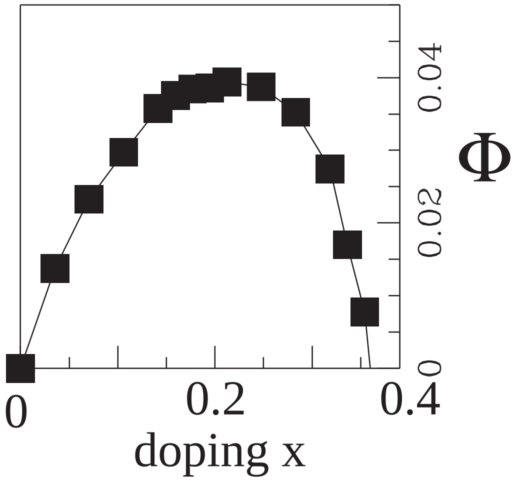

Figure 5.4: Doping dependence of the superconducting order parameter Φ from VMC calculations of Paramekanti, *et al.* [128]. Model parameters: $U = 12t$, $t' = -t/4$.

where $\hat{\alpha}, \hat{\beta} = \hat{x}, \hat{y}$. In the limit of large $|\mathbf{r} - \mathbf{r}'|$, $F_{\alpha,\beta}$ is related to Φ^2 via $F_{\alpha,\beta} \rightarrow \pm\Phi^2$ with + (−) sign obtained for $\hat{a} \parallel (\perp)$ to $\hat{b}$, indicating d-wave superconductivity [128]. The doping dependence of the superconducting order parameter Φ is depicted in figure 5.4 (VMC calculations of Paramekanti, *et al.* [128]). It is not identical to Δ as first noted by Gros [79, 122]. The VMC calculation match the RMFT result (figure 4.3), where Φ vanishes linearly as $x \rightarrow 0$. The vanishing order parameter Φ indicates a Mott insulating phase at $x = 0$, where superconductivity is destroyed due to the suppression of particle number fluctuations. At finite doping x a superconducting state is realized within the range $0 < x < 0.35$.

5.3.2 Derivation of spectral features from ground state properties

Next we follow [128] and analyze the one-particle spectral function $A(\mathbf{k}, \omega)$ by calculating the moments,

$$M_l(\mathbf{k}) = \int_{-\infty}^{0} d\omega\, \omega^l A(\mathbf{k}, \omega) \ , \tag{5.11}$$

in the projected d-wave ground state at $T = 0$. This ansatz allows to obtain information about $A(\mathbf{k}, \omega)$ from ground state expectation values without the

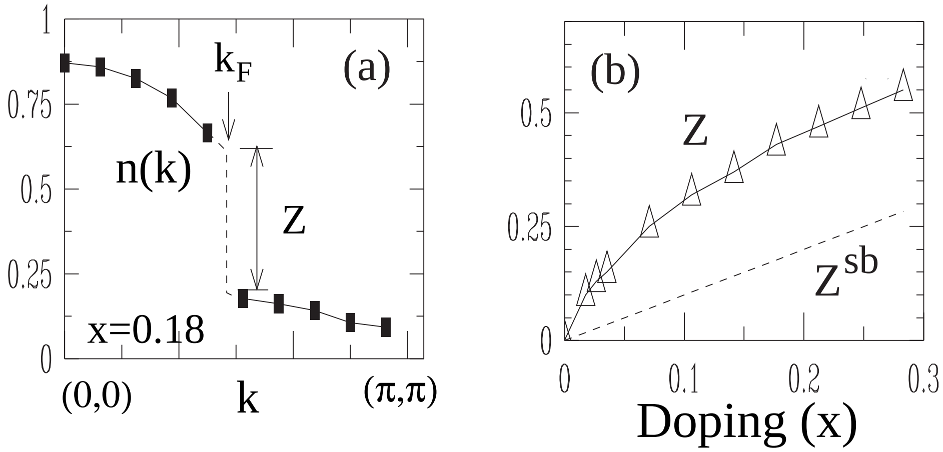

Figure 5.5: (a) The momentum distribution function $n(\mathbf{k})$ plotted along the diagonal $\mathbf{k} = (k, k)$ showing the jump at k_F which implies a gapless nodal quasiparticle with spectral weight Z. (b) Nodal quasiparticle weight $Z(x)$ as a function of doping x compared with the simple SBMFT result $Z^{\mathrm{sb}}(x) = x$. Model parameters: $U = 12t$, $t' = -t/4$. From [128].

need for explicit representations of the excited states. We first concentrate on the zeroth moment $M_0(\mathbf{k}) \equiv n(\mathbf{k})$, which is equivalent to the moment distribution $n(\mathbf{k})$. Figure 5.5(a) shows that $n(\mathbf{k})$ has a jump along $(0, 0)$ to (π, π). This implies the existence of gapless quasiparticles and allows to write the low energy part of the spectral function along the diagonal as

$$A(\mathbf{k}, \omega) = Z\delta(\omega - \xi_k) + A^{\mathrm{inc}} \ , \tag{5.12}$$

where $\xi_k = v_F(k - k_F)$ is the quasiparticle dispersion and A^{inc} a smooth incoherent part. The locating of the discontinuity determines the Fermi point k_F and its magnitude gives the quasiparticle weight Z. Figure 5.5(b) reveals a significant doping dependence and shows that Z vanishes when approaching the Mott-Hubbard insulator $x = 0$. This behavior is in agreement with more direct calculations, which explicitly include quasiparticle states (chapters 6 and 7) as well as experiments.

To determine the nodal Fermi velocity v_F, we have to evaluate the first moment $M_1(\mathbf{k}) = \langle c^\dagger_{\mathbf{k}\sigma}[H, c_{\mathbf{k}\sigma}]\rangle$ along the nodal direction. Due to the singular behavior of $A(\mathbf{k}, \omega)$ at k_F, it can be written as,

$$M_1(\mathbf{k}) = Z\xi_k\Theta(-\xi_k) + \text{smooth part} \ . \tag{5.13}$$

Since the slope $dM_1(\mathbf{k})/dk$ has a discontinuity of Zv_F at k_F, Paramekanti, *et al.* could extract the nodal Fermi velocity v_F in the way presented in figure

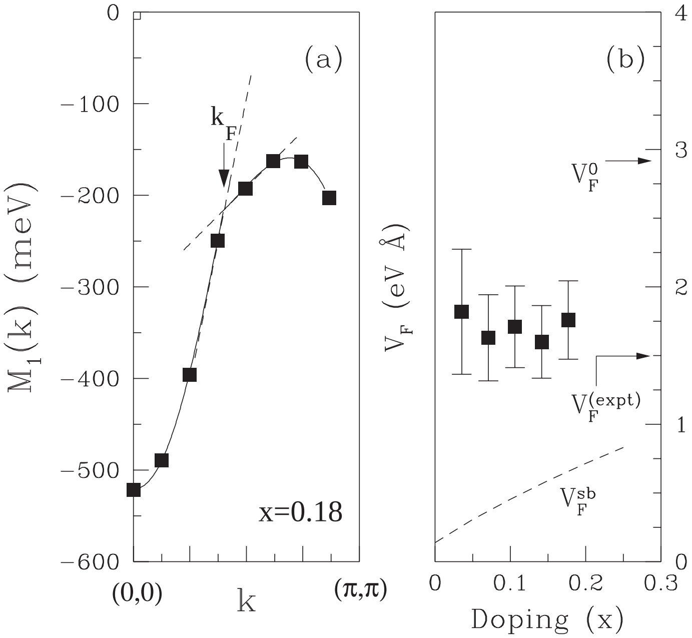

Figure 5.6: (a) The first moment $M_1(\mathbf{k})$ of the spectral function along the zone diagonal, with smooth fits for $k < k_F$ and $k > k_F$, showing a discontinuity of Zv_F in its slope at k_F. (b) Doping dependence of the nodal quasiparticle velocity obtained from the slope discontinuity of $M_1(\mathbf{k})$. Error bars come from fits to $M_1(\mathbf{k})$ and errors in Z. Also shown are the bare nodal velocity v_F^0, the slave boson mean field $v_F^{\mathrm{sb}}(x)$ (dashed line), and the ARPES estimate $v_F^{(\mathrm{expt})}$ [13, 14]. Model parameters: $U = 12t$, $t' = -t/4$. From [128].

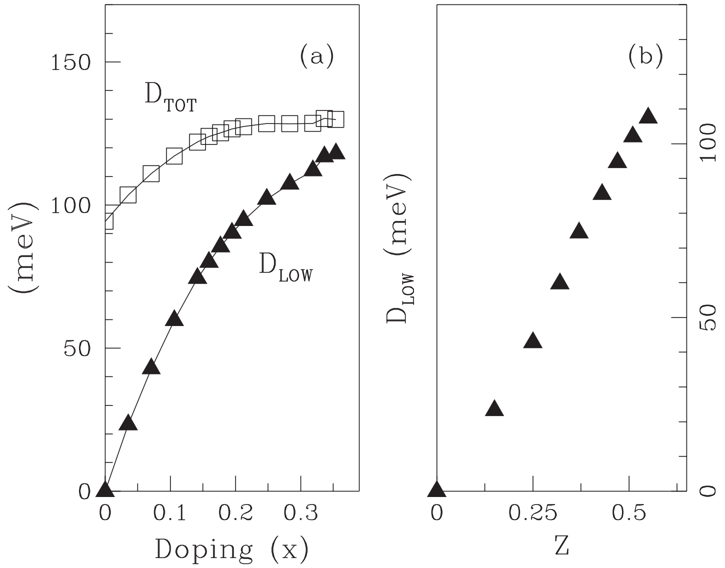

Figure 5.7: (a) Doping dependence of the total (D_{tot}) and low energy (D_{low}) optical spectral weights (b) The optical spectral weight D_{low} versus the nodal quasiparticle weight Z. Model parameters: $U = 12t$, $t' = -t/4$. From [128].

5.6(a). The doping dependence of v_F is given in figure 5.6(b) together with its bare value v_F^0. The so obtained Fermi velocity is only weakly doping dependent and consistent with the ARPES data. However, this estimate of v_F is rather inaccurate compared to the direct evaluation [121] from the quasiparticle excitation energies discussed in Chapter 7.

Ground state expectation values also provide important information about the optical conductivity in the Hubbard and the t-J model. The total optical spectral weight $D_{\text{tot}}(x)$ can be calculated by [99]

$$\int_0^\infty d\omega\, \Re\,\sigma(\omega) = \pi \sum_{\mathbf{k}} m^{-1}(\mathbf{k}) n(\mathbf{k}) \equiv \pi D_{\text{tot}}/2\ , \tag{5.14}$$

where $m^{-1}(\mathbf{k}) = (\partial^2 \epsilon(\mathbf{k})/\partial \mathbf{k}_x \partial \mathbf{k}_x)$ is the non-interacting mass tensor. $\epsilon(\mathbf{k})$ is the non-interacting dispersion and we set $\hbar = c = e = 1$. Since the integral in (5.14) goes from 0 to $+\infty$, it includes contributions from the upper Hubbard band and is thus finite even at $x = 0$ as shown in figure 5.7(a).

Paramekanti, *et al.* [99, 128] emphasized that the low frequency optical weight, or Drude weight [174],

$$D_{\text{low}} = \partial^2 \langle H_A \rangle / \partial A^2 \ , \tag{5.15}$$

is more interesting, because the upper cutoff is chosen smaller than U and thus excludes the upper Hubbard band. In (5.15), A is the electron-magnetic vector potential, which is introduced into the Hamiltonian (2.1) in terms of a Peierls substitution [174],

$$c^\dagger_{i\sigma} c_{j\sigma} \rightarrow c^\dagger_{i\sigma} c_{j\sigma} \, \exp\left(i \, \mathrm{e} \mathbf{A} \left(\mathbf{R}_i - \mathbf{R}_j\right)\right) \ , \tag{5.16}$$

where we used $\mathbf{A} = (A, 0)$ and set $\hbar = c = 1$ for simplicity. As shown in figure 5.7(a), the Drude weight D_{low} vanishes linearly for $x \rightarrow 0$. This demonstrates that the Gutzwiller projected superconductor indeed describes an insulator in the half-filled limit, which can be argued to be a general property of projected states [99]. The VMC results for the Drude weight D_{low} resemble experimental data in magnitude as well as in the doping dependence quite well [99]. By plotting D_{low} versus Z (from the nodal point) Paramekanti, *et al.* also illustrated that $D_{\text{low}} \propto Z$, see figure 5.7(b).

The Drude weight D_{low} also provides an upper bound to the superfluid stiffness D_s, *i.e.*, $D_s \leq D_{\text{low}}$ [175]. It follows that $D_s \rightarrow 0$ as $x \rightarrow 0$ in agreement with experiments [176]. Since the penetration depth λ_{L} is related to D_s by $\lambda_{\text{L}}^{-2} = 4\pi e^2 D_s / \hbar^2 c^2 d_c$, where d_c is the mean-interlayer spacing along the c axis in a layered compound, Paramekanti, *et al.* [99] could also estimate a lower bound for λ_{L} which is again consistent with experimental data.

Above VMC calculations based on a Gutzwiller projected superconducting ground state describe several key features of HTSC remarkable well. The results are in general agreement with RMFT and confirm the usefulness of projected wave functions in the context of HTSC. Although restricted to $T = 0$ above ansatz can give some hints onto the finite temperature regime. The superconducting order parameter Φ resembles the doping dependence of T_c and vanishes at half-filling, while the superconducting gap (expected to scale with Δ) remains finite. This indicates that the underdoped regime exhibits strong pairing but weak inter-pair phase coherence, which could lead to the break down of superconductivity and to the well-known pseudogap behavior.

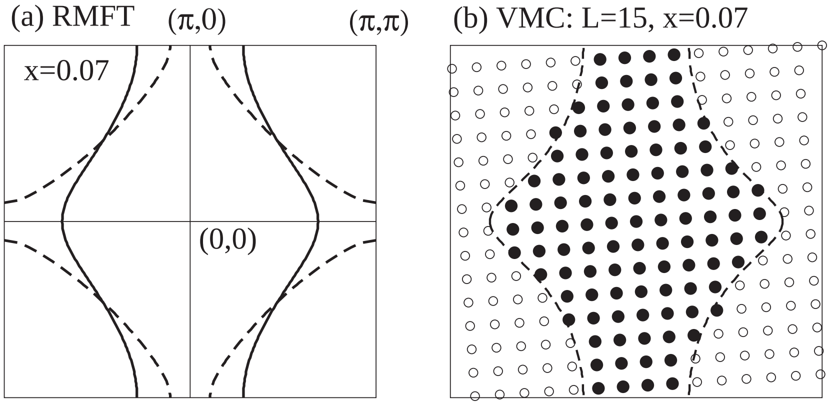

Figure 5.8: Fermi surface of the isotropic t-J model with $J = 0.3t$ and $t' = -0.3t$ at $x = 0.07$ (a) RMFT results for the Fermi surface of the normal state with $\Delta_{\mathbf{k}} \equiv 0$ (quasi 1D state, solid line) and the optimal d-wave state (isotropic, dashed line). (b) Best quasi 1D state on a $(15^2 + 1)$-sites lattice by VMC; filled circles indicate the Fermi surface. From [8].

5.4 Investigation of the Pomeranchuk instability

In section 5.2 we discussed various states that coexist and/or compete with superconductivity in the Hubbard and the t-J model. As a further example of a competing order we present VMC calculations of Edegger, *et al.* [8] indicating a tetragonal symmetry breaking of the 2D Fermi surface due to strong electron correlations. As illustrated in figure 5.8(a), this instability results in a deformation of the Fermi surface, which becomes quasi one dimensional, although the underlying two dimensional (2D) lattice is still isotropic. Motivated by the Fermi surface depicted in figure 5.8(a), the state resulting from the tetragonal symmetry breaking was denoted as a “quasi 1D state”.

The instability towards a quasi 1D state was first reported by Yamase and Kohno [177, 178] within slave boson mean field theory (SBMFT) for the 2D t-J model and later by Halboth and Metzner [179] within a renormalization group (RG) study for the 2D Hubbard model in the limit of weak coupling. Subsequently, several authors [8, 180, 181, 182, 183, 184, 185, 186, 187, 188, 189, 190, 191, 192, 193] investigated this tetragonal symmetry breaking, which was also called “Pomeranchuk instability” (PI).

The VMC technique provides an excellent opportunity to check the predictions from previous SBMFT and RG studies. However, the projected wave function must be extended to allow for a possible quasi 1D state as well as for finite d- and s-wave pairing. When calculating $a_{\mathbf{k}} = \Delta_{\mathbf{k}}/(\xi_{\mathbf{k}} + \sqrt{\xi_{\mathbf{k}}^2 + \Delta_{\mathbf{k}}^2})$ we choose,

$$\begin{aligned} \xi_{\mathbf{k}} = & - \; 2\left[(1+\delta_{\text{var}}^{\text{1D}})\cos k_x + (1-\delta_{\text{var}}^{\text{1D}})\cos k_y\right] \\ & - \; 4t'_{\text{var}}\cos k_x \cos k_y \; - \; \mu_{\text{var}} \end{aligned} \tag{5.17}$$

and

$$\Delta_{\mathbf{k}} = \Delta_{\text{var}}^{(d)}(\cos k_x - \cos k_y) + \Delta_{\text{var}}^{(s)}(\cos k_x + \cos k_y) \ . \tag{5.18}$$

and therefore get the following five variational parameters: (i) the asymmetry $\delta_{\text{var}}^{\text{1D}}$ between the $x-$ and the $y-$direction; (ii) the variational next nearest neighbor hopping term t'_{var}; (iii) a variational chemical potential μ_{var}; (iv) and (v) variational parameters for $d-$ and $s-$wave pairing, $\Delta_{\text{var}}^{(d)}$ and $\Delta_{\text{var}}^{(s)}$, respectively. Using standard VMC techniques as discussed before, Edegger, *et al.* [8] computed the energy expectation values and minimized the energy by searching for the optimal set of variational parameters.

5.4.1 Isotropic lattice

We first present results for the isotropic t-J Hamiltonian, with model parameters $J = 0.3t$ and $t' = -0.3t$. These are reasonable model parameters for the phenomenology of the high temperature superconductors. The optimal solution for various values of hole concentration, $x = 0 - 0.3$, is determined by searching through the whole variational parameter space. We find that the pure isotropic projected $d-$wave state always optimizes the ground state energy, *i.e.*, the $s-$wave parameter $\Delta_{\text{var}}^{(s)}$ and the asymmetry $\delta_{\text{var}}^{\text{1D}}$ vanish for all values of x, within the numerical resolution [$\Delta\Delta_{\text{var}}^{(s)} = 0.05$ and $\Delta\delta_{\text{var}}^{\text{1D}} = 0.05$].

In figure 5.9(a) (circles) we show the condensation energy per site, e_{cond}, of the optimal state with respect to the projected isotropic Fermi sea. The condensation energy e_{cond} is calculated by comparing the VMC energy expectation values in the projected Fermi sea and optimal $d-$wave states. We see a continuous increase of $|e_{\text{cond}}|$ and of the superconducting $d-$wave parameter [shown in figure 5.9(b)] as doping x decreases. The optimal variational value for t'_{var} is given in figure 5.9(c). These results show that the additional variational parameters $\Delta_{\text{var}}^{(s)}$ and $\delta_{\text{var}}^{\text{1D}}$ are not relevant for improving the ground state in the isotropic t-J model.

To uncover the PI, it is necessary to suppress superconductivity by setting $\Delta_{\mathbf{k}} \equiv 0$. Doing so, the VMC calculations indeed reveal a PI; we obtain an

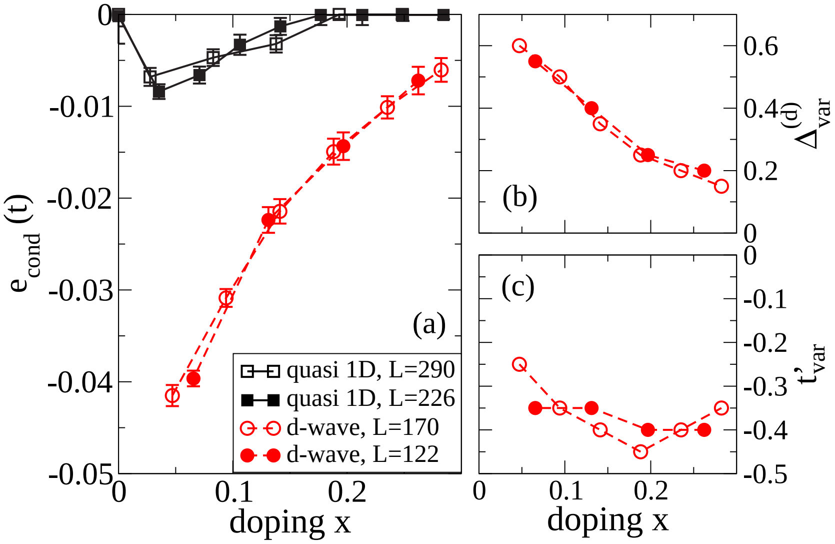

Figure 5.9: (a) VMC results for condensation energies per site e_{cond} of the quasi 1D state ($\delta_{\mathrm{var}}^{1\mathrm{D}} \neq 0$, $\Delta_{\mathbf{k}} \equiv 0$) and the d-wave state ($\Delta_{\mathbf{k}} \neq 0$, $\delta_{\mathrm{var}}^{1\mathrm{D}} \equiv 0$) with $t' = -0.3\,t$; see (5.17) and (5.18) for the definition of these states. Optimal variational parameters $\Delta_{\mathrm{var}}^{(d)}$ and t'_{var} of the d-wave state are shown in (b) and (c). Optimal variational parameters $\delta_{\mathrm{var}}^{1\mathrm{D}}$ and t'_{var} of the quasi 1D state are given in figure 5.10. The errors in (b) and (c) are $\Delta\Delta_{\mathrm{var}}^{(d)} = 0.05$ and $\Delta t'_{\mathrm{var}} = 0.05$, respectively. System sizes: $L = 11^2 + 1 = 122$, $L = 13^2 + 1 = 170$, $L = 15^2 + 1 = 226$, and $L = 17^2 + 1 = 290$. From [8].

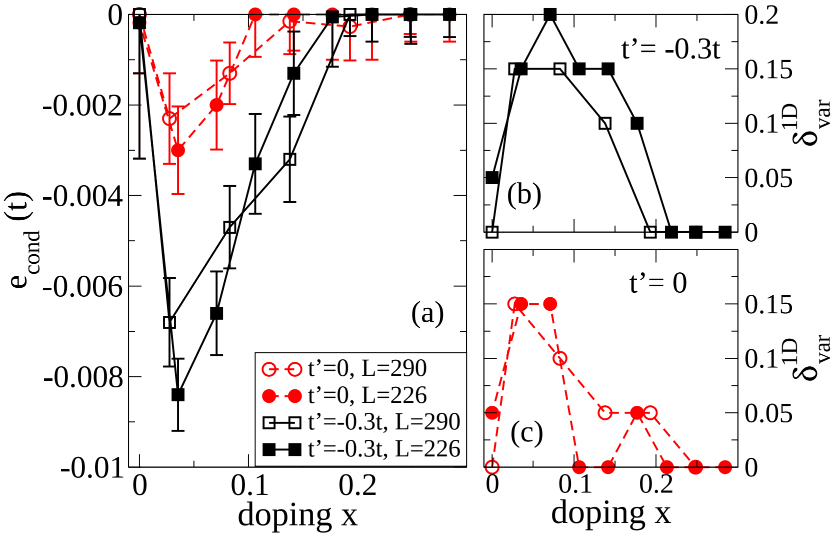

Figure 5.10: VMC results for a quasi 1D state for the isotropic t-J model ($J = 0.3t$) with $t' = 0$ (circles) and $t' = -0.3t$ (squares). Doping dependence x of (a) the condensation energy per site, e_{cond}, and (b),(c) the optimal variational δ^{1D}_{var}. The errors in (b) and (c) are $\Delta\delta^{1D}_{\text{var}} = 0.05$. System sizes: $L = 15^2 + 1 = 226$ and $L = 17^2 + 1 = 290$. From [8].

small improvement of the energy expectation value relative to the isotropic projected Fermi sea by using a finite asymmetry δ^{1D}_{var}, although the underlying lattice is still isotropic. We compare the condensation energy of this state to that of the $d-$wave state. Results are shown in figure 5.9(a). As for the $d-$wave state, $|e_{\text{cond}}|$ for the quasi 1D state initially increases as x decreases. However its energy gain is much less than that of the $d-$wave, and so the latter is always favored on an isotropic lattice. Furthermore, note that the condensation energy of the quasi 1D state saturates and finally vanishes very close to half-filling. We will come back to this point later.

The resulting VMC Fermi surface of the optimal quasi 1D state at $x = 0.07$ is shown in figure 5.8(b). It reveals why finite size effects become important in the VMC calculations when dealing with a finite asymmetry in the projected Fermi sea. Varying δ^{1D}_{var} causes discontinuous changes of the Fermi surface on a finite lattice. The occupied states regroup for certain δ^{1D}_{var} leading to small yet discontinuous changes in the FS as a function of the variational parameter δ^{1D}_{var}.

These finite size effects cause a rather large error for the optimal value of asymmetry, $\Delta\delta^{1D}_{\text{var}} = 0.05$, and for the effective next nearest neighbor hopping, $\Delta t'_{\text{var}} = 0.05 - 0.1$. The jump size increases with decreasing system size,

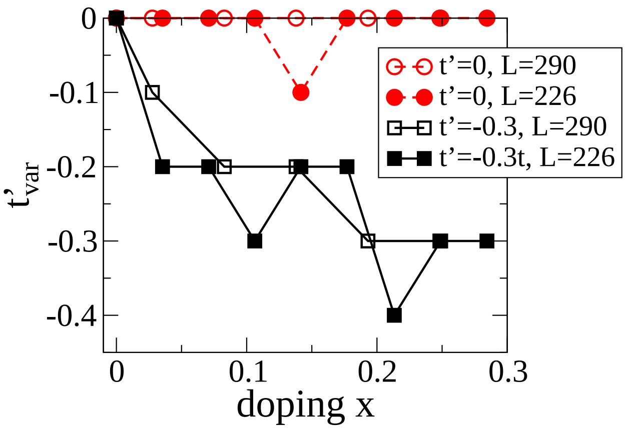

Figure 5.11: VMC results for the quasi 1D state in the isotropic t-J model ($J = 0.3t$) with $t' = 0$ (circles) and $t' = -0.3t$ (squares). Doping dependence x of the optimal variational t'_{var}. $\Delta t'_{\text{var}} = 0.1$; System sizes: $L = 15^2 + 1 = 226$ and $L = 17^2 + 1 = 290$. From [8].

thus requiring sufficiently large lattices. The problem is less severe when considering a superconducting state, where the occupancy in momentum space changes continuously at the Fermi surface.

To consider the effect of t' on the PI, we compared the two cases, $t' = 0$ and $t' = -0.3t$, in the absence of superconducting order ($\Delta_{\mathbf{k}} \equiv 0$). The PI is stronger for $t' < 0$, yielding a larger condensation energy [figure 5.10(a)]. As seen in figure 5.10(b), the anisotropy is significant even at higher doping levels and exists up to $x \approx 0.2$ for $t' = -0.3t$. For $t' = 0$, the $\delta^{\text{1D}}_{\text{var}}$ is significant only in the range, $x = 0.03 - 0.10$ [figure 5.10(c)]. In figure 5.11 we show the optimal variational value for t'_{var}. Interestingly, $t'_{\text{var}} \to 0$ for $x \to 0$ even for a bare dispersion $t' = -0.3t$. Recently, we reported a similar renormalization of the next nearest neighbor hopping terms due to strong coupling effects within RMFT [7, 9], which will be discussed further in detail in section 6.5.3.

The PI can also be studied by RMFT (figure 5.12) in analogy to above VMC results by allowing for a finite asymmetry when solving the gap equation. RMFT or SBMFT analyzes also provide a better understanding for the origin of the PI. Let us therefore consider the effective hopping $\tilde{t}_\tau$ in the τ-direction,

$$\tilde{t}_\tau \equiv g_t \, t_\tau + \frac{3g_s}{8} J \, \tilde{\xi}_\tau \,, \tag{5.19}$$

which can be read off from the RMFT dispersion $\xi_{\mathbf{k}}$ in (4.12). Here, $J = 4t_\tau^2/U$, $\tilde{\xi}_\tau \equiv \sum_\sigma \langle c^\dagger_{i,\sigma} c_{i+\tau,\sigma} \rangle_{\Psi_0}$, and $\tau = \hat{x}, \hat{y}$. The renormalization factors for the kinetic energy, $g_t = 2x/(1+x)$, and for the spin-spin correlation,

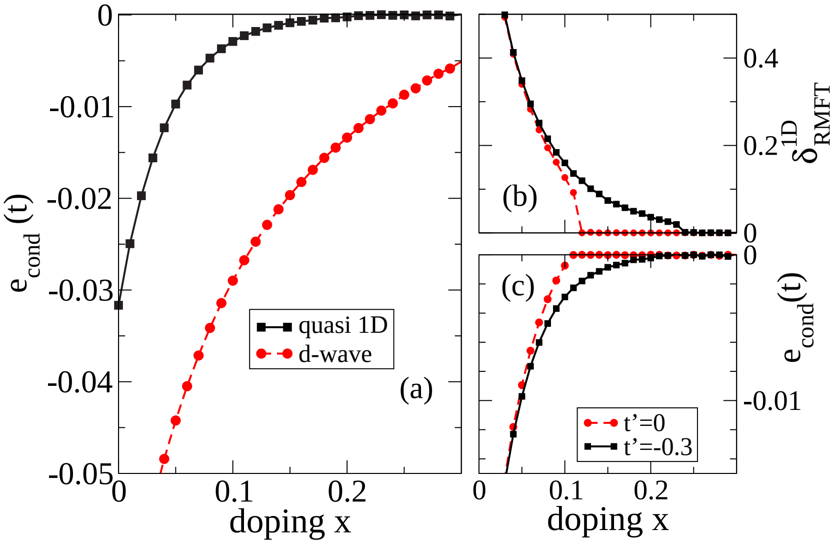

Figure 5.12: RMFT results for the isotropic t-J model with $J = 0.3t$. (a) Condensation energy per site relative to the isotropic non-superconducting solution ($\Delta_{\mathbf{k}} \equiv 0$, $\tilde{\xi}_x = \tilde{\xi}_y$) for the quasi 1D state ($\Delta_\tau \equiv 0$) and for the optimal d-wave state with $t' = -0.3t$. (b) Asymmetry and (c) condensation energy per site for the quasi 1D state with $t' = 0$ and $t' = -0.3$, respectively. The order parameter characterizing the asymmetry, $\delta^{1\mathrm{D}}_{\mathrm{RMFT}}$ is given by $\delta^{1\mathrm{D}}_{\mathrm{RMFT}} \equiv (\tilde{t}_x - \tilde{t}_y)/(\tilde{t}_x + \tilde{t}_y)$. The RMFT results in (a)-(c) can be directly compared to VMC calculations in figure 5.9 and figure 5.10. From [8].

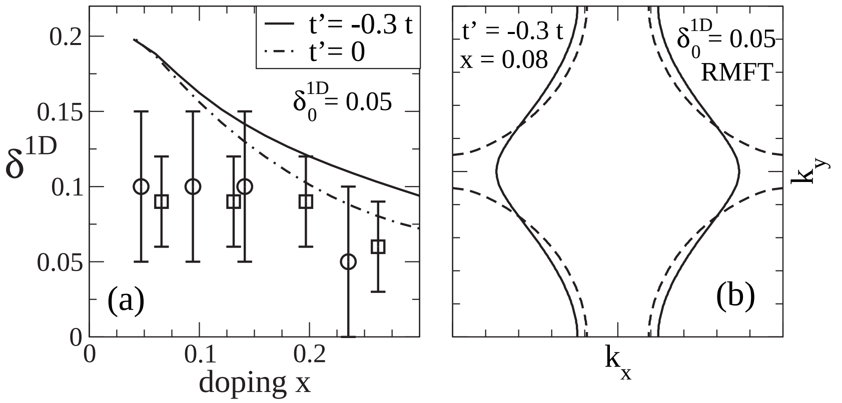

Figure 5.13: RMFT and VMC results for the $d+s$-wave ground state of the anisotropic t-J model with $J=0.3t$ and $\delta_0^{1\mathrm{D}} \equiv (t_x-t_y)/(t_x+t_y)=0.05$. (a) Effective asymmetry $\delta^{1\mathrm{D}} \equiv (\tilde{t}_x-\tilde{t}_y)/(\tilde{t}_x+\tilde{t}_y)$ from RMFT as a function of hole doping x for (dashed) $t'=0$ and (solid) $t'=-0.3t$. VMC results for $t'=0$ are given by squares and circles for $L=122$ and $L=170$, respectively. (b) RMFT Fermi surface (solid lines) of the $d+s$-wave ground state and the tight binding dispersion (dashed) at $x=0.08$ with $t'=-0.3t$ and $\delta_{1\mathrm{D}}^0=0.025$. From [8].

$g_s=4/(1+x)^2$, are derived within the GA. (5.19) shows that the tendency to a quasi 1D state stems from the J-term [2nd term in (5.19)] because it includes the factor $\tilde{\xi}_\tau$. For an isotropic dispersion it is the only quantity in (5.19) that may cause an anisotropy in the effective hopping $\tilde{t}_\tau$. Similar arguments apply for the enhancement of a bare asymmetry $\delta_0^{1\mathrm{D}}$ in a slightly anisotropic lattice (see also discussion below). The origin of the PI may also be understood in the framework of a Landau-Ginzburg analysis as shown by Yamase and Kohno within SBMFT [177, 178].

Although there is good overall agreement between the VMC data and SBMFT results by Yamase and Kohno [177, 178], we find clear and significant discrepancies in the limit $x \to 0$. As seen in figure 5.10(a)-(c) the asymmetry goes to zero at $x=0$ within the VMC calculations. On the other hand, SBMFT as well as RMFT (see figure 5.12) predict a pure 1D state at half-filling when $\Delta_{\mathbf{k}} \equiv 0$. This hints at limitations of the mean field theories when treating states near half-filling as discussed in more detail in [8].

5.4.2 Anisotropic lattice

Above results from VMC and RMFT confirm that a quasi 1D state is always suppressed by the d-wave pairing state. A PI occurs only when $\Delta_{\mathbf{k}} \equiv 0$. However, the situation can be quite different when the underlying lattice structure is anisotropic. In this case, the tendency towards a quasi 1D state is present even in the superconducting state. SBMFT [177, 178] predicts an optimal state which has a dominant d-wave symmetry with a small s-wave contribution. Interestingly, the bare anisotropy δ_0^{1D} of the lattice is enhanced due to the electron correlations. Here we re-examine this prediction within the RMFT and VMC schemes.

Results from RMFT are shown in figure 5.13(a) and (b) and agree quantitatively with the SBMFT data from [177, 178]. As seen in figure 5.13(a), the bare asymmetry of $\delta_0^{\mathrm{1D}} = 0.05$ increases within the RMFT calculations up to about $\delta_{\mathrm{opt}}^{\mathrm{1D}} = 0.2$ in the underdoped regime. These results are confirmed to some extent by VMC calculations for $t' = 0$ in figure 5.13(a) (circles and squares), that show an increase of the asymmetry up to about $\delta_{\mathrm{var}}^{\mathrm{1D}} \approx 0.1$. However, owing to numerical difficulties, the errors in these VMC calculations are quite large. In figure 5.13(b), we compare the Fermi surface obtained from the bare dispersion ($\delta_0^{\mathrm{1D}} = 0.05$) with that of the optimal superconducting state obtained by solving the RMFT equations self consistently for $x = 0.08$. As seen in the figure, the enhancement of anisotropy due to strong correlations may even lead to a change in the topology of the underlying Fermi surface.

Above VMC study for the PI is only one out of several possible instabilities in the t-J model, which is mainly governed by the superexchange J. Since $J \propto 4t^2/U$, a small asymmetry in the bare hopping integral t becomes twice as large in the superexchange energy. Hence, it is natural that the effects discussed in this paper are largest in the underdoped regime, where the dispersion is mainly determined by J. The tendency towards a quasi one-dimensional state may be also enhanced if phonons are coupled to the lattice.

Chapter 6

Quasiparticle states within renormalized mean field theory

Extending the RMFT to excited states requires the consideration of Gutzwiller-Bogoliubov quasiparticles within the t-J and the Hubbard model. These Gutzwiller-Bogoliubov excitations then allow for a systematic analysis of the single particle spectral function and explain momentum- and doping-dependent features in ARPES and STM experiments. Apart from these key results, we discuss the renormalization of the current carried by Gutzwiller-Bogoliubov quasiparticles and the consequences for the suppression of the superfluid density. As an application of above quasiparticle studies, we determine the underlying Fermi surface and discuss discrepancies between different approaches.

6.1 Coherent and incoherent spectral weight

Understanding spectral features of HTSC requires a thorough consideration of excited states. In this section we mainly focus on the shift of spectral weight from coherent quasiparticles (QPs) towards an incoherent background. Stimulated by STM, which reveals a striking particle-hole asymmetry in the spectra of underdoped HTSC [37, 40, 41], this problem was recently intensively investigated by RMFT [6, 127, 194] and VMC methods [6, 99, 128, 195, 196, 197, 198, 199, 200]. As nicely seen in the experiments, *e.g.*, in figure 1(c) and 3(e) of [40] or figure 1.11, the spectral weight on the hole side of the spectrum is distinct more pronounced than the particle side.

6.1.1 Sum rules for the spectral weight

The asymmetry in the STM spectra may be explained qualitatively by considering sum rules [194, 201, 202, 203, 204] for the one-particle spectral function,

$$\begin{aligned} A(\mathbf{k},\omega) &= \sum_m \langle 0|c^\dagger_{\mathbf{k}\sigma}|m\rangle\langle m|c_{\mathbf{k}\sigma}|0\rangle\,\delta\left(\omega + (E_m - E_0)\right) && (6.1a) \\ &\quad + \sum_m \langle 0|c_{\mathbf{k}\sigma}|m\rangle\langle m|c^\dagger_{\mathbf{k}\sigma}|0\rangle\,\delta\left(\omega - (E_m - E_0)\right)\ , && (6.1b) \end{aligned}$$

for doped Mott insulators with

$$\int_{-\infty}^{\infty} d\omega\, A(\mathbf{k},\omega) \;=\; 1\ . \tag{6.2}$$

In (6.1a) and (6.1b), we use the $T = 0$ spectral representation of $A(\mathbf{k},\omega)$, where $|m\rangle$ are the exact many-body eigenstates with energies E_m. The ground state is given by $m = 0$, and ω is measured with respect to the chemical potential. We are now interested in the low energy spectral weight of a doped Mott insulator described by a Gutzwiller projected ground state, *i.e.*, $|0\rangle \sim |\Psi\rangle \equiv P_G|\Psi_0\rangle$.

When removing a hole from the ground state [as in (6.1a)] certainly no doubly occupied sites are created. Thus, the resulting state is situated in the so-called “lower Hubbard band” (LHB) and involves only low energy excitations, *i.e.*, $0 < E_m - E_0 \ll U$ (excitation energies much smaller than the Hubbard U). Thus, at the hole side, the low energy spectral weight corresponding to momentum $\mathbf{k}$ and spin σ is given by,

$$\int_{-\infty}^{0} d\omega\, A(\mathbf{k},\omega) = \langle 0|c^\dagger_{\mathbf{k}\sigma}c_{\mathbf{k}\sigma}|0\rangle = \langle n_{\mathbf{k}\sigma}\rangle_\Psi\ . \tag{6.3}$$

By summing over all spin and momenta, we obtain the total low energy spectral weight for the hole side,

$$\frac{1}{L}\sum_{\mathbf{k},\sigma}\int_{-\infty}^{0} d\omega\, A(\mathbf{k},\omega) = \frac{1}{L}\sum_{\mathbf{k},\sigma}\langle n_{\mathbf{k}\sigma}\rangle_\Psi = n\ . \tag{6.4}$$

We note that similar sum rules can be derived for the dynamical conductivity, *viz.*, the f-sum rule [205].

The situation is different when adding an electron to the ground state [as in (6.1b)]. In such a process a part of the resulting state is located in the "upper Hubbard band" (UHB), *i.e.*, a doubly occupied site may be created. Therefore, we have to choose an upper cutoff Ω_L (located between LHB and UHB) to extract the low energy spectral weight. By integrating $A(\mathbf{k},\omega)$ from 0 to Ω_L, we restrict ourselves solely to the Gutzwiller projected eigenstates out of all $|m\rangle$, and we obtain[1],

$$\int_0^{\Omega_L} d\omega\, A(\mathbf{k},\omega) = \langle 0|c_{\mathbf{k}\sigma} P_G c^\dagger_{\mathbf{k}\sigma}|0\rangle = \langle P_G c_{\mathbf{k}\sigma} P_G c^\dagger_{\mathbf{k}\sigma} P_G\rangle_{\Psi_0} \,. \tag{6.5}$$

Summing again over all spin and momenta and making use of Fourier transformation, we find the total low energy spectral weight for the electron side to be,

$$\begin{aligned}
\frac{1}{L}\sum_{\mathbf{k},\sigma}\int_0^{\Omega_L} d\omega\, A(\mathbf{k},\omega) &= \frac{1}{L}\sum_{\mathbf{k},\sigma}\langle P_G c_{\mathbf{k}\sigma}\, P_G\, c^\dagger_{\mathbf{k}\sigma}\, P_G\,\rangle_{\Psi_0} && \text{(6.6a)}\\
&= \frac{1}{L}\sum_{l,\sigma}\langle P_G\, c_{l\sigma}(1-n_{l-\sigma})\, c^\dagger_{l\sigma}\, P_G\rangle_{\Psi_0} && \text{(6.6b)}\\
&= \frac{1}{L}\sum_{l,\sigma}\langle (1-n_{l-\sigma})(1-n_{l\sigma})\rangle_{\Psi} && \text{(6.6c)}\\
&= 2\cdot(1-n)\,, && \text{(6.6d)}
\end{aligned}$$

where we used, $P_G\, c^\dagger_{l\sigma}\, P_G = (1-n_{l-\sigma})\, c^\dagger_{l\sigma}\, P_G$ (for a site l), to get (6.6b).

From (6.4) and (6.6), we find that it is more difficult to add an electron to the LHB than to extract one in a doped Mott insulator. This feature increases towards half-filling. For a hole density $x = 1-n$ the total spectral weight at the particle side is reduced to $2x = 2(1-n)$, while the hole side of the spectral weight is not much affected. However, above sum rules solely explain the particle-hole asymmetry of the total spectral weight, but tell us little about the energy distribution of spectral weight within the LHB.

Note, that the total spin-integrated spectral weight is 2, and the integrated spectral weight of the upper Hubbard band is consequently, $2-n-2\cdot(1-n) = n$, which agrees with the Hubbard-I approximation for the paramagnetic case [206].

6.1.2 Definition of coherent quasiparticle excitations

To explain the distribution of spectral weight at low energies, we approximate the eigenstates $|m\rangle$ by the Gutzwiller-Bogoliubov quasiparticles, equation

---

[1] For a more detailed reasoning of this step we refer to [194].

(4.14), derived from RMFT [7, 194]. We formulate particle-like Gutzwiller-Bogoliubov QPs by,

$$|\Psi^{\mathrm{N}+1}_{\mathbf{k}\sigma}\rangle = P_{\mathrm{N}+1} P_G \gamma^\dagger_{\mathbf{k}\sigma} |\Psi_0\rangle \ , \tag{6.7}$$

as well as hole-like Gutzwiller-Bogoliubov QPs with the same momentum and spin by,

$$|\Psi^{\mathrm{N}-1}_{\mathbf{k}\sigma}\rangle = P_{\mathrm{N}-1} P_G \gamma^\dagger_{\mathbf{k}\sigma} |\Psi_0\rangle \ . \tag{6.8}$$

We note that in the following we work in the canonical scheme, *i.e.*, we fix the particle number N by the operator P_{N} and thus the ground state is $|\Psi^{\mathrm{N}}\rangle = P_{\mathrm{N}} P_G |\Psi_0\rangle$. To avoid confusions we include an index N for the particle number in the wave function. On mean field level, the energies corresponding to the states (6.7) and (6.8) are given by the RMFT excitations $E_{\mathbf{k}}$ as discussed in section 4.2.

Using (6.7) and (6.8) in (6.1a) and (6.1b) yields,

$$A(\mathbf{k},\omega) = Z^+_{\mathbf{k}} u^2_{\mathbf{k}}\, \delta(\omega - E_{\mathbf{k}}) + Z^-_{\mathbf{k}} v^2_{\mathbf{k}}\, \delta(\omega + E_{\mathbf{k}}) + A^{\mathrm{inc}}(\mathbf{k},\omega) \ , \tag{6.9}$$

with the QP weights $\tilde{Z}^\pm_{\mathbf{k}\sigma}$ given by,

$$\tilde{Z}^+_{\mathbf{k}\sigma} \equiv Z^+_{\mathbf{k}} u^2_{\mathbf{k}} = \frac{|\langle \Psi^{\mathrm{N}+1}_{\mathbf{k}\sigma} | c^\dagger_{\mathbf{k}\sigma} | \Psi^{\mathrm{N}}_0 \rangle|^2}{\langle \Psi^{\mathrm{N}+1}_{\mathbf{k}\sigma} | \Psi^{\mathrm{N}+1}_{\mathbf{k}\sigma} \rangle \langle \Psi^{\mathrm{N}}_0 | \Psi^{\mathrm{N}}_0 \rangle} \ , \tag{6.10}$$

and

$$\tilde{Z}^-_{\mathbf{k}\sigma} \equiv Z^-_{\mathbf{k}} v^2_{\mathbf{k}} = \frac{|\langle \Psi^{\mathrm{N}-1}_{-\mathbf{k}-\sigma} | c_{\mathbf{k}\sigma} | \Psi^{\mathrm{N}}_0 \rangle|^2}{\langle \Psi^{\mathrm{N}-1}_{-\mathbf{k}-\sigma} | \Psi^{\mathrm{N}-1}_{-\mathbf{k}-\sigma} \rangle \langle \Psi^{\mathrm{N}}_0 | \Psi^{\mathrm{N}}_0 \rangle} \ . \tag{6.11}$$

Here, we distinguish between the QP weight $\tilde{Z}^\pm_{\mathbf{k}\sigma}$ mostly used in VMC calculations and the QP weight renormalization $Z^\pm_{\mathbf{k}\sigma}$ often given within RMFT studies. In (6.9) the Gutzwiller-Bogoliubov QPs cause δ-peaked excitations, which are associated with the coherent peaks, *e.g.*, as seen in ARPES. For projected wave functions, the weight of these coherent excitations is renormalized due the Gutzwiller projection by a factor $Z^\pm_{\mathbf{k}}$. Therefore, some part of the spectral weight is not covered by the Gutzwiller-Bogoliubov excitations, (6.7) and (6.8), demanding the presence of an incoherent background $A^{\mathrm{inc}}(\mathbf{k},\omega)$.

It is now controversial, whether the asymmetry in the HTSC comes from the incoherent part dictated by the spectral sum rules, or is even present in the coherent QP spectrum [6, 127, 194, 197, 198]. As we show below, recent works based on the GA support the former [7, 194], *i.e.*, a particle-hole symmetric quasiparticle weight renormalization,

$$Z_{\mathbf{k}} = Z^+_{\mathbf{k}} = Z^-_{\mathbf{k}} \ . \tag{6.12}$$

However, recent VMC calculations [197] (discussed in section 7.1) claim that this symmetry is exactly fulfilled only for $\mathbf{k}$ at the (underlying) Fermi surface. Therefore, zero (or very low) energy excitations would still exhibit particle-hole symmetry, however, coherent excitations at higher energies could cause an asymmetry [198].

6.1.3 Incoherent background of the spectral weight

Next we shortly discuss the incoherent background at the hole side. By using the spectral representation, (6.1a) and (6.1b), together with $A(\mathbf{k},\omega)$ from (6.9), we find the relation,

$$\langle n_{\mathbf{k}\sigma}\rangle_\Psi = Z^-_{\mathbf{k}} u^2_{\mathbf{k}} \ + \ n^{\text{inc}}_{\mathbf{k}\sigma} \ , \tag{6.13}$$

with

$$n^{\text{inc}}_{\mathbf{k}\sigma} = \int_{-\infty}^{0} d\omega\, A^{\text{inc}}(\mathbf{k},\omega) \ . \tag{6.14}$$

Thus, the momentum distribution, $\langle n_{\mathbf{k}\sigma}\rangle$, provides the total spectral weight with momentum $\mathbf{k}$ and spin σ at the hole side, *i.e.*, the coherent weight $Z^-_{\mathbf{k}} u^2_{\mathbf{k}}$ overlaid by the incoherent background $n^{\text{inc}}_{\mathbf{k}\sigma}$. We will calculate these quantities in section 6.3 by the GA and illustrate their distributions within the first Brillouin zone.

6.1.4 Divergent k-dependent self-energy

In section 5.3 we already presented VMC calculations for the QP weight renormalization at the nodal point $\mathbf{k}_F$. These calculations show that $Z \to 0$ for $x \to 0$, where $Z = Z^+_{\mathbf{k}_F} = Z^-_{\mathbf{k}_F}$. Before extending our considerations to all $\mathbf{k}$-points, we discuss consequences for the self-energy in the half-filled limit. Due to the vanishing gap along the nodal direction, $(0,0) \to (\pi,\pi)$, we can approximate the Green's function in the vicinity of $\mathbf{k}_F$ by $G^{-1}(\mathbf{k},\omega) = \omega - \epsilon(\mathbf{k}) - \mu - \Sigma(\mathbf{k},\omega)$, where $\Sigma \equiv \Sigma' + i\Sigma''$. Standard arguments then lead to the results,

$$Z = \left(1 - \frac{\partial \Sigma'}{\partial \omega}\right)^{-1} \ , \quad v_{_F} = Z\left(v^0_{_F} + \frac{\partial \Sigma'}{\partial \mathbf{k}}\right) \ , \tag{6.15}$$

where the right hand side is evaluated at the node $(\mathbf{k}_F, \omega = 0)$. Since $Z \to 0$ for $x \to 0$, $|\partial\Sigma'/\partial\omega|$ diverges like $1/x$ in this limit. Due to the finite Fermi velocity v_F (see section 4.3 and section 5.3), a compensating divergence in the **k**-dependence of the self-energy with

$$\frac{\partial \Sigma'}{\partial \mathbf{k}} \sim \frac{1}{x} \ . \tag{6.16}$$

automatically shows up. Above limit behavior of v_F and Z is also experimentally observed and transcends orthodox Landau-Fermi liquid behavior, where the **k**-dependence of the self-energy is usually small.

Equation (6.16) constitutes a key experimental result for the HTSC, since ARPES shows unambiguously that $v_F \to$ const and $Z \to 0$ for $x \to 0$ [13, 14, 26, 27]. The fact that (6.16) naturally results within the Gutzwiller-RVB framework provides a strong supporting argument for the theory. It is a consequence of the vanishing of the number of free charge carriers $\sim 1-n$ due to the projection close to half-filling. The number of charge carriers is, in contrast, $\sim n$ and not singular within normal Fermi liquid theory. These considerations lead to further consequences for higher-energy features of the one-particle self-energy, which have been explored by Randeria, *et al.* [207].

6.2 Calculation of the quasiparticle weight within RMFT

To evaluate the QP weight in (6.10) and (6.11) within RMFT, we follow [6] and use the GA for partially projected states as presented in section 3.3. For simplification we work with a particle excitation,

$$|\Psi^{\mathrm{N}+1}_{\mathbf{k}\sigma}\rangle = P_{\mathrm{N}+1} P_G c^{\dagger}_{\mathbf{k}\sigma} |\Psi_0\rangle \ , \tag{6.17}$$

and a hole excitation,

$$|\Psi^{\mathrm{N}-1}_{\mathbf{k}\sigma}\rangle = P_{\mathrm{N}-1} P_G c_{-\mathbf{k}-\sigma} |\Psi_0\rangle \ . \tag{6.18}$$

However, such a re-definition does not effect the final results since all calculations include norms and, $\gamma^{\dagger}_{\mathbf{k}\sigma}|\Psi_0\rangle \sim c^{\dagger}_{\mathbf{k}\sigma}|\Psi_0\rangle \sim c_{-\mathbf{k}-\sigma}|\Psi_0\rangle$, for a BCS wave function $|\Psi_0\rangle$.

6.2.1 Norms of the quasiparticle excitations

Any calculation involving $|\Psi^{\mathrm{N}\pm1}_{\mathbf{k}\sigma}\rangle$ needs the respective norms,

$$N^{\mathrm{N}\pm1}_{\mathbf{k}\sigma} = \langle \Psi^{\mathrm{N}\pm1}_{\mathbf{k}\sigma} | \Psi^{\mathrm{N}\pm1}_{\mathbf{k}\sigma} \rangle \ .$$

We now calculate these norms within the generalized GA. For the particle excitation, we get,

$$\frac{N^{\mathrm{N}+1}_{\mathbf{k}\sigma}}{N^{\mathrm{N}}_{G}} = 1 - n \,+\, g_t\left(n_\sigma - n^0_{\mathbf{k}\sigma}\right) = g_t\left(1 - n^0_{\mathbf{k}\sigma}\right) \;, \tag{6.19}$$

where $g_t = (1-n)/(1-n_\sigma)$, $N^{\mathrm{N}}_G = \langle\Psi^{\mathrm{N}}|\Psi^{\mathrm{N}}\rangle$, and $n^0_{\mathbf{k}\sigma} = \langle c^\dagger_{\mathbf{k}\sigma}c_{\mathbf{k}\sigma}\rangle_{\Psi_0}$ is the momentum distribution function in the unprojected wave function. We note that we will restrict ourselves to the non-magnetic case $n_\sigma = n_\uparrow = n_\downarrow = n/2$ in the following. The derivation of equation (6.19) is given by

$$\begin{aligned}
N^{\mathrm{N}+1}_{\mathbf{k}\sigma} &= \langle\Psi_0|c_{\mathbf{k}\sigma}P_{\mathrm{N}+1}P_GP_GP_{\mathrm{N}+1}c^\dagger_{\mathbf{k}\sigma}|\Psi_0\rangle \qquad (6.20)\\
&= \frac{1}{L}\sum_{l,m}\mathrm{e}^{i\mathbf{k}(l-m)}\langle\Psi^{\mathrm{N}}_0|P'_l(1-n_{l-\sigma})c_{l\sigma}c^\dagger_{m\sigma}(1-n_{m-\sigma})P'_m|\Psi^{\mathrm{N}}_0\rangle\\
&= \frac{1}{L}\sum_{l}\langle\Psi^{\mathrm{N}}_0|P'_l(1-n_{l\sigma})(1-n_{l-\sigma})P'_l|\Psi^{\mathrm{N}}_0\rangle\\
&\qquad\qquad + \frac{1}{L}\sum_{l\neq m}\mathrm{e}^{i\mathbf{k}(l-m)}\langle\Psi^{\mathrm{N}}_0|P_Gc_{l\sigma}c^\dagger_{m\sigma}P_G|\Psi^{\mathrm{N}}_0\rangle\\
&= N^{\mathrm{N}}_G\frac{\langle\Psi^{\mathrm{N}}|(1-n)|\Psi^{\mathrm{N}}\rangle}{\langle\Psi^{\mathrm{N}}|\Psi^{\mathrm{N}}\rangle} - \frac{N^{\mathrm{N}}_G}{L}\sum_{l\neq m}\mathrm{e}^{i\mathbf{k}(l-m)}\frac{\langle\Psi^{\mathrm{N}}|c^\dagger_{m\sigma}c_{l\sigma}|\Psi^{\mathrm{N}}\rangle}{\langle\Psi^{\mathrm{N}}|\Psi^{\mathrm{N}}\rangle}\;,
\end{aligned}$$

where we have used (3.71) for the diagonal contribution in the last step. Invoking the Gutzwiller approximation for the off-diagonal term, (6.19) follows directly from (6.20).

The normalization of the hole excitation can be done analogously. We note that $P_Gc_{m\sigma} = c_{m\sigma}P'_m$ with $P'_m = \prod_{i\neq m}(1-\hat{n}_{i\uparrow}\hat{n}_{i\downarrow})$ (see section 3.3) and get,

$$\begin{aligned}
\frac{N^{\mathrm{N}-1}_{-\mathbf{k}-\sigma}}{N^{\mathrm{N}}_G} &= \frac{1}{N^{\mathrm{N}}_GL}\sum_{l,m}\mathrm{e}^{i\mathbf{k}(l-m)}\langle\Psi^{\mathrm{N}}_0|P'_lc^\dagger_{l\sigma}c_{m\sigma}P'_m|\Psi^{\mathrm{N}}_0\rangle \qquad (6.21)\\
&= \frac{1}{X}\Big[Xn_\sigma + (1-X)\Big] \,+\, \frac{1}{N^{\mathrm{N}}_GL}\sum_{l\neq m}\mathrm{e}^{i\mathbf{k}(l-m)}\langle\Psi^{\mathrm{N}}_0|P'_{lm}c^\dagger_{l\sigma}c_{m\sigma}P'_{lm}|\Psi^{\mathrm{N}}_0\rangle\;,
\end{aligned}$$

where $X = \langle P_G\rangle_0/\langle P'_l\rangle_0$ and $P'_{lm} = \prod_{i\neq l,m}(1-n_{i,\uparrow}n_{i,\downarrow})$ as defined in section 3.3. The term, $1/X[Xn_\sigma + (1-X)]$, in (6.21) corresponds to the on-site contribution $l = m$, *viz.*, the expectation value $\langle\Psi^{\mathrm{N}}_0|P'_ln_{l\sigma}P'_l|\Psi^{\mathrm{N}}_0\rangle$, which can be evaluated by (3.69) and (3.70). The last term in (6.21) describes a hopping process between two reservoir sites. The generalized Gutzwiller approximation assumes that the matrix elements are proportional to the square roots of the corresponding densities, (3.68)-(3.70).

Invoking the Gutzwiller approximation and using (3.66) for X, we get,

$$\begin{aligned}\frac{N^{\mathrm{N}-1}_{-\mathbf{k}-\sigma}}{N^{\mathrm{N}}_{G}} &= \frac{\langle\Psi^{\mathrm{N}-1}_{-\mathbf{k}-\sigma}|\Psi^{\mathrm{N}-1}_{-\mathbf{k}-\sigma}\rangle}{\langle\Psi|\Psi\rangle} = n_\sigma + \frac{1-X}{X} \\ &+ \frac{n^0_{\mathbf{k}\sigma}-n_\sigma}{X^2 n_\sigma(1-n_\sigma)}\Big[\sqrt{X(1-n)}\sqrt{Xn_\sigma}+\sqrt{Xn_{-\sigma}}\sqrt{1-X}\,\Big]^2 ,\end{aligned} \tag{6.22}$$

for the normalization of the hole excitation relative to the norm of the Gutzwiller wave function. The general expression, equation (6.22), for the hole normalization, can be simplified upon using the Gutzwiller result (3.67) for the relative norm X. We then get,

$$\begin{aligned}&\frac{n^0_{\mathbf{k}\sigma}-n_\sigma}{n_\sigma(1-n_\sigma)}\Big[\sqrt{1-n}\sqrt{n_\sigma}+\sqrt{n_{-\sigma}}\sqrt{(1-X)/X}\,\Big]^2 \\ &\qquad = (n^0_{\mathbf{k}\sigma}-n_\sigma)\frac{[(1-n)+n_{-\sigma}]^2}{(1-n_\sigma)(1-n)} = (n^0_{\mathbf{k}\sigma}-n_\sigma)\frac{1-n_\sigma}{(1-n)} ,\end{aligned}$$

for the last term in (6.22). Finally, we obtain the simple result,

$$\frac{N^{\mathrm{N}-1}_{-\mathbf{k}-\sigma}}{N^{\mathrm{N}}_{G}} = n^0_{\mathbf{k}\sigma}\frac{1-n_\sigma}{(1-n)} = \frac{n^0_{\mathbf{k}\sigma}}{g_t} \tag{6.23}$$

It is interesting to compare this result for the normalization of the hole excitation with the corresponding expression, equation (6.19), for the particle excitation. The vanishing of the latter at half filling could have been expected. But the divergence of $N^{\mathrm{N}-1}_{\mathbf{k}\sigma}$ as $n \to 1$ is surprising.

6.2.2 Gutzwiller approximation for the quasiparticle weight

We first concentrate on calculating $Z^+_{\mathbf{k}}$ by (6.10). We can determine the numerator using the result of (6.19),

$$\begin{aligned}\frac{\langle\Psi_0|c_{\mathbf{k}\sigma}P_G P_{\mathrm{N}+1}c^\dagger_{\mathbf{k}\sigma}P_{\mathrm{N}}P_G|\Psi_0\rangle}{N^{\mathrm{N}}_G} &= \frac{\langle\Psi^{\mathrm{N}}_0|c_{\mathbf{k}\sigma}P_G P_G c^\dagger_{\mathbf{k}\sigma}|\Psi^{\mathrm{N}}_0\rangle}{N^{\mathrm{N}}_G} \\ &= \frac{N^{\mathrm{N}+1}_{\mathbf{k}\sigma}}{N^{\mathrm{N}}_G} = g_t(1-n^0_{\mathbf{k}\sigma}) .\end{aligned} \tag{6.24}$$

From the above expression we find that the QP weight for particle like excitations takes the form,

$$Z^+_{\mathbf{k}}u^2_{\mathbf{k}} = \frac{|\langle\Psi^{\mathrm{N}+1}_{\mathbf{k}\sigma}|c^\dagger_{\mathbf{k}\sigma}|\Psi^{\mathrm{N}}_0\rangle|^2}{\langle\Psi^{\mathrm{N}+1}_{\mathbf{k}\sigma}|\Psi^{\mathrm{N}+1}_{\mathbf{k}\sigma}\rangle\langle\Psi^{\mathrm{N}}_0|\Psi^{\mathrm{N}}_0\rangle} = \frac{g^2_t(1-n^0_{\mathbf{k}\sigma})^2}{g_t(1-n^0_{\mathbf{k}\sigma})} = g_t(1-n^0_{\mathbf{k}\sigma}) . \tag{6.25}$$

Since $1 - n^0_{\mathbf{k}\sigma} = u^2_{\mathbf{k}}$, it follows $Z^+_{\mathbf{k}} = g_t$. Thus the QP weight vanishes at half filling $n \to 1$, implying that the addition of a coherent electrons is not possible exactly at half filling because of the restriction in the Hilbert space.

Next we consider the QP for hole-like excitations in a projected superconducting state. Naively, we might expect this process to be allowed at half filling, since the removal of electrons is not forbidden by the projection operator. However, we are solely interested in the coherent excitations, which may behave quite different than the total spectral weight. Therefore, we consider the numerator of (6.11) and follow the same procedure used to evaluate the norm of the hole excitation before. We find,

$$
\begin{aligned}
\frac{\langle\Psi_0|c^\dagger_{\mathbf{k}\sigma}P_{\mathrm{N}-1}P_G c_{\mathbf{k}\sigma}P_G P_{\mathrm{N}}|\Psi^{\mathrm{N}}_0\rangle}{N^{\mathrm{N}}_G} &= \frac{1}{N^{\mathrm{N}}_G L}\sum_{l,m} \mathrm{e}^{i\mathbf{k}(l-m)}\langle\Psi^{\mathrm{N}}_0|P'_l c^\dagger_{l\sigma}c_{m\sigma}P|\Psi^{\mathrm{N}}_0\rangle \\
= \frac{Xn_\sigma}{X} + \frac{1}{N_G L}\sum_{l\neq m} \mathrm{e}^{i\mathbf{k}(l-m)}\langle\Psi^{\mathrm{N}}_0|P'_l c^\dagger_{l\sigma}c_{m\sigma}P'_l|\Psi^{\mathrm{N}}_0\rangle & \\
= \frac{Xn_\sigma}{X} + (n^0_{\mathbf{k}\sigma} - n_\sigma)\frac{\left[\sqrt{Xn_{-\sigma}}\sqrt{1-X} + \sqrt{X(1-n)}\sqrt{Xn_\sigma}\right]\sqrt{1-n}\sqrt{n_\sigma}}{X(1-n_\sigma)n_\sigma} & \\
= n_\sigma + (n^0_{\mathbf{k}\sigma} - n_\sigma)\frac{n_{-\sigma}n_\sigma + (1-n)n_\sigma}{(1-n_\sigma)n_\sigma} = n^0_{\mathbf{k}\sigma}\ . & \qquad (6.26)
\end{aligned}
$$

For more calculational deals we refer to section 3.3. Using above expression together with the norm of the hole excitation, (6.22), we obtain the QP weight for hole-like excitation,

$$
Z^-_{\mathbf{k}} v^2_{\mathbf{k}} = \frac{|\langle\Psi^{\mathrm{N}-1}_{-\mathbf{k}-\sigma}|c_{\mathbf{k}\sigma}|\Psi^{\mathrm{N}}_0\rangle|^2}{\langle\Psi^{\mathrm{N}-1}_{-\mathbf{k}-\sigma}|\Psi^{\mathrm{N}-1}_{-\mathbf{k}-\sigma}\rangle\langle\Psi^{\mathrm{N}}_0|\Psi^{\mathrm{N}}_0\rangle} = \frac{n^0_{\mathbf{k}\sigma}n^0_{\mathbf{k}\sigma}}{n^0_{\mathbf{k}\sigma}/g_t} = g_t n^0_{\mathbf{k}\sigma}, \qquad (6.27)
$$

an interesting result, in that it vanishes at half filling ($n_\uparrow = n_\downarrow = 0.5$) too. It also follows $Z^-_{\mathbf{k}} = Z^+_{\mathbf{k}} = g_t$, *i.e.*, a particle-hole symmetric QP weight renormalization.

These results show that the coherent QP weight does not cause a particle-hole asymmetry, thus, indicating that the incoherent background is responsible for the bias in the STM results. The symmetric coherent weight is also seen in the calculations for the Hubbard model (include transformation e^{-iS}) [7, 194]. However, the RMFT results for $\tilde{Z}^+_{\mathbf{k}} = Z^+_{\mathbf{k}}u^2_{\mathbf{k}}$ and $\tilde{Z}^+_{\mathbf{k}} = Z^+_{\mathbf{k}}u^2_{\mathbf{k}}$ does not exactly match recent VMC calculations [197], which directly evaluate $\tilde{Z}^+_{\mathbf{k}}$ and $\tilde{Z}^+_{\mathbf{k}}$ (see section 7.1). Nevertheless, the general doping dependence of above QP weight qualitatively agrees with VMC results and with the coherent weight seen in ARPES measurements [7].

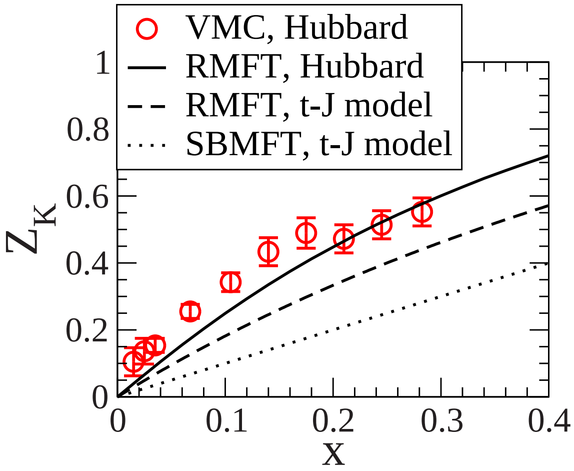

Figure 6.1: Renormalization $Z_{\mathbf{k}}$ of the Gutzwiller-Bogoliubov nodal quasiparticle as a function of doping x. The model parameters are $t = -t'/4$ and $U = 12t$. RMFT results for the Hubbard and the t-J model are compared with VMC data for the Hubbard model (from [128]) and with the SBMFT result in the t-J model. From [7].

6.3 Quasiparticle weight for the Hubbard model in the strong coupling limit

In the previous section we illustrated how one can determine the QP within the GA. In this section we follow [7, 194] and extend above calculation to the Hubbard Hamiltonian, in analogy to the extensions of the RMFT discussed in section 4.3. By using a re-transformed ground state, $|\Psi\rangle \equiv e^{-iS} P_G P_{\mathrm{N}} |\Psi_0\rangle$ as well as re-transformed excited states,

$$|\Psi^{\mathrm{N}\pm 1}_{\mathbf{k}\sigma}\rangle \equiv e^{-iS} P_G P_{\mathrm{N}\pm 1} \gamma^{\dagger}_{\mathbf{k}\sigma} |\Psi_0\rangle \ , \tag{6.28}$$

we can systematically study the QP weight renormalization within the Hubbard model in the strong coupling limit. Evaluating the canonical transformation e^{-iS} in order $\mathcal{O}(t/U)$ gives the following particle-hole symmetric QP weight renormalization [7], $Z_{\mathbf{k}} = Z^{+}_{\mathbf{k}} = Z^{-}_{\mathbf{k}}$,

$$Z_{\mathbf{k}} \approx g_t + \frac{g_3}{U} \left(\frac{1-x^2}{2} \epsilon^0_{\mathbf{k}} + \frac{3-x}{L} \sum_{\mathbf{k}'} v^2_{\mathbf{k}'} \epsilon^0_{\mathbf{k}'} \right) \ , \tag{6.29}$$

with $\epsilon^0_{\mathbf{k}} = 2t(\cos k_x + \cos k_y) + 4\, t' \cos k_x \cos k_y$. Equation (6.29) also includes corrections from the next nearest neighbor hopping term t'. The renormalization $Z_{\mathbf{k}}$ of the nodal QP weight is plotted as a solid line in figure 6.1,

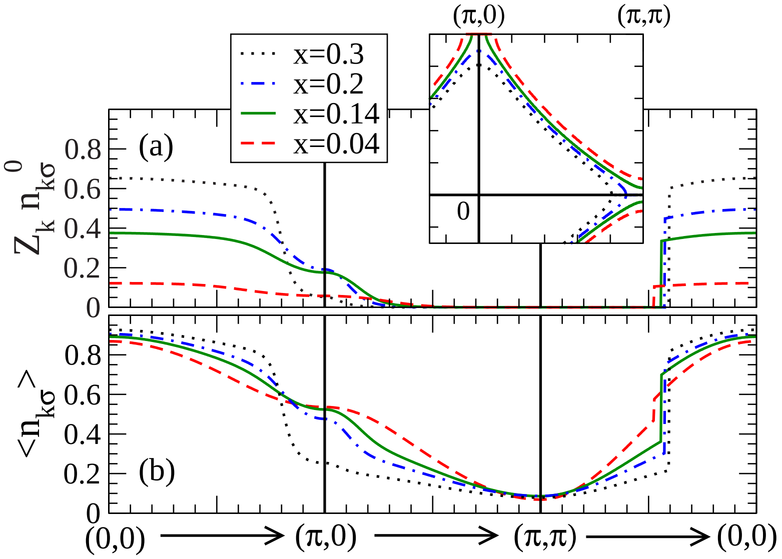

Figure 6.2: (a) Quasiparticle weight $Z_{\mathbf{k}} n^0_{\mathbf{k}\sigma}$ and (b) momentum distribution $\langle n_{\mathbf{k}\sigma}\rangle$ of the Gutzwiller-Bogoliubov quasiparticle for different doping x; The corresponding Fermi surface, $\xi_{\mathbf{k}} = 0$, is shown in the inset of (a). The model parameters are $t = -t'/4$ and $U = 12t$. From [7].

and agrees well with VMC results for the Hubbard model [128]. The dashed line corresponds to the RMFT result for the t-J model, $Z_{\mathbf{k}} = g_t$, which is compared to the dotted line, $Z_{\mathbf{k}} = x$, from slave boson mean field theory (SBMFT).

The spectral weight of the coherent peak, measured in ARPES, is related to the QP weight $\tilde{Z}^-_{\mathbf{k}} = Z^-_{\mathbf{k}} n^0_{\mathbf{k}\sigma}$; it is shown in figure 6.2(a) along the directions, $(0,0) \to (\pi,0)$, $(\pi,0) \to (\pi,\pi)$, and $(\pi,\pi) \to (0,0)$ for different x. As seen in the figure, the QP spectral weight is severely modified by Gutzwiller projection. It decreases with doping, and vanishes at half filling. This causes a shift of spectral weight to an incoherent background as seen in the momentum distribution function, $\langle n_{\mathbf{k}\sigma}\rangle \approx Z_k\, v_k^2 + n^{\mathrm{inc}}_{\mathbf{k}\sigma} + \mathcal{O}(t/U)^2$. While the first term corresponds to the coherent QP weight, the second gives the distribution of the incoherent part. We obtain,

$$n^{\mathrm{inc}}_{\mathbf{k}\sigma} \approx \frac{(1-x)^2}{2(1+x)} + \sum_{\tau} \frac{t_\tau}{2U} \cos(\mathbf{k}\tau) \left[\frac{(1-x)^3}{1+x} + \left(\frac{3g_s+1}{2} - g_3 \frac{3+x}{2} \right) |\tilde{\Delta}_\tau|^2 + \left(\frac{3g_s-1}{2} - g_3 \frac{3-x}{2} \right) \tilde{\xi}_\tau^2 \right] , \qquad (6.30)$$

which is a smooth function of $\mathbf{k}$, where $\tilde{\Delta}_\tau$ and $\tilde{\xi}_\tau$ are the pairing and

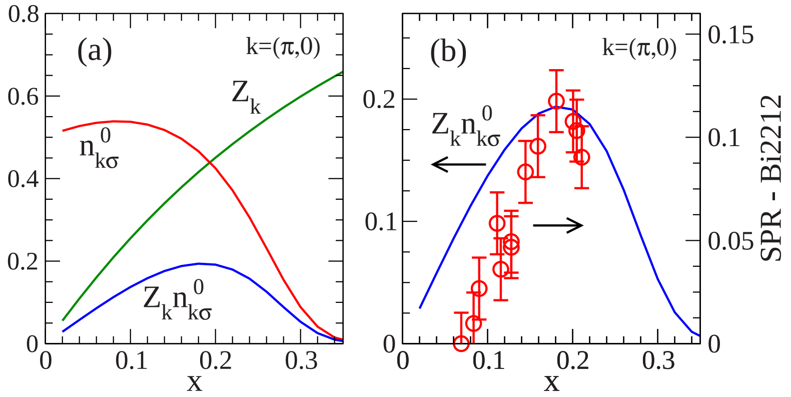

Figure 6.3: Doping dependence at the antinodal point, $\mathbf{k} = (\pi, 0)$: (a) QP renormalization $Z_{\mathbf{k}}$ the unrenormalized QP weight, $n^0_{\mathbf{k}\sigma} = v^2_{\mathbf{k}}$, and the renormalized coherent QP weight $Z_{\mathbf{k}} v^2_{\mathbf{k}}$; (b) coherent weight $Z_{\mathbf{k}}\, v^2_{\mathbf{k}}$ compared with the experimentally determined Superconducting Peak Ratio (SPR, ratio of coherent spectral weight relative to the total spectral weight) for Bi2212 [26]; see also figure 1.8. The model parameters are $t = -t'/4$ and $U = 12t$. From [7].

hopping amplitudes between nearest and next nearest neighbor sites, $\tau = (\pm 1, 0), (0, \pm 1), (\pm 1, \pm 1)$, as defined in section 4. Results are shown in figure 6.2(b) . The incoherent weight is spread over the entire Brillouin zone, and overlies the coherent part from the Gutzwiller-Bogoliubov quasiparticles. At half-filling, all weight becomes incoherent. Above results are in qualitatively agreement with calculations for the t-J model, which is recovered by neglecting the t/U-corrections in above equations.

6.3.1 Non monotonic behavior of the QP weight at $(\pi, 0)$

In this subsection we consider the coherent QP weight $Z_{\mathbf{k}} v^2_{\mathbf{k}}$ at the antinodal point $\mathbf{k} = (\pi, 0)$ within the Hubbard model in the strong coupling limit ($U = 12t$). As seen in figure 6.2(a) and figure 6.3, it exhibits a non monotonic behavior as a function of doping. Within above theory, this effect arises from a combination of the effects due to the Gutzwiller projection and to the topology change [see insert of figure 6.2(a)] of the underlying Fermi surface (FS); figure 6.3(a) illustrates this clearly. While the QP weight renormalization, $Z_{\mathbf{k}}$, increases with increasing doping, $n^0_{\mathbf{k}} = v^2_{\mathbf{k}}$, decreases due to the topology change, which occurs at $x \approx 0.15 - 0.20$ for the present choice of hopping

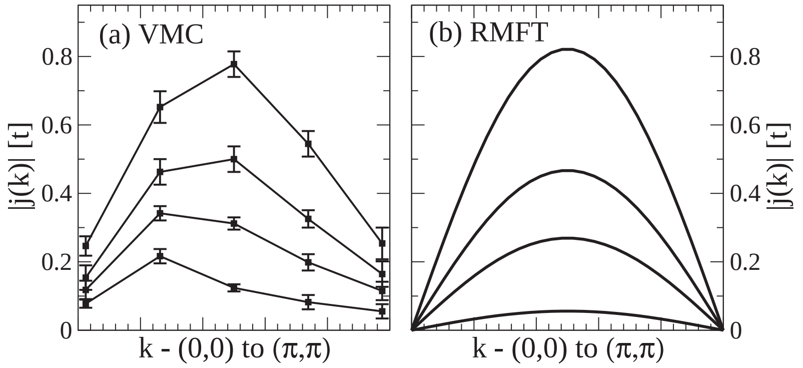

Figure 6.4: The magnitude of the current $|\mathbf{j}(\mathbf{k})|$ along the nodal direction, $(0,0)$ to (π,π). (a) VMC calculations on a 10×10-lattice (data taken from [196]) and (b) RMFT results are compared for the doping levels $x = 0.01, 0.05, 0.09, 0.17$ (increasing magnitude). From [10].

parameters ($t' = -t/4$). The change of the FS seems to be a generic feature of hole doped Cuprates [208, 209], although the exact doping concentration x, for which this occurs, is sensitive to the ratio between various hopping parameters. The combined effect of strong correlations and topology change leads to a maximum of the QP weight for the doping level, x, at which the underlying FS changes topology. Indications for such a behavior have already been published [26, 210]. Feng, *et al.* [26] extracted the superconducting peak ratio [SPR, illustrated in figure 6.3(b)] which is proportional to the coherent QP spectral weight, $Z_{\mathbf{k}}\, v_{\mathbf{k}}^2$. They found that the SPR increases with small x, attains a maximum value around $x \approx 0.2$ where it begins to decrease. Ding, *et al.* [210], reported similar results from ARPES. Although the topology change does not influence the stability of the superconducting state within RMFT, the superconducting pairing parameter Φ (related to T_c) and the QP weight $Z_{\mathbf{k}} v_{\mathbf{k}}^2$ show some similarity as a function of doping. However, we emphasize that this similarity does not result from any direct relation between these two quantities.

6.4 Quasiparticle current renormalization[2]

An important issue in the phenomenology of the high temperature superconductors is the role played by nodal quasiparticle (NQP) excitations in suppressing the superfluid density ρ_s. As pointed out by several authors

---

[2] This section follows a recent article of Edegger, *et al.* [10].

[211, 212, 213], the proliferation of NQPs at finite temperatures decreases $\rho_s(T)$, presumable by [211],

$$\frac{\rho_s(T)}{m} = \frac{\rho_s^{(0)}}{m} - \frac{2\ln 2}{\pi}\alpha^2\left(\frac{v_F}{v_2}\right)T , \tag{6.31}$$

where v_F and v_2 are the NQP velocities in the longitudinal and transverse directions respectively, and $\rho_s^{(0)}$, the zero temperature superfluid density. The renormalization factor α (also called effective charge [213]) relates the current carried by the quasiparticle to its velocity,

$$\mathbf{j}(\mathbf{k}) = -e\alpha\mathbf{v}(\mathbf{k}) .$$

Assuming that superconductivity is destroyed by thermal NQPs , T_c is determined by simply setting (6.31) to zero, *i.e.*, determining the temperature at which the superfluid density vanishes [211, 212]. The behavior of T_c as a function of doping is then governed by the doping dependencies of the various quantities in (6.31). The latter can be calculated within the framework of the Resonating Valence Bond theory. Numerical [128] calculations show that $\rho_s^{(0)} \to 0$ as $x \to 0$. The nodal velocity v_F is approximately constant [7], whereas the transverse velocity v_2 increases as the insulator ($x = 0$) is approached. The situation is rather unclear for the renormalization factor α. While some theories argue for a constant α [213], recent experimental (measurement of the superfluid density [214]) as well as theoretical results [10, 196] seem to support the conclusion that α decreases as $x \to 0$.

To clarify this issue, we follow Edegger, *et al.* [10] and use RMFT to calculate the current renormalization for the t-J model with $J = t/3$. For the superfluid density at zero temperature, RMFT yields a doping dependence of,

$$\rho_s^{(0)} \sim g_t \equiv \frac{2x}{1+x} , \tag{6.32}$$

where we applied [174],

$$\rho_s^{(0)} \sim \left\langle \sum_\sigma t_\tau (c^\dagger_{i+\tau,\sigma}c_{i,\sigma} + c^\dagger_{i,\sigma}c_{i+\tau,\sigma}) \right\rangle_\Psi , \tag{6.33}$$

and evaluated (6.33) by the Gutzwiller approximation. Here, we used $\tau = \hat{x}, \hat{y}$ and neglected corrections due to the re-transformation e^{-iS} of the wave function to the Hubbard model, *i.e.*, we set $e^{-iS} = 1$. Using linear response theory for the superfluid density [174] and restricting ourselves to low temperatures, we recover (6.31) within RMFT [10]. The renormalization factor α can be

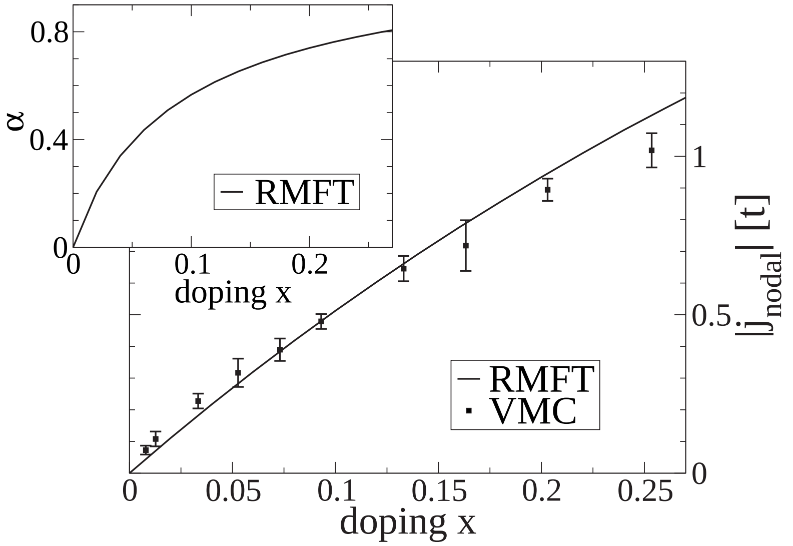

Figure 6.5: Magnitude of the nodal current as a function of doping. RMFT results are compared with the VMC calculations on a 20 × 20-lattice (data taken from [196]). Insert: RMFT result for the current renormalization factor, $\alpha \equiv |\mathbf{j}_{\text{nodal}}|/v_F$, as a function of doping x. From [10].

derived by considering the current carried by the Gutzwiller projected Bogoliubov quasiparticle states $|\Psi_{\mathbf{k}\sigma}\rangle$,

$$\mathbf{j}(\mathbf{k}) \equiv i\, e\, \langle \sum_{\langle ij\rangle,\sigma} t_{ij}\, \Big(c^\dagger_{i,\sigma}\, c_{j,\sigma} - c^\dagger_{j,\sigma}\, c_{i,\sigma} \Big) \rangle_{\Psi_{\mathbf{k}\sigma}} \; . \tag{6.34}$$

By invoking the Gutzwiller renormalization scheme, we find,

$$\mathbf{j}(\mathbf{k}) \;=\; -\, e\, g_t \frac{d}{dk} \epsilon^0(\mathbf{k}), \tag{6.35}$$

where $\epsilon^0(\mathbf{k})$ is the unrenormalized tight binding dispersion relation; again we set $e^{-iS} = 1$ for simplicity, *i.e.*, we neglect any t/U-corrections in (6.34) and (6.35). Combining (6.32) and (6.35) allows us to extract α. At the nodal point, we get $\alpha = g_t v_F^0 / v_F$, where v_F^0 is the unrenormalized Fermi velocity. The results are shown in figure 6.4 and figure 6.5, where we compare them with VMC data taken from [196]. The results are in excellent agreement and show that the renormalization factor $\alpha \to 0$, as $x \to 0$. We may now analyze the x dependence of $d\rho_s(T)/dT \propto \alpha^2 v_F / v_2$. We show the results for this quantity in figure 6.6(a). Note that $v_F/v_2 \propto v_F/\Delta_{SC}$ already shows a significant x-dependence and may explain the experimentally observed doping dependence of $d\rho_s(T)/dT$ [214]. However, multiplication by α^2 leads to

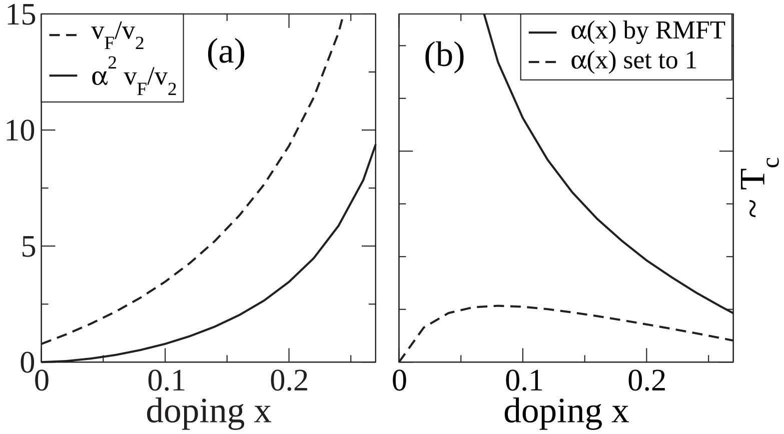

Figure 6.6: (a) Doping dependence of v_F/v_2 and $\alpha^2 v_F/v_2$ from RMFT with $t' = -0.2t$ and $U = 12t$ in the large U Hubbard model. (b) Doping dependence of T_c from setting (6.31) to zero: (i) $\alpha(x)$ from RMFT (ii) $\alpha(x)$ is set equal to 1 by hand. From [10].

a slope $d\rho_s(T)/dT$ that vanishes as $x \to 0$, *i.e.*, as $x \to 0$, the effective NQP charge vanishes faster than the superfluid density does. Therefore, we get an useless estimate for T_c by setting (6.31) to zero as shown in figure 6.6.

This problem was noted by Lee and Wen [211, 212] in the context of the $U(1)$ gauge theory of the t-J model. They argued that an $SU(2)$ formulation may resolve the problem, yielding a constant α. However, a constant α does not completely agree with the experimentally observed x-dependence of the superconducting dome either [maximal T_c at $x \approx 0.08$, see figure 6.6(b)]. There are several possible reasons for the discrepancy. It may be that the RMFT result for α is indeed correct, in which case, the issue can be resolved by more experiments explicitly extracting α in the underdoped regime. This would automatically mean that T_c is not determined by NQPs, *i.e.*, (6.31), and one needs to look for other possibilities such as vortex proliferation as mechanisms that set the scale for T_c.

Another possibility is that the theoretical framework behind the Gutzwiller RVB theory misses a crucial ingredient in the derivation of (6.31) and the calculation of the effective current renormalization α. Indeed, the applicability of the standard Kubo formula for ρ_s [174] in a projected Hilbert space may be questioned and one needs to reexamine this calculation carefully to check whether (6.31) is indeed correct.

A recent more phenomenological approach argues that the overall temperature dependence of the superfluid density at low dopings is well described by a three-dimensional strongly anisotropic weakly interacting Bose gas [215]. However, more work is necessary to clarifying if these arguments are valid on a microscopic basis.

6.5 Determining the underlying Fermi surface of strongly correlated superconductors

We present a study of the underlying Fermi surface (FS) in the HTSC as published within one of our recent papers [9]. The results shed light on the meaning of a FS in a superconducting state and make connection to the its definitions in a normal Fermi liquid. The conclusions from [9] were confirmed by a more recent study of Sensarma, *et al.* [216].

The notion of a FS is one of the most ingenious concepts developed by solid state physicists during the past century [217]. It plays a central role in our understanding of interacting electron systems. Extraordinary efforts have been undertaken, both by experiment and by theory, to reveal the FS of the high temperature superconductors (HTSC), the most prominent class of strongly correlated superconductors. Here, we discuss some of the prevalent methods used to determine the FS and show that they lead generally to erroneous results close to half filling and at low temperatures, due to the large superconducting gap (pseudogap) below (above) the superconducting transition temperature. Below findings provide a perspective on the interplay between strong correlations and superconductivity and highlight the importance of strong coupling theories [11, 45, 76] for the characterization as well as the determination of the underlying FS in ARPES experiments.

During the last decade ARPES has emerged as a powerful tool [13, 14] to study the electronic structure of the HTSC. This is also because ARPES is a direct method to probe the FS, the locus in momentum space where the one electron excitations are gapless [217]. However, since the low temperature phase of the HTSC has a superconducting or pseudogap with d-wave symmetry, an FS can be defined only along the nodal directions or along the so-called Fermi arcs [13, 14, 29, 30, 31], respectively. The full "underlying FS" emerges only when the pairing interactions are turned off, either by a Gedanken experiment, or by raising the temperature. Its experimental determination presents a great challenge since ARPES is more accurate at lower temperatures. Since the FS plays a key role in our understanding of condensed matter, it is of importance to know what is exactly measured by ARPES in a superconducting or in a pseudogap state. The problem becomes even more acute in HTSC due to the presence of strong correlation effects [11, 45, 76]. Hence, it is desirable to examine a reference d-wave superconducting state with aspects of strong correlation built explicitly in its construction. Motivated by these considerations, we consider the FS of a strongly correlated d-wave superconductor [7, 76] and discuss the results in the context of ARPES in HTSC.

6.5.1 Fermi vs. Luttinger surface

We begin by highlighting the differences between a Fermi and a Luttinger surface. The FS is determined by the poles of the one electron Green's function $G(\mathbf{k},\omega)$, *viz.*, by $\mathrm{Re}\, G(\mathbf{k},\omega=0) \equiv \pm\infty$ [217]. The Luttinger surface is defined as the locus of points in reciprocal space, where the real part of the one particle Green's function changes sign [218]. In the Fermi liquid state of normal metals, the Luttinger surface coincides with the FS. In a Mott-Hubbard insulator the Green's function changes sign due to a characteristic $1/\omega$-divergence of the single particle self energy [219, 220] at momenta $\mathbf{k}$ of the non-interacting Fermi surface. In the HTSC the gapped states destroy the FS but only mask the Luttinger surface. Hence, it seems natural to relate the Luttinger surface of the superconducting and of the pseudogap states with the concept of an "underlying FS", and ask if such a surface can be determined by ARPES.

The single particle Green's function is given by,

$$G(\mathbf{k},\omega) \equiv \sum_n \frac{|\langle n|c^\dagger_{\mathbf{k}\sigma}|0\rangle|^2}{\omega-(E_n-E_0)+i0^+} + \sum_n \frac{|\langle n|c_{\mathbf{k}\sigma}|0\rangle|^2}{\omega+(E_n-E_0)+i0^+}\ , \tag{6.36}$$

where E_n are the eigenvalues corresponding the eigenstates $|n\rangle$ of the Hamiltonian; the ground state and its energy are given by $|0\rangle$ and E_0, respectively. In order to perform explicit analytic calculations we approximate the coherent part of (6.36) by the RMFT results for the Hubbard model (see section 4.3 and section 6.3). In analogy to section 6.1.2 for the spectral function $A(\mathbf{k},\omega)$, we use, $Z_{\mathbf{k}}u_{\mathbf{k}}^2 = |\langle n|c^\dagger_{k\sigma}|0\rangle|^2$, $Z_{\mathbf{k}}v_{\mathbf{k}}^2 = |\langle n|c_{k\sigma}|0\rangle|^2$, and, $E_{\mathbf{k}} = E_n - E_0$. Thus, we find the RMFT result for the coherent part of the Green's function,

$$G(\mathbf{k},\omega) \approx \frac{Z_{\mathbf{k}}u_k^2}{\omega-E_{\mathbf{k}}+i0^+} + \frac{Z_{\mathbf{k}}v_{\mathbf{k}}^2}{\omega+E_{\mathbf{k}}+i0^+}\ . \tag{6.37}$$

Within RMFT the elementary excitations in the superconducting d-wave ground state are given by the dispersion relation,

$$E_{\mathbf{k}} \;=\; \sqrt{\xi_{\mathbf{k}}^2 + \Delta_{\mathbf{k}}^2}\;, \tag{6.38}$$

where $\xi_{\mathbf{k}}$ and $\Delta_{\mathbf{k}}$ are determined by (4.19) and (4.20), respectively. We can now evaluate $\operatorname{Re} G(\mathbf{k}, \omega = 0)$ by (6.37) and find,

$$\operatorname{Re} G(\mathbf{k}, \omega = 0) = \frac{Z_{\mathbf{k}}}{E_{\mathbf{k}}}(v_{\mathbf{k}}^2 - u_{\mathbf{k}}^2) = -\frac{Z_{\mathbf{k}}}{E_{\mathbf{k}}^2}\,\xi_{\mathbf{k}}\;, \tag{6.39}$$

where the right hand side follows from the mean field relation, $v_{\mathbf{k}}^2 = 1 - u_{\mathbf{k}}^2 = (1 - \xi_{\mathbf{k}}/E_{\mathbf{k}})/2$ [see (4.8)]. The poles of $\operatorname{Re} G(\mathbf{k}, \omega = 0)$, which determine the FS, are therefore given by

$$E_{\mathbf{k}} \equiv 0\;. \tag{6.40}$$

However, for a d-wave superconductor, equation (6.40) is fulfilled only at the nodal points; consequently a FS is well defined solely at these points. Alternatively, we can consider the Luttinger surface, defined by sign changes in the Green's functions at $\omega = 0$. From (6.39), we find sign changes whenever

$$\xi_{\mathbf{k}} \equiv 0\;. \tag{6.41}$$

From above equations, we conclude that the Luttinger surface is determined by the condition $\xi_{\mathbf{k}} \equiv 0$, which is also the definition of the normal state FS when $\Delta_{\mathbf{k}} \equiv 0$. In the following, we discuss two methods commonly used to determine the underlying FS, *viz.*, the Luttinger surface, of the HTSC by ARPES [13, 14, 221].

6.5.2 Fermi surface determination

In the so-called "maximal intensity method" the intensity of ARPES spectra at zero frequency is used to map out the underlying FS. This quantity is determined by $A(\mathbf{k}, \omega = 0) = -\frac{1}{\pi}\operatorname{Im} G(\mathbf{k}, \omega = 0)$, which becomes

$$\sim \frac{\Gamma_{\mathbf{k}}}{E_{\mathbf{k}}^2 + \Gamma_{\mathbf{k}}^2}\;, \tag{6.42}$$

if we replace 0^+ by a finite broadening $\Gamma_{\mathbf{k}}$ in (6.37). The $\Gamma_{\mathbf{k}}$ is determined both by the experimental resolution and the width of the quasiparticle peak. When the momentum dependence of $\Gamma_{\mathbf{k}}$ is small compared to that of $E_{\mathbf{k}}$ (as

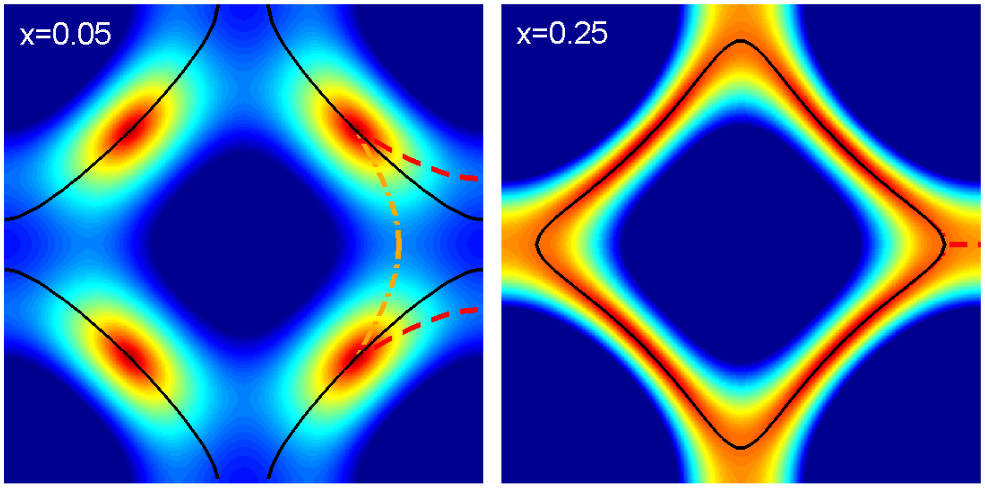

Figure 6.7: The zero frequency spectral intensity (deduced from the inverse of $E_{\mathbf{k}}$) in the first Brillouin zone for hole dopings $x = 0.05$ (left) and $x = 0.25$ (right). The color coding blue/red corresponds to the low/high zero frequency spectral intensity. The ridges of maximal intensity are indicated by the (dashed) red and (dashed-doted) orange lines respectively, the Luttinger surface by the black line. From [9].

is usually the case), the maximal intensity is given by the set of momenta $\hbar\mathbf{k}$ for which $E_{\mathbf{k}}$ is minimal.

To examine the accuracy of this method in determining the underlying FS, we calculate this quantity for a strongly correlated d-wave superconducting state. All calculations are done with model parameters for HTSC using the renormalized mean field theory (RMFT) [7, 76], for which the quasiparticle dispersion $E_{\mathbf{k}}$ retains the form of (6.38). In figure 6.7, we show results for the spectral intensity at zero frequency as well as the locus of the Luttinger surface. The former is deduced from the inverse of $E_{\mathbf{k}}$.

For large hole doping, $x = 0.25$, the superconducting gap is small and the Luttinger surface is close to the points in momentum space for which the zero frequency intensity is maximal. But for smaller doping, $x = 0.05$, the gap is substantial and the Luttinger surface deviates qualitatively from the maximal intensity surface due to the momentum dependence of $\Delta_{\mathbf{k}}$ (see ridges in figure 6.7). We have verified that this behavior persists for a wide range of $|\Delta_{\mathbf{k}}|$, and not just the values estimated from RMFT. Figure 6.7(left) also reveals that the maximum intensity splits into two ridges (orange inner, red outer). Although not widely discussed in the literature, this splitting may be deduced from experimental data, *e.g.*, the intensity plots in $E - \mathbf{k}$ space

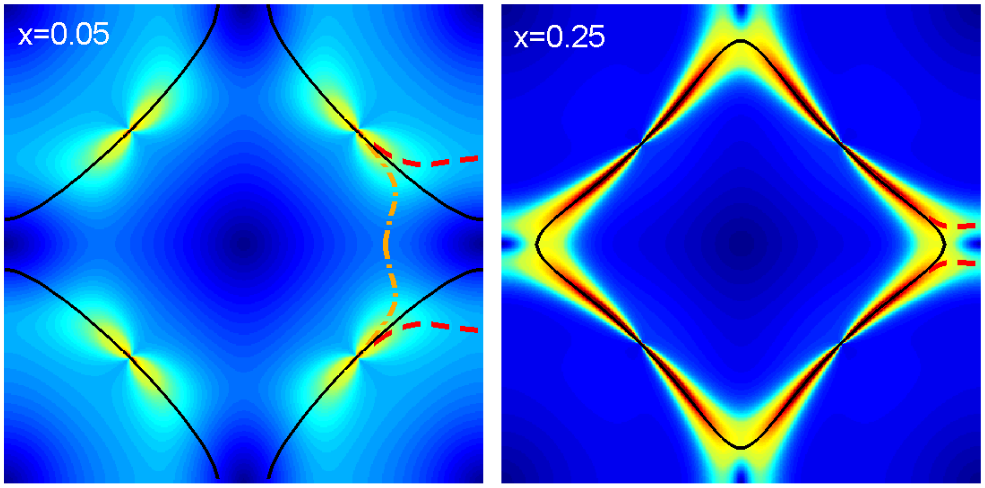

Figure 6.8: The gradient of the momentum distribution function, $|n_{\mathbf{k}}|$, in the first Brillouin zone, for hole dopings $x = 0.05$ (left) and $x = 0.25$ (right). The color coding is blue/red for small/large values of $|\nabla_{\mathbf{k}} n_{\mathbf{k}}|$. The ridges of maximal $|\nabla_{\mathbf{k}} n_{\mathbf{k}}|$ are indicated by the (dashed) red and (dashed-doted) orange lines respectively, the Luttinger surface by the black line. From [9].

along symmetric lines $(0,0) \to (\pi,0) \to (\pi,\pi)$ in [209]. It follows that when the gap or the pseudogap is large, the criterion of maximal spectral intensity alone does not suffice to identify the correct FS and it is necessary to supplement the analysis of the zero frequency ARPES intensity, (6.42), with a dispersion relation such as (6.38). These considerations explain why the (outer) maximal intensity ridges seen in ARPES (at low temperatures in the underdoped regime) may yield an underlying FS whose volume is too large. In particular, this effect is seen in $Ca_{2-x}Na_xCuO_2Cl_2$ [222], which also exhibits quite a large pseudogap [223].

Another method used in extracting the Luttinger surface is the "maximal gradient method". The method is based on the fact that the FS is given by the set of **k**-values for which the momentum distribution function $n_{\mathbf{k}}$ shows a jump discontinuity. When this discontinuity is smeared out, say, by thermal broadening or a small gap, the gradient of $n_{\mathbf{k}}$, $|\nabla_{\mathbf{k}} n_{\mathbf{k}}|$, is assumed to be maximal at the locus of the underlying FS.

We calculated $|\nabla_{\mathbf{k}} n_{\mathbf{k}}|$ within RMFT and show our results in figure 6.7. We see that the maximal gradient surface is very sensitive to the presence of even small gaps. For example, the superconducting gap at $x = 0.25$ is quite small. Nonetheless, the electron-like Luttinger surface (determined by $\xi_{\mathbf{k}} \equiv 0$) is not clearly revealed by the ridges in $|\nabla_{\mathbf{k}} n_{\mathbf{k}}|$. Similar deviations of $|\nabla_{\mathbf{k}} n_{\mathbf{k}}|$ from the

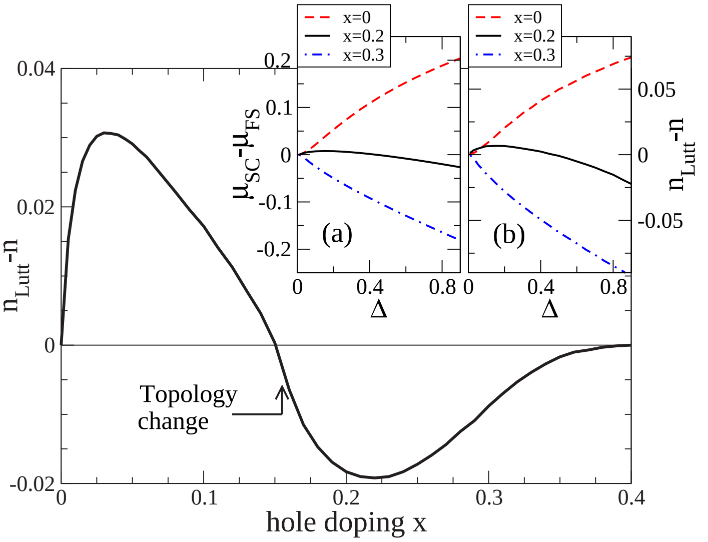

Figure 6.9: The deviation, $n_{Lutt} - n$, of the actual volume of the Luttinger surface from the Luttinger sum-rule, as a function of hole-doping x. Calculations are performed by RMFT ($t' = -t/4$, $U = 12t$). The deviation is minimal when the topology of the Luttinger surface changes from hole-like to electron-like. Inserts (a) and (b): Model calculation for the renormalization of the chemical potential, $\mu_{SC} - \mu_{FS}$, and the resulting $n_{\text{Lutt}} - n$ as a function of the d-wave order Δ, for various doping x. From [9].

underlying surface are also obtained from a high temperature expansion of the t-J model [224] and dynamical cluster approximation in the Hubbard model [225]. We conclude that the maximal gradient method alone cannot be used to determine the underlying FS unambiguously from numerical [224, 225] or ARPES data [226, 227].

The notion that the underlying FS of a pseudogapped or a superconducting state is identical to the Luttinger surface is only approximately correct [218, 228]. In the Fermi liquid state of normal metals, the FS satisfies the Luttinger sum rule; the volume enclosed by the FS is identical to the total number of conducting electrons. But, in a superconductor, the chemical potential is generally renormalized and is a function of the superconducting order parameter, $\mu = \mu_{SC}(\Delta)$. The number of states $n_{Lutt}(\Delta)$ enclosed by the resulting Luttinger surface, $\xi_{\mathbf{k}} \equiv 0$, then deviates from the true particle number n, as the results in figure 6.9 show. However, this effect is small (a few percent) and unlikely to be discerned experimentally. The discrepancy between $n_{Lutt}(\Delta)$ and n vanishes when particle-hole symmetry is present. Further, it changes sign when the geometry of the Luttinger surface changes

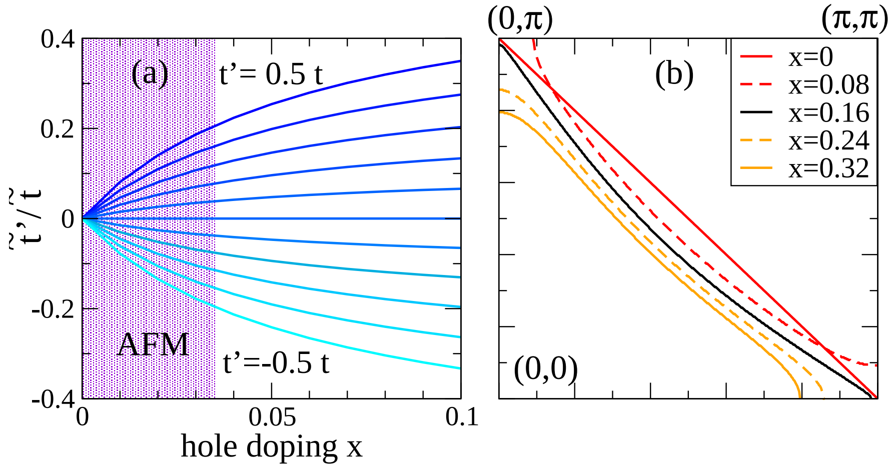

Figure 6.10: (a) Renormalization of the next nearest neighbor hopping amplitude, $t' \to \tilde{t}'$, as a function of hole doping concentration x for various values of bare t'. All effective $\tilde{t}'$ are renormalized to zero at half filling by the large Coulomb repulsion. We highlight the region for which we expect the superconducting d-wave state to become unstable against antiferromagnetism (AFM) due to the nearly perfect nesting of the Luttinger surface. (b) The geometry of the Luttinger surface for the high temperature superconductors ($t' = -t/4$). The change is non-monotonic for small doping x, when the Luttinger surface is renormalized to perfect nesting due to the strong Coulomb interaction. For $x = 0.16$, the topology of the Luttinger surface changes from hole-like to electron-like. Calculations are performed for the Hubbard model with $U = 12t$, using RMFT. From [9].

from hole-like to electron-like, as seen in figure 6.9.

6.5.3 Renormalization of the Fermi surface towards perfect nesting

Finally, we focus on the influence of the strong electron-electron interactions on the geometry of the Luttinger surface close to half filling. The Cu-O planes of the HTSC are characterized by a nearest neighbor (NN) hopping parameter $t \approx 300$ meV and a next nearest neighbor (NNN) hopping parameter $t' \approx -t/4$. These parameters are the bare parameters, and determine the dispersion relation,

$$\epsilon_{\mathbf{k}} \;=\; -2t(\cos k_x + \cos k_y) - 2t'\Big(\cos(k_x + k_y) + \cos(k_x - k_y)\Big)\,, \qquad (6.43)$$

in the absence of any electron-electron interaction. On the other hand, true hopping processes are influenced by the Coulomb interaction (here $U = 12\,t$) leading to a renormalization of the effective hopping matrix elements,

$$t \;\rightarrow\; \tilde{t} = \tilde{t}(U), \qquad t' \;\rightarrow\; \tilde{t}' = \tilde{t}'(U). \tag{6.44}$$

We extract $\tilde{t}$ and $\tilde{t}'$ from the RMFT dispersion $\xi_{\mathbf{k}}$ in (4.19), see section 4.3, and find close to half-filling $\tilde{t} \propto J = 4t^2/U$ and $\tilde{t}' \rightarrow 0$, *i.e.*, the NNN hopping is renormalized to zero. This behavior is illustrated in figure 6.10. The resulting Luttinger surface renormalizes to perfect nesting. A similar behavior has been observed in recent variational studies of organic charge transfer-salt superconductors [75].

At half filling the Hubbard model reduces to a spin-model with NN $J = 4t^2/U$ and a frustrating NNN $J' = 4(t')^2/U$. The ground state wave function obeys the so-called Marshall sign rule[3] in the absence of frustration, $J' = 0$, *viz.*, when the underlying Fermi surface is perfectly nested by the reciprocal magnetic ordering vector $Q = (\pi, \pi)$ (in units of the inverse lattice constant). Hence, any deviation from the Marshall sign rule as a function of the frustrating J' can be used to determine the degree of effective frustration present in the ground state. We emphasize this is a qualitative statement of the ground state wave function. A numerical study has found, that the Marshall sign rule remains valid even for small but finite J', *viz.*, the effective frustration renormalizes to zero [230]. Such a behavior is in agreement with the results presented in figure 6.10. This renormalization of the underlying Fermi-surface to perfect nesting close to half-filling is unique to strong coupling theories such as RMFT.

In summary, we showed that the accurate determination of the underlying FS in underdoped HTSC is a demanding task and that a pictorial analysis of the experimental data alone is often insufficient for an unambiguous determination of the FS. Commonly used methods like the zero frequency spectral intensity or the gradient of $n_{\mathbf{k}}$ can yield significant deviations from the true Luttinger surface as shown in figure 6.7 and figure 6.8. Indeed, a clear distinction between electron- and hole-like underlying FS cannot be made solely by analyzing the spectral intensity maps when the gaps are large and strongly $\mathbf{k}$-dependent. Such analyzes have to be supplemented by a minimal modeling of the gapped states. Furthermore, the underlying FS in the pseudogapped or superconducting state fulfills Luttinger theorem only approximately, owing to the dependence of the chemical potential on the superconducting gap. We also demonstrated that the strong correlations renormalize the ratio $\tilde{t}'/\tilde{t}$ near half filling, yielding a Luttinger surface which is perfectly nested. This suggests in a very natural way that the strong coupling mean field superconducting state is unstable to antiferromagnetism at low doping. These findings resulting from the combined effects of strong correlations and d-wave superconductivity, allow for a more precise interpretation of experiments that determine the FS of HTSC.

---

[3] Marshall [229] showed that the ground state of the spin-$\frac{1}{2}$ Heisenberg Hamiltonian on any bipartite lattice will be a singlet. Furthermore, the ground state wave function picks up a sign whenever two antiparallel spins from different sublattices are interchanged. This is the Marshall sign rule.

Chapter 7

Quasiparticle states within the variational Monte Carlo scheme

VMC calculations for the QP weight in the t-J model only agree qualitatively with the approximative RMFT results. Minor deviations from the RMFT studies may explain a contribution of the coherent excitations to the distinct particle-hole asymmetry seen in the STM spectra. Apart from the QP weight, we also discuss excitation energies determined by VMC calculations, which match well with previous RMFT results.

7.1 Direct calculation of the quasiparticle weight

RMFT together with GA is an useful tool to analyze QP features in strongly correlated superconducting states. However, the RMFT and GA are approximative methods and it is desirable to check their predictions numerically by VMC calculations. This consideration motivated several authors [195, 196, 197, 198, 199, 200] to calculate the QP weight, (6.10) and (6.11) directly via the evaluation of appropriate expectation values within the projected wavefunction $|\Psi\rangle$. These VMC studies confirm the RMFT prediction, that the QP weight decreases towards half-filling, where it finally vanishes. However, as we will show below, the VMC results reveal some limitations of the RMFT concerning the determinination of the detailed doping- and $\mathbf{k}$-dependence of the QP weight. We note that most of the VMC calculations presented below do not include a re-transformed trial wave function and describe observables in the t-J model. These calculations can be directly compared to the RMFT results from section 6.2.

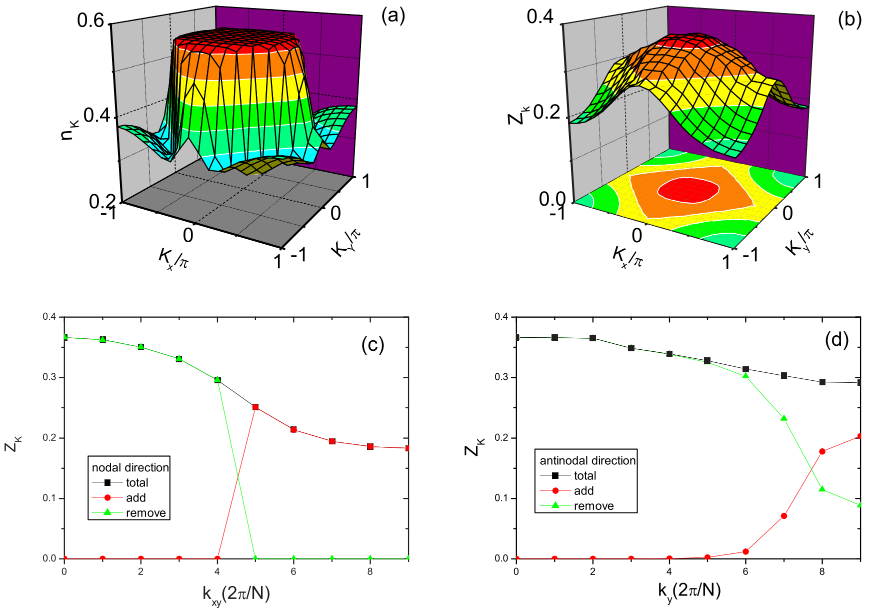

Figure 7.1: VMC result for Gutzwiller projected d-wave BCS state on a 18×18 lattice with 42 holes ($x \simeq 0.13$) and $\Delta/t = 0.1$. (a) Momentum distribution function $\langle n_{\mathbf{k}} \rangle$. (b) Total QP weight $\tilde{Z}_{\mathbf{k}}^{\text{tot}}$. (c) QP weight in the $(0,0)-(\pi,\pi)$ direction. (d) QP weight in the $(0,0)-(0,\pi)$ direction (total $\tilde{Z}_{\mathbf{k}}^{\text{tot}}$, add $\tilde{Z}_{\mathbf{k}}^{+}$, remove $\tilde{Z}_{\mathbf{k}}^{-}$). Results correspond to the t-J model since the re-transformation of the wave function was neglected. From [197].

To calculate the QP weight within the VMC scheme, most authors use two helpful exact relations for Gutzwiller projected wave functions. First, one finds for the QP weight $\tilde{Z}_{\mathbf{k}\sigma}$ of electron-like excitations, that [195, 196, 197, 198, 199],

$$\tilde{Z}^{+}_{\mathbf{k}\sigma} = \frac{1+x}{2} - \langle n_{\mathbf{k}\sigma}\rangle_{\Psi^{\mathrm{N}}}, \tag{7.1}$$

can be derived without any approximation and assumption. Thus $\tilde{Z}^{+}_{\mathbf{k}\sigma}$ can be calculated from the momentum distribution of the ground state $|\Psi^{\mathrm{N}}\rangle$ [195, 196].

For the QP weight $\tilde{Z}^{-}_{\mathbf{k}\sigma}$, there is no exact relation corresponding to (7.1). However, several authors showed [198, 199, 200] that $\tilde{Z}^{+}_{\mathbf{k}\sigma}$ and $\tilde{Z}^{-}_{\mathbf{k}\sigma}$ combined satisfy the exact relation,

$$\tilde{Z}^{+}_{-\mathbf{k}-\sigma} \cdot \tilde{Z}^{-}_{\mathbf{k}\sigma} = \frac{|\,\langle \Psi^{\mathrm{N}}|c^{\dagger}_{\mathbf{k}\sigma}c^{\dagger}_{-\mathbf{k}-\sigma}\mid \Psi^{\mathrm{N}-2}\rangle\,|^{2}}{\langle \Psi^{\mathrm{N}}\mid \Psi^{\mathrm{N}}\rangle\langle \Psi^{\mathrm{N}-2}\mid \Psi^{\mathrm{N}-2}\rangle} \equiv P_{\mathbf{k}}\ . \tag{7.2}$$

This relation is very useful, because the matrix elements contributing to $P_{\mathbf{k}}$ only involve ground states with different particle numbers. The quantity $P_{\mathbf{k}}$ is closely related to the off-diagonal long-range order in the pairing correlation and can be calculated straightforward by VMC techniques (see, *e.g.*, [198]). Equation (7.2) was also confirmed numerically [200]. However, we note that (7.1) and (7.2) are only valid for the projected wave functions $P_G|\Psi\rangle$, and become incorrect for the re-transformed wave function $e^{-iS}P_G|\Psi\rangle$, since the canonical transformation e^{-iS} does not commute with the electron and the projection operators.

7.1.1 Momentum dependence of the quasiparticle weight

VMC results for the QP weights $\tilde{Z}^{+}_{\mathbf{k}}$ (adding an electron) and $\tilde{Z}^{-}_{\mathbf{k}}$ (removing an electron), together with the total weight, $\tilde{Z}^{\mathrm{tot}}_{\mathbf{k}} = \tilde{Z}^{+}_{\mathbf{k}} + \tilde{Z}^{-}_{\mathbf{k}}$, are summarized in figure 7.1. These calculations show that $\tilde{Z}^{\mathrm{tot}}_{\mathbf{k}}$ is continuous over the whole Brillouin zone, thus supporting the idea that $Z^{+}_{\mathbf{k}} = Z^{-}_{\mathbf{k}}$ at the (underlying) Fermi surface [197]. However, away from the Fermi surface, figure 7.1 also exhibits some deviations from the simple RMFT calculations [$\tilde{Z}^{+}_{\mathbf{k}} = g_t u^2_{\mathbf{k}}$ and $\tilde{Z}^{-}_{\mathbf{k}} = g_t v^2_{\mathbf{k}}$ with $g_t = 2x/(1+x)$]. For instance, inside the Brillouin zone and along the nodal direction, RMFT gives a constant QP weight $\tilde{Z}^{-}_{\mathbf{k}}$ (since $\langle n_{\mathbf{k}\sigma}\rangle = v^2_{\mathbf{k}}$ is constant along the nodal direction in the t-J model, see figure 7.2) whereas the VMC calculations [green triangles in figure 7.1(c)] clearly show a non-constant behavior.

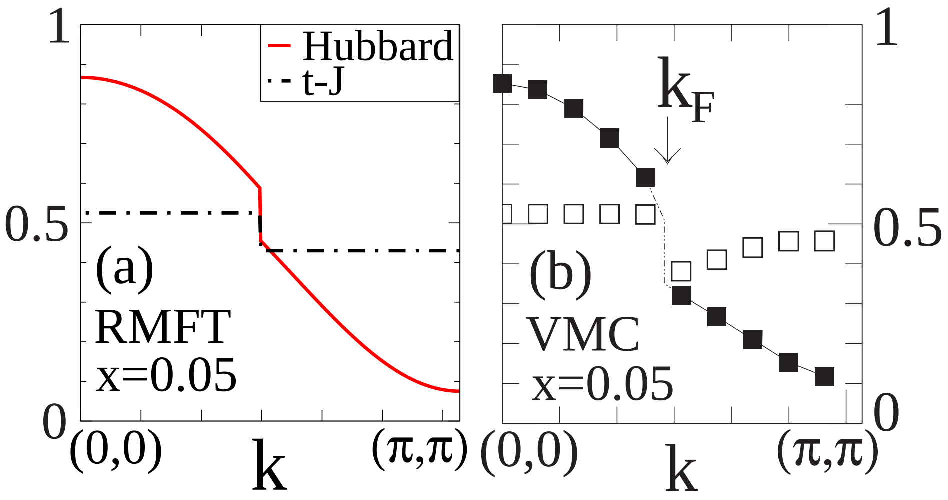

Figure 7.2: The momentum distribution $\langle n_{\mathbf{k}} \rangle$ along the nodal direction $\mathbf{k} = (k, k)$ for the Hubbard [black squares in (b)] and the t-J model [white squares in (b)] from (a) RMFT and (b) VMC calculations, respectively. The calculations are based on the full t-J Hamiltonian (2.6) with $t' = -t/4$ and $U = 12t$ at a doping level $x = 0.05$. Expectation values for the Hubbard model are evaluated within a re-transformed wave function, see (4.21b), whereas these corrections are neglected in the t-J model. The RMFT calculations are based on the results from section 6.2 and section 6.3; the VMC data are taken from [99].

In the absence of a superconducting gap the quasiparticle weight at the Fermi surface is determined by the jump in the moment distribution $\langle n_{\mathbf{k}\sigma}\rangle$, as discussed in section 5.3.2. Furthermore, $\tilde{Z}^{+}_{\mathbf{k}}$ is generally related via (7.1) to $\langle n_{\mathbf{k}\sigma}\rangle$ for the t-J model. Due to this tight relation between $\langle n_{\mathbf{k}\sigma}\rangle$ and $\tilde{Z}^{+}_{\mathbf{k}}$ we re-consider the moment dependence of $\langle n_{\mathbf{k}\sigma}\rangle$ in the VMC and the RMFT calculations. In figure 7.2 we show RMFT as well as VMC results for the moment dependence of $\langle n_{\mathbf{k}\sigma}\rangle$ along the nodal direction determined within the Hubbard and the t-J model, respectively. We note that expectation values for the Hubbard model are obtained by applying a re-transformed wave function $e^{-iS}|\Psi\rangle$, which can be evaluated in order $\mathcal{O}(t/U)$; see (4.21b) in section 4.3. In contrary, the re-transformation e^{-iS} is neglected for the calculation of observables in the t-J model. Figure 7.2(a) shows that, except of the jump at the Fermi point $\mathbf{k}_F$, the RMFT gives a constant $\langle n_{\mathbf{k}\sigma}\rangle$ along the nodal direction for the t-J model. However, VMC calculations at the same doping level ($x = 0.05$) and for the same model parameters exhibit a non-monotonic behavior near the Fermi point, see white squares in figure 7.2(b). This effect comes from the correlated hopping nature of the electron in the projected Hilbert space and is not covered by the RMFT result. This also explains discrepancies between the RMFT and the VMC method in determining the quasiparticle weight and reveals some limitations of the RMFT in calculating moment dependent quantities. However, including the re-transformation of the wave function for the Hubbard model, removes the non-monotonic behavior of $\langle n_{\mathbf{k}\sigma}\rangle$ in the VMC data, figure 7.2(b). Therefore, RMFT and VMC results give a better qualitative agreement, when $\langle n_{\mathbf{k}\sigma}\rangle$ is calculated within the Hubbard model, compare solid line in figure 7.2(a) with black squares in (b).

7.1.2 Doping dependence of the mean quasiparticle weight

Some discrepancies between VMC and RMFT in the doping dependence of the coherent QP weight have been discussed by Chou, *et al.* [198]. The authors calculate the average coherent QP weight for removing an electron,

$$\tilde{Z}^{-}_{\text{ave}} \equiv \frac{1}{L}\sum_{\mathbf{k}} \tilde{Z}^{-}_{\mathbf{k}\sigma}, \tag{7.3}$$

by the VMC scheme and compare it with the RMFT results. As shown in figure 7.3, VMC calculations give a significantly larger coherent QP weight than RMFT at the hole side, which is directly related to a reduction of the (average) incoherent background $n^{\text{inc}}_{\text{ave}}$ by the same amount.

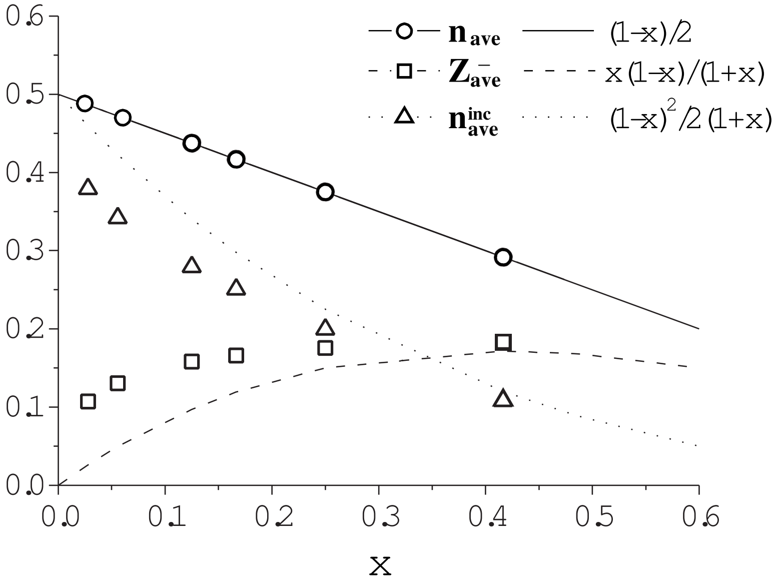

Figure 7.3: The doping dependence of average QP weights Z^{-}_{ave} for removing an electron in a d-wave state obtained by VMC calculations (12×12 lattice, $t' = 0$) and by RMFT, respectively. The results are for the t-J model (no re-transformation of the wave function). The squares (triangles) are the VMC results for Z^{-}_{ave} ($n^{\text{inc}}_{\text{ave}} = n_{\text{ave}} - Z^{-}_{\text{ave}}$) with $n_{\text{ave}} = 1/L \sum_{\mathbf{k}} \langle n_{\mathbf{k}\sigma} \rangle_{\Psi} = (1-x)/2$. The dashed and dotted lines without data points represent results by RMFT. From [198].

On the other hand the average QP weight for adding an electron,

$$\tilde{Z}^{+}_{\text{ave}} \equiv \frac{1}{L}\sum_{\mathbf{k}} \tilde{Z}^{+}_{\mathbf{k}\sigma} = \frac{1+x}{2} - \frac{1}{L}\sum_{\mathbf{k}} \langle n_{\mathbf{k}\sigma}\rangle_{\Psi} = \frac{1+x}{2} - \frac{1-x}{2} = x \ , \tag{7.4}$$

is exactly the same in the RMFT and the VMC scheme, where we used (7.1) in (7.4). Thus, it was argued [198], that the increased coherent weight at the hole side seen in the VMC calculations, can explain the particle-hole asymmetry in the tunneling experiments. However, considering the large asymmetry in the experiments and the predictions from sum rules, it is probably that at least at higher energies a considerable part of the asymmetry is caused by the incoherent background.

7.2 VMC calculations for the quasiparticle energy

In the previous section, we have shown how one can determine the spectral weight of Gutzwiller-Bogoliubov QP excitations with VMC calculations. Now we turn to the corresponding excitation energies $E_{\mathbf{k}}$. Similar to the QP weight, $E_{\mathbf{k}}$ could deviate to some extent from the RMFT results (chapter 4). The amount of agreement can be checked by directly calculating the energy corresponding to the excited state $|\Psi^{\mathrm{N}\pm 1}_{\mathbf{k},\sigma}\rangle$, equations (6.7) and (6.8), within the t-J model. Substracting the ground state energy, we obtain the excitation energy,

$$E = \langle H_{t-J}\rangle_{\Psi^{\mathrm{N}\pm1}_{\mathbf{k},\sigma}} - \langle H_{t-J}\rangle_{\Psi^{\mathrm{N}}} \ . \tag{7.5}$$

We discuss now the VMC calculations of Yunoki, *et al.* [121], who also included a Jastrow factors into the wave functions to improve the ground state energy. Figure 7.4 illustrates a typical dispersion along the nodal direction obtained by determining $E_{\mathbf{k}} = |E|$ for every $\mathbf{k}$-point separately. As shown in the figure, a tight-binding dispersion fits well to the numerical data, and it is possible to extract interesting quantities like the nodal Fermi velocity v_F or the nodal Fermi point $|\mathbf{k}_F|$.

By repeating the calculation from figure 7.4 for various electron densities, one can determine the doping dependence of v_F and $|\mathbf{k}_F|$. Figure 7.5(a) illustrates that the Fermi velocity only slightly decreases when approaching half-filling as already seen from RMFT ([7], section 4.3). The results of Yunoki, *et al.* also agree with previous VMC calculations utilizing the moments of the

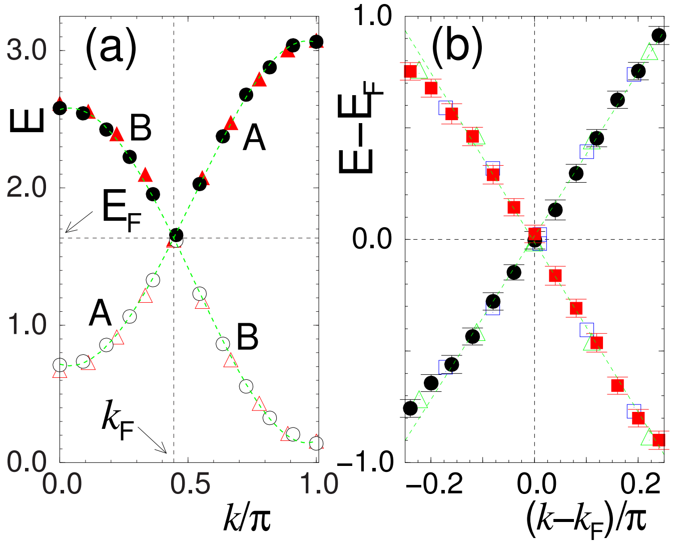

Figure 7.4: Dispersion E in the nodal direction for the 2D t-J model with J/t=0.3 and t'/t=−0.2 at x=0.099. (a) Full dispersion for L=162 (triangles) and 242 (circles). The electron removal (addition) spectrum is denoted by open (solid) symbols. The dashed lines are tight binding fits. (b) Same as (a) but focusing on the excitations near E_{F}. In addition to the data for L=162 (open triangles) and 242 (open squares), results for $L = 1250$ (solid squares and circles) are also plotted. From [121].

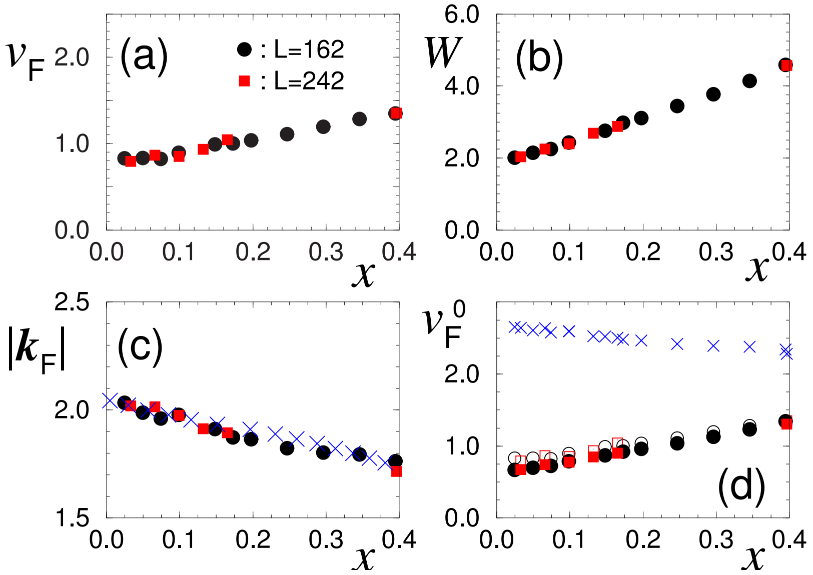

Figure 7.5: (a) Nodal Fermi velocity v_{F}, (b) bandwidth W, (c) nodal Fermi momentum $|\mathbf{k}_{\mathrm{F}}|$, and (d) unrenormalized Fermi velocity v_{F}^0 (crosses) compared to v_F for the 2D t-J model with J/t=0.3 and t'/t=−0.2 at different x. From [121].

spectral function ([128], section 5.3), as well as with ARPES experiments [27, 131, 132, 133, 134]. In figure 7.5(c), we see the doping dependence of the nodal Fermi point $|\mathbf{k}_F|$, which matches experimental and RMFT predictions. The renormalized band width W is given in figure 7.5(b); it is tightly related to v_F. Figure 7.5(d) illustrates a comparison between the Fermi velocity v_F and the unrenormalized velocity v_F^0, revealing the strong renormalization effects due to the Gutzwiller projection. However, it is important to note that, in contrast to the QP weight $\tilde{Z}_{\mathbf{k}}$, the Fermi velocity does not vanish in the half-filled limit

While Yunoki *et al.* [121] only considers the nodal dispersion, Yunoki recently extended these VMC calculations to the whole Brillouin zone [200]. His results fit quite well to the RMFT dispersion, giving further support for the Gutzwiller-Bogoliubov QP picture. In conclusion, above VMC calculations for the spectral weight and the QP excitations, yield a good qualitative agreement with RMFT. Two key features emerge consistently from these two approaches; a finite and constant Fermi velocity contrasting with a vanishing QP weight in the half-filled limit. In the underdoped regime some discrepancies for the QP weights show up as discussed in the previous section.

Chapter 8

Summary and outlook

In this thesis we have summarized a large number of studies, which view Gutzwiller projected wave functions as an appropriate way to describe high temperature superconductivity in the Cuprates. We have shown that projected wave functions provide a straightforward implementation of the RVB picture and describe many key features of the high temperature superconductors.

Numerical and analytical calculations within this Gutzwiller-RVB theory successfully explain a superconducting state with d-wave pairing symmetry. Incorporation of antiferromagnetic order and next-nearest neighbor hopping then allows for a quantitative description of the Cuprate phase diagram within the t-J and the Hubbard model. Sophisticated variational Monte Carlo calculations (VMC) give detailed information about the size of the antiferromagnetic region and the stability against phase separation. These ground state properties seen in the VMC technique were recently confirmed by various quantum cluster methods, giving further support to the Gutzwiller-RVB picture.

Besides the VMC technique, the effect of projection can be treated by Gutzwiller approximation, which then allows for a formulation of a renormalized mean field theory (RMFT). The RMFT results agree in general with VMC calculations and provide systematic analytic expressions for doping-dependent features.

Within the Gutzwiller-RVB picture, high temperature superconductors are viewed as doped Mott insulators, *i.e.*, restriction to single occupied orbitals due to strong correlation effects. That causes a significant decrease in the mobility of electrons (holes) near half-filling as correctly described within above microscopic calculations. The resulting renormalization of the kinetic energy explains the decrease of the superconducting order parameter, of the superfluid density, and of the Drude weight when approaching half-filling. RMFT and VMC calculations also explain the large superconducting gap and the small quasiparticle weight in the underdoped Cuprates. Further, the modeling of charge ordered states, impurity sites, or vortex cores qualitative agrees with experiments.

While the quasiparticle weight Z vanishes in the half-filled limit, the nodal Fermi velocity v_F stays finite. We have shown that RMFT and VMC calculations explain this interesting experimental observation by effects of the superexchange interaction on the dispersion. However, in the half-filled limit, such a behavior ($Z \to 0$ and $v_F = \text{const}$) immediately results in a divergence of the ω- as well as of the $\mathbf{k}$-dependence of the self-energy.

The consequences of these divergences for any Fermi liquid description at finite doping are still controversial. While some authors think Gutzwiller projected superconductors can be classified within Landau theory as BCS liquids, Anderson suggested in a recent work [231] that projected wave functions contain the essential physics to explain the non-Fermi liquid behavior of the strange metal normal state.

Apart form the successes of Gutzwiller-RVB theory, the driving mechanism in destroying superconductivity in the underdoped regime is still an open question. Within Gutzwiller-RVB theory it is often argued that phase fluctuations suppress superconductivity and result a pseudogap regime at low doping concentrations. However also other mechanisms like the destruction of the superfluid density by nodal excitations or the appearance of phase separation could, in principle, be consistent with the Gutzwiller-RVB picture, which states that the ground state is an RVB superconductor (projected BCS superconductor) with pairing mediated by the superexchange interaction J.

Above problem is tightly connected with the nature of the pseudogap state, which we view as a precursor of superconductivity with still existing local singlet pairing. Therefore, the pseudogap is described by an RVB liquid phase, which breaks down at T^*. Much support for this idea comes from the experimental observation that the BCS ratio, $\Delta/(2k_BT^*)$, is constant and in agreement with mean field theory for all doping levels, when we use the onset temperature of the pseudogap T^* instead of T_c.

Since it is rather easy to explain T^*, the key question remains the transition from the superconducting to the pseudogap phase. Answering it would yield to a better understanding of the high temperature superconductors and could explain puzzling features such as the presence of a Nernst phase. Thus, more detailed extensions of the Gutzwiller-RVB picture to finite temperatures should be a main issue of future work.

Appendix A

Deutsche Zusammenfassung

Diese Arbeit behandelt die Theorie der Hochtemperatursupraleitung vom Gesichtspunkt stark korrelierter Elektronensysteme. Im Speziellen werden Gutzwiller projizierte Wellenfunktionen diskutiert. Die dabei verwendete Gutzwiller-Projektion eliminiert Doppelbesetzungen in Orbitalen mit starker lokaler Abstoßung und ermöglicht dadurch die Behandlung starker Elektron-Korrelationen.

Nach einem allgemeinen Überblick über die Hochtemperatursupraleitung diskutieren wir Andersons "Resonating Valence Bond" (RVB)-Bild und seine Implementierung mittels renormierter Molekularfeld-Theorie (RMFT) und variationellem Monte Carlo (VMC). Es wird dabei ein detaillierter Überblick über die RMFT and das VMC gegeben, wobei der Schwerpunkt bei unseren kürzlich veröffentlichten Beiträgen [5, 6, 7, 8, 9, 10] liegt. Die dabei diskutierten Berechnungen basieren großteils auf dem zweidimensionalen Hubbard und t-J Modell.

In unseren theoretischen Betrachtungen interessieren wir uns vor allem für spektrale Eigenschaften von Gutzwiller-Bogoliubov Quasiteilchen, die über die Konstruktion von angeregten Zuständen durch VMC and RMFT Techniken behandelt werden können. Wir illustrieren wie sich mit Hilfe dieser Methoden das Anregungsspektrum und das dazugehörende Quasiteilchen-Gewicht bestimmen lässt. Die daraus gewonnen theoretischen Ergebnisse stimmen sehr gut mit experimentellen Daten aus winkelaufgelöster Photoemissionsspektroskopie (ARPES) und Rastertunnelmikroskopie (STM) überein und zeigen, dass Gutzwiller projizierte Wellefunktionen einen vielversprechenden Ansatz zur Beschreibung der Hochtemperatursupraleitung in den Cuprate-Verbindungen liefern.

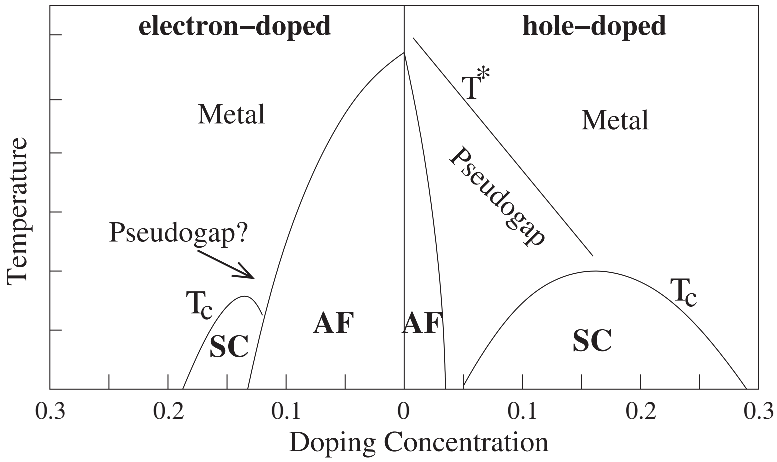

Figure A.1: Allgemeines Phasendiagramm für die Cuprate-Hochtemperatursupraleiter (antiferromagnetischer Bereich AF, supraleitender Bereich SC). Die Temperatur unter welcher die Supraleitung (der Pseudogap) beobachtet wird, ist durch T_c (T^*) gekennzeichnet.

Im Folgenden fassen wir die einzelnen Kapitel dieser Arbeit kurz zusammen und geben damit einen Einblick in die jeweiligen Schwerpunkte und Ergebnisse.

In der Einleitung (Kapitel 1) begründen wir das Dissertationsthema und diskutieren grundlegende Ergebnisse aus dem Gebiet der Hochtemperatursupraleitung. Wir erläutern die Kristallstruktur der Cuprate, die im Allgemeinen aus zweidimensionalen Kupfer-Oxid Ebenen besteht und betrachten das Temperatur-Dotierung Phasendiagram (Figure A.1). Wie in Figure A.1 dargestellt, können in den Cuprate-Verbindungen bei geeigneter Dotierung und Temperatur neben der Supraleitung weitere interessante Phasen auftreten. Die undotierte Verbindung ist bis ungefähr 300 Kelvin ein antiferromagnetischer Mott-Hubbard Isolator. Bei Dotierung mit Löchern oder Elektronen kommt es bei tiefen Temperaturen zur Supraleitung. Im unterdotieren Bereich (weniger als optimale Dotierung) kann auch ein so genannter Pseudogap auftreten, der nicht supraleitend ist, jedoch (zumindest in einem gewissen Teil der Brillouin-Zone) eine Anregungslücke besitzt. Der Zusammenhang des Pseudogaps mit der Supraleitung ist noch relativ umstritten weshalb wir im Laufe der Arbeit einige Male näher darauf eingehen.

In der Einleitung werden weiters experimentelle Ergebnisse für die unterschiedlichen Bereiche des Phasendiagramms diskutiert, wobei wir uns wegen der Relevanz für die späteren theoretischen Betrachtungen vor allem auf ARPES und STM Resultate konzentrieren. Am Ende der Einleitung werden auch alternative theoretische Ansätze abseits der Gutzwiller-RVB Theorie kurz diskutiert, um die Komplexität und Vielfältigkeit des Gebietes aufzuzeigen.

Kapitel 2 widmet sich den Grundlagen der RVB Theorie [45], in der angenommen wird, dass der Grundzustand der Hochtemperatursupraleiter als eine Flüssigkeit aus Spin-Singlets betrachtet werden kann. Dieser Zustand wird auch RVB Zustand genannt und gibt eine sehr gute variationelle Energie für das zweidimensionale Heisenberg Modell. Durch das Dotieren einer halbgefüllten nichtleitenden Spin-Singlet-Flüssigkeit kann ein supraleitender RVB Zustand entstehen. Die grundlegende Idee hinter diesem Mechanismus ist, dass die magnetischen Paare bei endlicher Dotierung beweglich werden und somit geladene supraleitende Paare formen.

In Kapitel 2 diskutieren wir auch mögliche Umsetzungen eines RVB Zustandes in Festkörpern. Abseits der Hochtemperatursupraleiter könnte dieser Zustand für Supraleitung in den Cobaltaten und in einigen organischen Verbindungen von Relevanz sein. Es ist jedoch wichtig zu erwähnen, dass der RVB Zustand im halbgefüllten Hubbard Modell gegenüber Antiferromagnetismus, Inhomogenitäten und/oder “Valence Bond crystals” instabil ist. Diese Instabilitäten können aber bei endlicher Dotierung überwunden werden und ein supraleitender RVB Grundzustand kann sich ausbilden.

Die Gutzwiller-Näherung wird in Kapitel 3 behandelt. Es handelt sich dabei um ein geradliniges Verfahren zum Auswerten von Erwartungswerten in Gutzwiller projizierten Wellenfunktionen. Dabei werden die Effekte der Gutzwiller-Projektion durch einen statistischen Gewichtsfaktor absorbiert, was eine analytische Behandlung von stark korrelierten Wellenfunktionen ermöglicht.

Die Ableitung der Gutzwiller-Gewichtsfaktor (Renormierungsfaktoren) kann durch Hilbert-Raum Zählargumente beziehungsweise durch Betrachtung des Limes unendlicher Dimension erfolgen. Neben diesen zwei grundlegenden Ansätzen zur Gutzwiller-Näherung, konzentrieren wir uns in Kapitel 3 vor allem auf die Erweiterungen, die wir in den Arbeiten *“Particle number renormalization in nearly half filled Mott Hubbard superconductors”* [5] und *“Evaluation of matrix elements in partially projected wave functions”* [6] eingeführt haben. Erstere [5] behandelt die Unterschiede zwischen den Gutzwiller-Näherungen in kanonischen und groß-kanonischen Ensembles. Diese Unterschiede werden auch durch den Vergleich mit VMC Daten bestätigt. Die zweite Arbeit [6] beinhaltet eine Erweiterung der Gutzwiller-Näherung auf teilweise projizierte Wellenfunktionen, in denen ein so genannter Reservoir-Gitterplatz von der Gutzwiller-Projektion ausgenommen ist. Diese Art der Gutzwiller-Näherung wird bei Berechnungen für Gutzwiller-Bogoliubov Qua-

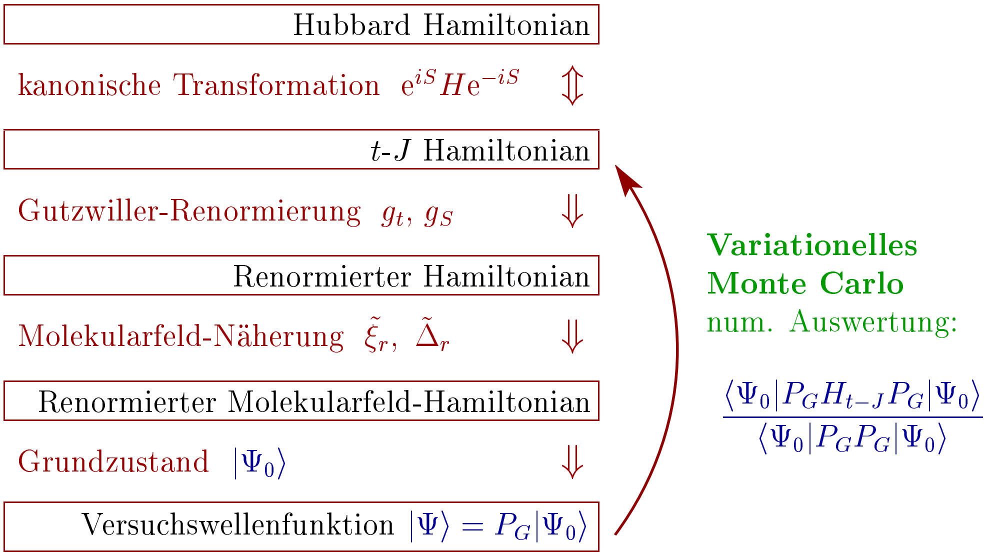
Hubbard Hamiltonian
kanonische Transformation $e^{iS}He^{-iS}$ $\Updownarrow$
t-J Hamiltonian
Gutzwiller-Renormierung g_t, g_S $\Downarrow$
Renormierter Hamiltonian
Molekularfeld-Näherung $\tilde{\xi}_r$, $\tilde{\Delta}_r$ $\Downarrow$
Renormierter Molekularfeld-Hamiltonian
Grundzustand $|\Psi_0\rangle$ $\Downarrow$
Versuchswellenfunktion $|\Psi\rangle = P_G|\Psi_0\rangle$
Variationelles
Monte Carlo
num. Auswertung:
$\frac{\langle\Psi_0|P_G H_{t-J} P_G|\Psi_0\rangle}{\langle\Psi_0|P_G P_G|\Psi_0\rangle}$

Figure A.2: Schematische Darstellung der RMFT Methode. Die dargestellten Schritte umfassen die kanonische Transformation vom Hubbard zum t-J Modell, die Gutzwiller-Renormierung mit dem Einführen von Renormierungsfaktoren g_t (für die kinetische Energie) und g_S (für den Superaustauch-Term), die Molekularfeld-Näherung für den renormierten Hamiltonian, sowie das Ableiten eines Grundzustandes $|\Psi_0\rangle$, der dann für eine projizierte Versuchswellenfunktion $|\Psi\rangle = P_G|\Psi_0\rangle$ in der numerischen Auswertung mittels variationellen Monte Carlo genutzt werden kann.

siteilchenanregungen notwendig, da in diesem Fall teilweise projizierte Wellenfunktionen durch das Vertauschen der Elektronoperatoren mit dem Gutzwiller-Projektionsoperator auftreten können. Eine solche Gutzwiller-Näherung wird in Kapitel 6 verwendet.

Auf der Basis der Gutzwiller-Näherung (auch Gutzwiller-Renormierung genannt) lässt sich eine renormierte Molekularfeldtheorie (RMFT) für das t-J Modell [76] entwickeln. In Kapitel 4 präsentieren wir einen Überblick über diesen Ansatz, der eine zentrale Rolle in der Gutzwiller-RVB Theorie der Hochtemperatursupraleitung spielt. Die wesentlichen Schritte der RMFT Methode, die in Übereinstimmung mit experimentellen Beobachtungen in den Hochtemperatursupraleitern einen d-Wellen Grundzustand liefert, sind in Figure A.2 kurz zusammengefasst und werden in Kapitel 4 im Detail diskutiert.

Weiters betrachten wir in Kapitel 4 Erfolge und wichtige Ergänzungen der RMFT. Dabei basiert ein wichtiger Teil auf unserer Arbeit, Edegger, *et al.*

[7], in der die RMFT für das Hubbard Modell verwendet wird.

In Kapitel 5 wird die variationelle Monte Carlo (VMC) Technik, die eine genaue Auswertung von Erwartungswerten in Gutzwiller projizierten Wellenfunktionen ermöglicht, behandelt. Wir erläutern technische Details zu dieser Methode und zeigen wie VMC für die variationelle Suche eines Grundzustand im zweidimensionalen Hubbard und t-J Modell eingesetzt werden kann. Wir diskutieren die Verbesserung der Versuchswellenfunktion durch den Einbau neuer Ordnungen, z.B. Antiferromagnetismus oder Fluss-Zustände, sowie auch durch die Verwendung von Jastrow-Faktoren. Desweiteren betrachten wir dotierungsabhängige spektrale Eigenschaften projizierter Wellenfunktionen, die sehr gut mit den experimentellen Ergebnissen für die Cuprate-Hochtemperatursupraleiter übereinstimmen. Am Ende des Kapitels 5 diskutieren wir unsere numerische Studie, Edegger, *et al.* [8], die auf eine mögliche spontane Brechung der Fermiflächen-Symmetrie im isotropen zweidimensionalen t-J Modell hinweist.

Die Erweiterung der RMFT auf angeregte Zustände verlangt die Betrachtung von Gutzwiller-Bogoliubov Quasiteilchen innerhalb des t-J und Hubbard Modells. Wie in Kapitel 6 geschildert, ermöglichen Gutzwiller-Bogoliubov Anregungen eine systematische Analyse (siehe auch Edegger, *et al.* [7]) der Einteilchen-Spektralfunktion und erklären die impuls- und dotierungsabhängigen Eigenschaften in ARPES und STM Experimenten. Abseits dieser Schlüsselresultate diskutieren wir die Renormierung des von Quasiteilchen transportierten Stroms und die Konsequenz für die Unterdrückung der "superfluid density". Als eine Anwendung obiger Quasiteilchenstudien folgen wir Gros, *et al.* [9] und bestimmen die Fermifläche in einem d-Wellen Grundzustand.

In Kapitel 7 werden die RMFT Ergebnisse für die Quasiteilchen-Eigenschaften mit VMC Daten verglichen. Abgesehen von kleineren Abweichungen in der detaillierten Dotierungs- und Impulsabhängigkeit zeigen die beiden Methoden gute Übereinstimmung. Dabei treten zwei Hauptergebnisse konsistent in den RMFT und VMC Rechnungen auf; eine konstante Fermi-Geschwindigkeit aber ein verschwindendes Quasiteilchengewicht bei Annäherung an Halbfüllung. Dieses Verhalten, das mit den experimentellen Beobachtungen in den Cupraten übereinstimmt, bewirkt Divergenzen in der Impuls- wie auch der Energieabhängigkeit der Einteilchen-Selbstenergie. Das natürliche Auftreten dieser Divergenzen überschreitet eine normale Fermi-Flüssigkeit Beschreibung und unterstützt die hier diskutierte Gutzwiller-RVB Theorie.

Das letzte Kapitel der Doktorarbeit fasst die Schlüsselergebnisse zusammen und gibt einen kurzen Ausblick auf zukünftige Forschungsfragen. Es wird aufgezeigt, dass die in dieser Arbeit betrachtete Gutzwiller-RVB Theorie viele experimentelle Ergebnisse für die Hochtemperatursupraleiter richtig beschreibt. Als eine offene Frage für die Zukunft wird die systematische Erweiterung der Gutzwiller-RVB Theorie auf endliche Temperaturen angesprochen.

Bibliography

[1] J.G. Bednorz and K.A. Müller, Z. Phys. **64**, 189 (1986).

[2] M.R. Norman and C. Pepin, Rep. Prog. Phys. **66**, 1547 (2003).

[3] C.C. Tsuei and J.R. Kirtley, Rev. Mod. Phys. **72**, 969 (2000).

[4] D.J. Scalapino, cond-mat/0610710 (unpublished).

[5] B. Edegger, N. Fukushima, C. Gros, and V.N. Muthukumar, Phys. Rev. B **72**, 134504 (2005).

[6] N. Fukushima, B. Edegger, V.N. Muthukumar, and C. Gros, Phys. Rev. B **72**, 144505 (2005).

[7] B. Edegger, V.N. Muthukumar, C. Gros, and P.W. Anderson, Phys. Rev. Lett. **96**, 207002 (2006).

[8] B. Edegger, V.N. Muthukumar, C. Gros, Phys. Rev. B **74**, 165109 (2006).

[9] C. Gros, B. Edegger, V. N. Muthukumar, and P. W. Anderson, PNAS **103**, 14298 (2006).

[10] B. Edegger, V.N. Muthukumar, and C. Gros, Physica C, to be published.

[11] P.A. Lee, N. Nagaosa, and X.-G. Wen, Rev. Mod. Phys. **78**, 17 (2006).

[12] M.R. Norman, D.P. Pines, and C. Kallin, Adv. Phys. **54**, 715 (2005).

[13] A. Damascelli, Z. Hussain, and Z.-X. Shen, Rev. Mod. Phys. **75**, 473 (2003).

[14] J.C. Campuzano, M.R. Norman, and M. Randeria, in *Physics of Conventional and Unconventional Superconductors*, (Springer Verlag 2004); cond-mat/0209476.

[15] F.C. Zhang and T. Rice, Phys. Rev. B **37**, 3759 (1988).

[16] N.P. Ong, Y. Wang, S. Ono, Y. Ando, and S. Uchida, Ann. Phys. **13**, 9 (2004).

[17] Y. Wang, S. Ono, Y. Onose, G. Gu, Y. Ando, Y. Tokura, S. Uchida, and N.P. Ong, Science **299**, 86 (2003).

[18] S.A. Kivelson, E. Fradkin, V. Oganesyan, I.P. Bindloss, J.M. Tranquada, A. Kapitulnik, and C. Howald, Rev. Mod. Phys. **75**, 1201 (2003).

[19] J.M. Tranquada, to appear as a chapter in "Treatise of High Temperature Superconductivity" by J. Robert Schrieffer; cond-mat/0512115.

[20] C.M. Varma , P.B. Littlewood , S. Schmitt-Rink, E. Abrahams, and A.E. Ruckentstein, Phys. Rev. Lett. **63** 1996 (1989).

[21] E. Dagotto, Science **309**, 257 (2005).

[22] J. Mesot, M.R. Norman, H. Ding, M. Randeria, J.C. Campuzano, A. Paramekanti, H.M. Fretwell, A. Kaminski, T. Takeuchi, T. Yokoya, T. Sato, T. Takahashi, T. Mochiku, and K. Kadowaki, Phys. Rev. Lett. **83**, 840 (1999).

[23] J. C. Campuzano, H. Ding, M.R. Norman, H.M. Fretwell, M. Randeria, A. Kaminski, J. Mesot, T. Takeuchi, T. Sato, T. Yokoya, T. Takahashi, T. Mochiku, K. Kadowaki, P. Guptasarma, D.G. Hinks, Z. Konstantinovic, Z.Z. Li, and H. Raffy, Phys. Rev. Lett. **83**, 3709 (1999).

[24] H. Won and K. Maki, Phys. Rev. B **49**, 1397 (1994).

[25] M. Kugler, O. Fischer, Ch. Renner, S. Ono, and Y. Ando, Phys. Rev. Lett. **86**, 4911 (2001).

[26] D.L. Feng, D.H. Lu, K.M. Shen, C. Kim, H. Eisaki, A. Damascelli, R. Yoshizaki, J.-i. Shimoyama, K. Kishio, G.D. Gu, S. Oh, A. Andrus, J. O'Donnell, J.N. Eckstein, and Z.-X. Shen, Science **289** 277 (2000).

[27] X.J. Zhou, T. Yoshida, A. Lanzara, P. V. Bogdanov, S.A. Kellar, K.M. Shen, W.L. Yang, F. Ronning, T. Sasagawa, T. Kakeshita, T. Noda, H. Eisaki, S. Uchida, C.T. Lin, F. Zhou, J.W. Xiong, W.X. Ti, Z.X. Zhao, A. Fujimori, Z. Hussain, and Z.-X. Shen, Nature **423**, 398 (2003).

[28] M. Chiao, R.W. Hill, C. Lupien, L. Taillefer, P. Lambert, R. Gagnon, and P. Fournier, Phys. Rev. B **62**, 3554 (2000).

[29] A.G. Loeser, Z.-X. Shen, D.S. Dessau, D.S. Marshall, C.H. Park, P. Fournier, and A. Kapitulnik, Science **273**, 325 (1996).

[30] D.S. Marshall, D.S. Dessau, A.G. Loeser, C-H. Park, A.Y. Matsuura, J.N. Eckstein, I. Bozovic, P. Fournier, A. Kapitulnik, W.E. Spicer, and Z.-X. Shen, Phys. Rev. Lett. **76**, 4841 (1996).

[31] M.R. Norman, H. Ding, M. Randeria, J. C. Campuzano, T. Yokoya, T. Takeuchi, T. Takahashi,T. Mochiku, K. Kadowaki, P. Guptasarma, and D.G. Hinks, Nature **392**, 157 (1998).

[32] A. Kanigel, M.R. Norman, M. Randeria, U. Chatterjee, S. Suoma, A. Kaminski, H. M. Fretwell, S. Rosenkranz, M. Shi, T. Sato, T. Takahashi, Z.Z. Li, H. Raffy, K. Kadowaki, D. Hinks, L. Ozyuzer, and J.C. Campuzano, Nature Physics **2**, 447 (2006).

[33] E.W. Hudson, S.H. Pan, A.K. Gupta, K.-W. Ng, J.C. Davis, Science **285**, 88 (1999).

[34] A. Yazdani, C.M. Howald, C.P. Lutz, A. Kapitulnik, and D. M. Eigler, Phys. Rev. Lett. **83**, 176 (1999).

[35] S.H. Pan, E.W. Hudson, K.M. Lang, H. Eisaki, S. Uchida, and J.C. Davis, Nature **403**, 746 (2003).

[36] I. Maggio-Aprile, Ch. Renner, A. Erb, E. Walker, and Ø. Fischer, Phys. Rev. Lett. **75**, 2754 (1995).

[37] Ch. Renner, B. Revaz, K. Kadowaki, I. Maggio-Aprile, and Ø. Fischer, Phys. Rev. Lett. **80**, 3606 (1998).

[38] S.H. Pan, E.W. Hudson, A.K. Gupta, K.-W. Ng, H. Eisaki, S. Uchida, and J.C. Davis, Phys. Rev. Lett. **85**, 1536 (2000).

[39] M. Vershinin, S. Misra, S. Ono, Y. Abe, Y. Ando, and A. Yazdani, Science **303**, 1995 (2004).

[40] T. Hanaguri, C. Lupien, Y. Kohsaka, D.-H. Lee, M. Azuma, M. Takano, H. Takagi, and J.C. Davis, Nature **430**, 1001 (2004).

[41] K. McElroy, D.-H. Lee, J.E. Hoffman, K.M. Lang, J. Lee, E.W. Hudson, H. Eisaki, S. Uchida, and J.C. Davis, Phys. Rev. Lett. **94**, 197005 (2005).

[42] V.J. Emery, Phys. Rev. Lett. **58**, 3759 (1987).

[43] C.M. Varma, S. Schmitt-Rink, and E. Abrahams, Solid State Commun. **62**, 681 (1987).

[44] E. Dagotto, Rev. Mod. Phys. **66**, 763 (1994).

[45] P.W. Anderson, Science **235**, 1196 (1987).

[46] T. Moriya and K. Ueda, Adv. Phys. **49**, 555 (2000).

[47] Y. Yanase, T. Jujo, T. Nomura, H. Ikeda, T. Hotta, and K. Yamada, Phys. Rep. **387**, 1 (2003).

[48] A.V. Chubukov, D. Pines, and J. Schmalian, in "The Physics of Conventional and Unconventional Superconductors" edited by K.H. Bennemann and J.B. Ketterson; cond-mat/0201140 (2002).

[49] S.A. Kivelson and E. Fradkin, to appear as a chapter in "Treatise of High Temperature Superconductivity" by J. Robert Schrieffer; cond-mat/0507459.

[50] E.W. Carlson, V.J. Emery, S.A. Kivelson, and D. Orgad, in "The Physics of Conventional and Unconventional Superconductors", edited by K.H. Bennemann and J.B. Ketterson; cond-mat/0206217 (2002).

[51] E. Demler, W. Hanke, and S.-C. Zhang, Rev. Mod. Phys. **76**, 909 (2004).

[52] T. Maier, M. Jarrell, T. Pruschke, and M.H. Hettler, Rev. Mod. Phys. **77**, 1027 (2005).

[53] C.M. Varma, Phys. Rev. B **73**, 155113 (2006).

[54] S. Chakravarty, R.B. Laughlin, D.K. Morr, and C. Nayak, Phys. Rev. B **63**, 094503 (2001).

[55] Q. Chen, J. Stajic, S. Tan, and K. Levin, Phys. Rep. **412**, 1 (2005).

[56] Y. Endoh, K. Yamada, R.J. Birgeneau, D.R. Gabbe, H.P. Jenssen, M.A. Kastner, C.J. Peters, P.J. Picone, T.R. Thurston, J.M. Tranquada, G. Shirane, Y. Hidaka, M. Oda, Y. Enomoto, M. Suzuki, and T. Murakami, Phys. Rev. B **37**, 7443 (1988).

[57] S. Chakravarty, B.I. Halperin, and D.R. Nelson, Phys. Rev. B **39**, 2344 (1989).

[58] P.W. Anderson, Mat. Res. Bull **8**, 153 (1973).

[59] P. Fazekas and P.W. Anderson, Philos. Mag. **30**, 432 (1974).

[60] S. Liang, B. Doucot, and P. W. Anderson, Phys. Rev. Lett. **61**, 365 (1988).

[61] C.L. Kane, P.A. Lee, and N. Read, Phys. Rev. B **39**, 6880 (1989).

[62] C. Gros and M.D. Johnson Phys. Rev. B **40**, 9423 (1989).

[63] P.W. Anderson, Physica B **318**, 28 (2002).

[64] M.E. Zhitomirsky and K. Ueda, Phys. Rev. B **54**, 9007 (1996).

[65] L. Capriotti and S. Sorella, Phys. Rev. Lett. **84**, 3173 (2000).

[66] K. Takano, Y. Kito, Y. Ono, and K. Sano, Phys. Rev. Lett. **91**, 197202 (2003).

[67] L. Capriotti, F. Becca, A. Parola, and S. Sorella, Phys. Rev. Lett. **87**, 097201 (2001).

[68] M. Mambrini, A. Laeuchli, D. Poilblanc, and F. Mila, Phys. Rev. B **74**, 144422 (2006).

[69] C. Weber, A. Laeuchli, F. Mila, T. Giamarchi, Phys. Rev. B **73**, 014519 (2006).

[70] G. Baskaran, Phys. Rev. Lett. **91**, 097003 (2003).

[71] B. Kumar and B.S. Shastry, Phys. Rev. B **68**, 104508 (2003).

[72] M. Ogata, J. Phys. Soc. Jpn. **72**, 1839 (2003).

[73] B.J. Powell, R.H. McKenzie, Phys. Rev. Lett. **94**, 047004 (2005).

[74] J.Y. Gan, Y. Chen, Z.B. Su, and F.C. Zhang, Phys. Rev. Lett. **94**, 067005 (2005).

[75] J. Liu, J. Schmalian, and N. Trivedi, Phys. Rev. Lett. **94**, 127003 (2005).

[76] F.C. Zhang, C. Gros, T. M. Rice, and H. Shiba, Supercond. Sci. Tech. **1**, 36 (1988); also available ascond-mat/0311604.

[77] G. Kotliar and J. Liu, Phys. Rev. B **38**, 5142 (1988).

[78] Y. Suzumura, Y. Hasegawa, and H. Fukuyama, J. Phys. Soc. Jpn. **57**, 2768 (1988).

[79] C. Gros, Phys. Rev. B **38**, 931 (1988).

[80] H. Yokoyama and H. Shiba, J. Phys. Soc. Jpn **57**, 2482 (1988).

[81] P.W. Anderson, cond-mat/0406038 (unpublished).

[82] H.-X. Huang, Y.-Q. Li, F.-C. Zhang, Phys. Rev. B **71**, 184514 (2005).

[83] D. Poilblanc, Phys. Rev. B **72**, 060508 (R) (2005).

[84] C. Li, S. Zhou, Z. Wang, Phys. Rev. B **73**, 060501(R) (2006).

[85] A. Himeda and M. Ogata, Phys. Rev. B **60**, R9935 (1999).

[86] G.J. Chen, R. Joynt, F.C. Zhang, and G. Gros, Phys. Rev. B **42**, 2662 (1990).

[87] T. Giamarchi and C. Lhuillier, **43**, 12943 (1991).

[88] D.A. Ivanov, Phys. Rev. B **70**, 104503 (2004).

[89] C.T. Shih, Y.C. Chen, C.P. Chou, and T.K. Lee, Phys. Rev. B **70**, 220502(R) (2004).

[90] M. Ogata and A. Himeda, J. Phys. Soc. Jpn. **72**, 374 (2003).

[91] H. Tsuchiura, Y. Tanaka, M. Ogata, and S. Kashiwaya, J. Phys. Soc. Jpn. **68**, 2510 (1999).

[92] H. Tsuchiura, Y. Tanaka, M. Ogata, and S. Kashiwaya, Phys. Rev. Lett. **84**, 3165 (2000).

[93] H. Tsuchiura, Y. Tanaka, M. Ogata, and S. Kashiwaya Phys. Rev. B **64**, 140501 (2001).

[94] A. Himeda, M. Ogata, Y. Tanaka, and S. Kashiwaya, J. Phys. Soc. Jpn. **66**, 3367 (1997).

[95] H. Tsuchiura, M. Ogata, Y. Tanaka, and S. Kashiwaya, Phys. Rev. B **68**, 012509 (2003).

[96] P.W. Anderson, Phys. Rev. Lett. **96**, 017001 (2005).

[97] V.J. Emery and S.A. Kivelson, Nature **374**, 434 (1995).

[98] C. Gros, R. Joynt, and T.M. Rice, Phys. Rev. B **36**, 381 (1987).

[99] A. Paramekanti, M. Randeria, and N. Trivedi, Phys. Rev. B **70**, 054504 (2004).

[100] M.C. Gutzwiller, Phys. Rev. Lett. **10**, 159 (1963).

[101] W.F. Brinkman and T.M. Rice, Phys. Rev. B **2**, 4302 (1970).

[102] D. Vollhardt, Rev. Mod. Phys. **56**, 99 (1984).

[103] K. Seiler, C. Gros, T.M. Rice, K. Ueda, and D. Vollhardt, J. Low. Temp. Phys. **64**, 195 (1986).

[104] T. Ogawa, K. Kanda, and T. Matsubara, Prog. Theor. Phys. **53**, 614 (1975).

[105] W. Metzner and D. Vollhardt, Phys. Rev. B **37**, 7382 (1988).

[106] F. Gebhard, Phys. Rev. B **41**, 9452 (1990).

[107] J. Bünemann, F. Gebhard, K. Radnoczi, and P. Fazekas, J. Phys. Condens. Matter **17** 3807 (2005).

[108] J. Bünemann, F. Gebhard, T. Ohm, S. Weiser, and W. Weber, "Frontiers in Magnetic Materials", ed. A. Narlikar, Springer (2005); cond-mat/0503332.

[109] S.E. Barnes, J. Phys. F **6**, 1375 (1976).

[110] P. Coleman, Phys. Rev. B **29**, 3035 (1984).

[111] G. Kotliar and A.E. Ruckenstein, Phys. Rev. Lett. **57**, 1362 (1986).

[112] G. Baskaran, Z. Zou, and P. W. Anderson, Solid State Commun. **63**, 973 (1987).

[113] M. Capello, F. Becca, M. Fabrizio, S. Sorella, and E. Tosatti, Phys. Rev. Lett. **94**, 026406 (2005).

[114] T. Watanabe, H. Yokoyama, Y.Tanaka, and J. Inoue, J. Phys. Soc. Jpn **75**, 074707, (2006).

[115] C.S. Hellberg and E.J. Mele, Phys. Rev. Lett. **67**, 2080 (1991).

[116] R. Valenti and C. Gros, Phys. Rev. Lett. **68**, 2402 (1992).

[117] D.A. Ivanov and P.A. Lee, Phys. Rev. B **68**, 132501 (2003).

[118] Y. Ran, M. Hermele, P.A. Lee, and X.-G. Wen, cond-mat/0611414 (unpublished)

[119] R. Jastrow, Phys. Rev. 98, 1479 (1955).

[120] S. Sorella, G.B. Martins, F. Becca, C. Gazza, L. Capriotti, A. Parola, and E. Dagotto, Phys. Rev. Lett. **88**, 117002 (2002).

[121] S. Yunoki, E. Dagotto, and S. Sorella, Phys. Rev. Lett. **94**, 037001 (2005).

[122] C. Gros, Ann. Phys. **189**, 53 (1989).

[123] M. Lugas, L. Spanu, F. Becca, and S. Sorella, Phys. Rev. B **74**, 165122 (2006).

[124] D. Vollhardt, P. Wölfle, and P.W. Anderson, Phys. Rev. B **35**, 6703 (1987).

[125] T.M. Rice and K. Ueda, Phys. Rev. Lett. **55**, 995 (1985).

[126] C.M. Varma, W. Weber, and L.J. Randall, Phys. Rev. B **33**, 1015 (1986).

[127] P. W. Anderson and N. P. Ong, cond-mat/0405518 (unpublished).

[128] A. Paramekanti, M. Randeria, and N. Trivedi, Phys. Rev. Lett. **87**, 217002 (2001).

[129] I. Affleck, Z. Zou, T. Hsu, and P.W. Anderson, Phys. Rev. B. **38**, 745 (1988).

[130] P.W. Anderson, J. Phys. Chem. Solids **63**, 2145 (2002).

[131] S.V. Borisenko, A.A. Kordyuk, V. Zabolotnyy, J. Geck, D. Inosov, A. Koitzsch, J. Fink, M. Knupfer, B. Büchner, V. Hinkov, C.T. Lin, B. Keimer, T. Wolf, S.G. Chiuzbaian, L. Patthey, and R. Follath, Phys. Rev. Lett. **96**, 117004 (2006).

[132] A.A. Kordyuk, S.V. Borisenko, A. Koitzsch, J. Fink, M. Knupfer, and H. Berger, Phys. Rev. B **71**, 214513 (2005); A.A. Kordyuk, private communication.

[133] P.V. Bogdanov, A. Lanzara, S.A. Kellar, X.J. Zhou, E.D. Lu, W.J. Zheng, G. Gu, J.-I. Shimoyama, K. Kishio, H. Ikeda, R. Yoshizaki, Z. Hussain, and Z. X. Shen, Phys. Rev. Lett. **85**, 2581 (2000).

[134] P.D. Johnson, T. Valla, A.V. Fedorov, Z. Yusof, B.O. Wells, Q. Li, A.R. Moodenbaugh, G.D. Gu, N. Koshizuka, C. Kendziora, Sha Jian, and D.G. Hinks, Phys. Rev. Lett. **87**, 177007 (2001).

[135] D. Senechal, P.L. Lavertu, M.A. Marois, and A.M.S. Tremblay, Phys. Rev. Lett. **94**, 156404 (2005).

[136] M. Aichhorn and E. Arrigoni, Europhys. Lett. **71**, 117 (2005).

[137] B. Lake, G. Aeppli, K.N. Clausen, D.F. McMorrow, K. Lefmann, N.E. Hussey, N. Mangkorntong, M. Nohara, H. Takagi, T.E. Mason, and A. Schröder, Science **291**, 1759 (2001).

[138] B. Lake, H.M. Ronnow, N.B. Christensen, G. Aeppli, K. Lefmann, D.F. McMorrow, P. Vorderwisch, P. Smeibidl, N. Mangkorntong, T. Sasagawa, M. Nohara, H. Takagi, and T.E. Mason, Nature **415**, 299 (2002).

[139] B. Khaykovich, Y.S. Lee, R.W. Erwin, S.-H. Lee, S. Wakimoto, K.J. Thomas, M.A. Kastner, and R.J. Birgeneau, Phys. Rev. B **66**, 014528 (2002).

[140] R.I. Miller, R.F. Kiefl, J.H. Brewer, J.E. Sonier, J. Chakhalian, S. Dunsiger, G.D. Morris, A.N. Price, D.A. Bonn, W.H. Hardy, and R. Liang, Phys. Rev. Lett. **88**, 137002 (2002).

[141] V.F. Mitrovic, E.E. Sigmund, M. Eschrig, H.N. Bachman, W.P. Halperin, A.P. Reyes, P. Kuhns, and W.G. Moulton, Nature **413**, 501 (2001).

[142] K. Kakuyanagi, K.I. Kumagai, and Y. Matsuda, Phys. Rev. B **65**, 060503(R) (2002).

[143] S.-D. Liang and T.K. Lee, Phys. Rev. B **65**, 214529 (2002).

[144] Y. Tanuma, Y. Tanaka, M. Ogata, and S. Kashiwaya, J. Phys. Soc. Jpn. **67**, 1118 (1998).

[145] Y. Tanuma, Y. Tanaka, M. Ogata, and S. Kashiwaya, Phys. Rev. B **60**, 9817 (1999).

[146] F.-C. Zhang, Phys. Rev. Lett. **90**, 207002 (2003).

[147] R.B. Laughlin, cond-mat/0209269 (unpublished).

[148] J.Y. Gan, F.C. Zhang, Z.B. Su, Phys. Rev. B **71**, 014508 (2005).

[149] T.K. Kopec, Phys. Rev. B **70**, 054518 (2004).

[150] B. Normand, A.M. Oles, Phys. Rev. B **70**, 134407 (2004).

[151] F. Yuan, Q. Yuan, and C.S. Ting, Phys. Rev. B **71**, 104505 (2005).

[152] Q.-H. Wang, Z.D. Wang, Y. Chen, F.-C. Zhang, Phys. Rev. B **73**, 092507 (2006).

[153] G. Seibold and J. Lorenzana, Phys. Rev. Lett. **86**, 2605 (2001).

[154] J. Lorenzana and G. Seibold, Phys. Rev. Lett. **90**, 066404 (2003).

[155] G. Seibold, F. Becca, P. Rubin, and J. Lorenzana, Phys. Rev. B **69**, 155113 (2004).

[156] G. Seibold, J. Lorenzana, Phys. Rev. Lett. **94**, 107006 (2005).

[157] G. Seibold, J. Lorenzana, Phys. Rev. B **73**, 144515 (2006).

[158] G. Seibold, J. Lorenzana, and M. Grilli, cond-mat/0606010 (unpublished).

[159] P. Horsch and T.A. Kaplan, J. Phys. C **16**, L1203 (1983).

[160] D. Ceperley, G. V. Chester, and M.H. Kalos, Phys. Rev. B **16**, 3081 (1977).

[161] H. Yokoyama and M. Ogata, J. Phys. Soc. Jpn. **65**, 3615 (1996).

[162] N. Trivedi and D.M. Ceperly, Phys. Rev. B **41**, 4552 (1990).

[163] M.C. Buonaura and S. Sorella, Phys. Rev. B **57**, 11446 (1998).

[164] D.A. Ivanov, P.A. Lee, and X.-G. Wen, Phys. Rev. Lett. **84**, 3958 (2000).

[165] A. Himeda and H. Ogata, Phys. Rev. Lett. **85**, 4345 (2000).

[166] C.T. Shih, T.K. Lee, R. Eder, C.-Y. Mou, and Y.C. Chen, Phys. Rev. Lett. **92**, 227002 (2005).

[167] E. Pavarini, I. Dasgupta, T. Saha-Dasgupta, O. Jepsen, and O.K. Andersen, Phys. Rev. Lett 87 047003 (2001).

[168] A. Himeda, T. Kato, and M. Ogata, Phys. Rev. Lett. **88**, 117001 (2002).

[169] C. Weber, D. Poilblanc, S. Capponi, F. Mila, and C. Jaudet, cond-mat/0601301 (unpublished).

[170] C.T. Shih, Y.C. Chen, H.Q. Lin, and T.K. Lee, Phys. Rev. Lett. **81**, 1294 (1998).

[171] T.K. Lee, C.T. Shih, Y.C. Chen, and H.Q. Lin, Phys. Rev. Lett. **89**, 279702 (2002).

[172] S. Sorella, A. Parola, F. Becca, L. Capriotti, C. Gazza, E. Dagotto, and G. Martins, Phys. Rev. Lett. **89**, 279703 (2002).

[173] P.W. Anderson, P.A. Lee, M. Randeria, T.M. Rice, N. Trivedi, and F.C. Zhang, J. Phys. Condens. Matter **16**, R755 (2004).

[174] D.J. Scalapino, S.R. White, S.-C. Zhang, Phys. Rev. B **47**, 7995 (1993).

[175] A. Paramekanti, N. Trivedi and M. Randeria, Phys. Rev. B **57**, 11639 (1998).

[176] Y.J. Uemura, G.M. Luke, B.J. Sternlieb, J.H. Brewer, J.F. Carolan, W.N. Hardy, R. Kadono, J.R. Kempton, R.F. Kiefl, S.R. Kreitzman, P. Mulhern, T.M. Riseman, D.Ll. Williams, B.X. Yang, S. Uchida, H. Takagi, J. Gopalakrishnan, A.W. Sleight, M.A. Subramanian, C.L. Chien, M.Z. Cieplak, G. Xiao, V.Y. Lee, B.W. Statt, C.E. Stronach, W.J. Kossler, and X.H. Yu, Phys. Rev. Lett. **62**, 2317 (1989).

[177] H. Yamase and H. Kohno, J. Phys. Soc. Jpn. **69**, 2151 (2000).

[178] H. Yamase and H. Kohno, J. Phys. Soc. Jpn. **69**, 332 (2000).

[179] C. J. Halboth and W. Metzner, Phys. Rev. Lett. **85**, 5162 (2000).

[180] B. Valenzuela and M. A. H. Vozmediano, Phys. Rev. B **63**, 153103 (2001).

[181] I. Grote, E. Körding, and F. Wegner, J. Low Temp. Phys. **126**, 1385 (2002).

[182] C. Honerkamp, M. Salmhofer, and T. M. Rice, Eur. Phys. J. B **27**, 127 (2002).

[183] A. Neumayr and W. Metzner, Phys. Rev. B **67**, 035112 (2003).

[184] H. Yamase, Phys. Rev. Lett. **93**, 266404 (2004).

[185] A. Miyanaga and H. Yamase, Phys. Rev. B **73**, 174513 (2006).

[186] W. Metzner, D. Rohe, and S. Andergassen, Phys. Rev. Lett. **91**, 066402 (2003).

[187] I. Khavkine, C.-H. Chung, V. Oganesyan, and H.-Y. Kee, Phys. Rev. B **70**, 155110 (2004).

[188] E.C. Carter and A.J. Schofield, Phys. Rev. B **70**, 045107 (2004).

[189] H. Yamase, V. Oganesyan, and W. Metzner, Phys. Rev. B **72**, 035114 (2005).

[190] L. Dell'Anna and W. Metzner, Phys. Rev. B **73**, 045127 (2006).

[191] H. Yamase and W. Metzner, Phys. Rev. B **73**, 214517 (2006).

[192] Y.-J. Kao and H.-Y. Kee, Phys. Rev. B **72**, 24502 (2005).

[193] E.C. Carter and A.J. Schofield, Phys. Rev. B 70, 045107 (2004).

[194] M. Randeria, R. Sensarma, N. Trivedi, and F.-C. Zhang, Phys. Rev. Lett. **95**, 137001 (2005).

[195] S. Yunoki, Phys. Rev. B 72, 092505 (2005).

[196] C.P. Nave, D.A.Ivanov and P.A. Lee, Phys. Rev. B 73, 104502 (2006).

[197] H.-Y. Yang, F. Yang, Y.-J. Jiang, and T. Li, cond-mat/0604488 (unpublished).

[198] C.-P. Chou, T.K. Lee, C.-M. Ho, Phys. Rev. B 74, 092503 (2006).

[199] S. Bieri and D. Ivanov, cond-mat/0608047 (unpublished).

[200] S. Yunoki, cond-mat/0610444 (unpublished).

[201] A.B. Harris and R.V. Lange, Phys. Rev. **157**, 295 (1967).

[202] M.B.J. Meinders, H. Eskes, and G.A. Sawatzky, Phys. Rev. B **48**, 3916 (1993).

[203] H. Eskes and A. M. Oles, Phys. Rev. Lett. **73**, 1279 (1994).

[204] H. Eskes, A.M. Oles, M.B.J. Meinders, and W. Stephan, Phys. Rev. B **50**, 17980 (1994).

[205] D. Baeriswyl, C. Gros, and T.M. Rice, Phys. Rev. B **35**, 8391 (1987).

[206] J. Hubbard, Proc. Roy. Soc. London A **276**, 238 (1963).

[207] M. Randeria, A. Paramekanti, and N. Trivedi, Phys. Rev. B **69**, 144509 (2004).

[208] A. Kaminski, S. Rosenkranz, H.M. Fretwell, M.R. Norman, M. Randeria, J.C. Campuzano, J-M. Park, Z.Z. Li, and H. Raffy, Phys. Rev. B **73**, 174511 (2006).

[209] T. Yoshida, X.J. Zhou, K. Tanaka, W.L. Yang, Z. Hussain, Z.-X. Shen, A. Fujimori, S. Komiya, Y. Ando, H. Eisaki, T. Kakeshita, and S. Uchida, cond-mat/0510608 (unpublished).

[210] H. Ding, J.R. Engelbrecht, Z. Wang, J.C. Campuzano, S.-C. Wang, H.-B. Yang, R. Rogan, T. Takahashi, K. Kadowaki, and D.G. Hinks, Phys. Rev. Lett. **87**, 227001 (2001).

[211] P.A. Lee and X.-G. Wen, Phys. Rev. Lett. **78**, 4111 (1997).

[212] X.-G. Wen and P.A. Lee, Phys. Rev. Lett. **80**, 2193 (1998).

[213] L.B. Ioffe and A. J. Millis, J. Phys. Chem. Solids, **63**, 2259 (2002).

[214] D.M. Broun, P.J. Turner, W.A. Huttema, S. Ozcan, B. Morgan, R. Liang, W.N. Hardy, and D.A. Bonn, cond-mat/0509223 (unpublished).

[215] I.F. Herbut, Phys. Rev. Lett. **94**, 237001 (2005).

[216] R. Sensarma, M. Randeria, N. Trivedi, cond-mat/0607006 (unpublished).

[217] D. Pines and P. Noziéres, *The Theory of Quantum Liquids* (Addison-Wesley) (1966).

[218] I. Dzyaloshinskii, Phys. Rev. B **68**, 085113 (2003).

[219] C. Gros, W. Wenzel, R. Valentí, G. Hülsenbeck, and J. Stolze, Europhys. Lett. **27**, 299 (1994).

[220] T.D. Stanescu, P.W. Phillips, and T.-P. Choy, cond-mat/0602280 (unpublished).

[221] J. Mesot, M. Randeria, M.R. Norman, A. Kaminski, H.M. Fretwell, J.C. Campuzano, H. Ding, T. Takeuchi, T. Sato, T. Yokoya, T. Takahashi, I. Chong, T. Terashima, M. Takano, T. Mochiku, and K. Kadowaki, Phys. Rev. B **63**, 224516 (2001).

[222] K.M. Shen, F. Ronning, D.H. Lu, F. Baumberger, N.J.C. Ingle, W.S. Lee, W. Meevasana, Y. Kohsaka, M. Azuma, M. Takano, H. Takagi, and Z.-X. Shen, Science **307**, 901 (2005).

[223] Y. Kohsaka, K. Iwaya, S. Satow, T. Hanaguri, M. Azuma, M. Takano, and H. Takagi, Phys. Rev. Lett. **93**, 097004 (2004).

[224] W.O. Putikka, M.U. Luchini, and R.R.P. Singh, Phys. Rev. Lett. **81**, 2966 (1998).

[225] T.A. Maier, T. Pruschke, and M. Jarrell, Phys. Rev. B **66**, 075102 (2002).

[226] J.C. Campuzano, H. Ding, M.R. Norman, M. Randeira, A.F. Bellman, T. Yokoya, T. Takahashi, H. Katayama-Yoshida, T. Mochiku, and K. Kadowaki, Phys. Rev. B **53**, R14737 (1996).

[227] F. Ronning, C. Kim, D. L. Feng, D. S. Marshall, A. G. Loeser, L. L. Miller, J. N. Eckstein, I. Bozovic, and Z.-X. Shen, Science **282**, 2067 (1998).

[228] A. Rosch, cond-mat/0602656 (unpublished).

[229] W. Marshall, Proc. Roy. Soc. (London) A **232**, 48 (1955).

[230] J. Richter, N.B. Ivanov, and K. Retzlaff, Europhys. Lett. **25**, 545 (1994).

[231] P.W. Anderson, Nature Physics **2**, 626 (2006).

Curriculum Vitae

Bernhard Edegger

WORKING ADDRESS

Institut für Theoretische Physik
Max-von-Laue-Str. 1
60438 Frankfurt am Main
Germany
Phone: +49 69 798-47825
Fax: +49 69 798-47832
Email: bernhard.edegger@itp.uni-frankfurt.de

PERSONAL DETAILS

Gender: Male
Date of birth: 11th of March, 1981
Place of birth: Graz, Austria
Citizenship: Austrian

EDUCATION

since 04/2005	PhD studies at the "Johann Wolfgang Goethe University" (Frankfurt) under the supervision of Prof. Claudius Gros PhD thesis on "High temperature superconductivity"
10/2004–03/2005	PhD studies at the "Universität des Saarlandes" under the supervision of Prof. Claudius Gros
10/1999–04/2004	Technical University Graz (TU Graz) Graduated in Technical Physics with honors Diploma Thesis on "Charge Order in NaV_2O_5" under the supervision of Prof. Hans Gerd Evertz (Theoretical Physics)
09/1995–06/1999	Gymnasium Deutschlandsberg Passed "Matura" with honors

Research Stays

10/2006	University of Hong Kong, Hong Kong Collaboration with Prof. F.C. Zhang
2005-2006	3 stays at Princeton University (USA) with a duration of 5 month in total Collaboration with Prof. P.W. Anderson and Prof. V.N. Muthukumar
11/2003	Phillips-University Marburg, Germany Collaboration with Prof. R. Noack

Scientific Work

2 papers published in Physical Review Letters

1 paper published in Proceedings of the National Academy of Sciences

4 papers published in Physical Review B

Referee for Physical Review B

Presentations at 9 conferences/workshops within the last 3 years

Veröffentlichungen von Bernhard Edegger

9 B. Edegger, V. N. Muthukumar, and C. Gros,
"Renormalization of the nodal quasiparticle current in the Resonating Valence Bond (RVB) theory",
Physica C (in Print, M2S-HTSC Proceedings).

8 B. Edegger, V. N. Muthukumar, and C. Gros,
"Spontaneous breaking of the Fermi surface symmetry in the $t-J$ model: a numerical study",
Phys. Rev. B **74**, 165109 (2006).

7 C. Gros, B. Edegger, V. N. Muthukumar, and P. W. Anderson,
"Determining the underlying Fermi surface of strongly correlated superconductors",
PNAS **103**, 14298 (2006).

6 B. Edegger, V. N. Muthukumar, C. Gros, and P. W. Anderson
"Electronic structure of strongly correlated d-wave superconductors",
Phys. Rev. Lett. **96**, 207002 (2006).

5 B. Edegger, H. G. Evertz, R. Noack
"Creation and destruction of a spin gap in weakly coupled quarter-filled ladders",
Phys. Rev. Lett. **96**, 146401 (2006).

4 B. Edegger, N. Fukushima, V. N. Muthukumar, C. Gros
"Particle number renormalization in nearly half filled Mott Hubbard superconductors",
Phys. Rev. B **72**, 134504 (2005).

3 N. Fukushima, B. Edegger, V.N. Muthukumar, C. Gros,
"Evaluation of matrix elements in partially projected wave functions",
Phys. Rev. B **72**, 144505 (2005).

2 B. Edegger, H. G. Evertz, R. Noack
"Charge order induced by electron-lattice interaction in NaV_2O_5",
Phys. Rev. B **72**, 085131 (2005).

1 B. Edegger
"Charge ordering in NaV_2O_5",
Diploma Thesis, TU Graz (2004).

Danksagung

Am Ende meiner Doktorarbeit möchte ich mich bei allen Menschen bedanken, die mich in den letzten Jahren unterstützt und mir ermöglicht haben so erfolgreich auf dem Gebiet der Hochtemperatursupraleitung zu arbeiten.

In diesem Zusammenhang bin ich vor allem meinem Betreuer Prof. C. Gros sehr dankbar, der mir die Gelegenheit zu so vielen Forschungsaufenthalten sowie auch Workshop- und Konferenzteilnahmen gab. Zudem ermöglichte er mir immer ein sehr flexibles Arbeiten, das auch sicherlich sehr zum guten Gelingen meiner Arbeit beigetragen hat.

Neben Prof. C. Gros, profitierte ich sehr von der Zusammenarbeit mit Prof. V.N. Muthukumar, der auch wesentlich für das Zustandekommen und die Finanzierung meiner Forschungsaufenthalte an der Princeton University verantwortlich war.

Prof. P.W. Anderson danke ich für interessante Diskussionen und die bereitwillige Übernahme der Begutachtung. Weiters bin ich Prof. F.C. Zhang dankbar für die Einladung und Finanzierung meines Forschungsaufenthaltes an der University of Hong Kong.

Zudem danke ich den vielen, hier nicht einzeln erwähnten, Mitarbeitern an den Physikinstituten in Saarbrücken und in Frankfurt, die mir bei kleinen wie auch größeren Problemen behilflich waren.

Meiner Familie danke ich für die Geduld und die stetige moralische Unterstützung.